

COMPOSITE MATERIALS

Testing, Design, and Acceptance Criteria

ABDUL-HAMID ZUREICH
ALAN T. NETTLES
Editors

STP 1416



STP 1416

Composite Materials: Testing, Design, and Acceptance Criteria

A. Zureick and A. T. Nettles, editors

ASTM Stock Number: STP1416



ASTM International
100 Barr Harbor Drive
PO Box C700
West Conshohocken, PA 19428-2959

Printed in the U.S.A.

Library of Congress Cataloging-in-Publication Data

Composite materials : testing, design, and acceptance criteria / A. Zureick and A. T.

Nettles, editors.

p. cm.

"ASTM stock number: STP1416."

Includes bibliographical references and index.

ISBN 0-8031-2893-2

1. Composite materials—Congresses. I. Zureick, Abdul-Hamid. II. Nettles, A. T. (Alan T.)

TA418.9.C6 C5545 2002

620.1'18—dc21

2002066562

Copyright © 2002 AMERICAN SOCIETY FOR TESTING AND MATERIALS INTERNATIONAL, West Conshohocken, PA. All rights reserved. This material may not be reproduced or copied, in whole or in part, in any printed, mechanical, electronic, film, or other distribution and storage media, without the written consent of the publisher.

Photocopy Rights

Authorization to photocopy items for internal, personal, or educational classroom use, or the internal, personal, or educational classroom use of specific clients, is granted by ASTM International provided that the appropriate fee is paid to the Copyright Clearance Center, 222 Rosewood Drive, Danvers, MA 01923; Tel: 978-750-8400; online: <http://www.copyright.com/>.

Peer Review Policy

Each paper published in this volume was evaluated by two peer reviewers and at least one editor. The authors addressed all of the reviewers' comments to the satisfaction of both the technical editor(s) and the ASTM Committee on Publications.

To make technical information available as quickly as possible, the peer-reviewed papers in this publication were prepared "camera-ready" as submitted by the authors.

The quality of the papers in this publication reflects not only the obvious efforts of the authors and the technical editor(s), but also the work of the peer reviewers. In keeping with long-standing publication practices, ASTM International maintains the anonymity of the peer reviewers. The ASTM Committee on Publications acknowledges with appreciation their dedication and contribution of time and effort on behalf of ASTM International.

Foreword

This publication, *Composite Materials: Testing, Design, and Acceptance Criteria*, contains papers presented at the symposium of the same name held in Phoenix, Arizona, on 26–27 March, 2001. The symposium was sponsored by ASTM International Committee D30 on Composite Materials. The symposium co-chairmen were A.-H. Zureick, Georgia Institute of Technology, Atlanta, Georgia and A. T. Nettles, NASA Marshall Space Flight Center, Huntsville, Alabama.

Contents

Tabbed Versus Untabbed Fiber-Reinforced Composite Compression Specimens —D. F. ADAMS	3
Multi-Axial Composite Tube Test Method —D. COHEN	17
Finite Element Analysis of Unidirectional Composite Compression Test Specimens: A Parametric Study —P. J. JOYCE, M. G. VIOLETTE, AND T. J. MOON	30
Structural Integrity Assessment of Composite Pressure Test Box Through Full Scale Test —B. K. PARIDA, P. K. DASH, S. A. HAKEEM, AND K. CHELLADURAI	69
Qualification Using a Nested Experimental Design —D. RUFFNER AND P. JOUIN	85
The Development and Use of a Common Database for Composite Materials —P. SHYPRYKEVICH, J. S. TOMBLIN, AND M. G. VANGEL	99
A Comparison of Quasi-Static Indentation Testing to Low Velocity Impact Testing —A. T. NETTLES AND M. J. DOUGLAS	116
Detection and Characterization of Imperfections in Composite Pressure Vessels —J. L. WALKER, S. S. RUSSELL, AND M. D. LANSING	131
Damage Resistance and Damage Tolerance of Pultruded Composite Sheet Materials —R. PRABHAKARAN, M. SAHA, M. DOUGLAS, AND A. T. NETTLES	139
Mechanical Degradation of Continuous Glass Fibre-Reinforced Thermoplastics Under Static and Cyclic Loading: A Prepreg Laminate—Technical Textile Comparison —J. F. NEFT, K. SCHULTE, AND P. SCHWARZER	156
Philosophies for Assessing Durability of Commercial and Infrastructure Composite Systems —S. W. CASE, K. L. REIFSNIDER, AND J. J. LESKO	173
Computational Prediction of Yarn Structure of 3D-Braided Composites —G. TERPANT, P. KRISHNASWAMI, AND Y. WANG	188

Principles for Recovering Micro-Stress in Multi-Level Analysis—Y. WANG, C. SUN, X. SUN, AND N. J. PAGANO	200
Measurement of CTE at Reduced Temperature for Stressed Specimens— H. ZHU, W.-Y. LI, A. A. TSENG, AND P. PHELON	212
The Effect of Moisture, Matrix and Ply Orientation on Delamination Resistance, Failure Criteria and Fracture Morphology in CFRP— E. S. GREENHALGH AND S. SINGH	221
Interlaminar Crack Propagation in CFRP: Effects of Temperature and Loading Conditions on Fracture Morphology and Toughness—A. SJÖGREN, L. E. ASP, E. S. GREENHALGH, AND M. J. HILEY	235
Buckling and Fracture Behavior of Tapered Composite Panels Containing Ply Drops—B. K. PARIDA, K. VIJAYARAJU, AND P. D. MANGALGIRI	253
Author Index	271
Subject Index	273

Donald F. Adams¹

Tabbed Versus Untabbed Fiber-Reinforced Composite Compression Specimens

Reference: Adams, D.F., "Tabbed Versus Untabbed Fiber-Reinforced Composite Compression Specimens," *Composite Materials: Testing, Design, and Acceptance Criteria, ASTM STP 1416*, A. Zureick and A.T. Nettles, Eds., American Society for Testing and Materials International, West Conshohocken, PA, 2002.

Abstract: The development of suitable specimen configurations and loading methods for the compression testing of high strength composite materials has received considerable attention during the past decade, and especially during the past five years. Both experimental and analytical investigations of very specific aspects of specimen and test fixture configurations have been performed. Many seemingly conflicting results have been presented, leading to considerable confusion within the composite materials testing community. However, a definite conclusion appears to now be emerging, viz., the use of tabs on compression test specimens has a detrimental influence on measured strength. This has been qualitatively suspected for some time since analytical studies and detailed finite element analyses consistently predict induced stress concentrations at the tab ends of the specimen gage section. Numerous approaches have been followed to minimize these stress concentrations, of course including the total elimination of tabs. Key analytical and experimental results, taken from the extensive published literature as well as from the author's own recent work, are presented and compared, to demonstrate the consistent trends that actually do exist in the seemingly scattered and confusing published literature. Finally, options currently available for the successful compression testing of high strength composite materials are presented.

Keywords: compression testing, compressive strength, specimen configurations, specimen tabs, loading methods, analysis, testing

The Purpose of Specimen Tabs

There are two fundamental ways of applying a compressive force to laboratory test specimens, viz., end loading or shear loading. As implied, end loading is the direct application of opposing compressive forces at the ends of the specimen. Shear loading is the application of opposing shear force distributions at each end of the specimen; these shear forces being distributed over some prescribed length of the specimen faces. These shear forces induce a compressive force in the gage section of the specimen, i.e.,

¹ President, Wyoming Test Fixtures, Inc., 421 S. 19th Street, Laramie, WY 82070, and Professor Emeritus, Mechanical Engineering Department, University of Wyoming, Laramie, WY 82071.

the central region of the specimen between the end regions where the shear forces are applied.

High strength composite materials, e.g., those exhibiting axial compressive strengths above about 1 GPa (150 ksi), are particularly difficult to test using either of these load introduction methods. Such materials tend also to be relatively stiff, and highly orthotropic. In particular, the transverse tensile and compressive strengths and the longitudinal shear strength are low relative to the axial compressive (and tensile) strength. A unidirectionally reinforced composite material is an example of such a composite.

End loading typically results in crushing of the specimen ends, due to the difficulty of introducing the compressive force uniformly over the end of the specimen (being compounded by the high stiffness of the material). Any loading nonuniformity creates local stress concentrations, which are not readily redistributed because of the high orthotropy of the material (in particular here a relatively low shear strength), leading to premature failure (brooming and crushing) at the specimen ends. The most common method of reducing the average stress at the specimen ends and thus making the stress concentrations less critical is to bond tabs (doublers) adhesively on opposing faces at each end of the specimen, as shown in Figure 1. These tabs increase the contact area over which the end loading is applied. Thus, when local stress concentrations do occur at the ends, the maximum stress will hopefully still be less than that in the gage section of the specimen, resulting in gage section failures as desired. Of course, any force applied at the end of a tab must be transferred via shear into the test specimen itself over the length of the tab. Thus, a tabbed, end-loaded specimen is effectively being subjected to a combination of end and shear loading.

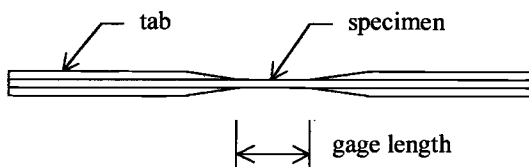


Figure 1 – *Typical tapered tab compression test specimen.*

In the case of pure shear loading, all of the applied force is introduced via a shear transfer mechanism. Although end crushing is nonexistent, local stress concentrations are still a problem, occurring along the specimen surfaces where the shear forces are acting. These shear forces are applied using grips of some type, which clamp the specimen surfaces at each end and transfer force by friction. Smooth, flat grip surfaces would aid, although not guarantee, uniform shear force transfer. However, smooth grip surfaces result in relatively low coefficients of friction, thus requiring very high clamping forces to prevent slipping. But by definition, the transverse (here compressive) strength of the highly orthotropic material being tested is relatively low, resulting in potential crushing of the specimen in the gripped regions. Thus, more aggressive grip faces are usually used, which dig into the surface of the specimen, increasing the effective coefficient of friction and permitting the use of lower clamping forces. These aggressive grip faces would

damage the surface of the test specimen, weakening the material. Thus, tabs are bonded onto the specimen surfaces to protect them.

In summary, whether end- or shear-loaded, the test of a high compressive strength specimen typically incorporates tabs.

The Detrimental Consequences of Using Tabs

For the reasons discussed in the previous section, high compressive strength composite material test specimens typically incorporate adhesively bonded tabs. Detailed stress analyses, particularly finite element analyses, conducted during the past ten or more years, have clearly shown that stress concentrations are induced in the test specimen at the ends of the tabs adjacent to the gage length [1-14]. A typical example is shown in Figure 2. Transverse normal and longitudinal shear stress concentrations exist also. How detrimental these stress concentrations actually are in reducing the measured compressive strength of the material has not been clearly established. Nevertheless, extensive studies, both analytical and experimental, have been conducted to seek ways of reducing these stress concentrations.

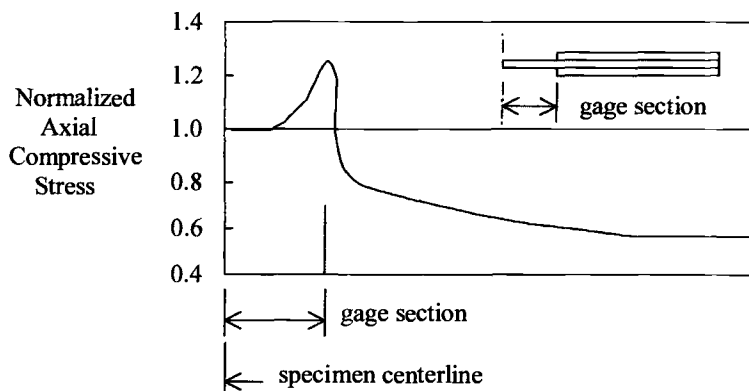
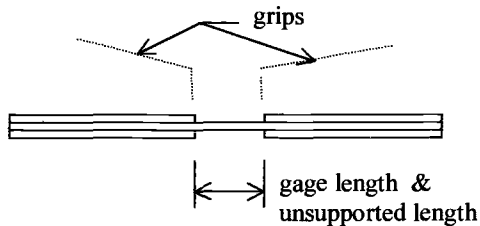


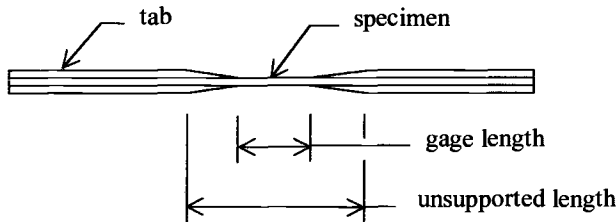
Figure 2 – Schematic of a typical axial compressive stress distribution along the length of a tabbed specimen near its surface.

Only relatively recently have some general conclusions been generally accepted. These will be discussed in detail later. However, in brief summary, more compliant tabs reduce the stress concentrations. But compliant materials tend not to be as strong as stiffer materials, compliance and strength typically being contrary properties. The tabs must be strong enough to transfer the required shear stresses from the testing machine grips to the specimen. Thus a compromise must be made. Tapering the ends of the tabs at the gage section also reduces the induced stress concentrations. Thus the more taper the better. However, the longer the taper, the longer the unsupported length (between the grips) of

the specimen, as shown in Figure 3, which can induce gross buckling rather than a compressive failure. Thus, once again a compromise must be made, resulting in the stress concentration possibly being reduced, but not eliminated.



a) untapered (90°) tabs



b) tapered tabs

Figure 3 – *Unsupported specimen lengths of tabbed specimens of equal gage length.*

Of course, making the long gage length specimen thicker can prevent buckling. However, the axial compressive stress through the thickness of the specimen gage section then becomes more nonuniform, the stresses introduced at the specimen surfaces tending to remain localized at these surfaces. For example, Figure 4 indicates that even at the center of the gage section, i.e., at the maximum distance from the tab ends, the axial compressive stress in a 10 mm (0.39 in.) thick specimen has still not attained a uniform stress state, although the stress is relatively uniform for a 2 mm (0.080 in.) thick specimen. This stress nonuniformity in a thick specimen compounds the seriousness of the stress concentrations at the tab ends. Thus, simply increasing the specimen thickness by adding additional layers having the same lay-up as the original laminate is not a viable solution.

Since tabs are typically bonded to the test specimen, optimum adhesive material properties and bond line thicknesses have been studied. Just as for the tab material itself, a more compliant adhesive is better. Correspondingly, a thicker bond line is better, being better able to blunt the stress concentration induced by the tab. However, just as for the tabs, more compliant adhesives tend to be lower in shear strength than stiff adhesives. Also, thick bond lines tend to be weaker than thin bond lines because of the less favorable

stress states that develop under shear loading. Thus, the best adhesive in terms of reducing stress concentrations may not be strong enough to transfer the required shear loads. Once again a compromise must be made when selecting the adhesive, and the stress concentration is not eliminated.

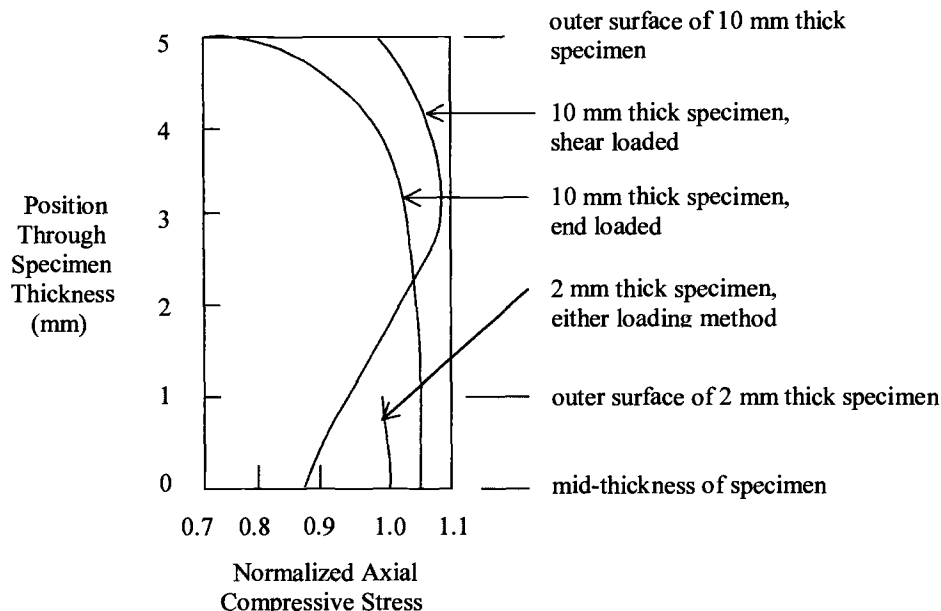


Figure 4 – Axial compressive stress distribution through the thickness of a tabbed specimen at the mid-length of the gage section for two different loading conditions (untapered steel tabs, 0.18 mm thick adhesive bond line, end loading).

The Perceived Current Status of Compression Testing

As a result of the problems summarized in the two previous sections, the compression testing of high strength composite materials has remained a compromise. Equally unfortunate, but understandably, different groups have selected different compromises, with equally justifiable reasons. Thus, consensus is not likely to be achieved under the present state of affairs.

One common, but by no means universally accepted, compromise at present is to utilize end loading (such as the so-called Modified ASTM D 695 Compression Test Method, which will be defined later), untapered compliant tabs (such as glass fabric/epoxy), and a strong adhesive of medium bond line thickness (many of which are available). Many would disagree with this compromise.

Before presenting a new appraisal of the current status of compression testing, it is important to summarize recent key studies, both analytical and experimental, which permit

this new view. The available literature tends to be very scattered, and thus a concentrated effort has been made to gather and digest it, as summarized in the following two sections.

Key Analyses

It will be noted that the first fourteen references here are listed chronologically. Although a few simple, closed form analyses were attempted initially [2,3], most of the major works have been finite element analyses [1, 4-14]. Significant interest in characterizing the compression properties of composite materials was just emerging at the time most of these works were being published. For example, the first ASTM test method developed specifically for compression testing high performance composite materials, ASTM Test Method for Compressive Properties of Polymer Matrix Composite Materials with Unsupported Gage Section by Shear Loading (D 3410), was not issued until 1975. At that time, it contained only the so-called Celanese compression test method, the IITRI compression test method not being added to this standard until 1987. It was at about this same time that Bogetti, et. al. [4] and Westberg and Abdallah [5] published their frequently quoted finite element analyses.

However, one of the first researchers to analyze in depth the problems associated with the then accepted methods of compression testing composite materials was Tan [6-8], in the early 1990s. This was soon followed by the extensive finite element analyses of Xie and Adams [11-14]. Most of the prior analyses in the published literature, including those by Tan, had been two-dimensional and linearly elastic in nature. Xie and Adams developed and utilized a three-dimensional elastoplastic analysis of the orthotropic composite material [15,16]. Interestingly, their results showed that for the particular problem of analyzing a highly orthotropic (typically unidirectional) composite material compression specimen, a three-dimensional analysis was not generally necessary. The variations in stresses across the width of the specimen were shown to be negligible, and the influences of material nonlinearities were relatively small. This was a significant finding in that it gave additional confidence in all of the prior analyses, and permitted the use of much simpler two-dimensional linearly elastic analyses in future studies.

While there are always worthwhile additional analyses that can be performed, it appears that the predictions of compression specimen stress states now available in the literature, as referenced above, almost all lead to the same general conclusions, as summarized below.

- The clamping forces exerted on the specimen by the grips used to apply a shear loading introduce a significant axial compressive stress concentration right at the ends of the grips. This stress concentration is very localized.
- When tabs are used on either shear-loaded or end-loaded compression specimens, axial stress concentrations are also induced in the specimen at the ends of the tabs. These stresses are more severe for shear-loaded specimens since the tab influences then combine with the grip influences noted above.
- The tab- and grip-induced through-thickness normal stresses and longitudinal shear stresses, while low in magnitude relative to the axial compressive stress, are not always negligible because the corresponding strengths of the material are also

relatively low. Either individually or in combination with the axial compressive stress they can cause failure in some cases.

- Away from the region of local stress concentration, the axial compressive stress is more uniform through the thickness for a thinner specimen. Since tabs transfer forces into the specimen at the specimen surface, some axial distance is required for the axial compressive stress to become uniform through the thickness of the specimen, and for the transverse normal and longitudinal shear stresses to decay to zero. That is, even though the surface stress concentration at the ends of the tabs decays within a relatively short distance into the gage section, typically within 0.013-0.025 mm (0.050-0.100 in.), the compressive stress near the specimen surface of a thick, shear-loaded specimen may still be significantly higher than that in the interior, even at a considerable distance from the tab end.
- More compliant tabs, a more compliant adhesive, a thicker adhesive bond line, a smaller tab taper angle, and end loading rather than shear loading all reduce the stress concentration at the tab tip to varying degrees, but they do not eliminate it. As discussed in the previous section, there is always a trade-off that must be made, so that the most favorable limits of each of these parameters individually cannot be attained.

Key Experimental Studies

The increasing amount of experimental data that has become available during the past several years is now strongly supporting the conclusions of the analytical studies cited above. Publications of experimental results of particular significance include [5, 17-37]. Again, these references are listed in chronological order here, to emphasize the rate of data generation in recent years. Reviews are presented in [38-41].

As one example of the progress that has been made, Smoot [17] in his M.S. thesis work published in 1982, indicated that there was an influence of the specimen gage length being short, although the prior work of Westberg and Abdallah [5] had not indicated such. It was not until the detailed experimental work of Adams and Lewis [24] was published nine years later, in 1991, that this view changed. This was a significant finding since the then (and still) commonly used test method, "Compressive Properties of Oriented Fiber-Resin Composites," (SACMA Recommended Method SRM1-88), utilizes a very short 0.048 mm (0.188 in.) gage length specimen. For example, ASTM D 3410 recommends a 12.7 mm (0.50 in.) gage length, more than two and one-half times longer. Reference [24] clearly demonstrated that measured compressive strength is not dependent on specimen gage length (as long as Euler buckling does not occur). Figure 5 is a sketch of some of the above data, indicating that, until the onset of buckling, there is no significant influence of specimen gage length, even for very short gage lengths. In fact, for the 0.025 mm (0.1 in.) specimens tested in Reference 24, the tabs were almost touching at failure due to elastic deflections, indicating this to be very close to a lower limit of gage length. All specimens tested to generate Figure 5 had similar widths and thicknesses.

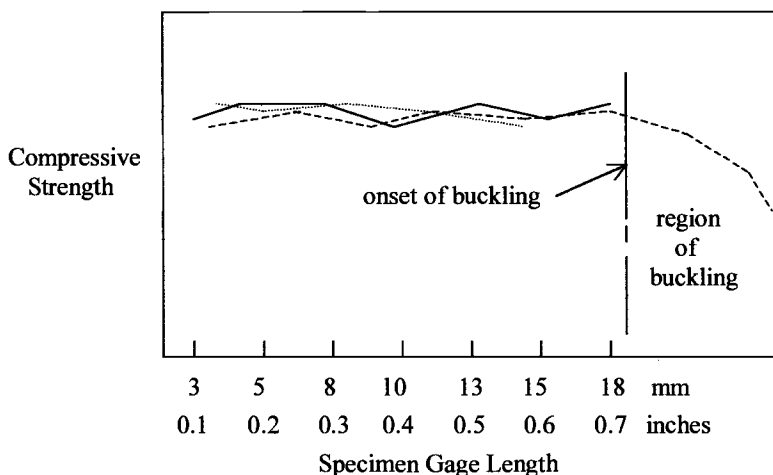


Figure 5 – Compressive strength of unidirectional carbon/epoxy composites as a function of specimen gage length..

Some of the early experimental efforts were also not well controlled. For example, in the early 1980's ASTM conducted round robin testing [24] to compare the above two test methods. The SACMA SRM1-88 method faired very poorly, and thus was not added to the standard during the next revision of ASTM D 3410 in 1987. Yet it has since been convincingly demonstrated [24, 28, 29, 31-34, 40] since then that in fact it produces results at least as good as the ASTM D 3410 method. A number of the laboratories participating in the ASTM round robin had never even previously used the SACMA SRM1-88 method, and did not conduct the tests properly.

Because of the difficulties associated with compression testing high strength composites, true strengths were not being achieved at the time. Thus, sometimes even minor modifications to test methods resulted in noticeable increases in measured strengths. This led to a period of significant activity to achieve higher and higher compressive strengths, which were assumed to be closer to the "true" strength. Kim and Crasto [18,22] were among the first, with their "mini-sandwich" axial compression specimen, viz., thin unidirectional composite layers bonded to the surfaces of a neat resin core. They "backed out" the composite strength using a simple analysis. Several years later Welsh and Adams [28,32] replicated and extended their results. The mini-sandwich specimen produced compressive strengths from 25 to 50% higher than any being obtained with the ASTM and SACMA standard tests.

At about the same time the concept of testing cross-ply or angle-ply laminates containing 0° plies and then backing out the 0° ply axial strength was introduced [42], as summarized in [40]. Detailed results are presented in [28,29,33]. Compressive strengths as much as 75 percent higher than those obtained using the standard tests were obtained.

It was finally realized that the values being obtained in the laboratory under special testing conditions, while perhaps approaching the true compressive strengths of the various unidirectional composite materials tested, were not those that would be attained

in an actual composite structure [34,40]. What were needed were design values. The published literature was searched for typical laminate strength data, from which the unidirectional ply axial strength was backed out [34]. It was found that for any given composite material there was, within experimental scatter, a common 0° ply axial compressive strength. All of the available compression test methods were then reevaluated, to determine which produced this "design value". It was found that the mini-sandwich specimen, the thickness-tapered specimen [30], and [90/0]_{ns} cross-ply laminate test configurations were all suitable. Testing of a [90/0]_{ns} laminate is particularly attractive as an untabbed straight-sided test specimen can be used with a combined loading test fixture, as will be discussed. The SACMA SRM1-88 test method is not suitable without tabs, as end crushing may occur, as previously discussed. The ASTM D 3410 methods are also less desirable because of the high clamping forces exerted on the specimen by the wedge grips.

This quest for higher and higher compressive strengths again raised the issue as to the degrading influence of specimen tabs. Perhaps a key work, which has received relatively little attention to date, was that by Tan and Knight [9]. They determined the influence of specimen tabs by analyzing and testing unidirectional composite specimens with tapered tabs of various taper angles. In particular, they tested specimens with tab taper angles of 14°, 30°, 45° and 90°, although they did not report any 14° taper data (presumably because all of those specimens buckled). Although they used short gage length (5.08 mm, i.e., 0.20 in.) specimens, they encountered increasing problems of specimen buckling as the tab taper angle was decreased (as the unsupported length increased, as discussed previously in relation to Figure 3). Thus, their amount of valid data was limited. They plotted measured compressive strength versus tab taper angle for their valid data and then extrapolated the strength to zero taper angle. In this way they estimated the strength of an untabbed specimen.

What is particularly interesting is that, now studying their results in retrospect, the extrapolated compressive strength values they obtained agree very well with the attained "design values" discussed in the previous paragraph, which were not established until several years later. Also interesting is that the influence of tab taper angle (the presence of tabs) was not negligible. For example, for a unidirectional carbon/epoxy composite, the compressive strength increased from 1.34 GPa (194 ksi) for 90° tabs to 1.69 GPa (245 ksi) for 30° tabs, and to an extrapolated value of 1.92 GPa (278 ksi) for no tabs. The difference between the 30° and 90° tab taper results is much greater than the three to six percent difference observed by Adams and Odom [25] three years earlier using the same carbon/epoxy composite material. However, the trends were the same. Adams and Odom [25] had not considered their own results to be conclusive as their differences were about the same as the scatter in their experimental data. Tan and Knight did note the existence of Reference 25, but did not discuss its contents or make any comparisons with their own results. Again in retrospect, the data of Adams and Odom [25] appear to have been trying to send a message.

Development of a New ASTM Standard

These types of results ultimately led to the development of a new test fixture for testing cross-ply laminates, the Wyoming Combined Loading Compression (CLC) Test

Method [34,37], which has now been adopted by ASTM as "Standard Test Method for Determining the Compressive Properties of Polymer Matrix Composite Laminates Using a Combined Loading Compression (CLC) Test Fixture" (ASTM D 6641-01). An untabbed, straight-sided test specimen is lightly clamped (relative to the ASTM D 3410 methods) at each end between blocks having roughened surfaces. Thus, a significant

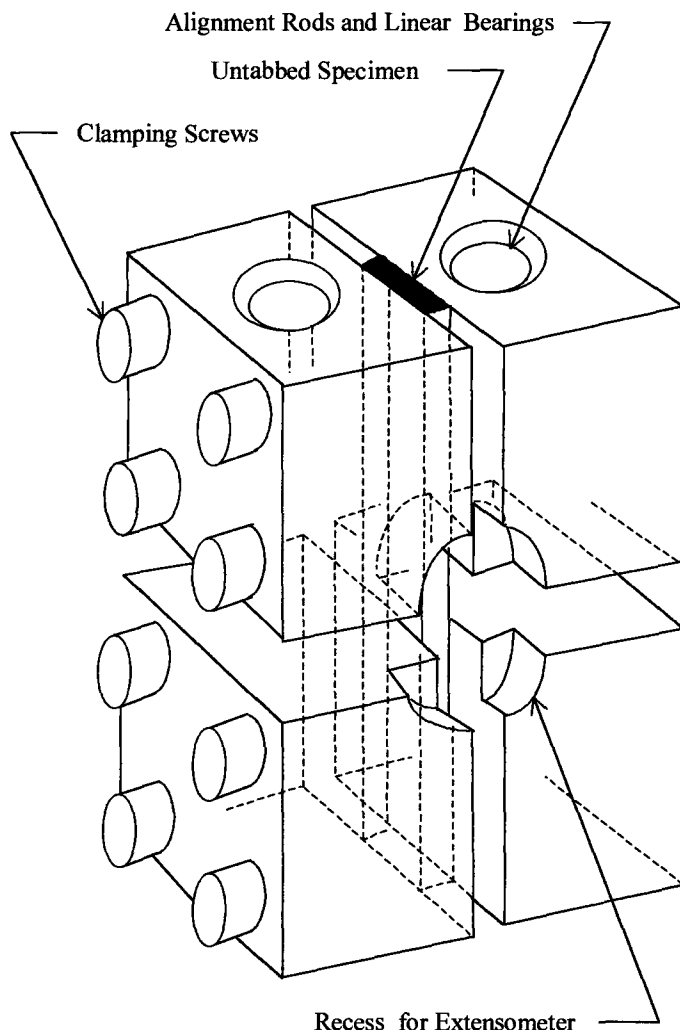


Figure 6 – Wyoming combined loading compression (CLC) test fixture (ASTM D 6641-01) with untabbed specimen installed.

shear loading component can be attained without the detrimental influences of either tabs or wedge grips. This shear loading component reduces the end loading sufficiently so that end crushing does not occur. An added bonus is that the test specimen is close to the ultimate in simplicity. A sketch of the CLC fixture is shown in Figure 6. Full details of the use of the fixture are given in ASTM D 6641-01.

This CLC fixture can also be used to test other laminates [34], including unidirectional composites [35]. However, if the laminate strength is too high, either end crushing will occur or the clamping force (shear component) necessary to prevent end crushing becomes so high that stress concentrations are introduced, just as when using tabbed specimens or wedge grips. Extensive experimental data for a wide range of laminate configurations are presented in Reference 34.

In this case, one very viable modification is to use an untabbed thickness-tapered specimen with the CLC fixture [30,35]. This is particularly attractive when testing unidirectional composites. This concept is beginning to attract attention now that it has been demonstrated [30,35] that thickness-tapering a specimen is not difficult, a primary concern of potential users. Experimental data are contained in both of these references.

Summary

It has now been adequately demonstrated, both analytically and experimentally, that the use of conventional tabs on compression specimens is not an acceptable approach to attaining design values for high axial compressive strength composites. The tabs always introduce detrimental stress concentrations. Correspondingly, the use of wedge grips is not desirable. They introduce through-thickness stresses, and local stress concentrations at the grip ends. End loading of an untabbed specimen cannot be performed because of end crushing.

The most attractive approach at the present time is to test an untabbed, straight-sided specimen of constant thickness in a combined loading compression test fixture [34]. If the axial compressive strength of the specimen is so high that an unacceptable level of fixture clamping force is required to prevent end crushing (e.g., a high strength unidirectional composite), the specimen can be thickness-tapered [30,35]. This reduces the total applied force required at the specimen ends to initiate a failure in the reduced thickness (gage) section, thus eliminating end crushing.

References

- [1] Woolstencroft, D.H., Curtis, A.R., and Haresceugh, R.I., "A Comparison of Test Techniques Used for the Evaluation of the Unidirectional Compressive Strength of Carbon Fibre-Reinforced Plastic," *Composites*, Vol 12, 1981, pp. 275-280.
- [2] Reiss, R., Yao, T.M., and Clark, R.K., "Effect of Load Introduction in Compression Testing of Composite Laminates," *Compression Testing of Homogeneous Materials and Composites, ASTM STP 808*, R. Chait and R. Papirno, Eds., American Society for Testing and Materials, West Conshohocken, PA, 1983, pp. 200-220.
- [3] Rehfield, L.W., Armanios, E.A., and Changli, Q. "Analysis of Behavior of Fibrous Composite Compression Specimens," *Recent Advances in Composites in the United States and Japan, ASTM STP 864*, J.R. Vinson and M. Taya, Eds.,

- American Society for Testing and Materials, West Conshohocken, PA, 1985, pp. 236-252.
- [4] Bogetti, T.A., Gillespie, Jr., J.W., and Pipes, R.B., "Evaluation of the IITRI Compression Test Method for Stiffness and Strength Determination," *Composites Science and Technology*, Vol. 32, 1988, pp. 57-76.
 - [5] Westberg, R.L., and Abdallah, M.G., "An Experimental and Analytical Evaluation of Three Compressive Test Methods for Unidirectional Graphite/Epoxy Composites," *Proceedings of the 6th International Congress on Experimental Mechanics - Vol. 1*, Society for Experimental Mechanics, Bethel, CT, 1988, pp. 350-361
 - [6] Tan, S.C., "Analysis of ASTM D 3410 Compression Test Specimens," *AIAA Journal*, Vol. 29, No. 1, 1990, pp. 1344-1346.
 - [7] Tan, S.C., "Stress Analysis and the Testing of Celanese and IITRI Compression Specimens," *Composites Science and Technology*, Vol. 44, 1992, pp. 57-70.
 - [8] Tan, S.C., "Analysis of a Mini-Sandwich Compression Test Specimen," *Composites Science and Technology*, Vol. 47, 1993, pp. 369-382.
 - [9] Tan, S.C., and Knight, M., "An Extrapolation Method for the Evaluation of Compression Strength of Laminated Composites," *Compression Response of Composite Structures, ASTM STP 1185*, S.E. Groves and A.L. Highsmith, Eds., American Society for Testing and Materials, West Conshohocken, PA, 1994, pp. 323-337.
 - [10] Kim, R.Y., Crasto, A.S., and Yum, Y.J., "Analysis of a Miniature Sandwich Compression Specimen," *Compression Response of Composite Structures, ASTM STP 1185*, S.E. Groves and A.L. Highsmith, Eds., American Society for Testing and Materials, West Conshohocken, PA, 1994, pp. 338-350.
 - [11] Xie, M., and Adams, D.F., "Effect of Specimen Tab Configuration on Compression Testing of Composite Materials," *Journal of Composites Technology & Research*, JCTRER, Vol. 17, No. 2, April 1995, pp. 77-83.
 - [12] Xie, M., and Adams, D.F., "Effect of Loading Method on Compression Testing of Composite Materials," *Journal of Composite Materials*, Vol. 29, No. 12, 1995, pp. 1581-1600.
 - [13] Xie, M. and Adams, D.F., "Influence of Unidirectional Composite Compression Specimen Thickness and Loading Method," *Proceedings of the American Society for Composites 10th Technical Conference on Composite Materials*, 1995.
 - [14] Adams, D.F., and Finley, G.A., "Analysis of Thickness-Tapered Unidirectional Composite Compression Specimens," *Journal of Composite Materials*, Vol. 31, No. 22, 1997, pp. 2283-2308.
 - [15] Xie, M., and Adams, D.F., "A Study of Compression and Shear Test Methods for Composite Materials Using a Nonlinear Finite Element Analysis," Report No. UW-CMRG-R-94-102, Composite Materials Research Group, University of Wyoming, Laramie, Wyoming, June 1994.
 - [16] Xie, M., and Adams, D.F., "A Plasticity Model for Unidirectional Composite Materials and its Applications in Modeling Composites Testing," *Composites Science and Technology*, Vol. 54, 1995, pp. 11-21.
 - [17] Smoot, M.A., "Compressive Response of Hercules AS1/3501-6 Graphite/Epoxy Composites," Report No. CCM-82-16, Center for Composite Materials, University of Delaware, Newark, DE, June 1982.

- [18] Kim, R.Y., and Crasto, A.S., "A Longitudinal Compression Test for Composites Using a Sandwich Specimen," *Journal of Composite Materials*, Vol. 26, No. 13, 1992, pp. 1915-1929.
- [19] Adsit, N.R., "Compression Testing of Graphite/Epoxy," *Compression Testing of Homogeneous Materials and Composites, ASTM STP 808*, American Society for Testing and Materials, West Conshohocken, PA, 1983, pp. 175-196.
- [20] Berg, J.S., and Adams, D.F., "An Evaluation of Composite Material Compression Test Methods," *Journal of Composites Technology and Research*, Vol. 11, No. 2, Summer 1989, pp. 41-46.
- [21] Odom, E.M., and Adams, D.F., "Failure Modes of Unidirectional Carbon/Epoxy Composite Compression Specimens," *Composites*, Vol. 21, No. 4, July 1990, pp. 289-296.
- [22] Crasto, A.S., and Kim, R.Y., "Compression Strengths of Advanced Composites from a Novel Mini-Sandwich Beam," *SAMPE Quarterly*, Vol. 22, No. 3, April 1991, pp. 29-39.
- [23] Adams, D.F., and Odom, E.M., "Influence of Test Fixture Configuration on the Measured Compressive Strength of a Composite Material," *Journal of Composites Technology and Research*, Vol. 13, No. 1, Spring 1991, pp. 36-40.
- [24] Adams, D.F., and Lewis, E.Q., "Influence of Specimen Gage Length and Loading Method on the Axial Compressive Strength of a Unidirectional Composite Material," *Experimental Mechanics*, Vol. 31, No. 1, March 1991, pp. 14-20.
- [25] Adams, D.F., and Odom, E.M., "Influence of Specimen Tabs on the Compressive Strength of a Unidirectional Composite Material," *Journal of Composite Materials*, Vol. 25, No. 6, June 1991, pp. 774-786.
- [26] Hahn, S.E., "An Experimental/Analytical Investigation of Combined Shear/End Loaded Compression Strength Testing of Unidirectional Composites, M.S. Thesis, Virginia Polytechnic Institute and State University, Blacksburg, VA, May 1992.
- [27] Hahn, S.E., and Reifsnider, K.L., "Combined Shear and End Loaded Compression Strength Testing of Advanced Composite Materials," *Proceedings of the 6th Japan-U.S. Conference on Composite Materials*, June 1992.
- [28] Welsh, J.S., and Adams, D.F., "Unidirectional Composite Compression Strengths Obtained by Testing Mini-Sandwich, Angle-, and Cross-Ply Laminates," Report No. UW-CMRG-R-95-106, Composite Materials Research Group, University of Wyoming, April 1995.
- [29] Welsh, J.S., and Adams, D.F., "Unidirectional Composite Compression Strengths Obtained by Testing Cross-Ply Laminates," *Journal of Composites Technology & Research*, Vol. 18, No. 4, October 1996, pp. 241-248.
- [30] Adams, D.F., and Finley, G.A., "Experimental Study of Thickness-Tapered Unidirectional Composite Compression Specimens," *Experimental Mechanics*, Vol. 36, No. 4, December 1996, pp. 348-355.
- [31] Welsh, J.S., and Adams, D.F., "Current Status of Compression Test Methods for Composite Materials," *SAMPE Journal*, Vol. 33, No. 1, January 1997, pp. 35-43.
- [32] Welsh, J.S., and Adams, D.F., "An Experimental Investigation of the Mini-Sandwich Laminate as Used to Obtain Unidirectional Composite Compression Strengths," *Journal of Composite Materials*, Vol. 31, No. 3, February 1997, pp. 293-314.

- [33] Welsh, J.S., and Adams, D.F., "Testing of Angle-Ply Laminates to Obtain Unidirectional Composite Compression Strengths," *Composites-Part A*, Vol. 28A, No. 4, April 1997, pp. 387-389.
- [34] Adams, D.F., and Welsh, J.S., "The Wyoming Combined Loading Compression (CLC) Test Method, *Journal of Composites Technology & Research*, Vol. 19, No. 3, July 1997, pp. 123-133.
- [35] Coguill, S.L., and Adams, D.F., "Use of the Wyoming Combined Loading Compression (CLC) Fixture to Test Unidirectional Composites," *Proceedings of the 44th International SAMPE Symposium*, May 1999, pp. 2322-2331.
- [36] Zhu, H., and Adams, D.F., "A Study of the Influence of Specimen Tabbing on the Failure of Unidirectional Composite Materials," Report No. UW-CMRG-R-99-109, Composite Materials Research Group, University of Wyoming, October 1999.
- [37] Wegner, P.M., and Adams, D.F., "Verification of the Combined Load Compression (CLC) Test Method," Report No. DOT/FAA/AR-00/26, Federal Aviation Administration Technical Center, Atlantic City, NJ, August 2000.
- [38] Camponeschi, E.T., Jr., "Compression of Composite Materials: A Review," Report No. DTRC-87/050, David Taylor Research Center, Annapolis, MD, November 1987.
- [39] Adams, D.F. "A Comparison of Composite Material Compression Test Methods in Current Use," *Proceedings of the 34th International SAMPE Symposium*, May 1989, pp. 1422-1433.
- [40] Adams, D.F., "Current Status of Compression Testing of Composite Materials," *Proceedings of the 40th International SAMPE Symposium*, May 1995, pp. 1831-1843.
- [41] Chaterjee, S.N., Adams, D.F., and Oplinger, D.W., "Test Methods for Composites, a Status Report, Vol. II. Compression Test Methods," Report No. DOT/FAA/CT-93/17, II, Federal Aviation Administration Technical Center, Atlantic City, NJ, June 1993.
- [42] Rawlinson, R.A., "The Use of Crossply and Angleply Composite Test Specimens to Generate Improved Material Property Data," *Proceedings of the 36th International SAMPE Symposium*, April 1991, pp. 1058-1068.

David Cohen¹

Multi-Axial Composite Tube Test Method²

Reference: Cohen, D., "Multi-Axial Composite Tube Test Method," *Composite Materials: Testing, Design, and Acceptance Criteria, ASTM STP 1416*, A. Zureick and A. T. Nettles, Eds., American Society for Testing and Materials International, West Conshohocken, PA, 2002.

Abstract: This paper discusses a new multi-axial 10.2-cm (4-in.) composite tube test method. This test method is capable of loading a 10.2 cm composite tube by internal pressure, torsion, and tension/compression. The method improves on an older biaxially loaded (internal pressure and axial load) tube design used extensively by Swanson and coworkers [1-5] to characterize the failure mode of fiber dominated pressure vessels.

The 10.2 cm tube test method has been used successfully to test composite tubes by internal pressure combined with torsion and axial tension/compression. Tubes were tested at both ambient and hot/wet conditions. Tubes with various lay-ups, including, hoop and helical, and all helical configurations were tested.

This paper discusses the development of the test method. This followed by the presentation of test data for $\pm 25/90/\pm 25$ composite tube loaded in biaxially (internal pressure combined with axial load), pure torsion, and combined biaxial with torsion load. The test data offered are limited due to space restriction. Additional data will be presented in other ASTM publications.

Keywords: tube, composite, multi-axial, test, pressure, torsion, tension/compression, helical, filament wound, carbon fiber, epoxy resin, failure criteria

While there is a significant body of research [5-14] related to the failure theory of anisotropic composite materials, interest in this subject area has not diminished. This is apparent from the a recent conference led by the United Kingdom Institute of Mechanical Engineering devoted to the subject of designing with fiber composites for critical applications [12]. The stated reason of the meeting, which was funded by the Engineering and Physical Sciences Research Council of the United Kingdom, was "to explore the failure of polymer-composite structures and debate the mechanisms and criteria for the prediction of their performance." It was further stated that "the meeting was chiefly memorable for the amount of heat and excitement that was generated over the question of the validity of established failure criteria."

¹ Technical Manager, Composites Development Center (CDC), Toray Composites (America), Inc. 19002 50th Ave. East, Tacoma, WA, 98446.

² This work was conducted while the author was employed by Alliant Techsystems, Inc.

While there are many failure criteria, there is a considerable lack of good experimental data to support or refute these criteria. A lot of coupon data is questionable because of the edge effect that may influence the initiation of failure. In addition, for the most part coupons can only be loaded in one loading mode at a time (i.e., tensile, compression, shear, etc). Composite tubes provide a unique structural component for conducting multi-axial composite tests, while eliminating the edge effect found in flat coupons.

Swanson et al. [1-5, 15] have used a 10.2 cm (4-in.) composite tube loaded biaxially to investigate the failure mode of fiber dominated internally pressurized structures. This test method has shown to be highly effective in determining and characterizing this failure mode. Swanson and his associates have shown that for such structures and failure modes the maximum fiber strain criterion was most accurate. It is interesting to note that this criterion was found to be valid regardless of the stress ratio imposed by varying the axial load component.

Over the past 20 years tubular composite samples loaded with internal pressure, axial load, torsional load, and/or a combination of these loads have been used by many other researchers [9, 16-21]. The need for the present development arose from the necessity to evaluate the strength of filament wound rocket motor composite boosters that were subjected to a combination of biaxial (internal pressure and axial load) and torsional load. At the time a modified version of Swanson's 10.2 cm biaxial tube could only be tested under relatively low combined biaxial and torsion (1,020 N-m) loads. Therefore, Swanson's tube test method was completely redone as highlighted in this paper. The paper does not discuss differences between this current test method and the many other methods presented in the literature. Rather, the focus is on this method's simplicity and versatility with possible application for standardization.

The objective of the current development was to improve on Swanson's 10.2 cm biaxial tube design to allow for internal pressure combined with axial tension/compression and torsion loads, simultaneously. The objective was then to generate a wide spectrum of composite multi-axial test data to be used in validating acceptable failure criteria, for pressure vessel applications, and in particular for the composite pressure vessel dome design. As a composite pressure vessel is pressurized, the dome laminate experienced significant material nonlinear performance associated with the highly nonlinear in-plane shear response. This is coupled with possible changes in the meridian stresses from tensile to compressive. The compressive stresses can also produce highly nonlinear responses in the material. The very significant material nonlinear behavior, coupled with the very notable geometric nonlinearity of the dome structure, makes accurate analysis and failure prediction of the dome structure very complex.

When the dome stresses are high enough, intralaminar cracks (crazing) will form leading to progressive damage. This damage does not lead to catastrophic structural failure, but does cause significant stiffness change and redistribution of stresses. In order to be able to predict such behavior accurately, the resin-dominated nonlinear response coupled with progressive damage needs to be incorporated into the analysis model (e.g., finite element). An accurate analysis model then needs to be coupled with failure criteria, which incorporate the progressive damage eventually leading to structural failure. The models to predict complex structural behavior ultimately need to be verified experimentally.

The current paper discusses upgrades to the Swanson 10.2 cm biaxial composite tube test method [1-5]. This upgrade consists of a 10.2 cm composite tube that can be loaded by internal pressure combined with tension/compression and torsion loads. This is followed by the presentation of test data for $\pm 25/90/\pm 25$ composite tube loaded biaxially, in pure torsion, and biaxial combined with torsion load. Biaxial test data is compared to old data generated with the old biaxial tube test method.

Approach

The tube design used by Swanson [1-5] had molded EC2216 adhesive tapped build-ups at the ends to transfer the axial load through an end gripping system. The tapered buildup had a conical shape used to transfer the axial load gradually into the gage section [1]. This particular design was not capable of transferring compression and/or torsion loads. The new tube design has glass build-ups (Figure 1) replacing the adhesive. The glass build-ups are wound as the multiple samples are fabricated and co-cured as one 244-cm (96-in.) long tube. The 244-cm long tube is cut into seven specimens and the glass build-ups are machined with tapers and a straight cylindrical section (Figure 1).

Following the machining step, two stainless steel end fittings are bonded to the tube (Figure 2). The steel end fittings are used to impart to the specimen the axial and torsion load components. The stainless steel end fittings have an outer part and an inner part that can be disassembled (Figure 1) for ease of bonding and removal following the test.



Figure 1—*Multi-axial composite tube.*



Figure 2—*Bonding of stainless steel ends.*

Before bonding, the end cap bonding surfaces are sand blasted and degreased. The glass end tabs are also cleaned and degreased before bonding. Following the tests, the end caps are removed by placing them in an oven at 400°C to break the adhesive bond. The end caps are cleaned and reused.

The 10.2-cm (4-in.) tube test hardware was designed for two test configurations. The first configuration is the standard biaxial test model (Figure 3). In this case, the tube is loaded axially by a ball-bearing clevis design and by internal pressure. The ball-bearing clevis end fitting design is identical to the one used on the old biaxial 10.2-cm (4-in.) test arrangement. The second test configuration is used to conduct multi-axial tension/compression, internal pressure, and torsion tests (Figure 4). For this test configuration, a rigid attachment is used for both the load cell and the hydraulic ram sides (Figure 4).

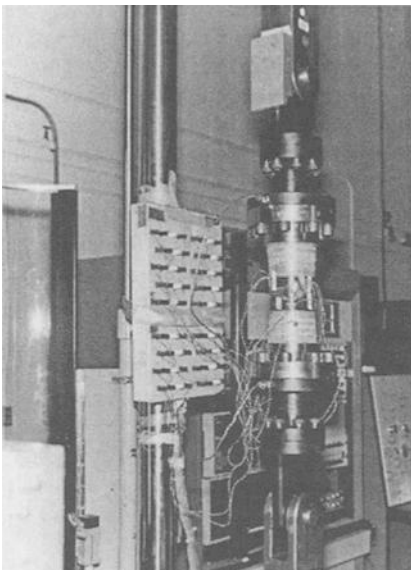


Figure 3—*Biaxial test setup.*

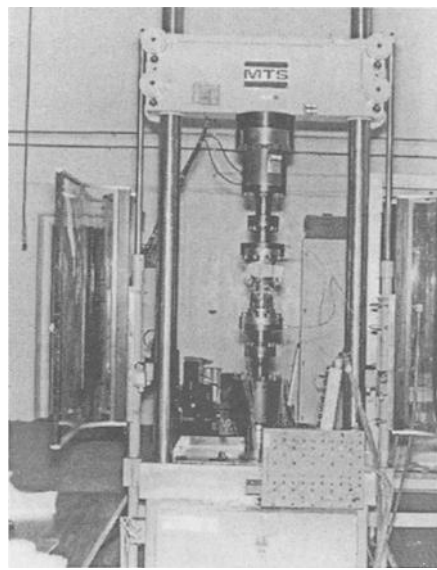


Figure 4—*Multi-axial test setup.*

A specially designed bladder internally pressurizes the tube. This rubber bladder is fitted over an aluminum plug and has two integral O-rings molded on each end (Figure 5). The aluminum plug with the bladder over it is inserted inside the tube (items³ 10 and 11 and 12 and 13, Fig. 5) so that the O-ring is sealed against the inside surface of the stainless steel end cap (items 2 and 3, Fig. 5). The bladder is pressurized by fluid that is passed through a stud in the tube adapter (item 14, Fig. 5) through channels in the aluminum plug. The aluminum plug is free to rotate relative to the studs and/or the composite tube stainless steel end caps, thereby providing free axial expansion and/or rotation of the tube. The plug is held in the axial position by two springs (item 26, Fig. 5) that are placed over the tube adapter's stud (on both sides).

³ Items in Figure 5 are identified with a number that is enclosed by a circle.

To prevent damage to the internal bladder from composite debris after failure, the tube is lined with a 2.54 mm thick rubber liner that is bonded to the inside surface of the tube. The tube is then instrumented with foil strain gages and/or long wire gages. A 10.2 cm tube biaxial test configuration in the 445 KN (100 kips) MTS servo-hydraulic tensile machine is shown in Figure 3. The second multi-axial test configuration is shown in Figure 4. Current load capabilities are:

Axial load (tension/compression)	445 KN	(100 kips)
Internal pressure	137.9 MPa	(20 ksi)
Torsion	814 KN-m	(600 kips-ft.)

These load limits are primarily associated with the test machine limitations for the particular load frame used. Higher axial and/or torsion loads are possible if a different servo-hydraulic load frame is used. The capability of the bonded end cap is somewhat questionable. However, for higher load requirements the end cap could be pinned to the tube to increase the load transfer capability.

To validate the new test method seven composite specimens were tested—four specimens were tested in a biaxial mode and three were tested in a combined biaxial—torsion mode. The four specimens' biaxial data were compared to historical data⁴. In order to compare the new test results to the historical data, the tube used to make the four specimens was fabricated using the same manufacturing parameters that were used to fabricate the old tube to which the current data is compared. The old tests included ten specimens fabricated from IM7⁵-12K W-sized carbon fiber and HBRF-55A⁶ resin with the old formulation⁷. The new tube was fabricated with the same IM7-12K W-sized carbon fiber using modified HBRF-55A resin formulation⁸. The old resin was not available and therefore cannot be duplicated exactly. The effect of the resin on strength in the 10.2 cm tube is not exactly known. However, during the time of the switch from Epi Rez 5022 to RD-2 diluent, multiple 50.8-cm (20-in.) cylinder ring tests [22] with IM7W fiber show the two resin systems give identical

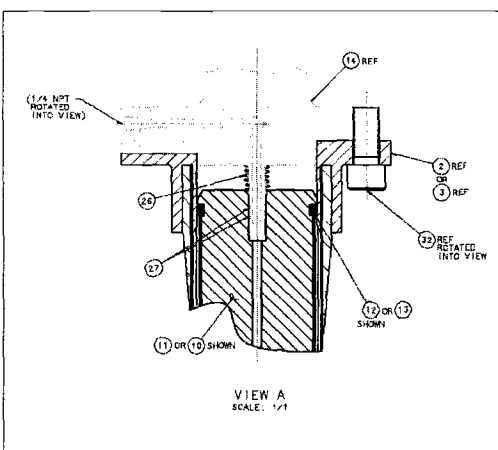


Figure 5—Bladder sealing configuration.

⁴ The original Swanson 10.2 cm biaxial tube test method was developed in corporation with Alliant Techsystems (formerly, Hercules Aerospace Co.) and used extensively to characterize filament wound composite structures in biaxial loading.

⁵ IM7 is high modulus high strength carbon fiber manufactured by Hexcel Corp. (formerly, Hercules Aerospace Co.). W-size is solvent base fiber sizing phased out in the mid-90th because of EPA environmental restrictions.

⁶ HBRF-55A is a Hercules Bacchus Resin Formulation resin base on Shell's EPON 826 epoxy.

⁷ The old formulation of HBRF-55A resin used Shell's EpiRez 5022 diluent.

⁸ The new formulation uses Vantico's RD-2 diluent.

fiber strain translation. Both tube lay-ups were a standard $\pm 25/90_3/\pm 25$ with nominal tube wall thickness of 1.27-mm (0.05-in). The bandwidth, tension, and resin content were all the same on the new tube as on the old tube.

One tube from the group of seven samples was tested to failure in pure torsion. The tube was instrumented with three-element rosette strain gages located at the center of the gage section at 120° azimuth from each other (Figure 6). The gages were placed in a $-45/0/+45$ pattern.

Finally, one tube was tested to failure in multi-axial internal pressure, axial, and torsion load. The axial load is proportional to the internal pressure and is increased at the rate of 11.341 lb/psi. The tube was instrumented with three-element rosette strain gages located at the center of the gage section at 120° azimuth from each other (Figure 6). The gages were placed in a $-45/0/+45$ pattern. Additional hoop foil strain gages were also added at five axial locations along the gage section at each azimuth (Figure 6). However, due to the limitation in the number of channels that can be used to collect data the two strain gages at ± 1.9 cm from the centerline were not used. The tube was loaded as follows.

Loading Step	Torsion Load (N-m)	Pressure (MPa) + Axial Load (kN)
1	3,955	0
2	3,955	21 + 151
3	4,520	21 + 151
4	4,520	To failure

Results

The test results are summarized in Table 1 for both the new and old tubes. The new tube test results show a very consistent and somewhat higher performance. Consistency is measured by the relatively low coefficient of variance on pressure, hoop strains, and axial strains as compared to the old tube data. The new specimens (four specimens) were instrumented with three strain gage rosettes (CEA-06-250UR-350) at the tube's mid-gage location. The three strain gage rosettes (oriented at $0^\circ/45^\circ/90^\circ$ where 0° is parallel to the tube axis) were mounted at 120° around the specimen's outer circumference from each other. Additionally, two 6.5 Ohm/ft. long wire gages were mounted 2.54-cm (1-in.) from

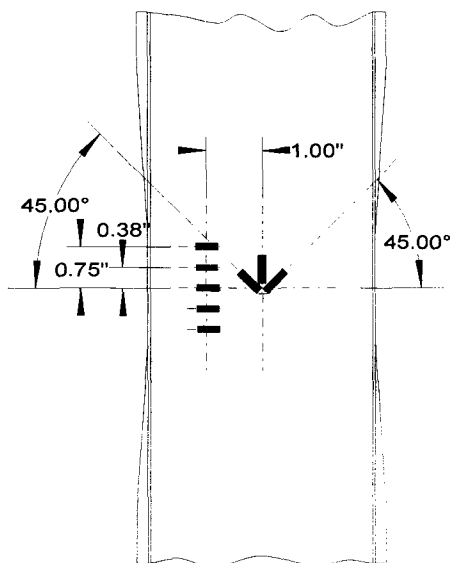


Figure 6—Tube Instrumentation Schematic

each other (1.27 cm from the tube's mid-gage center line on each side). The old specimen was instrumented with three long wire gages—one at the mid-gage centerline and the other two on either side of the mid-gage centerline. Details of the instrumentation are not available, which makes it somewhat difficult to compare the results. The axial gages were standard, single element foil gages that were oriented in the axial direction.

The new biaxial 10.2-cm (4-in.) test performed extremely well compared to the old test setup. The new biaxial 10.2 cm test average failure pressure was 6.9% higher and the long wire gage average failure hoop strain was 4.4% higher. Fiber lot strength data for the old tubes are not available and therefore, a more precise comparison of performance is difficult. However, given the 7% higher pressure and 4% higher hoop strain it is unlikely that the entire difference can be explained by fiber lot strength differences alone. The coefficients of variance for both the failure pressure and failure loads were also significantly lower in the new design as compare to the old design.

Table 1—*Summary of biaxial tube test results.*

Measured Parameter	Old Tube		New Tube	
	Average	Cv (%)	Average	Cv (%)
Failure pressure, MPa (psi)	33.50 (4,858)	3.3	35.81 (5,194)	1.4
Failure axial load, kN (kips)	242.5 (54.52)	4.1	257.8 (57.95)	1.6
Foil gage hoop strain (%)	N/A	N/A	1.627	0.6
Long wire gage hoop strain (%)	1.478	3.2	1.543	2.1
Foil gage axial strain (%)	0.956	8.7	0.587	0.7

The lamina stresses and strains at the average failure loads are summarized in Table 2. The lamina strengths are reported in Table 3. The data in Table 2 lists the maximum fiber strain to be 14% higher than the value recorded in Table 3. The fiber strain to failure greatly depends on the resin type[23], fiber volume[24], and test method. For example IM7 fiber tow tests with DER332 resin, as reported by the manufacturer, routinely yielded between 1.6% to 1.8% strain to failure [25]. Hence based on the data it may be concluded that the delivered fiber strength in the tube was nearly 100% relative to the strength reported by the fiber supplier. The maximum fiber strain criterion has been shown to be the most appropriate failure criterion for hoop fiber failure in pressure vessel [1-4, 22]. However, if one uses the maximum fiber stress criterion it should be noted that the fiber strength data reported in Table 3 are based on tow strength for which fiber volume is considered 100%. Therefore, the maximum fiber stress in Table 2 needs to be normalized to 100%. The fiber volume in the tubes was around 65% (although it was not measured).

Table 2—*Stresses and strains in biaxial loaded tube*
(Avg. Failure Loads: Pressure = 35.8 MPa, Tension = 258 kN).

Ply Orientation (deg.)	Fiber Direction		Transverse		Radial Direction		In-Plane Shear	
	σ_{11} (MPa)	ε_{11} (%)	σ_{22} (MPa)	ε_{22} (%)	σ_{33} (MPa)	ε_{33} (%)	τ_{12} (MPa)	γ_{12} (%)
+25	1607	0.911	22.1	1.523	-35.9	-2.593	38.3	0.645
-25	1682	0.953	22.1	1.473	-34.5	-2.540	-31.0	-0.710
90	2896	1.683	12.4	0.775	-34.5	-2.580	3.4	0.073
+25	1600	0.900	31.7	1.478	-2.1	-0.890	25.5	0.597
-25	1675	0.944	31.0	1.426	-1.4	-0.838	-29.0	-0.667

Table 3—*IM7/55A lamina strength properties.*

Property/Direction	ASTM Test Method	No. of samples	Ultimate Stress (MPa)		Ultimate Strain (% strain)	
			Avg.	Cv, %	Avg.	Cv, %
Tensile/Fiber	Tow	24	4,282 ¹	10	1.48	11
Compressive/Fiber		10	993	10	0.80	10
Tension/Transverse	D5450	6	15.4	9.3	0.22	8.8
Shear/In-plane	D5448	6	63.4	3.8	3.8	11

1. Based on 100% fiber.

A photograph of the failed four biaxial specimens is shown in Figure 7. All tubes failed by hoop gage section failure. After the failure, the internal bladder contained the pressurizing fluid so no cleaning was required. The same bladder was used multiple times. Thus, the new test hardware proved to be extremely reliable and efficient. The

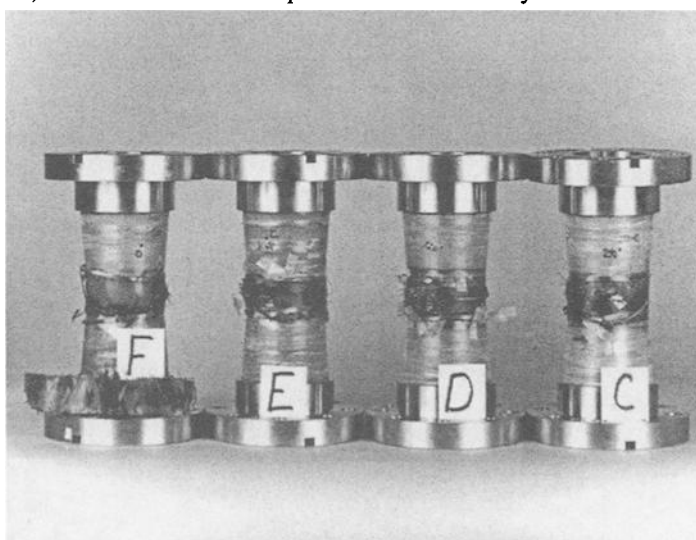


Figure 7—*Failure mode of four tubes tested by biaxial loading.*

new multi-axial 10.2 cm test method was used to develop nonlinear response for filament wound case material, damage accumulation behavior, and failure envelope. Results from these tests will be reported in other ASTM publications.

The tube that was loaded in pure torsion load failed at 4396 N-m (38,900 in.-lb.) and average 1.77% shear strain. Plot of the shear strain versus applied torque is shown in Figure 8. There are four curves that are presented in the figure—one curve for each rosette gage and one curve for the average. The plot shows very consistent results between the gages. Table 4 presents the lamina stresses and strains at failure as calculated by an elasticity program [26].

The maximum in-plan shear stress, 61.2 MPa (8.87 ksi) occurs at the 90° hoop layer. This failure stress is very close to the in-plane shear strength, 63.4 MPa (9.2 ksi), measured in a 10.2 cm (4-in.) hoop wound tube fabricated from the same resin and fiber tested in pure torsion to failure. Table 3 summarizes IM7/55A lamina strength properties as measured by the ASTM standards listed in the table. The maximum compressive stress and strain occur at the -25° helical layers (these stress and strain are slightly higher at the outer layer). The lamina maximum compressive strength is 993 MPa (144 ksi) and maximum strain at failure is 0.80% (Table 3). Hence, both the inplane shear in the hoop layer and the compressive stress in the helical layer are at or near the material strength. At failure the tube outer layer exhibited compressive buckling of the -25° helical (Figure 9). However, it should be noted that because of the winding pattern, the outer layer is a combination of $\pm 25^\circ$ layers. Therefore this localized failure affected a region of

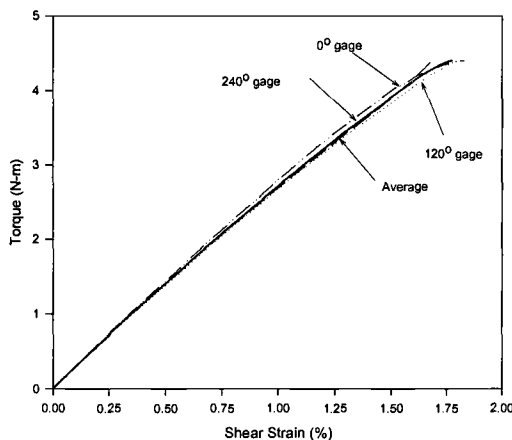


Figure 8—Shear strain versus applied torque for pure torsion test.



Figure 9—Failed tube loaded by torsion only.

approximately one helical bandwidth wide. Finally the transverse tension and compressive stresses in the $\pm 25^\circ$ are also very close to the lamina ultimate transverse strength.

Table 4—*Torsion load only*
(Failure Torsion = 4396 N-m).

Ply Orientation (deg.)	Fiber Direction		Transverse		Radial Direction		In-Plane Shear	
	σ_{11} (MPa)	ε_{11} (%)	σ_{22} (MPa)	ε_{22} (%)	σ_{33} (MPa)	ε_{33} (%)	τ_{12} (MPa)	γ_{12} (%)
+25	952	0.597	-20.7	0.633	-2.1	0.015	39.3	1.043
-25	-1027	-0.641	18.6	0.604	634	0.074	38.6	1.033
90	0	0.000	-1.4	-0.037	-0.7	0.011	61.2	-1.622
+25	972	0.607	-20.7	-0.643	-4.8	-0.016	40.0	1.061
-25	-1041	0.651	19.3	0.614	634	-0.074	39.3	1.051

Finally, the tube that was tested in axial tension, internal pressure, and torsion failed at 27.3 MPa (3,963 psi) pressure, 200 kN (45 kips) axial load, and 46 kN-m (41 in-kips) torsion load. The average hoop, axial, and shear strains at these loads were 1.33%, 0.70%, and 2.08%, respectively. The calculated (by elasticity program) hoop, axial, and shear strains using nominal fiber volume and ply thickness at the failure loads were 1.22%, 0.57%, and 1.64% strain, respectively. Plots of the average hoop, axial, and shear strains versus hoop and axial loads are plotted in Figure 10. The average hoop strains measured by the top, middle, and bottom strain gages versus pressure are plotted in Figure 11. The average strain of all gages is plotted as a solid line where the average of the individual strain gages at each location is plotted as symbols. The results show excellent agreement between the top, middle, and bottom gages indicating uniform hoop strain distribution along the tube gage section.

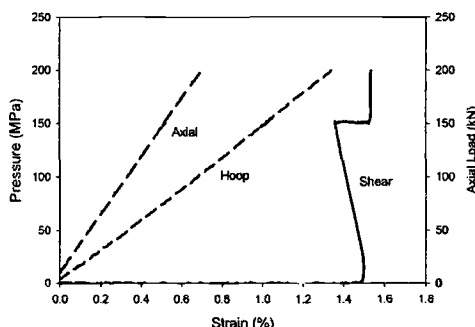


Figure 10—*Strains versus biaxial loads for tube loaded by internal pressure, axial load and torsion load.*

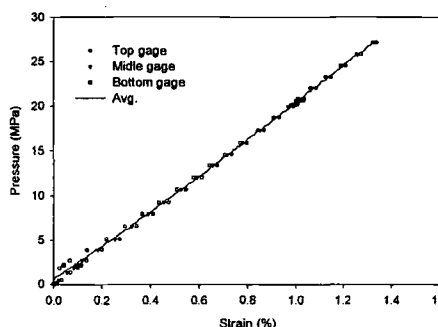


Figure 11—*Hoop strains versus pressure as function of gage locations.*

Table 5 lists the lamina stress and strain as calculated by the elasticity program at the failure loads. The IM7/55A lamina strength data was presented in Table 3. The results of the analysis indicate in-plane shear as the most likely failure scenario for this tube. The transverse tension stress in the -25° is higher than the lamina strength, thus suggests a possible progressive micro-crazing followed by catastrophic in-plane shear failure. The tube did fail in the gage section, by blowing into two pieces, exhibiting what appears to be a tensional failure. It is interesting that the tube that was loaded in pure torsion failed by what appears to be compressive buckling and not in-plane shear, whereas the tube that was loaded by combined biaxial and torsion load failed by what appears to be in-plane shear. The stress analysis results presented in Tables 2 and 5 do support the observed failure phenomenon. The tube test results showed some very significant nonlinear and progressive damage material responses, depending on the laminate lay-up. Because of space limitation the results from these tests will be discussed in a separate paper.

Table 5—*Lamina stresses and strains at failure loads*
(Failure Loads: Pressure = 27.3 MPa, Tension = 200 kN, Torsion = 46 kN-m).

Ply Orientation (deg.)	Fiber Direction		Transverse		Radial Direction		In-Plane Shear	
	σ_{11} (MPa)	ε_{11} (%)	σ_{22} (MPa)	ε_{22} (%)	σ_{33} (MPa)	ε_{33} (%)	τ_{12} (MPa)	γ_{12} (%)
+25	2179	1.292	4.8	0.554	-29.6	-2.099	70.3	1.546
-25	159	0.094	19.3	1.742	-25.5	-1.841	21.4	0.470
90	2144	1.272	5.5	0.555	-27.6	-1.994	-71.0	-1.557
+25	2193	1.294	13.1	0.505	-2.1	-0.711	69.6	1.527
-25	138	0.077	29.6	1.717	-0.1	-0.567	23.4	0.520

Conclusions

This paper reports on an improved 10.2 cm multi-axial tube test method. This test method is based on an earlier biaxial 10.2 cm tube test configuration developed by Swanson et al. [1-4]. One tube was tested in pure torsion and an additional tube was tested in biaxial internal pressure and axial load combined with torsion load. Both tubes exhibited failure mode that was consistent with the stress analysis results and the lamina strength. The tube that was tested by pure torsion appears to fail by compressive buckling of the outer helical layer. The tube that was loaded by biaxial combined with tensional load appears to fail by in-plane shear. Although the test data presented here are very limited, the results show the test method to be a unique tool in the investigation of failure modes in multi-layered filament wound material. This tool can be used to validate failure criteria given the absence of edge effects found in flat coupons. Because of space limitations more tube test data related to this test method will be presented in other publications.

References

- [1] Swanson, S.R., Christoforou, A. P. and Colvin, G. E., "Biaxial Testing of Fiber Composites Using Tubular Specimens," *Experimental Mechanics*, 1988: pp. 238-243.
- [2] Toombes, G.R., Swanson, S. R., and Cairns, D. S., "Biaxial Testing of Composite Tubes," *Experimental Mechanics*, Vol. 25, No. 2, 1985, pp. 186-192.
- [3] Swanson, S.R.a. and A.P. Chhristoforou, "Response of Quasi-Isotropic Carbon/Epoxy Laminate to Biaxial Stress," *J. of Composite Materials*, Vol. 20, 1988, pp. 457-471.
- [4] Swanson, S.R.a. and B.C. Trask, "Strength of Quasi-Isotropic Laminate under Off-Axis Loading," *Composites Science and Technology*, Vol. 34, 1989, pp. 19-34.
- [5] Christensen, R.M. and S.R. Swanson, "Evaluation of a New Failure Criterion for Fibrous Composite Materials," UCRL-98725, 1988, Lawrence Livermore National Laboratory.
- [6] Feng, W.W. and S.E. Groves, "On the Finite Strain Invariant Failure Criterion for Composites," *Journal of Composite Materials*, Vol. 25, No. 1, 1991, pp. 88-100.
- [7] Hashin, Z., "Failure Criteria for Unidirectional Fiber Composites," *J. Applied Mechanics*, Vol. 47, 1980, pp. 329-334.
- [8] Hoffman, O., "The Strength of Orthotropic Materials," *J. of Composite Materials*, Vol. 1, 1967, pp. 200-206.
- [9] Ikegami, K., Nose, Y., Yasunaga, T. and Shiratori, E., "Failure Criterion of Angle Ply Laminate of Fiber Reinforced Plastic and Applications to Optimize the Strength," *Fiber Science & Technology*, Vol. 16, 1982, pp. 175-190.
- [10] Kawata, K., "On the Criterion of Yield and Fracture of Angle-Ply Laminates Wound with Filament in Their Biaxial Tension," *J. Society of Materials Sciences*, Japan, Vol. 20, No. 214, 1971, pp. 879-885.
- [11] Kroll, L. and W. Hufenbach, "Physically Based Failure Criterion for Dimensioning of Thick-Walled Laminates," *Applied Composite Materials*, Vol. 4, 1997, pp. 321-332.
- [12] M. J. Hinton, P. D. Soden, and a.A.S. Kaddour, "Special Issue: Failure Criteria in Fiber-Reinforced-Polymer Composites," *Composites Science and Technology*, Vol. 58, July 1998 (entire issue).
- [13] Puck, A. and W. Schneider, "On Failure Mechanisms and Failure Criteria of Filament-Wound Glass Fiber/Resin Composites," *Plastics & Polymers*, Vol. 37, 1969, pp. 33-44.
- [14] Tsai, S.W., "A Survey of Macroscopic Failure Criteria for Composite Materials," *J. of Reinforced Plastic and Composites*, Vol. 3, 1984, p. 40.
- [15] Swanson, S.R., and Qian, Y., "Multiaxial Characterization of T800/3900-2 Carbon/Epoxy Composites," *Composites Science and Technology*, Vol. 43, 1992, pp. 197-203.
- [16] Guess, T.R., "Biaxial Testing of Composite Cylinders: Experimental-Theoretical Comparison," *Composites*, Vol. 11, No. 3, 1980, pp. 139-148.

- [17] Whitney, J.M., Grimes, G. C. and Francis, P. H., "Effect of End Attachment on the Strength of Fiber-Reinforced Composite Cylinders," *Experimental Mechanics*, Vol. 13, No. 5, 1973, pp. 185-192.
- [18] Duggen, M.F.a.B., J. A. "A New Test Specimen Geometry for Achieving Uniform Biaxial Stress Distribution in Laminated Composite Cylinders. in *International Conference on Composite Materials*, 1980, Paris, France.
- [19] Groves, S.E., Sanchez, R. J., and Feng, W. W., "Multiaxial failure characterization of composites," UCRL-JC 105244 Rev. 1, 1991, Lawrence Livermore National Laboratory.
- [20] Lee, C.S., Hwang, W., Park, H. C., and Han, K. S., "Failure of Carob/Epoxy Composite Tubes Under Combined Axial and Torsional Loading, 1. Experimental Results and Prediction of Biaxial Strength by the use of Neural Networks," *Composites Science and Technology*, Vol. 59, 1999, pp. 1779-1788.
- [21] Krempl, E.a.N., T-M., "Graphite/Epoxy [$\pm 45^\circ$]s Tubes: Their Static Axial and Shear Properties and Their Fatigue Behavior Under Completely Reversed Load Control Loading," *J. Composite Materials*, Vol. 16, May 1982, pp. 172-187.
- [22] Cohen, D., Toombes, Y. T., Johnson, A. K., and Hansen, M. F., "Pressurized Ring Test for Composite Pressure Vessel Hoop Strength and Stiffness Evaluation," *J. of Composites Technology & Research*, Vol. 17, No. 4, 1995, pp. 331-340.
- [23] Cohen, D.a.K.A.L., "The Influence of Epoxy Matrix Properties on Delivered Fiber Strength in Filament Wound Composite Pressure Vessels," *J. of Reinforced Plastic and Composites*, Vol. 10, March 1991, pp. 112-131.
- [24] Cohen, D., "Influence of Filament Winding Parameters on Composite Vessel Quality and Strength," *Composites Part A-Applied Science and Manufacturing*, Vol. 28A, 1997, pp. 1035-1047.
- [25] Cohen, D., "Application of Reliability and Fiber Probabilistic Strength Distribution Concepts to Composite Vessel Burst Strength Design," *J. of Composite Materials*, Vol. 26, No. 13, 1992, pp. 1984-2014.
- [26] Cohen, D., "Application of Material Nonlinearity to a Composite Pressure Vessel Design," *J. of Spacecraft and Rockets*, Vol. 28, No. 3, 1991, pp. 339-346.

Peter J. Joyce,¹ Melanie G. Violette,² and Tess. J. Moon³

Finite Element Analysis of Unidirectional Composite Compression Test Specimens: A Parametric Study

REFERENCE: Joyce, P. J., Violette, M. G., and Moon, T. J., "Finite Element Analysis of Unidirectional Composite Compression Test Specimens: A Parametric Study," *Composite Materials: Testing, Design, and Acceptance Criteria, ASTM STP 1416*, A. Zureick and A. T. Nettles, Eds., American Society for Testing and Materials International, West Conshohocken, PA, 2002.

ABSTRACT: This research undertakes a comprehensive parametric study of the ASTM D 6641 Combined Loading Compression (CLC) test fixture from Wyoming Test Fixtures (WTF) using numerical analysis to evaluate various test parameters associated with compression testing of unidirectional test specimens. A two-dimensional finite element analysis of the D 6641 CLC fixture was used to identify loading conditions and tabbing configurations that minimized the peak axial, shear, and through-thickness stress concentrations in the test specimen. Combined shear and end loading appears to offer a good compromise between reducing the tab tip stress concentrations inherent in shear loading, and avoiding premature failure by end brooming associated with end loading. Thin, tapered tabs made of compliant materials were found to have the smallest stress concentrations at the tab tip. Specimens with these tab configurations should yield higher measured compressive strengths since premature failure at the tab tip is less likely to occur. Partial debonding of the tab tip was found to increase the stress concentration compared to the fully-bonded case, but to move its location away from the gage section of the specimen. Tab tip debonding should be avoided for compressive strength testing.

KEYWORDS: composite materials, compression testing, combined loading, specimen optimization, stress analysis

Introduction

A wide variety of compression test fixtures has been developed over the past two decades in an attempt to measure the true compression strength of composite materials [1,2]

¹ Assistant Professor, Mechanical Engineering Dept., U.S. Naval Academy, 590 Holloway Rd, Annapolis, MD, 21402.

² Engineer, Raytheon Aircraft Company, Wichita, KS, 67206.

³ Associate Professor, Dept. of Mechanical Engineering, The University of Texas at Austin, Austin, TX, 78712.

Compression testing of unidirectional fiber-reinforced composite materials is especially challenging because of their highly orthotropic nature and their low through-thickness and shear strengths. Either shear or end loading may lead to artificially low measured strength values; end loading may result in premature failure by end brooming at the point of load introduction, while shear loading may lead to high stress concentrations due to the material's high longitudinal stiffness.

It is difficult to compare loading techniques used in the literature, since each loading technique is associated with a different test fixture and specimen geometry. Those who have attempted a head to head comparison of shear and end loading techniques often produce contradictory results. Despite or perhaps because of its relative simplicity, end loading is often used in industry for materials screening or quality assurance testing despite its propensity to measure only the lower bound limit of end crushing failure. No less than four different ASTM standards now describe how to extract the compressive properties of polymer matrix composites, (1) Test Method for Compressive Properties of Rigid Plastics (D 695-96), (2) Test Method for Compressive Properties of Polymer Matrix Composite Materials with Unsupported Gage Section by Shear Loading (D 3410-95), (3) Test Method for Compressive Properties of Unidirectional Polymer Matrix Composites Using a Sandwich Beam (D 5467-97), and (4) Test Method for Determining the Compressive Properties of Polymer Matrix Composite Laminates Using a Combined Loading Compression (CLC) Test Fixture (D6641-01). While some of these standards have clearly been developed with a particular class of composite materials in mind, that this many different test techniques exist simultaneously is indicative of the lack of consensus in the composites community.

Several investigators have proposed combined loading as an improved method of composite compression testing [3-9]. This technique reduces the stress concentration at the re-entrant corner of the end-tabs, compared to the shear case, while the clamping action of partial shear loading acts to inhibit both tab debonding and end brooming. The experimental evidence in support of this claim is limited and ambiguous at best, due to testing artifacts particular to any given test fixture. Furthermore, although Xie and Adams [9-11] modelled combined loading, their results are only hypothetical since they relate to no real test fixture.

In this paper we perform a two-dimensional finite element analysis of the ASTM D 6641 Combined Loading Compression (CLC) Test Fixture (manufactured by Wyoming Test Fixtures) for compression testing of unidirectional composite materials. The D 6641 CLC fixture, which was originally developed by the Composite Materials Research Group at the University of Wyoming for compression testing of cross-ply [12] or off-axis [13-14] laminates can be used to produce shear and end loading in any proportion desired, without changing the specimen configuration. The optimal specimen configuration to be used is the second issue addressed in this paper, specifically we are interested in a specimen configuration that permits direct measurement of the compressive strength properties of as-manufactured unidirectional composites; that is, without using special laminates requiring a "back-out factor", or specially "shaped" specimens.

The literature is full of different specimen and tabbing configurations, each with its peculiar advantages and disadvantages, which are often related to the test fixture for

which it was developed. For this investigation we were primarily interested in the widely used straight-sided, uniform thickness composite specimen with bonded end-tabs.

For compression testing of unidirectional composite laminates, ASTM Standard D 3410 suggests either steel or glass-fabric epoxy tabs with a 90° bevel angle. Recent studies have shown that steel and glass-fabric epoxy tabs produce comparable results for unidirectional carbon fiber-reinforced composites [15]. Other researchers have reported that decreasing the taper angle reduces the tab-tip stress concentrations [10,16]. Some investigators have observed debonded tabs during post mortem inspection of the test specimen [17,18], a number have proposed deliberate debonding as a way to improve specimen performance [15,19-23]. Again, there is no real consensus on the best specimen configuration and no one has performed an integrated study on the effect of different aspects of specimen design and tabbing.

The goal of this study was to evaluate the optimal method of loading introduction using the D 6641 CLC fixture, and to investigate various aspects of specimen design and tabbing by a systematic finite element analysis. The various loading conditions and specimen configurations were compared on the basis of the predicted stress distribution (uniformity and peak values) in the test coupon. With additional experimental validation, we hope to improve composite compression testing, particularly compression strength measurements, of unidirectional composite materials using the D 6641 CLC fixture.

A thorough literature review surveying both the extensive experimental work that has been performed in the area of composites compression testing, and the various analytical papers which have looked at compression test specimens was performed as part of the authors' dissertation research [24,25]; selected results have been included in this paper. In this paper we begin with an introduction of the D 6641 CLC fixture and a discussion of its general usage. In the succeeding sections we describe in detail the various tabbing configurations to be evaluated in this study, and the details of the finite element modelling and the boundary conditions imposed. Next we present the finite element results and a summary of our observations. In conclusion, we discuss optimal loading conditions and guidelines for optimal specimen tabbing.

The ASTM D 6641 Combined Loading Compression Test Fixture

The ASTM D 6641 Combined Loading Compression (CLC) Test Fixture is a relatively new fixture. It was originally adopted in our lab as part of an investigation to measure defect sensitivity in FRP laminate composites [25]. When our fixture was purchased from Wyoming Test Fixtures, its use had not yet been demonstrated for tabbed specimens or for that matter with unidirectional composite materials, it has since been adopted as a standard test method for compression testing of PMC laminates. The D 6641 CLC fixture, which is shown in Figure 1, modifies the WTF End-Loaded Side Supported (ELSS) Fixture by incorporating roughened clamping surfaces for shear load introduction into the specimen.

The D 6641 CLC fixture has several advantages. First, it is applicable to a wide range of specimen thicknesses and layups, since the proportion of shear and end loading may be adjusted as appropriate for each specimen. It has been demonstrated successfully for use in "backing out" unidirectional composite compression strengths [12-14] as well as for use with thickness tapered unidirectional specimens [26] with comparable results. The fixture is compact and lightweight, compared for example to the IITRI fixture.

(ASTM D3410 Procedure B), which makes it quick to heat up and cool down for environmental testing. It also is relatively inexpensive and easy to use. The post and linear bearings design used to align the top and bottom halves of the specimen (see Figure 1) minimizes friction carried in the alignment pins [14], thereby eliminating redundant load paths inherent in other similar fixtures [19-20]. The grip surfaces are thermal sprayed to minimize damage to the specimen from clamping, which may in fact negate the need to use tabbed specimens. The high resultant coefficient of friction in the grips is also advantageous for optimal shear loading without building up disproportionate transverse normal stresses, since lower clamping loads are sufficient, compared to the wedge grips of the IITRI fixture.

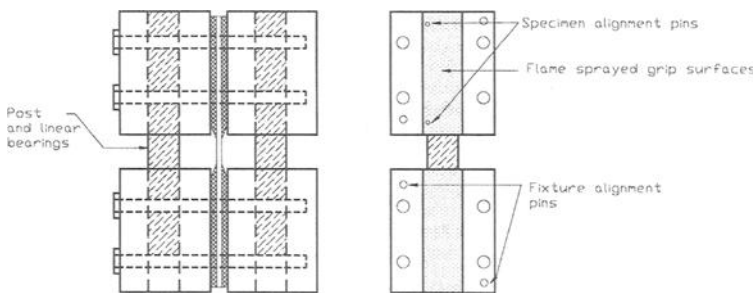


Figure 1-Schematic of WTF Combined Loading Compression Test Fixture and tabbed specimen.

Following the example of Rolfes [19-20] who designed a similar test fixture and in order to better understand the evolution of the combined loading condition; a special procedure was developed for loading the specimen in the D 6641 CLC fixture. Opening the fixture up completely, the bottom right and bottom left halves were fitted together (by the post and linear bearings) and then the specimen was introduced with both ends of the specimen inset approximately 0.5-1 mm with respect to the ends of the clamp blocks. The specimen alignment can be carefully checked at this point with the fixture wide open, using the spacer bar provided with the fixture to ensure good registration with the alignment pins in the bottom half of the fixture. Then the top half of the fixture was assembled this is carefully lowered onto the fixture alignment pins, then the clamp bolts are introduced and the bolt torque can be adjusted according to the test specifications. This way shear load is introduced first and the ratio of shear/end loading can be predicted *a priori* based on an estimate of the compressive failure load. When the load reaches the maximum friction force sustainable between the block and the specimen, the specimen slips in the blocks until it makes contact with the loading surface. Specimen damage due to slippage is not an issue when this procedure is used with tabbed specimens. Subsequent loading is by a combination of shear and end loading. The fixture can be used to achieve any combination of shear and end loading, by varying the bolt torque applied to the clamping bolts.

Methodology

Compression testing in the D 6641 CLC fixture was simulated using two-dimensional finite element analysis. Pure shear loading, pure end loading and combined loading were simulated using the actual fixture to guide selection of boundary conditions, including clamping pressure and the friction in the grips. We modelled a straight sided, uniform thickness test coupon with bonded end-tabs. The effects of tab material, tab thickness, tab tip geometry, and tab tip debonding were all examined for combined loading in the WTF CLC fixture. The various loading methods and specimen/tabling configurations were evaluated on the basis of the overall stress distribution in the test coupon as well the peak stresses occurring at the specimen/tab interface.

Specimen Optimization

Since we chose a relatively undocumented fixture (it has since been reported on several times [12-14,26] and even adopted by ASTM for use with D 6641-01), it followed that we had to choose a suitable specimen design with care. After reviewing the available literature on compression test techniques and composites mechanical testing, we elected to evaluate two different widely used techniques for diminishing the stress concentrations at the tab tip: tapered tabs and debonded tabs.

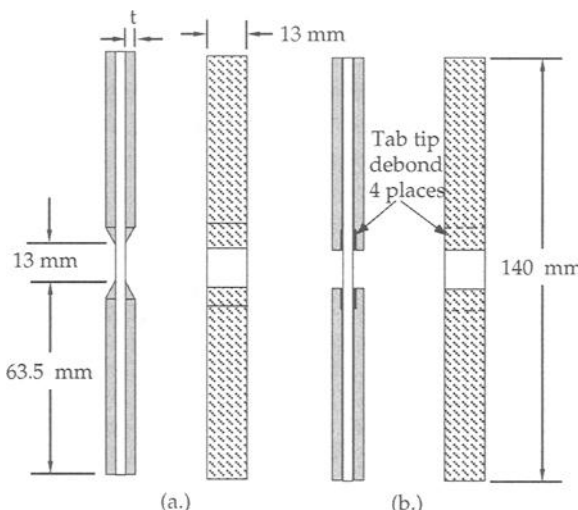


**Figure 2-Characteristic dimensions of two tab configurations,
(a.) tapered tabs, (b.) debonded tabs.**

A sketch of these two tabbing configurations is provided in Figure 2 for comparison. The general dimensions of the specimen coupon are 140 mm long, 2.5 mm thick, and 13 mm wide, with a 13 mm long unsupported gage length. The tab thicknesses studied were 1 mm, 1.5 mm, and 3.2 mm, with 3.2 mm considered the baseline case. The

adhesive layer thickness was 0.13 mm, based on thickness measurements of several test specimens.

The material analyzed in this investigation is a carbon-fiber reinforced thermoplastic composite, T300/P1700 from Amoco. This material has been extensively characterized as part of an earlier investigation of the effect of process-induced fiber waviness on compression strength of composites initiated by Adams and Hyer [27] at Virginia Tech and later continued at UT-Austin by Naley [28] and Joyce and Moon [25]. A summary of the T300/P1700 composite properties extracted from [27,28] is provided in Table 1. The properties used in this study are underlined.

Tab Material

ASTM Standard D 3410-95 lists steel and continuous E-glass fiber-reinforced polymer matrix materials as the most commonly used tab materials. The thinking on choice of tab material seems to vary but recent studies have concluded that more compliant tabs are beneficial [10,15]. To investigate the effect of tab material on the stress distributions in the composite coupon, four candidate tab materials were evaluated; steel, aluminum, glass-fabric/epoxy NEMA Grade G10, and unreinforced epoxy. The tab material properties used in this analysis are summarized in Table 2. The elastic constants for steel, aluminum, and epoxy were taken from [29]. The in-plane elastic properties for the G10 tab material were obtained from mechanical tests performed in our lab and the out-of-plane properties were extracted from [30] for lack of test data.

Table 1 – Summary of material properties for T300/P1700 composite.

Property	Symbol	Units	Source	
Longitudinal Modulus	E_x	GPa	[27]	[28] <u>122</u>
Transverse Modulus	E_y, E_z	GPa	8.3	<u>7.4</u>
In-plane Poisson's Ratio	ν_{xy}, ν_{xz}	-	0.35	<u>0.34</u>
Out-of-plane Poisson's Ratio	ν_{yz}	-	0.486	0.507
In-plane Shear Modulus	G_{xy}	GPa	4.1	<u>4.1</u>
Out-of-plane Shear Modulus	G_{xz}, G_{yz}	GPa	2.8	<u>2.5</u>
Longitudinal Compressive Strength	X_c	GPa	<u>0.96</u>	1.3
Transverse Compressive Strength	Y_c, Z_c	MPa	<u>125</u>	n/a
In-plane Shear Strength	S	MPa	<u>48</u>	n/a

Table 2 – Summary of tab properties.

Property	Symbol	Units	Tab Material			
			Steel	Aluminum	G10	Epoxy
Longitudinal Modulus	E_x	GPa	207	75.8	20.7	3.0
Transverse Modulus	E_y	GPa	207	75.8	20.7	3.0
Through-thickness Modulus	E_z	GPa	207	75.8	6.90	3.0
Poisson's Ratio	$\nu_{xy}, \nu_{xz}, \nu_{yz}$	-	0.3	0.33	0.191	0.37
Shear Modulus	G_{xy}, G_{xz}, G_{yz}	GPa	79.6	28.5	4.1	1.1

The adhesive was modelled as isotropic with $E = 2.19$ GPa and $\nu = 0.42$. The material properties for the adhesive were extracted from Ref. [30]. The choice of elastic constants for the adhesive layer was considered insignificant for this study. It has been demonstrated that the effects of varying adhesive layer stiffness on the stress concentrations resulting from both tension and compression testing are negligible [11,31]. However, it has been shown that neglecting the presence of an adhesive layer results in exaggerated stresses at the specimen/tab interface [11].

Tapered Tabs

The first specimen design incorporates untapered tabs, with a tab bevel angle of 90° as recommended in ASTM D 3410-95. Tapered tabs as proposed first by Rehfield et al. [32] and again by Adams and Odom [15] were evaluated for comparison. In testing thin composites where global buckling is a concern, a 30° taper angle provides a good starting point, since the effect on the unsupported gage length is minimized. Taper angles of 10° and 20° were also considered in this study.

An additional variation on the tapered tab incorporates a curved taper surface; this is commonly referred to in the literature as a waisted specimen [5,21] or a thickness-tapered specimen [33,34]. This specimen design often incorporates integral [$\pm 45^\circ$] tabs, hence the various names that imply a monolithic test coupon. Integral tabs are often designed so that the layer stiffness of the tab material is more compliant than the unidirectional test section; a close approximation in many cases would be glass-fabric/epoxy tab material. In order to generalize our results in terms of the effect of tab material, we modelled a straight-sided test piece with bonded end-tabs; the tab tip was tapered using a curved arc with radius equal to the tab thickness. It is referred to in this study as the “radius tab”.

Figure 3 shows the five tab geometries: square (untapered) tabs, 30° taper, 20° taper, 10° taper, and radius tabs. In Figure 3 we illustrate a quarter model of the specimen. The tab thickness in the illustration is 3.2 mm and the specimen half thickness is 1.27 mm.

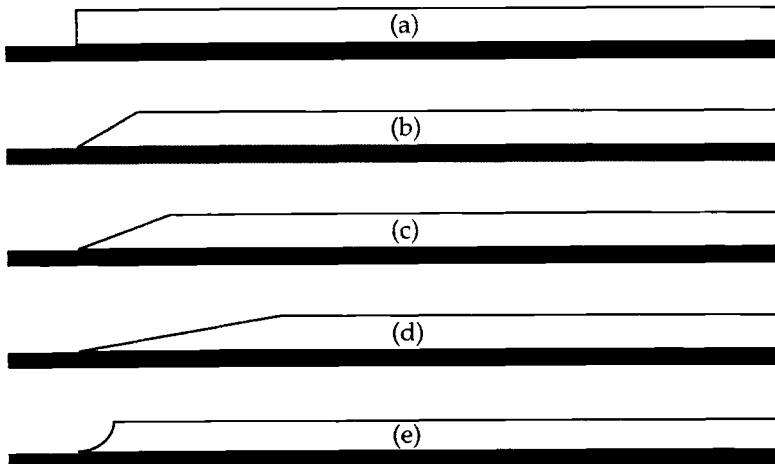


Figure 3-Five different tab geometries: (a) square (90°), (b) 30° tapered, (c) 20° tapered, (d) 10° tapered, and (e) radius tapered.

Debonded Tabs

It has been frequently observed in practice that compliant tabs may undergo some debonding at the tab tip during testing [15,17,18,22], frequently extending all the way back to the “elbow” of a tapered tab (where the taper begins and the flat part of the tab ends), owing to the Poisson expansion of the composite coupon. Observations of such *in-situ* debonds have led several researchers [15,19-22] to propose a specimen with deliberate debonds, which may be created by coating a small portion of the tab surface with Teflon tape or mold release compound prior to bonding the tab to the specimen. This design reduces the shear stress concentration effect, primarily by moving the stress concentration back from the tab tip, thereby yielding a more uniform stress field in the gage section.

We examined the effect of partially debonding the tab from the specimen for square, 10° tapered, and radius-tapered tabs. For the square tabs, we examined the difference between a deliberate debond, which included a Teflon insert with a low-friction interface, and an *in-situ* debond, which models a crack in the adhesive and has a higher coefficient of friction. Teflon, which was used in debond cases, was modelled with a modulus $E = 4.1$ GPa and Poisson's ratio $\nu = 0.42$.

Buckling Considerations

The maximum allowable gage section length was determined on the basis of column buckling analysis. Including the effects of transverse shear, and assuming a rectangular cross-section specimen, the expression [35] for the column buckling length, l , is

$$l = \frac{\pi t}{\sqrt{12}} \left[\frac{CE_x}{\sigma_{cr}} \left(1 - n \frac{\sigma_{cr}}{G_{xz}} \right) \right]^{\frac{1}{2}} \quad (1)$$

where t = specimen thickness, $C = 1$ for a pinned-end column or 4 for fixed-end column, E_x = longitudinal modulus, G_{xz} = through-thickness shear modulus, $n = 1.2$ for rectangular cross-sections, and σ_{cr} = buckling stress.

Because the specimen geometry must be prescribed prior to testing, the material properties must be assumed to estimate the permissible gage length. The ultimate compressive strength and the engineering constants for the T300/P1700 composite (see Table 1) were obtained from the literature [27,28]. All of the panels had a nominal thickness of 2.5 mm.

Figure 4 shows the buckling curves generated by Equation 1 for pinned-pinned and fixed-fixed end conditions. The maximum allowable gage length, with the assumption of pinned-pinned conditions, worked out to approximately 18 mm, see Figure 4 where the buckling curve for pinned/pinned end constraints intersects with the horizontal line indicating the compressive strength of the T300/P1700 composite. To be conservative, the unsupported gage length for all further analysis was decreased to 13 mm, marked Unsupported Gage Length in Figure 4. For either boundary condition, this gage length clearly leads to a buckling stress that is higher than the expected compressive strength.

Figure 4 shows the buckling curves generated by Equation 1 for pinned-pinned and fixed-fixed end conditions. The maximum allowable gage length, with the assumption of pinned-pinned conditions, worked out to approximately 18 mm, see Figure 4 where the buckling curve for pinned/pinned end constraints intersects with the horizontal line indicating the compressive strength of the T300/P1700 composite. To be conservative, the unsupported gage length for all further analysis was decreased to 13 mm, marked Unsupported Gage Length in Figure 4. For either boundary condition, this gage length clearly leads to a buckling stress that is higher than the expected compressive strength.

For a specimen with square end-tabs, selecting the maximum allowable unsupported gage length and appropriate end conditions is straightforward. Because the entire length of the tab is fully supported by the clamp blocks, the unsupported gage section is best modelled using a fixed-fixed end condition. Figure 4 indicates that an unsupported length of 13 mm may be extremely conservative for a specimen with square end-tabs.

In the case of tapered tabs, estimating the column buckling length is more difficult. If the tapered region provides sufficient lateral support against buckling, then the pinned-pinned end condition can be applied using the tab tip to tab tip distance as above. Since the flat part of the tab is fully supported by the clamp blocks, a fixed-fixed boundary condition might be used with the distance between the tab “elbows” where the taper begins. Using the distance between the “elbows” and the pinned-pinned end condition obviously underpredicts the buckling stress.

Marked on the fixed-fixed curve in Figure 4 are the distances between the “elbows” for the various taper angles and the three tab thicknesses considered in this study. Increasing the tab thickness or decreasing the taper angle increases the taper length and hence the distance between the “elbows”. The fixed-fixed buckling curve predicts a buckling stress greater than the compressive strength for all cases but one -- the thick (3.2 mm) 10° tapered tab. This is a conservative estimate because the tapered region of the tab will provide some lateral support depending on the thickness of the tab

and the stiffness of the tab material. This analysis demonstrates that reducing the taper angle produces an undesirable increase in the unsupported gage length, especially in the case of thick tabs, which may result in global buckling rather than compressive failure. The buckling curves predict that 10° may be too shallow for thick tabs (given a 13 mm unsupported gage length), especially in the case of compliant tabs where the lateral support afforded by the tab tip is expected to be minimal.

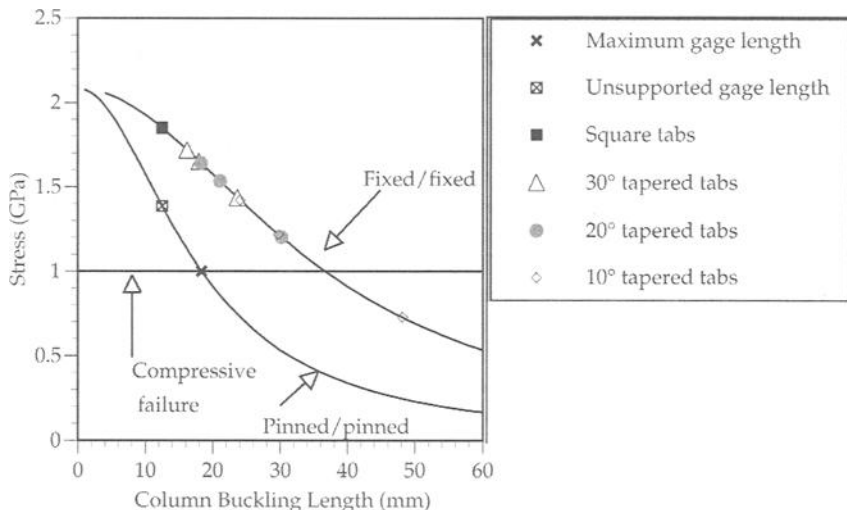


Figure 4 – Column buckling curves from Equation 1 and predicted buckling stresses for various tabbing configurations.

Finite Element Analysis

In order to evaluate the effects of loading method and tab design, a two-dimensional finite element model was developed using ABAQUS, Version 5.8 to compare the stress concentrations resulting from shear, end, and combined loading in the D 6641 Combined Loading Compression Test Fixture. The goal of this investigation was to evaluate the relative location and magnitude of the stress concentrations and the corresponding strain uniformity in the gage section, using the test fixture to define the appropriate boundary conditions.

Model Formulation

The finite element model included an explicit analysis of the specimen, the adhesive layer, the tab material, and the clamp blocks. The model is in two dimensions, the length and thickness directions of the specimen. Plane stress was assumed because it was felt that plane strain overconstrained both the out-of-plane deformations of the block and the specimen as well as the lengthwise deformation of the block and specimen at the grip/tab interface. Because the specimen is symmetric about two planes, only one quarter

of the specimen coupon was modelled, applying the appropriate boundary conditions at the planes of symmetry.

The finite element model used approximately 6000 linear (four-node) plane stress elements. The basic model of the specimen used 140 elements along the length, and 24 elements through the thickness. The node placement in both directions was biased so that the elements were concentrated in the region near the tab tip, or near the end of the bonded region for debond cases.

The adhesive layer and square tabs were modelled with three elements and 20 elements, respectively, through the thickness and 100 elements along the length. The clamp block was modeled using 15 elements through the thickness and 20 along the length.

In-situ tab debonding was modelled by untying the adhesive elements from the composite coupon in the vicinity of the tab tip, simulating a crack. The interface between the adhesive and the specimen was modeled using contact surfaces with a coefficient of friction $\mu = 0.1$. The actual coefficient of friction for sliding across a cracked epoxy interface is unknown; for the purposes of this study it was sufficient to assume it might be a couple orders of magnitude greater than the coefficient of friction resulting from deliberate debonding using a Teflon insert.

In the case of a debond that is deliberately introduced by a Teflon insert, the adhesive layer in the debond region was replaced with Teflon. The coefficient of friction along the debond surface between the Teflon and the specimen was assumed to be $\mu = 0.001$.

Because it is difficult to determine the actual properties and coefficient of friction in a debond, we checked the sensitivity of our results to the way the debond was modelled. For the *in-situ* case, changing the friction coefficient, μ , across the debond interface from 0.1 to 0.001 (as for the Teflon insert) increased the axial stress concentration slightly (5%). For the deliberate debond case, holding the friction coefficient constant at 0.001 but varying the elastic properties of the insert material showed that a stiffer insert material causes an increase in the stress concentration factors, especially $\sigma_z/\bar{\sigma}_x$.

Loading

The loading boundary conditions were applied in two steps; first the clamp load was applied and the specimen was loaded in pure shear through an applied uniform displacement of the clamp blocks. Then the specimen and blocks were end loaded through an applied uniform displacement of the clamp blocks and the loading end of the specimen, tabs, and adhesive. A schematic of the entire finite element model is included in Figure 5.

To model the previously described experimental procedure for this fixture, the end of the specimen is initially inset from the edge of the block by a small gap, marked Δ in Figure 5. The displacement of the clamp blocks in the first step of loading is equal to the gap size, Δ , simulating the first stage of the experimental procedure, pure shear loading up to the point where the specimen slips in the grips.

A preliminary study of the effect of gap size showed that a minimum gap size is required to achieve maximum shear loading, as shown for the case of pure shear loading

in Figure 6. The shear strain in the tab, and hence the load transferred into the specimen, is proportional to the displacement of the block, up to the point where the total friction force between the block and the tab reaches the limiting value of μN . The minimum gap required to develop 100% of the target load in the specimen was found to increase as the proportion of shear loading increases, and with a more compliant tab material. As shown in the figure, increasing the gap size beyond the threshold value did not affect the load transferred into the specimen. However, it did increase the number of iterations required to obtain a convergent solution.

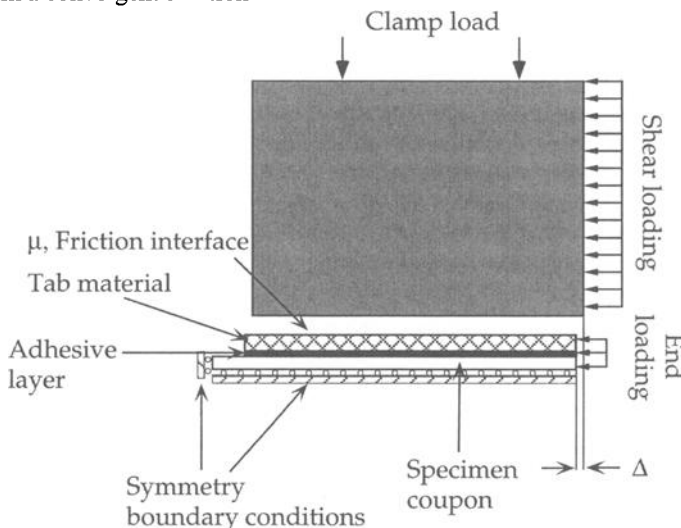


Figure 5 – Schematic of the finite element model.

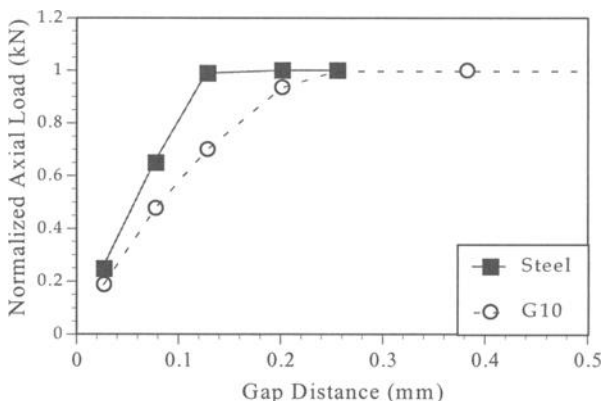


Figure 6 – Effect of gap size on axial load in specimen (Square, 3.2 mm tabs, shear loading).

A gap size of 0.25 mm was used for most cases in this study. However, in several cases, notably in the case of shear loading with epoxy tabs and in the case of the 10° tapered G10 tabs, this gap size was found to be insufficient to develop 100% of the target shear load. These cases were analyzed with a gap size of 0.5 mm instead.

The clamping pressure necessary to achieve shear loading through the tab faces is achieved by torquing the clamp bolts to achieve the desired level of normal force. In the finite element model, this load was simulated using two point loads, representing the preload in a pair of clamp bolts. The bolt torque in each clamp bolt is related to applied preload in each clamp bolt by the following relation derived for power screws [36]

$$\begin{aligned} T &= K F_i d \\ K &\approx 0.2 \\ F_i &= \frac{5T}{d} \end{aligned} \quad (2)$$

where T = the torque applied to the bolt, K = the torque coefficient, F_i = the force in each bolt, and d = the diameter of the bolt, 6.4 mm (0.25 in). The torque coefficient, K , has been found to be approximately equal to 0.20 no matter what size bolts are employed and whether the threads are coarse or fine [36].

In practice once the clamp bolts have been preloaded they behave more like an applied displacement boundary condition than a pair of applied point loads. As the specimen is loaded in compression, the transverse expansion of the specimen coupon due to the Poisson effect will increase the clamping pressure in the grips by a measurable amount, thereby increasing the effective shear load transferred into the specimen proportionally. The Poisson effect caused an 8% increase in the clamping pressure, which resulted in a higher gage section stress but a negligible change in the percent of the load introduced through shear. Because this error was insignificant and the modelling procedure was more straightforward for point loads, all of the numerical results discussed below were generated using an applied force boundary condition to model the clamping action of the D 6641 CLC fixture.

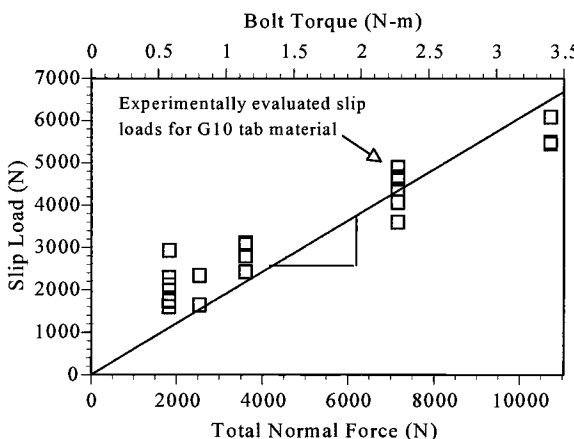


Figure 7 – Analysis of friction in grip surfaces.

The friction interface between the block and the top of the tab was modelled in ABAQUS as a pair of contact surfaces with a Coulomb friction model. The coefficient of friction for the grip surface between the flame sprayed clamp blocks and the tab surface was measured in a series of tests where a number of specimens were loaded only until they slipped in the clamp blocks. For G10 tabs, the coefficient of friction in the grips was estimated to be between 0.4 and 0.6 (see Figure 7), depending on how well the flame sprayed surfaces were cleaned prior to each test. A value of $\mu = 0.4$ was assumed throughout the analysis.

In the second step of the simulation, the end of the specimen and the clamp blocks were displaced simultaneously approximately 0.2 mm, simulating end loading. Since the method of loading introduction and the tabbing configuration varied, two to three computer runs were typically required to get the correct displacement for the specimen to yield the desired compressive axial stress $\bar{\sigma}_x = 965 \text{ MPa} \pm 0.5 \text{ MPa}$ in the gage section of the composite.

Three loading cases were evaluated in this study: pure shear load, pure end load, and combined shear and end load. The load transferred into the specimen by shear equals the total frictional force between the clamp blocks and the tab, which in turn is determined by the normal clamping force and the friction coefficient, μ . The nominal stress in the specimen $\bar{\sigma}_x = 965 \text{ MPa}$ corresponds to an axial force (in the quarter-model) of 15.6 kN.

For the pure shear case, the full axial force must be transferred by friction, which, with the assumed coefficient of friction of 0.4, requires a total normal clamping force of 38.9 kN, or 9.7 kN in each of the four bolts. From Equation 2, this normal force corresponds to a bolt torque of approximately 12.4 N-m (110 in-lbs).

The end load case starts by assuming a bolt torque of 0.6 N-m (5 in-lbs), which is the smallest that can be consistently applied to the clamp bolts, and is slightly larger than "finger-tight". Again using Equation 2, this corresponds to a normal force in each bolt of 0.47 kN, or a total normal force of 1.88 kN. The frictional force in this case is 0.75 kN, meaning that less than 5% of the load is delivered to the specimen through shear.

The combined loading case represents an intermediate bolt torque of 6.2 N-m (55 in-lbs), a total normal force of 19.4 kN, and frictional force of 7.75 kN. In this case, 50% of the axial loading comes in through the shear load and the other 50% by end loading.

Observations And Results

Effect of Load Introduction

The effect of loading method was investigated for square G10 tabs, 3.2 mm thick. Figure 8 shows the normalized axial stress distribution for a section along the long axis of the specimen (Section 1), one element below the specimen/tab interface since these values are more numerically reliable than those at the surface. The stresses were normalized with respect to the gage section value of the axial stress, $\bar{\sigma}_x$.

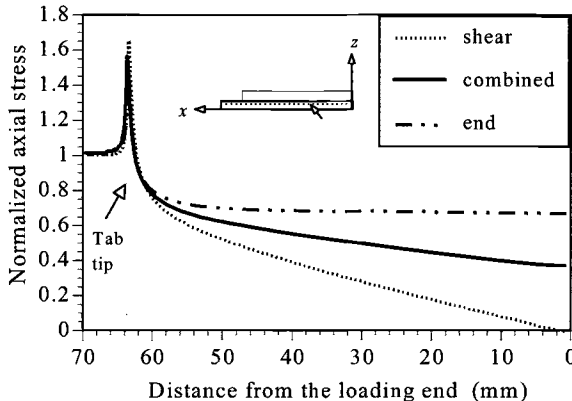


Figure 8 – Effect of load introduction on the axial stress distribution along the length of the specimen (Square, 3.2 mm thick, G10 tabs).

As expected, pure shear loading builds up axial load in the specimen through gradual shear transfer from the tabs until very close to the tab tip, where a discontinuity in the geometry as well as the stiffness account for a sharp spike in the stress distribution. The stresses are then relieved within the first 2.5 mm of the gage length. Our results are comparable in nature to those of Tan [16] and Ault and Waas [37] who both modelled pure shear loading using a uniform applied stress boundary condition.

Pure end loading, on the other hand, yields a much more constant stress distribution under the tabs, accompanied by a less pronounced stress concentration at the tab tip (approximately a 10% decrease compared to shear loading). The danger in end loading is not so much the stress concentration at the tab tip but end crushing failure at the loading end of the specimen failure. Combined loading has an intermediate tab tip stress concentration (a 6% decrease compared to shear loading), but also reduces the stress level at the loading end of the specimen compared to end loading, thereby reducing the tendency to fail by end crushing. Qualitatively our results are in good agreement with the prior analysis by Xie and Adams [9].

Figure 9 shows the axial stress distribution for a section taken in the specimen gage section just past the tab tip (Section 2). Clearly the axial stress distribution through the thickness is not strongly affected by the method of load introduction.

The shear and through-thickness stress components are small compared to the axial stress component. The shear and through-thickness stress components under the tab vary in direct proportion to the applied clamping pressure in the grips, as shown in Figures 10-11. For instance, the tab tip shear stress concentration factor, $\tau_{xz}/\bar{\sigma}_x$, and the tab tip stress concentration factor for the through-thickness stress component, $\sigma_z/\bar{\sigma}_x$, are 0.21 and 0.292, respectively, for pure shear loading, similar to the predictions obtained by Tan [16] for shear loading using a uniform applied stress boundary condition.

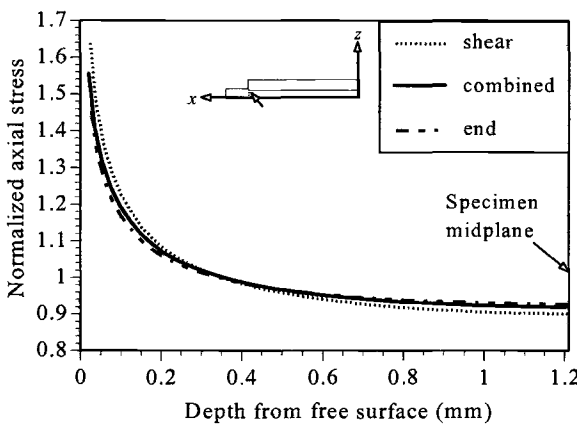


Figure 9 – Effect of load introduction on the axial stress distribution through the thickness of the specimen (Square, 3.2 mm thick, G10 tabs).

Pure end loading yields a 38% smaller value of $\tau_{xz}/\bar{\sigma}_x$ at the tab tip and a 38% decrease in the peak value of $\sigma_z/\bar{\sigma}_x$. It is also noteworthy to point out relatively flat shear stress distribution along Section 1, particularly near the loading end of the specimen. This is in sharp contrast to the high shear stress concentration predicted by Xie and Adams [9] at the loading end of the specimen, arising from the use of an applied uniform stress boundary condition to model end loading.

As before, combined loading produces an intermediate tab tip stress concentration factor of $\tau_{xz}/\bar{\sigma}_x = 0.165$ (a 21% decrease) and $\sigma_z/\bar{\sigma}_x = 0.226$ (a 23 % decrease). Again this result is qualitatively similar to that of Xie and Adams [9], except for the absence of a shear stress concentration at the loading end of the specimen, as described for pure end loading.

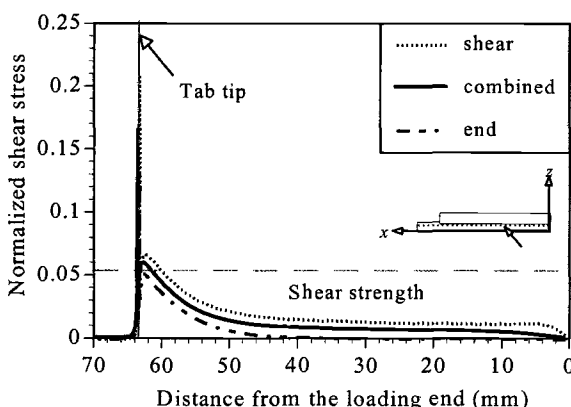


Figure 10 – Effect of load introduction on the shear stress distribution along the length of the specimen (Square, 3.2 mm thick, G10 tabs)

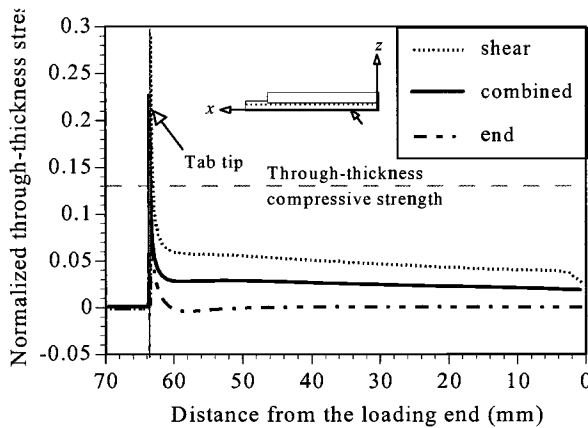


Figure 11 – Effect of load introduction on the through-thickness stress distribution along the length of the specimen (Square, 3.2 mm thick, G10 tabs)

While the shear stress and through-thickness stress components are small compared to the axial stress, it is important to compare them to the measured shear strength and the transverse tensile strength of the T300/P1700 composite since it is highly orthotropic. The strength values from Table 1, normalized by the nominal axial stress $\bar{\sigma}_x$, are shown as horizontal lines in Figures 10 and 11. The maximum values of shear and through-thickness stresses exceed their respective strengths over a very small region near the tab tip, which raises the possibility of localized failure as suggested by Wisnom [38]. However, it is also important to recall that the present analysis considers the constitutive behavior of the specimen, the adhesive and the tab material to be strictly linear elastic. Incorporating the effects of material nonlinearity is expected to significantly reduce the magnitude of the matrix dominated stress components, τ_{xz} and σ_z .

Figure 12 shows the clamping pressure distribution along the interface between the tab surface and the clamp block. The shear loaded case has the highest clamping pressure, as required to transfer the entire load from the block into the specimen by friction. It is also worth noting that the pressure distribution is nonuniform, indicating that an applied uniform stress boundary condition as used by previous investigators [9-11,20,33,34] is unrealistic for the D 6641 CLC fixture. For the shear loading case, the peak clamping pressure near the tab tip is 40% higher than the value that would be obtained if a uniform load were to be applied along the length of the end-tabs. Interestingly, the nonuniformity of the clamping pressure in the grips is even more exaggerated for the combined loading and end loading cases, although the pressures are lower.

The shearing deformation of the end-tabs allows the grip/tab friction interface to open, relieving the clamping pressure a short distance ahead of the tab tip. The greater the applied clamping pressure, the shorter the open distance. The shear deformation of the end-tabs causes the tab tip to bite into the specimen, which explains the spike in the through-thickness stress in the specimen at the tab tip.

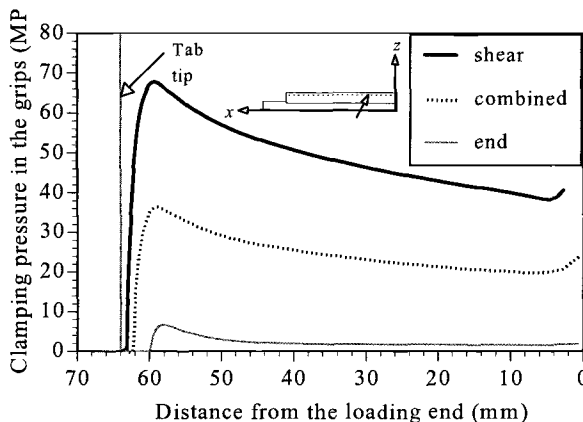


Figure 12 – Clamping pressure distribution along the surface of the tab (Square, 3.2 mm thick, G10 tabs).

The shear stress distribution along the clamp/tab interface has the same distribution as the pressure, but is smaller by a factor of the friction coefficient ($\mu = 0.4$).

Effect of Tab Material

The effect of tab material was investigated for square tabs of steel, aluminum, G10 glass-fabric/epoxy, and unreinforced epoxy under combined loading (6.2 N-m bolt torque). Figure 13 shows the axial stress distribution for Section 1 along the length of the specimen. Because stiffer tabs carry more of the load, we observe very low axial stresses in the composite coupon under the steel tabs, accompanied by a very steep load transfer into the coupon at the tab tip for steel tabs. In the instance of more compliant tabs such as G10 fiberglass or epoxy, the tabs carry less of the load, resulting in a more gradual shear transfer into the specimen gage length and reduced stress concentration at the tab tip. Of concern with the epoxy tabs in particular is the high stress levels at the loading end of the specimen, which may lead to failure by end crushing.

The tab tip stresses are better illustrated in Figure 14, which shows the axial stress distribution through the thickness just near the tab tip (Section 2). While the axial stress distribution is very uniform for compliant tabs such as epoxy, the shear transfer in the case of stiff tabs such as steel or aluminum produces a highly nonuniform through-thickness axial stress distribution.

The effects of tab material and loading method were evaluated simultaneously in Figures 15, 16 and 17 which show the maximum stress values along Section 1. Changing the stiffness of the tab material had a significant effect on the peak stresses. Stiff tabs proved to be relatively insensitive to the method of loading introduction, both because they are inefficient at transferring shear load gradually into the specimen, and because there exists a sharp stiffness discontinuity, making for an abrupt stress transfer even in the instance of pure end loading. However, a specimen with more compliant tabs clearly benefits from increased end loading since there is less of a stiffness discontinuity between the specimen and the tabs.

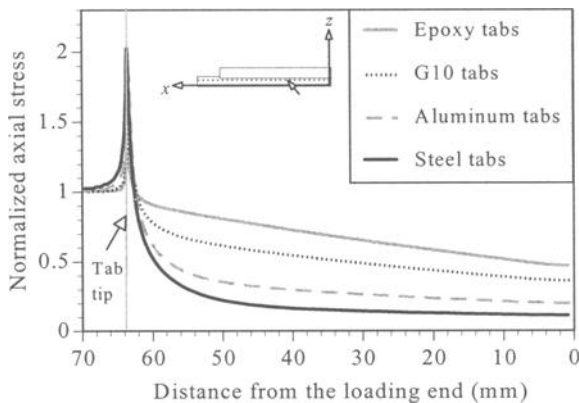


Figure 13 – Effect of tab material on the axial stress distribution along the length of the specimen (Square, 3.2 mm thick tabs, combined loading).

The results for an untabbed specimen are also included in Figures 15, 16, and 17. Figure 15 shows that an untabbed specimen yields the minimum axial stress concentration factor regardless of the loading method. Recall that tabs are generally included in the specimen design to prevent damage to the specimen itself in the case of shear loading test techniques, or alternatively as a means to eliminate failure by end crushing by effectively increasing the load bearing area of the specimen in the case of end loading test techniques. In the D 6641 CLC fixture with its flame sprayed gripping surfaces the need for tabs may be obviated at low bolt torque (~ 6 N·m); however, in practice there may be a lower limit to how much shear loading is needed before the specimen begins to fail instead by end crushing.

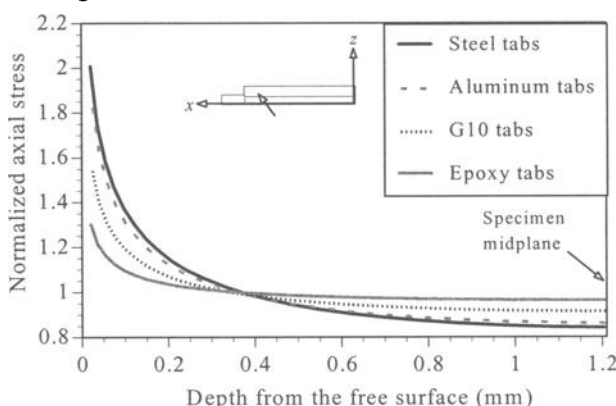


Figure 14 – Effect of tab material on the axial stress distribution through the thickness of the specimen (Square, 3.2 mm thick tabs, combined loading).

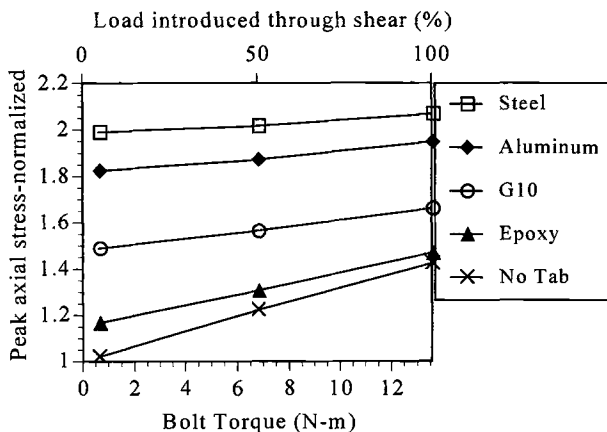


Figure 15 – Effect of loading method and tab material on peak axial stress in the specimen (Square, 3.2 mm thick tabs).

In Figures 16 and 17 we see the beneficial effects of compliant tabs, especially for moderate to high bolt torque (> 6 N-m). Not only are the stress concentration factors for compliant tabs lower than for stiff tabs, they are lower than for the untabbed specimen, since the tab acts to shield the specimen from the hard steel clamp blocks. In the case of pure end loading, the untabbed specimen yields the minimum tab tip stress concentrations. However, this specimen may prove impractical due to end crushing failure.

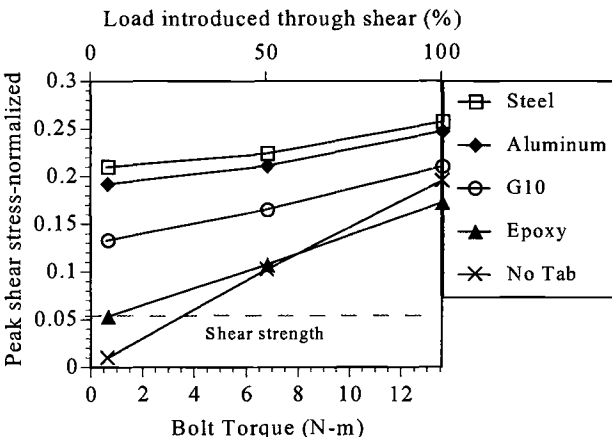


Figure 16 – Effect of loading method and tab material on peak shear stress in the specimen (Square, 3.2 mm thick tabs).

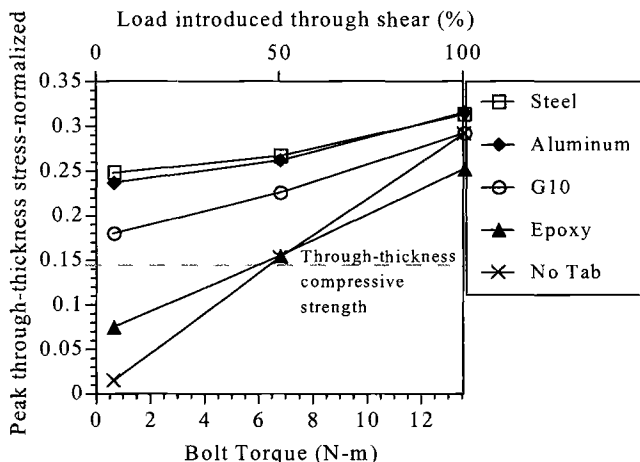


Figure 17 – Effect of loading method and tab material on peak through-thickness stress in the specimen (Square, 3.2 mm thick tabs).

The peak stresses in the specimen are related to the pressure distribution along the surface of the end-tabs, which is affected by the choice of tab material. Figure 18 shows the clamping pressure normalized by its nominal value, which is the total normal force divided by the area of the tab surface. Stiff end-tabs bear greater axial stress, resulting in higher shear stress in the tab. Increased shear deformation in the vicinity of the tab tip causes the grip/tab interface to open over a greater length than in the case of more compliant tabs, and results in a higher peak clamping pressure. The steel tab case has a peak clamping pressure nearly three times the nominal value, while the peak in the epoxy is only about 30% higher than nominal.

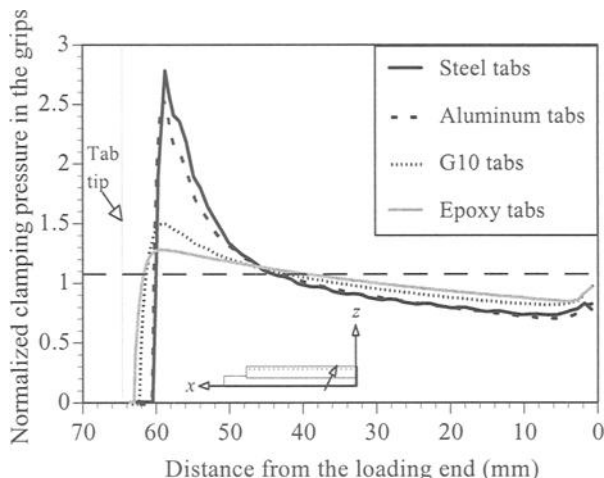


Figure 18 – Clamping pressure distribution along the surface of the tab (Square, 3.2 mm thick tabs, combined loading).

Effect of Tab Tip Geometry

Five different tab geometries were compared in this study: square (untapered) tabs, 30° taper, 20° taper, 10° taper, and radius tabs, which were shown in Figure 3. Each case had 3.2 mm thick tabs, and combined loading ($T = 6.2 \text{ N-m}$).

The effects of tab tip geometry and tab material were evaluated simultaneously. As expected, the overall stress distribution along the specimen/tab interface (Section 1) is not strongly affected by the tab tip geometry. However, the peak stresses and the distributions through the thickness of the specimen (Section 2) are strongly affected by the tab tip geometry.

The peak stresses are shown in Figures 19 to 21, with the radius-tab case plotted as 0° taper angle (shown connected by a dashed line) and square tab case as 90°. As in Figure 14, the peak stresses occur at the specimen/tab interface.

Figure 19 shows the same trend with respect to tab material that we demonstrated in Figure 15. No matter what the tab tip geometry, more compliant tabs yield a smaller axial stress concentration. Taper angle has a strong effect on the stress concentration in all three stress components, especially in the case of stiff tabs. It is interesting to note the sharp decrease in the tab tip stress concentration factor beginning with a taper angle of 30° for stiff tabs such as steel and aluminum, whereas in the case of compliant tabs, where the stress concentration is less significant to begin with, the effect of decreasing the taper angle is much less pronounced. A stiff tab material such as steel shows a far greater sensitivity to decreasing the tab taper angle, especially at the low end.

Interestingly, the peak axial stress in the radius tab case is comparable to or slightly higher than the 10° case. Although the radius tab is very thin at the tab tip, which would tend to cause a very low stress concentration, the length of the tapered region is even shorter than that of the 30° tapered tab; decreasing the distance over which load is transferred from the tab into the specimen tends to increase the stress concentration.

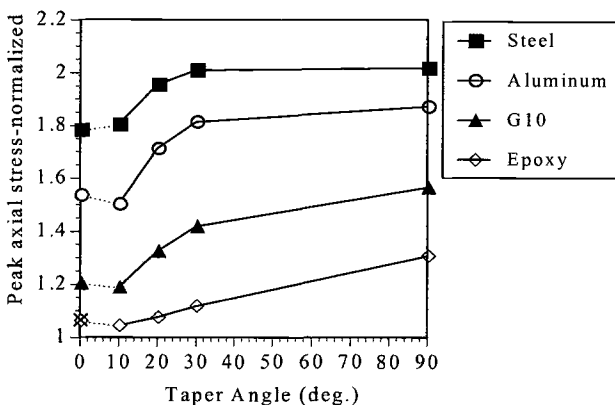


Figure 19 – Effect of tab material and tab tip geometry on peak axial stress in the specimen (3.2 mm thick tabs, combined loading).

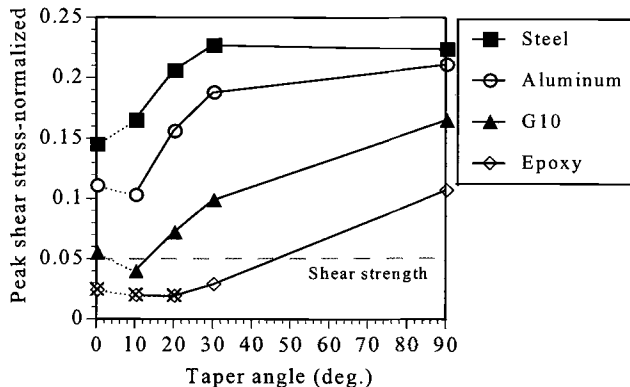


Figure 20 – Effect of tab material and tab tip geometry on peak shear stress in the specimen (3.2 mm thick tabs, combined loading).

The peak shear and through-thickness stresses in Figures 20 and 21 exhibit trends similar to those shown in Figure 19 for the peak axial stresses. However, in the case of epoxy tabs, which are very compliant, an interesting phenomenon is demonstrated at low taper angles. The peak value of shear stress (Figure 20) is the same for 10° and 20° and shows a slight increase for 30° taper angle. Similarly, the peak through-thickness stress (Figure 21) decreases for taper angle increasing from 10° to 30°. Inspection of a displaced view of the finite element model suggests this effect is related to the deformations in the tab tip, as the compliant tab material is unable to resist the lateral expansion of the test coupon due to Poisson's effect.

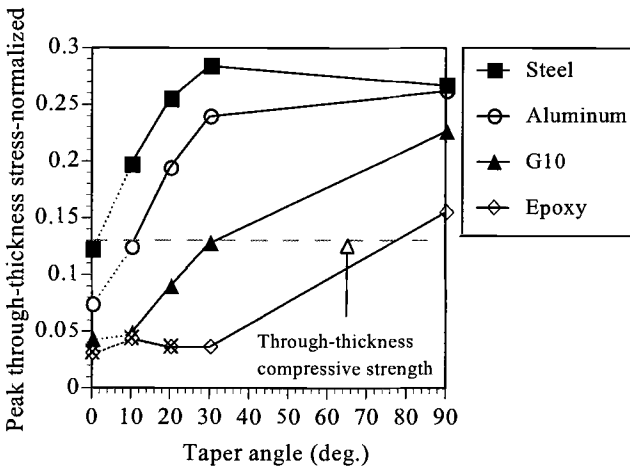


Figure 21 – Effect of tab material and tab tip geometry on peak through-thickness stress in the specimen (3.2 mm thick tabs, combined loading).

In almost every instance, the peak stresses occur at the tab tip. In the case of epoxy tabs with a very low taper angle, the shear and through-thickness stress concentrations move from the tab tip to the elbow of the tab, where the taper ends and the flat part begins. The cases, for which the stress concentration peak is at the elbow, rather than at the tab tip, are denoted with an X through the data point in the graph.

This effect is best explained by looking in detail at the stress distributions along the length of the specimen, as in Figures 22 and 23. Epoxy tabs provide little or no lateral support in the taper region of the tab and so the stress concentration due to the tab tip is diminished in comparison to the results shown in Figures 20 and 21 for G10, aluminum, and steel. The peak stress in this instance occurs instead at the elbow of the tab rather than at the tab tip.

Figures 20 to 23 again show the shear and through-thickness strengths of the composite specimen as horizontal lines. The peak values exceed the strength for all the square tabs, and several of the cases with stiffer tabs and high taper angles. However, the region over which the stress exceeds the strength value is both limited and dependent on the tab tip geometry.

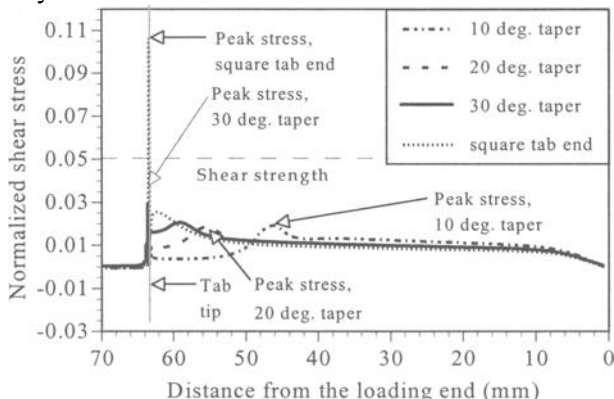


Figure 22- Effect of tab tip geometry on the shear stress distribution along the length of the specimen (3.2 mm thick, epoxy tabs, combined loading).

Figure 24 shows the effect of tab tip geometry on the shear stress distribution through the thickness of a specimen with G10 tabs. From Figure 24 we can see that although the peak shear stresses in Figure 20 may be in excess of the composite shear strength, the stresses quickly dissipate to within an acceptable level. The depth over which the shear stress exceeds the composite shear strength is about 15% of the specimen thickness in the case of square tabs, less than one tenth of the specimen thickness in the case of 30° tapered tabs, and only 3 elements (0.048 mm) for a specimen with 20° tapered tabs. The region over which the through-thickness stress exceeds the through-thickness compressive strength is even smaller and limited to only a few elements for most cases.

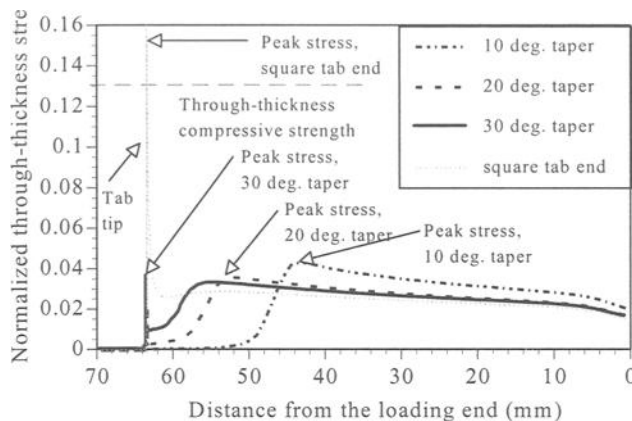


Figure 23 – Effect of tab tip geometry on through-thickness stress distribution along the length of the specimen (3.2 mm thick, epoxy tabs, combined loading).

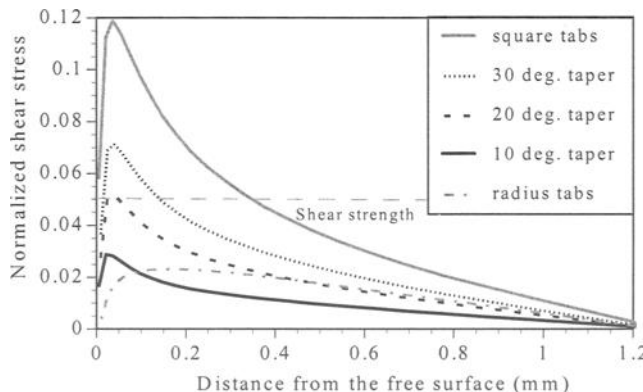


Figure 24 – Effect of tab tip geometry on shear stress distribution through the thickness of the specimen (3.2 mm thick, G10 tabs, combined loading).

Effect of Tab Thickness

The effect of tab thickness was investigated for square tabs of each material, and for G10 tabs with different taper angles. All cases had combined loading.

For the case of square tabs, the effects of tab thickness and tab material on the peak stresses were evaluated simultaneously in Figures 25-27. Also included in these three figures for comparison are the peak stresses for an untabbed specimen, as well as the results from an analysis, that included the adhesive layer but no tab.

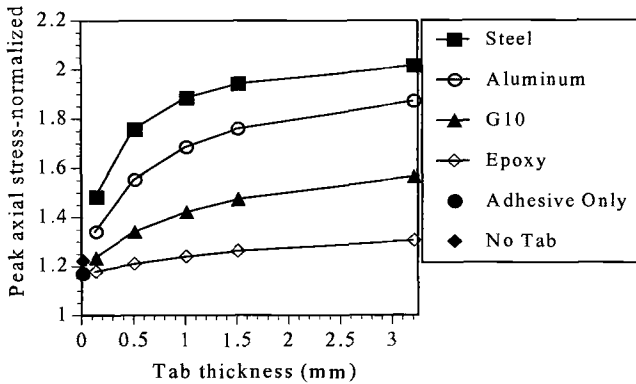


Figure 25 – Effect of tab material and thickness on peak axial stress in the specimen (Square tabs, combined loading).

It is clear once again that more compliant tabs yield lower stress concentrations. In the case of a specimen with G10 square tabs under combined loading, the tab tip axial stress concentration factor, $\sigma_x/\bar{\sigma}_x = 1.565$ for 3.2 mm thick tabs. Halving the tab thickness to 1.5 mm results in a 6% decrease in the axial stress concentration factor. An additional 33% decrease in thickness results in another 4% decrease in $\sigma_x/\bar{\sigma}_x$. Although it is not shown here, decreasing the tab thickness similarly decreases the axial stress gradient through the thickness.

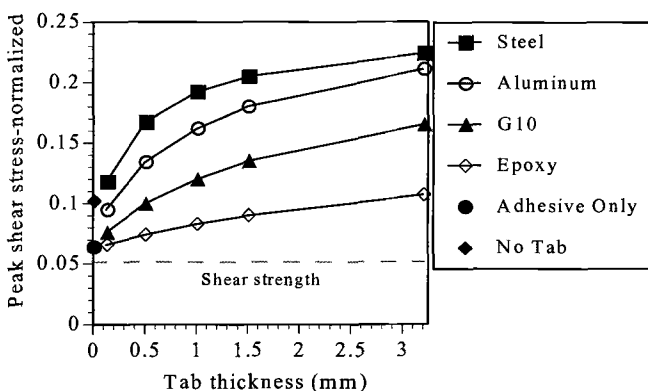


Figure 26 – Effect of tab material and thickness on peak shear stress in the specimen (Square tabs, combined loading).

If the end-tabs were perfectly bonded to the specimen, both the specimen and the end-tabs would have the same axial strain; hence, the load carried in the tab would be proportional to its overall tab stiffness, EA , (where E = Young's modulus and A is its cross-sectional area). Since the adhesive layer bonding the end-tabs to the specimen has a finite thickness and a relatively low Young's modulus, the adhesive layer allows some

difference in strain between tab and specimen. Nonetheless, thicker, stiffer tabs will carry a greater proportion of the load as shown in Figure 28, whereas thinner tabs carry a smaller fraction of the load. In the case of the square tab, the tab area A is constant for the full length of the tab, and the geometric discontinuity leads to a high stress concentration at the tab tip.

The effect of the adhesive stands out in Figures 26 and 27 and perhaps to a lesser extent in Figure 25. As EA decreases, the peak stress is converging to the adhesive-only prediction, which is markedly lower in magnitude than the peak stress predicted for the untabbed specimen. The adhesive has a very low Young's modulus, so it effectively smears out the stresses imposed by the rigid clamp blocks. The same can be said for the discrepancy in Figure 25 between the no-tab prediction and the adhesive only prediction; the shear lag caused by the compliant adhesive reduces the magnitude of the stress concentration caused by the clamp blocks at the end of the gage length.

In the case of tapered tabs, the geometric discontinuity at the tab tip is less severe, allowing for a more gradual transfer of load from the tab to the specimen. Although increasing the tab thickness increases the proportion of the load carried by the tab, it also increases the length of the tapered region over which this load is transferred to the specimen. Changing the thickness has the greatest effect on square tabs, and virtually no effect on 10° tapered tabs, as shown in Figure 29. The effect of decreasing the tab taper angle is less significant in thin tabs than in thick tabs.

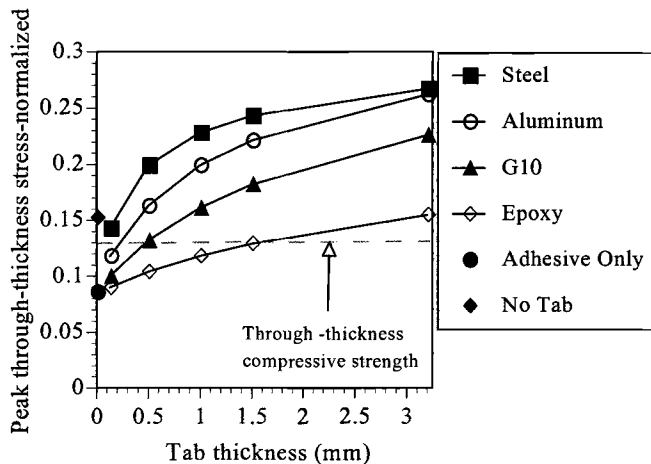


Figure 27 – Effect of tab material and thickness on peak through-thickness stress in the specimen (Square tabs, combined loading).

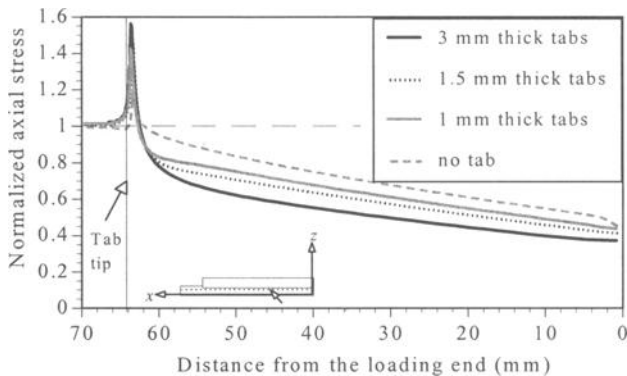


Figure 28 – Effect of tab thickness on axial stress distribution along the length of the specimen (Square, G10 tabs, combined loading).

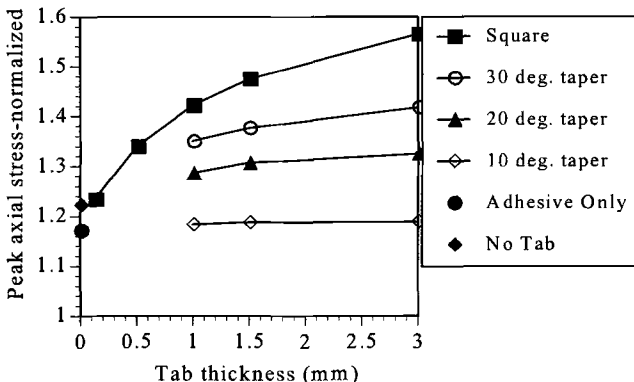


Figure 29- Effect of tab thickness and taper angle on peak axial stress in the specimen (G10 tabs, combined loading).

Effect of Debond

Finally, the effect of tab debonding at the tab tip was evaluated. Debonded square, tapered (10°) and radius tabs were compared to their fully-bonded counterparts for the case of combined loading ($T = 6.2$ N-m) and 3.2 mm thick G10 tabs.

First we compared the effects of deliberate tab debonding as in the Rolfs-Sendeckyj specimen [19-20] with the effects of *in-situ* tab debonding as observed by Adams and Odom [15]. Our results showed no significant difference in the stress distributions whether the debond was modelled as a Teflon insert with a low coefficient of friction, or as a discontinuity in the adhesive layer with a high coefficient of friction, simulating a crack in the adhesive. Figure 30 examines the effects of *in-situ* tab debonding for a specimen with square G10 tabs. The axial stress concentration is slightly

higher for the debond case than for the fully-bonded case. The stress distribution for the case of deliberate debonding is indistinguishable from the *in-situ* tab debonding case.

Although the magnitude of the peak axial stress is not strongly affected by the debond, its location is; the peak occurs not at the tab tip but under the tab, at the end of the adhesive (see Figure 30). The stresses are then relieved under the tab approaching the gage section. While this may offer the advantage of a more uniform strain field in the gage section of the specimen for the purposes of modulus evaluation, it does nothing to promote gage section failure for strength testing.

Since we observed no significant difference between the *in-situ* debond case and the case of deliberate debonding, the remainder of this section evaluates only the case of *in-situ* debonding.

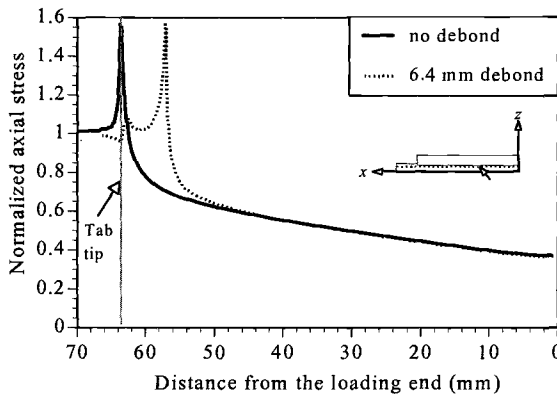


Figure 30 – Effect of tab debonding on axial stress distribution along the length of the specimen (Square, 3.2 mm thick, G10 tabs, combined loading).

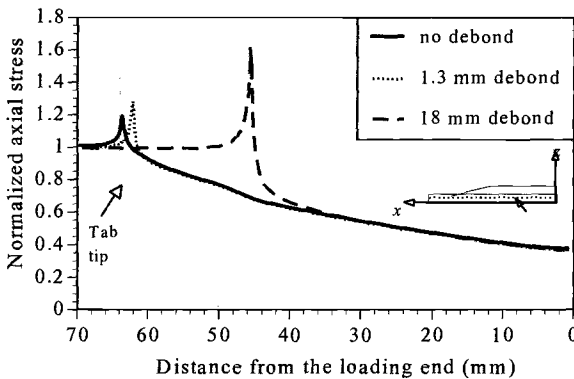


Figure 31 – Effect of *in-situ* tab debonding on axial stress distribution along the length of the specimen (10° tapered, 3.2 mm thick, G10 tabs, combined loading).

The effect of *in-situ* tab debonding in a specimen with G10 tabs with a 10° tab taper is shown in Figure 31. Three cases are illustrated: fully bonded, a short (1.3 mm)

debond, and a long (18 mm) debond stretching the entire length of the tapered region. It is clear that the effect of tab debonding is detrimental; the presence of even a very short crack in the adhesive amplifies the axial stress concentration by 8%, while a long crack increases the peak axial stress by 37%. As one would expect, the long debond case exhibits an axial stress concentration factor similar to a specimen with G10 tabs with square tab ends under the same loading conditions.

Finally we evaluated the effect of *in-situ* tab debonding in a specimen with G10 tabs with a 3.2 mm radius tab end (see Figure 32). Once again, it is clear that tab debonding has only detrimental effects on the axial stress concentration in the specimen; a 3.2 mm debond, simulating a crack in the adhesive extending to the elbow of the tab, increases the peak $\sigma_x/\bar{\sigma}_x$ by 30%.

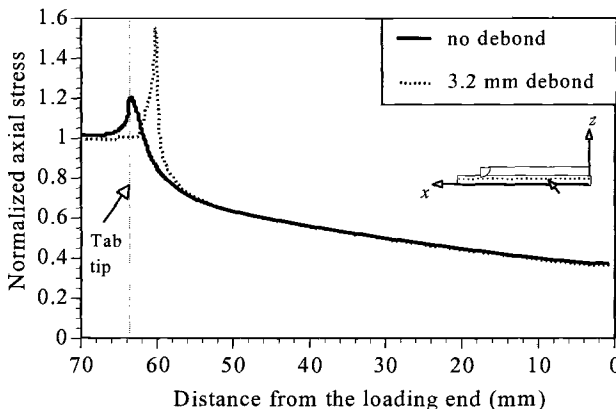


Figure 32 – Effect of *in-situ* tab debonding on axial stress distribution along the length of the specimen (Radius, 3.2 mm thick, G10 tabs, combined loading).

The effect of tab debonding on the peak axial and shear stress values is summarized in Figure 33. The results in this figure are for *in-situ* debonds; the 10° tapered results are for the long (18 mm) debond. From Figures 30 and 33, we can see that for square tabs, although the magnitude of the peak axial stress is unchanged, the axial stress concentration is removed from the gage section by tab debonding. The peak shear stress, however, is almost halved in the case of tab debonding for square end-tabs. This may be beneficial since shear stresses have been implicated as a cause of premature failure in compression testing [35].

The detrimental effects of *in-situ* debonding are clearly illustrated for tapered or radius tabs in Figure 33, which show a strong increase in both peak axial and shear stresses. While the gage section stress field may be more uniform because the stress concentration has been pushed back to the end of the adhesive (the tip of the debond), any advantage formerly afforded by the tab tip geometry is nullified by the presence of the tab tip debond and the stress concentration reverts to that of a specimen with square tab ends. The same trend can be observed for specimens with stiff tabs such as steel tabs.

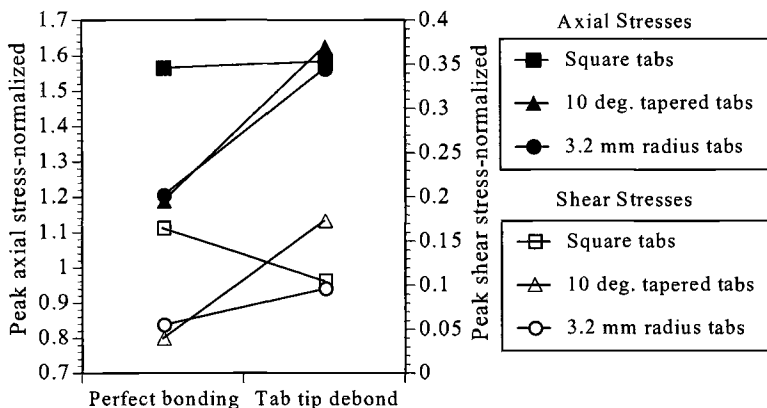


Figure 33 – Effect of *in-situ* tab debonding on peak axial and shear stresses (3.2 mm thick, G10 tabs, combined loading).

Summary of Results

The comparison of loading methods suggests that the specimen should be end loaded as much as possible without inducing undesirable failure mechanisms such as end brooming or crushing. Increasing the proportion of end loading not only reduces the axial stress concentration in the specimen, but also minimizes the shear and through-thickness stress components. Combined loading appears to be a good compromise, which decreases the tab tip stress concentrations from the level found in shear loading, but also decreases the stresses at the loading end of the specimen, which may prevent premature end failure characteristic of end loading.

Several tabbing configurations were examined in an attempt to optimize specimen performance. The finite element analysis predicts that more compliant tabs will yield lower stress concentrations in all three stress components (see Figures 15-21), regardless of tab geometry and loading condition.

In square tabs, it is the overall tab stiffness, EA , which governs the peak stress levels; thin tabs yield the same advantage in terms of lower stress concentrations as more compliant tab materials. While decreasing the thickness of square tabs by a factor of six (from 3.2 mm to 0.5 mm thick for square G10 tabs) yielded almost a 15% decrease in the axial stress concentration factor, the peak stress at the tab tip is still 30% higher than the nominal gage section stress (see Figure 25). Likewise, even for the thinnest square tabs, the peak shear stress at the tab tip is still two times higher than the nominal shear strength of the T300/P1700 composite (see Figure 26). While this may be a localized phenomenon, it is still of concern since compressive failure is driven by shear instability, and the presence of high shear stresses at the tab tip is likely to cause premature failure.

Next, the effects of tab tip geometry were evaluated. The finite element model was used to evaluate varying tab taper angle, as well as the effects of deliberate or *in-situ* tab debonding. Reducing the tab taper angle significantly reduced the tab tip stress concentrations; a 10° taper angle reduces the tab tip axial stress concentration in a specimen with 3.2 mm thick G10 tabs by almost 25% compared to 3.2 mm thick G10

tabs with square tab ends, and the peak shear and through-thickness stress values lie within acceptable limits as well (see Figures 19-21). However, thick end tabs with a 10° taper angle may be in danger of failure by global buckling.

While the finite element analysis predicts the optimal tabbing configuration to be compliant tabs with a shallow taper angle, this turns out to be the worst scenario in terms of global buckling (see Figure 4). If thick tabs are tapered to a very small taper angle, the effective gage length is significantly increased. An improved solution is to use thin tabs, in which case the effect of the tab taper length on the unsupported gage length is minimized. For example, for G10 tabs with a 10° taper angle, reducing the tab thickness from 3.2 mm to 1.5 mm has no significant effect on the tab tip stress concentrations (see Figure 29), but the unsupported length is reduced enough to virtually prohibit global buckling.

Finally we examined the effects of tab tip debonding in square, 10° tapered, and radius tabs, as shown in Figures 30-33. For the square tabs, the debond had little effect on the peak axial stress, and actually decreased the peak shear stress, but moved both stress concentrations back from the tab tip to the edge of the debond. For the tapered and radius tabs, the stress concentrations were also moved to the edge of the debond but were markedly increased compared to the fully-bonded case. The peak axial stress was comparable in all the debond cases; debonding a tapered tab completely eliminated the benefits of using a tapered end-tab. While moving the stress concentration away from the tab tip may lead to a more uniform strain field in the gage section, it will not provide a more accurate measure of composite compressive strength.

Discussion

The finite element model in this study explicitly included the test fixture's clamp blocks, which we believe is a more realistic way to model boundary conditions than by applying either uniform stress or uniform displacement on the tab surface. Indeed, Figures 12-18 show that the clamping pressure is nonuniform, especially for stiff tabs. Our model also included a uniform applied displacement in the second step of loading, which we feel is the only realistic way to model end loading.

Xie and Adams [9-11] modelled compression testing by applying uniform stresses on both the tab face and the end of the specimen. For end loading, they observed an upswing, or "tail" in the shear stress in the specimen at the loading end, which they suggested was a contributing factor in end brooming, and should be eliminated by using tabs of the same material as the test specimen. The stress concentration or "tail" arises in the instance of applied uniform stress, due to the load transfer from the more compliant elements (specimen and adhesive) into the stiffer elements (steel tabs), leading to a state of uniform strain in the specimen, adhesive, and tab. Our results (Figures 10 and 22) using an applied uniform displacement boundary condition to model end loading eliminate this erroneous stress concentration since the strains are inherently uniform.

Similarly, since the model developed by Xie and Adams was only hypothetical, the boundary conditions they chose for the clamping pressure for end loading seem unrealistic by comparison. End loading can be achieved in the D 6641 CLC fixture using very modest clamping pressure; therefore our results for this fixture show lower stress

concentrations arising from end loading, notably the through-thickness stress concentration.

A study of the effect of gap size showed that a minimum gap between the end of the specimen and the edge of the clamp blocks is required to achieve 100% of the target shear; increasing the gap size beyond the threshold value did not affect the magnitude of the load transferred into the specimen. As shown in Figure 6, the minimum gap required to develop 100% of the target load in the specimen was found to increase as the proportion of shear loading increases, and with a more compliant tab material. A gap size of 0.25 mm to 0.50 mm was sufficient for the cases in this study. This analysis suggests that care must be taken when placing a test specimen in the fixture, to ensure that the full shear load is developed in the specimen coupon before the specimen ends contact the loading surfaces. This is of secondary importance, since our other results demonstrate that the best test configuration favors end loading with just enough load introduced through shear to prevent end crushing of the specimen. The gap analysis result is interesting though, suggesting careful experimental verification and a review of the ASTM D 6641-01 procedure.

Since the constitutive behavior of the specimen, the adhesive and the tab material is modelled as strictly linear elastic, the current model predicts very high localized shear and through-thickness stresses in the specimen, the adhesive and the tab material in several instances. Bearing in mind this limitation, it is important to consider the results of this analysis to be strictly qualitative regarding the through-thickness and shear tab tip stress concentrations predicted for the various specimen/tabling configurations considered in this study. Incorporating the effects of material nonlinearity is expected to significantly reduce the magnitude of the matrix-dominated stress components, τ_x and σ_z . However, the axial stress component is expected to be unaffected by the material nonlinearity [9-11], since the material properties in the fiber direction are linear.

Conclusions

The finite element analysis in this study has developed a thorough picture of how the various factors influencing the stress distribution in composite compression testing act and interact. The results suggest use of combined shear and end loading, and a specimen with thin, compliant, tapered tabs. The finite element results favor end loading to the extent that undesirable failure mechanisms such as end brooming or crushing can be avoided; however, this limit was not clearly established using finite element analysis only. The problems associated with shear loading are clearly demonstrated by the finite element model results; in terms of the tab tip stress concentrations that develop no matter what the tabbing configuration. Combined shear and end loading as with the D 6641 CLC fixture offers an attractive compromise, in terms of reduced tab tip stress concentrations but also in terms of decreased stresses at the loading end of the specimen and increased constraint which may help prevent end brooming or crushing. Our results are in overall agreement with the previous work by Xie and Adams [9-11], however through the use of proper boundary conditions, we eliminated the stress concentration effect at the loading end of the specimen, previously thought to be responsible for end brooming failure.

In fact, the efficiency of the D 6641 CLC fixture at transferring shear load could be improved by modifying the grip/tab friction coefficient. Increasing the friction coefficient would decrease the normal force necessary to achieve a desired amount of shear load, and hence reduce the through-thickness stresses in the specimen. The friction model in this study was based on experimental observation of specimens with G10 tabs; a thorough evaluation of the friction resulting from other tab materials or surface conditions might yield a higher friction coefficient for the D 6641 CLC. Another possibility might be modifying the test fixture by roughing up the grip surfaces.

Several tabbing configurations were examined in an attempt to optimize specimen performance. Contrary to what Xie and Adams [9-11] concluded, using a uniform applied stress boundary condition, our finite element results demonstrate that more compliant tabs will yield lower stress concentrations in all three stress components (see Figures 15-21), regardless of tab geometry and loading condition. This is due to more explicit modelling of the boundary conditions arising from use of the actual dimensions and mechanics of the D 6641 CLC fixture (see Figure 8.) Furthermore, our analysis showed that, it is the overall tab stiffness, EA that governs the stress intensity incipient in tabbed specimens, that is, thin tabs yield the same advantage in terms of lower stress concentrations as more compliant tab materials.

The effects of tab tip geometry were also evaluated. The finite element model was used to evaluate varying tab taper angle, including radius tabs, as well as the effects of deliberate or *in-situ* tab debonding. Reducing the tab taper angle significantly reduced the tab tip stress concentrations. However, tapered tabs in particular increase the effective buckling length of the specimen. This problem must be carefully considered independently of the finite element analysis results to determine if the specimen geometry is in danger of failure by global buckling. The effects of using a shallow taper angle can be reduced by using thin tabs or radius tabs.

One possible alternative may be radius tabs. This analysis examined radius tabs with a tab tip radius equal to the tab thickness, in this case 3.2 mm. This specimen looks favorable both in terms of the tab tip stress concentrations (see Figures 19-21) and also with respect to global buckling. The peak shear stress predicted by the finite element model appears a little high, but this could be reduced through further specimen optimization, perhaps through the use of thinner tabs. The chief drawback to the radius tabs lies in the method of manufacture, milling a curved surface into a set of tabs prior to bonding them onto an already-manufactured composite may prove difficult, even prohibitive. These tabs appear to be most feasible when integral tabs are manufactured as part of the laminate as it is laid up and cured, as proposed by Curtis et al. [21]. Then the tab material is milled away from what becomes the specimen gage section, and a curved surface can be readily milled into the tab.

Finally we examined the effects of tab tip debonding in square, 10° tapered, and radius tabs, as shown in Figures 30-33. Tab tip debonding had a positive affect on the stress concentration in the specimen configuration with square tabs as implied by the work of [23]. However, in both the tapered tabs and the radius tabs, the stress concentration was markedly increased negating any positive effect derived from modifying the tab tip geometry. In all three cases, tab tip debonding also had the effect of shifting the location of the stress concentration away from the tab tip region, this helps in that it leads to a more uniform strain field in the gage section, but it does little to

increase the probability of an acceptable failure. Tab tip debonding is only beneficial as an alternative to using tapered tabs or radius tabs. From a practical perspective, it seems that even in the case of square tabs, tab tip debonding does little to help provide a more accurate measure of composite compressive strength.

The debilitating effects of tab tip debonding are of particular concern because our model does not explicitly predict failure in the adhesive, which in an actual specimen would lead to *in-situ* debonding. Real adhesives may fail "prematurely" making some of the predictions described as part of this investigation unattainable. Further tests to evaluate the critical interfacial strength of real adhesives are necessary before experimentalists can anticipate and avoid *in-situ* debonding.

The finite element model does not explicitly predict specimen failure, either by global buckling, end brooming, or due to the tab-tip stress concentrations. Which failure mode will prevail for a particular material, specimen configuration, and loading condition must be determined experimentally. The D 6641 Combined Loading Compression fixture makes possible a direct comparison of shear, end, and combined loading, which have previously required different fixtures and, often, different specimen geometries.

The recommendations in this study are therefore a good starting point for further experimental work. Several issues remain to be explored in depth; perhaps the most immediate question is the amount of end loading which leads to end failure for various specimen/tabling configurations, because this will place a practical limit on the proportion of end loading used in combined loading. Other issues are whether lower stress concentration factors at the tab tip lead directly to higher failure strengths, the significance of the shear and through-thickness stress components, and the proper end conditions for predicting buckling failure of tabbed specimens. The finite element analysis suggests that the D 6641 CLC fixture used in combined loading holds great potential to improve compression strength measurements of unidirectional composites once these issues have been satisfactorily resolved.

Acknowledgements

Financial support from Dr. Yapa Rajapakse of the Office of Naval Research under grant ONR-N00014-91-J-4091 is gratefully acknowledged. Additional support is provided by Dr. Bruce Kramer of the National Science Foundation under grant DDM-9258413. The authors would like to express their appreciation to Dr. Richard A. Schapery of the Aerospace Engineering and Engineering Mechanics Department, The University of Texas at Austin for the use of his laboratory facilities and equipment.

References

- [1] Schoeppner, G. A., and Sierakowski, R. L. "A Review of Compression Test Methods for Organic Matrix Composites," *Journal of Composites Technology & Research*, Vol. 12, No. 1, 1990, pp. 3-11.
- [2] Welsh, J. S., and Adams, D. F. "Current-Status of Compression Test Methods for Composite Materials," *SAMPE Journal*, Vol. 33, 1997, pp. 35-43.

- [3] Zhigun, I. G., Polyakov, V. A., and Mikhailov, V. V. "Peculiarities of Composite Testing in Compression," *Mekhanika Kompozitnykh Materialov*, Vol. 6, 1979, pp. 1111-1118 (in Russian.)
- [4] Tarnopol'skii, Y. M. and Kincis, T. Static Test Methods for Composites, Van Nostrand Reinhold Co. Inc., New York, New York, 1985.
- [5] Woolstencroft, D. H., Curtis, A. R. and Haresceugh, R. I. "A Comparison of Test Techniques Used for Evaluation of the Unidirectional Compressive Strength of Carbon Fiber Reinforced Plastics," *Composites*, Vol. 12, No. 4, 1981, pp. 275-280.
- [6] Barker, A. J. and Balasundaram, V. "Compression Testing of Carbon-Fibre Reinforced Plastics Exposed to Humid Environments," *Composites*, Vol. 18, No. 3, 1987, pp. 217-226.
- [7] Häberle, J. G. and Matthews, F. L. "An Improved Technique for Compression Testing of Unidirectional Fibre-Reinforced Plastics; Development and Results," *Composites*, Vol. 24, No. 5, 1994, pp. 358-371.
- [8] Hsiao, H. M., Daniel, I. M., and Wooh, S. C. "A New Compression Test Method for Thick Composites," *Journal of Composite Materials*, Vol. 29, 1995, pp. 1789-1806.
- [9] Xie, M. and Adams, D. F. "Effect of Loading Method on Compression Testing of Composite Materials," *Journal of Composite Materials*, Vol. 29, No. 12, 1995, pp. 1581-1600.
- [10] Xie, M. and Adams, D. F. "Effect of Specimen Tab Configuration on Compression Testing of Composite Materials," *Journal of Composites Technology & Research*, Vol. 17, No. 2, 1995, pp. 77-83.
- [11] Xie, M. and Adams, D.F. "Tab Adhesive in a Composite Compression Specimen," *Polymer Composites*, Vol. 16, No. 6, 1995, pp. 529-535.
- [12] Welsh, J. S. and Adams, D. F. "Unidirectional Composite Compression Strengths Obtained By Testing Cross-Ply Laminates," *Journal of Composites Technology & Research*, Vol. 18, No. 4, 1996, pp. 241-248.
- [13] Welsh, J. S. and Adams, D. F. "Testing of Angle-ply Laminates to Obtain Unidirectional Composite Compression Strengths," *Composites*, Part A, Vol. 28A, 1997, pp. 387-396.
- [14] Adams, D. F. and Welsh, J. S. "The Wyoming Combined Loading Compression (CLC) Test Method," *Journal of Composites Technology & Research*, Vol. 19, 1997, pp. 123-133.

- [15] Adams, D. F. and Odom, E. M. "Influence of Specimen Tabs on the Compressive Strength of a Unidirectional Composite Material," *Journal of Composite Materials*, Vol. 25, 1991, pp. 774-786.
- [16] Tan, S. C. "Stress Analysis and Testing of Celanese and IITRI Compression Specimens," *Composites Science and Technology*, Vol. 44, No. 1, 1992, pp. 57-70.
- [17] Sinclair, J. H. and Chamis, C. C. "Compressive Behavior of Unidirectional Fibrous Composites," *Compression Testing of Homogeneous Materials and Composites*, ASTM STP 808, Richard Chait and Ralph Papirno, Eds., American Society for Testing and Materials, 1983, pp. 155-174.
- [18] Adams, D. F. and Lewis, E. Q. "Influence of Specimen Gage Length and Loading Method on the Axial Compressive Strength of a Unidirectional Composite Material," *Experimental Mechanics*, Vol. 31, No. 2, 1991, pp. 14-20.
- [19] Rolfs, R. L. "Test Method for Compressive Properties of Oriented Fiber Composites with the Prototype Compression Fixture," Air Force Wright Aeronautical Laboratories Technical Memorandum, AFWAL-TM-85-222-FIBC, August 1985.
- [20] Rolfs, R. L. "Compressive Test Fixture Evaluation of Oriented Fiber Composites with the Prototype Compression Fixture," Air Force Wright Aeronautical Laboratories Technical Memorandum, AFWAL-TM-87-172-FIBC, January 1987.
- [21] Curtis, P. T., Gates, J., and Molyneux, C. G. "An Improved Engineering Test Method for Measurement of the Compressive Strength of Unidirectional Carbon Fibre Composites," *Composites*, Vol. 22, No. 5, 1991, pp. 363-368.
- [22] Häberle, J. G. and Matthews, F. L. "The Influence of Test Method on the Compressive Strength of Several Fiber-Reinforced Plastics," *Journal of Advanced Materials (SAMPE Quarterly)*, Vol. 25, No. 1, 1993, pp. 34-45.
- [23] Häberle, J. G. and Matthews, F. L. "An Improved Technique for Compression Testing of Unidirectional Fibre-Reinforced Plastics," *Composites*, Vol. 25, No. 5, 1994, pp. 358-371.
- [23] Joyce, P. J. "Experimental Investigation of Defect Criticality in Laminate Composites," Ph.D. thesis, The University of Texas at Austin, Austin, TX, 1999.
- [24] Violette, M. G. "Time-Dependent Compressive Strength of Unidirectional Viscoelastic Composite Materials," Ph.D. thesis, The University of Texas at Austin, Austin, TX, 2000.
- [25] Joyce, P. J. and Moon, T. J. "Compression Strength Reduction in Composites with In-Plane Fiber Waviness," *Composites: Fatigue and Fracture (Seventh Volume)*, ASTM

STP 1330, R. B. Bucinell, Ed. American Society for Testing and Materials, West Conshohocken, Penn., 1998, pp. 76-96.

[26] Coguill, S. L. and Adams, D. F., "Use of the Wyoming Combined Loading Compression (CLC) Fixture to Test Unidirectional Composites," Evolving and Revolutionary Technologies for the New Millennium, Proceedings of the 44th International SAMPE Symposium, L. J. Cohen, J. L. Bauer, and W. E. Davis, Eds. Society for the Advancement of Material and Process Engineering, Covina, Cal. 1999, pp. 2322-2331.

[27] Adams, D. O., and Hyer, M. W. "Effect of Layer Waviness on Compression Loaded Thermoplastic Composite Laminates," Technical Report, Virginia Polytechnic Institute and State University, 1992.

[28] Naley, M. "Fabrication and Testing of Unidirectional Thermoplastic Composite Plates with Varying Degrees of Fiber Waviness," Master's thesis, The University of Texas at Austin, Austin, TX, 1994.

[29] Cook, R. D. and Young, W. C. Advanced Mechanics of Materials, Macmillan Publishing Company, New York, New York, 1985.

[30] Daniels, J. A. and Sandhu, R. S. "Evaluation of Compression Specimens and Fixtures for Testing Unidirectional Composite Laminates," *Composite Materials: Testing and Design (Eleventh Volume)*, ASTM STP 1206, E. T. Camponeschi, Jr. Ed. American Society for Testing and Materials, West Conshohocken, Penn., 1993, pp. 103-123.

[31] Cunningham, M. E. Schoultz, S. V. and Toth, J. "Effect of End Tab Design on Tension Specimen Stress Concentration," *Recent Advances in Composites in the United States and Japan, ASTM STP 864*, American Society for Testing and Materials, West Conshohocken, Penn., 1985, pp. 253-262.

[32] Rehfield, L. W., Armanios, E. A. and Changli, Q. "Analysis of Behavior of Fibrous Composite Compression Specimens," *Recent Advances in Composites in the United States and Japan, ASTM STP 864*, American Society for Testing and Materials, West Conshohocken, Penn., 1985, pp. 236-252.

[33] Adams, D. F. and Finley, G. A. "Experimental Study of Thickness-tapered Unidirectional Composite Compression Specimens," *Experimental Mechanics*, Vol. 36, No. 4, 1996, pp. 345-352.

[34] Adams, D. F. and Finley, G. A. "Analysis of Thickness-Tapered Unidirectional Composite Compression Specimens," *Journal of Composite Materials*, Vol. 31, No. 22, 1997, pp. 2283-2308.

- [35] Timoshenko, S. Theory of Elastic Stability, Second Edition. Engineering Societies Monographs, McGraw-Hill Book Company, New York, New York, 1961.
- [36] Shigley, J. E. Mechanical Engineering Design, Third Edition. McGraw-Hill Book Company, New York, New York, 1977.
- [37] Ault, M., and Waas, A. "Finite Element Analysis of a Proposed Specimen for Compression Testing of Laminated Materials," AIAA Paper No. 93-1518, Presented at the AIAA SDM Meeting, La Jolla, California, 1993, pp. 1816-1819.
- [38] Wisnom, M. R. "Effect of Shear Stresses in Indirect Compression Tests of Unidirectional Carbon Fiber/Epoxy," *AIAA Journal*, Vol. 29, No. 10, 1990, pp. 1692-1697.

Basant K. Parida,¹ P. K. Dash,¹ S. A. Hakeem,² and K. Chelladurai²

Structural Integrity Assessment of Composite Pressure Test Box through Full Scale Test

Reference: Parida, B. K., Dash, P. K., Hakeem, S. A., and Chelladurai, K., "Structural Integrity Assessment of Composite Pressure Test Box through Full Scale Test," *Composite Materials: Testing, Design, and Acceptance Criteria, ASTM STP 1416*, A. Zureick and A. T. Nettles Eds., American Society for Testing and Materials International, West Conshohocken, PA, 2002.

Abstract: The design methodology of composites in aircraft structures normally follows a building block approach and validation of design allowables is carried out through coupon, feature, and full-scale component level tests. Another important aspect in the design of composites is to account for environmental degradation of strength and stiffness properties, especially under a hot-wet environment. This paper describes the methodology adopted for and the results obtained from full scale static load tests with and without pressurization, on two composite pressure test boxes, under room temperature and hot-wet environmental conditions. The test boxes representing a typical wing structure, were made of three bays with the middle bay consisting of composite spars and top and bottom skins. One of the two identical test boxes was subjected to almost saturation level moisture conditioning at 70°C and 85% RH in an environmental chamber. The test boxes were extensively strain-gaged with back to back strain gages fixed at pre-selected locations, and these were very carefully moisture-proofed to withstand the moisture-conditioning over long period and rigorous hot-wet test at $100 \pm 5^\circ\text{C}$ and $\geq 85\%$ RH. A component test rig and an aluminum test chamber were specially designed to undertake these tests, which involved application of loads and reactions that cause combined bending and torsion of the test box. Finite element analysis using "ELFINI" had predicted the test box to be buckling-critical. Through actual testing it has been validated that the top skins of the test boxes do not undergo buckling up to design ultimate load (DUL) and that the ultimate failure loads were well above the DUL of the test boxes, both under room temperature and hot-wet environmental conditions.

Keywords: carbon fiber composite, composite pressure test box, room temperature test, hot-wet environment, design limit load, design ultimate load, buckling strength

It is well known that over the last few decades, advanced composites like carbon fiber composites (CFC) have found increased use in aerospace vehicle structures because of their distinct advantages over metals in terms of specific strength, stiffness, and durability in a fatigue loading environment [1]. Although the use of composites in airframes was initially

¹Deputy Director and Deputy Head, respectively, Structural Integrity Division, National Aerospace Laboratories, P.O. Box: 1779, Bangalore 560 017, India

²Additional General Manager (Design) and Deputy Manager(Design), respectively, Aircraft Research and Design Centre, Hindustan Aeronautics Limited, P.O. Box: 1789, Bangalore 560017, India

limited to control surfaces, fairings, and other secondary structural elements, with better understanding of their in-service performance and greater confidence on the structural integrity of components made from composites, carbon (graphite) fiber reinforced composites have been successfully employed in primary structural components of aircraft like wings and empennage [2]. However, in view of the very limited database available on the long-term use of composites in safety-critical primary structural components of airframes, it is sometimes necessary to follow a building block approach for the airworthiness certification of any newly designed composite structure. The validation of a new design and the design allowables essentially boils down to testing on the order of a few thousands of test coupons, hundreds of structural elements/features like joints, a few dozen large panels, sub-components, and ultimately a few wing-boxes/full-scale components/airframes [3]. This is necessary because some of the analytical or empirical methods normally employed for the strength and life prediction of metallic structures are unsuitable for application to composite structures and the material non-homogeneity/anisotropy exhibited by the layered polymeric composites, necessitates extensive testing to demonstrate the desirable strength/stiffness properties. Further, epoxy matrix – based carbon fiber reinforced composites have shown appreciable strength degradation when subjected to elevated temperature and humid environment [4-5]. Parida et al. [6] have reviewed some of the earlier works on numerical analysis and testing of laminated composite panels and have presented buckling analysis results, both under room temperature and hot/wet environmental conditions. The airworthiness certification authorities normally require the designers of composite structures to demonstrate design ultimate load (DUL) carrying capacity of composite subcomponents/components through full-scale hot/wet environmental test under simulated service loads, both internal and external. It may be noted that the objective of carrying out such an elaborate and complicated testing exercise was not only to validate the design allowables but also to assess the prediction capability of the analytical/FEM tools employed in the design. Unfortunately, experimental data and details of composite box test under both room temperature and hot/wet environmental conditions are scarce in open literature. In this paper, the results of structural integrity assessment of a CFC pressure test box subjected to both internal pressure and external loading up to design ultimate load and beyond, under room temperature and hot/wet environmental conditions have been presented. The predicted values of strains on the top composite skin of the box obtained from FEM analysis have been compared with those obtained from the experiments, both under room temperature and hot/wet conditions.

Design of CFC Pressure Test Box

Description

A pressure test box representing structural details of a typical aircraft wing was designed and tested. The geometry and structural details of the test box are shown in Figure 1. It was a rectangular box of dimensions; 2234 mm length, 715 mm width, and 110 mm height. It had top and bottom skins made of carbon fiber composites. The top and bottom skins were bolted to substructure consisting of four spars and six ribs. The top skin between Spars 2 and 3 and Ribs 3 and 4 was the test panel. The strains at various locations, buckling, and failure of this test panel were under investigation.

The box was loaded at eight locations P_1 to P_8 as shown in Figure 1. The loads were all applied normal to the box in the z-direction. The box was supported at three locations R_1 to R_3 , shown in Figure 1. The reactions R_1 , R_2 , and R_3 were normal to box in the z-direction. The three reactions were statically determinate.

The box between Rib 3 and Rib 4 was sealed to facilitate application of pressure loading to the test panel.

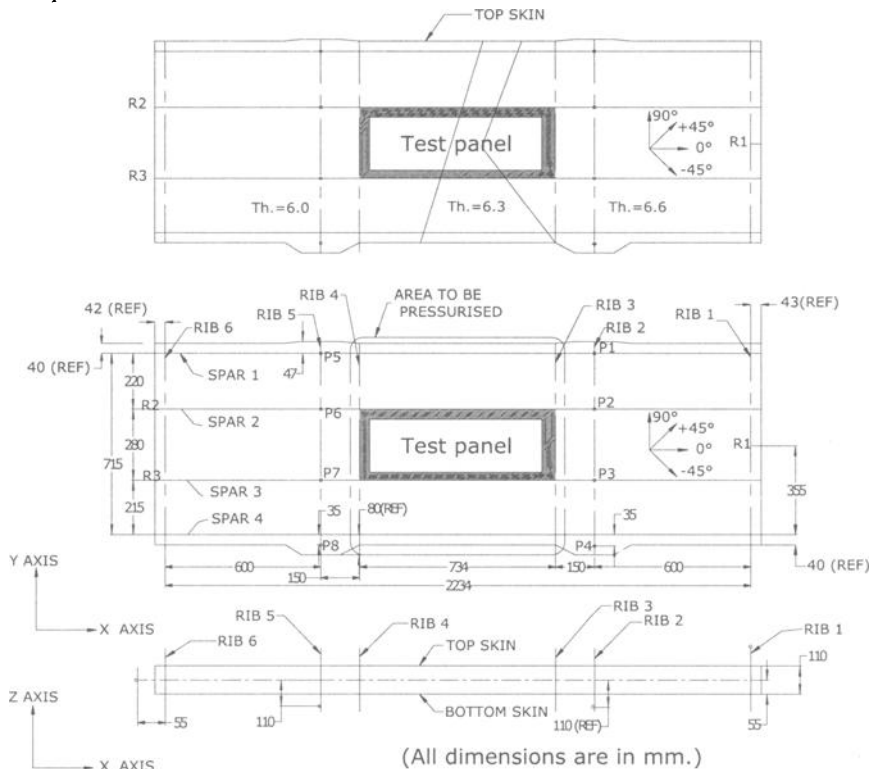


Figure 1 – Geometry and structural details of the composite pressure test box.

Materials

The top and bottom skins were made of unidirectional carbon-epoxy prepreg tapes of specification Fibredux 914C-TS-6-34. The nominal thickness of prepreg was 0.15 mm. The fiber volume fraction was 0.6. The four fiber directions were 0° , $+45^\circ$, 90° , -45° . These directions are shown in Figure 1. Spars 2 and 3 between Ribs 3 and 4 were made of bi-directional carbon-epoxy prepreg tapes of specification G803-914C-40. The nominal thickness of prepreg was 0.3 mm. All other spars, ribs and brackets were made of aluminum alloys of specification BS L 168 T6511.

Test Panel

The top skin between Spars 2 and 3 and Ribs 3 and 4 was the test panel. The 280 x 734 mm rectangular test panel had thickness distribution as shown in Figure 1. It had thicknesses of 6.6, 6.3, and 6.0 mm. The stacking sequence of the thicknesses is shown in Table 1. The stacking sequence was symmetric and unbalanced.

Table 1 -Stacking sequence of CFC test panel.

Thickness	Stacking Sequence
6.6 mm	[±45 ₂ /90 ₄ /±45/45/90/±45/45/90/45/0/90]s
6.3 mm	[±45 ₂ /90 ₄ /±45/45/90/±45 ₂ /45/90/45/0/90]s
6.0 mm	[±45 ₂ /90 ₄ /±45/45/90/±45 ₂ /45/0/90]s

The thickness distribution was achieved by means of dropping plies. The stacking sequence and the ply dropping were evolved as per recommended aircraft design practices [7]. The three different thicknesses and the ply dropping in the test panel were specifically introduced to study their effects on strains and buckling.

Loads

A factor of safety of 1.5 was used in the design. Therefore the design ultimate load (DUL) was equal to 1.5 times design limit load (DLL). The box and the test panel were designed not to fail or buckle before reaching DUL. The DUL are given in Table 2. Positive loads were acting up in the z-direction. The loads cause combined bending and torsion of the test box and the strains developed on the test panel were representative of the strains in a typical wing. The pressure loading was applied to simulate the fuel pressure in the outboard region of a typical wing.

Table 2 -Applied loads on the test box and support reactions.

Design Ultimate Loads (DUL)		Design Ultimate Pressure	
Locations	kN	Pressure	MPa
P ₁	98.6		
P ₂	-51.2		
P ₃	-82.2		
P ₄	-10.4		
P ₅	-33.7		
P ₆	-84.7		
P ₇	-44.2		
P ₈	60.3		

Design Ultimate Reactions	
Locations	kN
R ₁	63.4
R ₂	32.9
R ₃	51.2

Test Schedule

Number of Test Boxes

Two test boxes had been fabricated as per the design. Both the test boxes were identical. The first box was tested at room temperature / as received (RT/AR) condition. The second box was moisture conditioned and tested under hot/wet environmental condition.

Environmental Conditioning

The second test box was moisture conditioned in an environmental chamber maintained at $70^{\circ}\text{C} \pm 2^{\circ}\text{C}$ and $85\% \text{ RH} \pm 5\% \text{ RH}$. The moisture absorption during the conditioning was monitored using traveler coupons. The three traveler coupons, representative of the three thicknesses of the test panel, were weighed at frequent intervals to assess percentage moisture gain. Figure 2 shows the variation of moisture gain of the three traveler coupons plotted against

square root of time in hours. The moisture absorption reached a level of about 1.5% after 590 days. The moisture gained was with respect to the "as received" (nominally dry) condition.

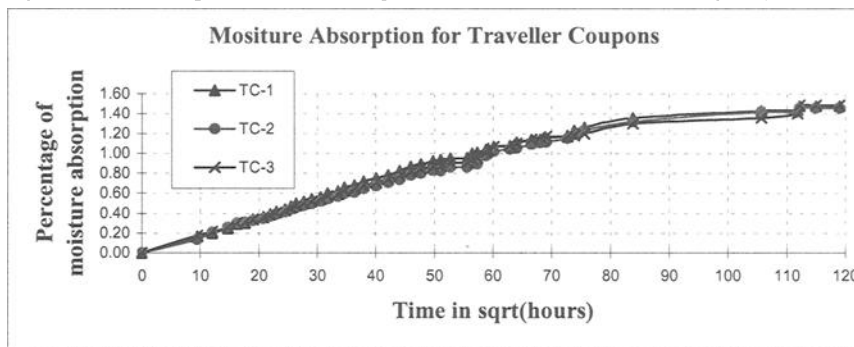


Figure 2 -Moisture Absorption characteristics of traveler coupons at 70 °C and 85% RH.

Strain Gaging

Both the test boxes were extensively strain gaged. Figure 3 shows the details of the strain gages in the test panel. In addition to the test zone, the outer and inner surfaces of the top skin, bottom skin and the webs of spars and ribs were also strain gaged. Each box was strain gaged with 88 rectangular strain rosettes. Therefore, strain data corresponding to total of 264 channels were recorded during each test.

These strain gages were compatible for use on composites and were employed with proper moisture-proofing. For the second test box that was moisture conditioned for hot/wet test, specific care was taken to install a four-layered moisture proofing to prevent moisture ingress and thereby protect against corrosion of the gage element. It is a matter of great satisfaction that even after 590 days of conditioning under harsh environment, not a single strain rosette had gone dead due to corrosion. This was achieved because of the extreme care taken for moisture proofing of the strain gage installations.

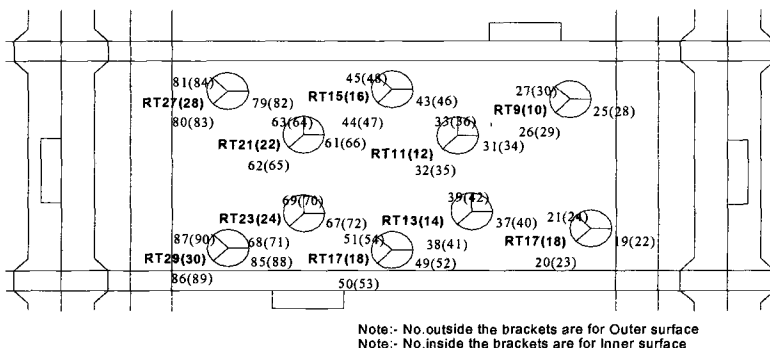


Figure 3 – Strain gage locations on the CFC test panel.

Displacement Gages

Deflections at prescribed seven locations at the bottom of the test box (on the bottom skin) were recorded during the tests. The LVDT locations are shown in Figure 4.

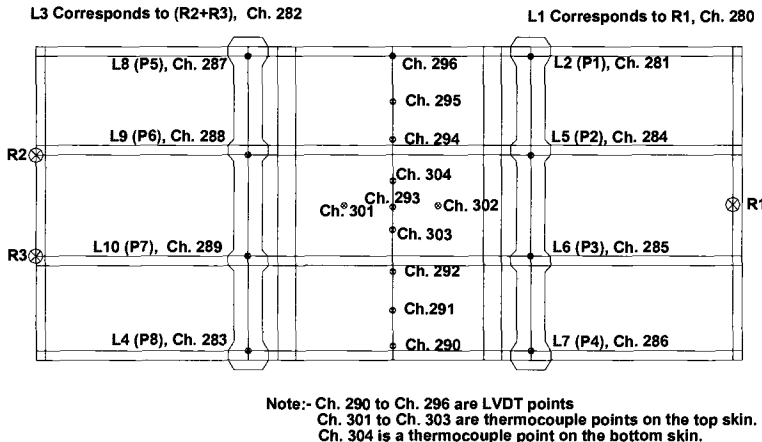


Figure 4 – LVDT and thermocouple locations

Test Sequence

The following test sequence was followed for the structural static test of the first box in the RT/AR condition as well as the second box under hot/wet condition.

- (i) Up to limit loads, without pressure
- (ii) Up to limit loads, with constant limit pressure
- (iii) Up to ultimate loads, without pressure
- (iv) Up to ultimate loads, with constant ultimate pressure
- (v) Up to failure loads without pressure

The loads were applied in steps of 10 % (or, in some selected stretches, in steps of 25 %) of limit load. After each load step, strain gage and LVDT data were recorded. Strain gage and LVDT data were recorded during unloading also. After unloading, the permanent set/residual strains were also recorded. Strain data of a few back-to-back strain gages in the test panel were monitored in real time to observe the linearity of the strain output and to monitor the onset of panel buckling.

Finite Element Analysis

The test box was analyzed using ELFINI software. ELFINI software is a finite element analysis computer software developed by the erstwhile Avions Marcel Dassault-Breguet Aviation of France [8]. The finite element meshing was performed using Computer Aided Three-Dimensional Interactive Analysis (CATIA) software [9]. The finite element model is shown in Figure 5. The finite element model has 5086 elements and 2411 nodes. The CFC top and bottom skins were modeled with ‘QD4T2PLATE’ elements. It is a four-noded, quadrilateral, anisotropic plate element with straight edges. It has six degrees of freedom at each node, namely, three translations, and three rotations. The element stiffness matrix was

computed by the layer properties: density, E_{11} , E_{22} , G_{12} , ν_{12} , thickness of layer, number of layers in each direction, and the angle of each fiber direction. The material properties used for the CFC top and bottom skins are shown in Table 3. The degraded material properties due to hot/wet environmental conditions are also shown in Table 3. These properties were based on extensive coupon level testing of the CFC material.

Table 3 - Elastic constants used in FEM analysis.

Elastic Constants	Room Temperature	Hot/Wet
Longitudinal Young's Modulus, E_{11}	130.0 GPa	127.0 GPa
Transverse Young's Modulus, E_{22}	10.0 GPa	5.0 GPa
In-plane Poisson's Ratio, ν_{12}	0.35	0.35
In-plane Shear Modulus, G_{12}	5.0 GPa	3.6 GPa

Spars 2 and 3 between Ribs 3 and 4 are made of bi-directional carbon-epoxy prepreg tapes of specification G803-914C-40. The material properties used are $E_{11} = E_{22} = 60.0$ GPa, $G_{12} = 5.0$ GPa and $\nu_{12} = 0.053$. Spars 1 and 4 and the segments of Spars 2 and 3 outside of Ribs 3 and 4 are made of aluminum alloy with material properties $E = 70.0$ GPa and $\nu = 0.3$. The flanges of the spars and ribs were modeled with bar elements. The bending stress carrying area of the webs was suitably lumped with the flange bar area. The webs of the composite spars were modeled with isotropic shear panel element with equivalent shear modulus. The flanges of the composite spars were modeled with bar elements with equivalent Young's modulus.

Linear Static Analysis

Linear static analysis of the first and second test boxes was performed for the following two load cases:

- (i) Design ultimate loads without pressure, and
- (ii) Design ultimate loads with design ultimate pressure.

The linear static analysis gives the nodal deflections, and micro-strains in each element. For the skin elements micro-strain data in each fiber direction was computed. The strains on the top and bottom surfaces of the skins were also computed. A typical micro-strain contour plot for the top skin outer surface in the 0° fiber direction is shown in Figure 6. This corresponds to the DUL with design ultimate pressure case for the first test box in the RT/AR condition. The complete range of results available from the linear static analysis makes it possible compare the strain gage and LVDT data obtained during the testing of the boxes.

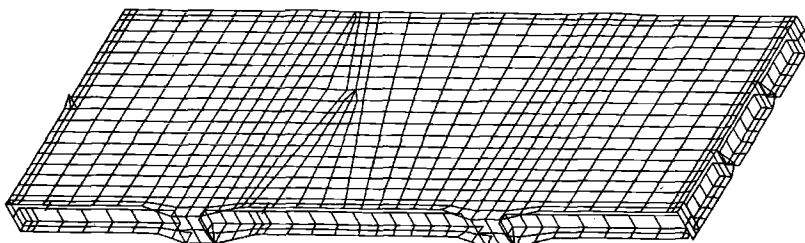


Figure 5 – Finite element mesh employed in ELFINI for FEM analysis of the test box.

Linear Buckling Analysis

Finite element method is a powerful method for predicting the linear buckling loads and buckling mode shapes. The buckling loads and buckling mode shapes were computed by solving for eigen values λ , which satisfy the following equation

$$\text{Det} ([K] - \lambda [G]) = 0 \quad (1)$$

where $[K]$ is the stiffness matrix and $[G]$ is the geometric stiffness matrix. The buckling loads are given by the eigen values and the corresponding eigen vectors represent the buckling mode shapes. The eigen values represent the buckling factors. The load at which buckling occurs is the FEA input load multiplied by the buckling factor. ELFINI uses the “inverse iteration on a subspace” method for the linear buckling analysis.

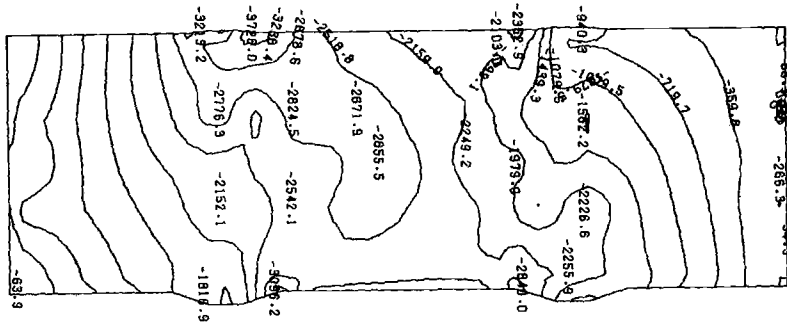


Figure 6 - Contour plot of micro-strain distribution for the CFC top skin outer surface along 0° ply direction (for ultimate load and ultimate pressure at room temperature).

Table 4 – Buckling factors obtained from FEM analysis.

Sl. No.	Condition	Buckling Mode	Buckling Factor
1	Room Temperature	1	1.248
2	Room Temperature	2	1.478
3	Hot/Wet	1	1.178
4	Hot/Wet	2	1.401

Testing of Pressure Test Box

Test Rig and Test Equipment

Keeping in view the complexity of support and loading conditions needed to conduct the structural static test of the pressure test boxes, both under RT/AR and hot/wet conditions, a test rig was specially designed, fabricated and erected at the Component Test Facility of Structural Integrity Division of National Aerospace Laboratories. Figure 8 shows the schematic diagram of the test rig with the test box in position for the test. In order to apply the eight loads on the test box, eight numbers of servo-hydraulic actuators of adequate capacity, along with load cells, were employed.

Fig. 7 shows the first two mode shapes for the RT/AR and hot/wet conditions. The buckling factors are shown in Table 4. The buckling factors and buckling mode shapes correspond to the load case of design ultimate loads without pressure.

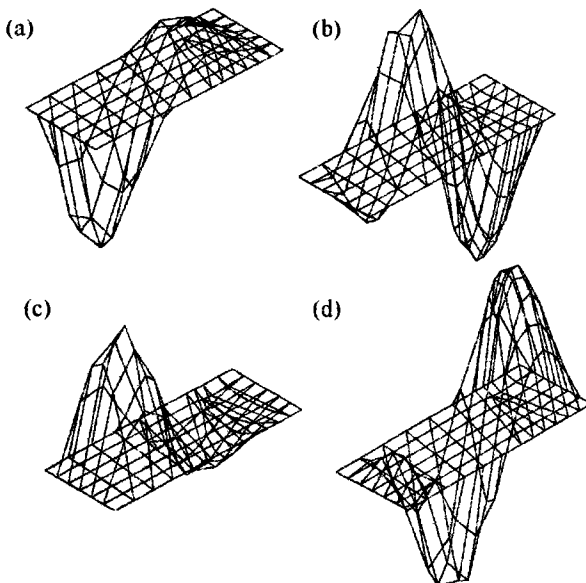


Figure 7-Mode shapes predicted by FEM analysis for test zone top-skin panel buckling: (a) first buckling mode at room temperature (b) second buckling mode at room temperature (c) first buckling mode under hot/wet condition and (d) second buckling mode under hot/wet condition.

An indigenously designed and developed multi-actuator (ten channel) servo-hydraulic test controller was used to conduct the computer-controlled test with options to select loading rate.

Measurement Group, System 4000, data acquisition system was used and all the strain gages, LVDTs, and load cells were connected to the data acquisition system. A compressed air pressure vessel was used for applying internal pressure to the test box.

Room Temperature Test

Figure 9 shows a view of the first test box undergoing RT/AR test. The test was conducted as per the test sequence described earlier. At each step of loading, the strain gage, LVDT and load cells data were recorded in the data acquisition system. It was observed that the strain gage output of all the strain gages were linear up to DUL. This implied that the test panel had not buckled at DUL. Typical strain gage outputs have been compared with those obtained from FEM analysis and shown later.

In the last test of the test sequence, namely the failure load test, the back-to-back strain gage outputs exhibited shallow divergence from linearity, indicating the beginning of bending of the test panel. Typical strain gage output of the back-to-back strain gages in the test panel has been shown later. The test was terminated at 185% of DLL, when one of the loading brackets failed.

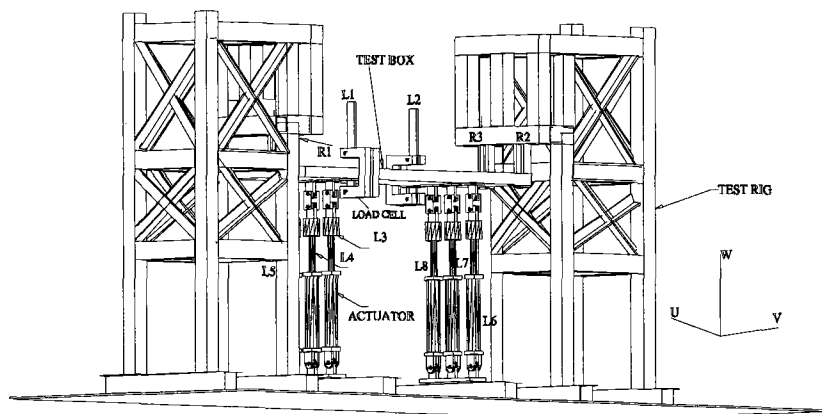


Figure 8 – Schematic diagram of the specially designed test rig for CFC pressure box test. The maximum height of the test rig is 2600 mm.

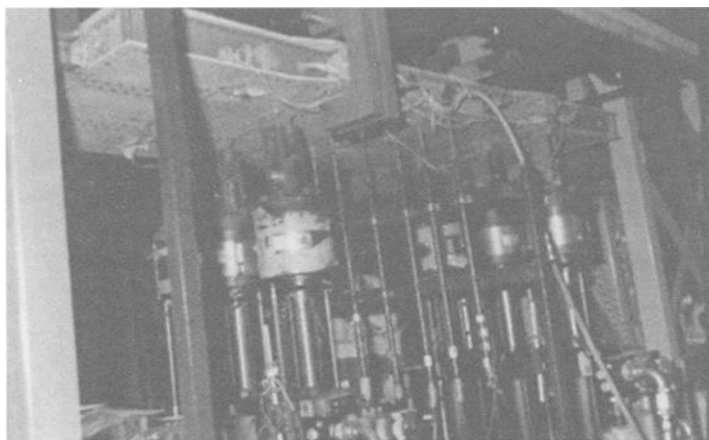


Figure 9 – A view of the CFC pressure test box undergoing room temperature test.

Hot/Wet Test

For the hot/wet test, the moisture conditioned second test box was installed inside an environmental test chamber mounted on the test rig. A view of the test set-up is shown in Figure 10. The chamber was made of aluminum frames and sheets. It was suitably insulated with asbestos and rubber sheets. Care was taken to provide clearances between chamber and test box at all sides and to route the huge bundles of strain gage lead wires out of the chamber for connection to the data acquisition system. A steam generator continuously supplied steam

to the chamber through four steam hoses. Four thermocouples fixed at different locations on the test panel were connected to the system 4000. The thermocouple outputs were monitored in real time to ensure that the entire hot/wet test was performed at $100^{\circ}\text{C} \pm 5^{\circ}\text{C}$ and $\geq 85\%$ RH environment. The temperature was maintained at the desired level through the control of steam inlet valves. Figure 11 shows the temperature variation of the four thermocouples during a typical hot/wet test.

The hot/wet test was also conducted as per the test sequence described earlier. Typical strain data obtained from the DUL test are shown later. The strain response up to DUL was almost linear. This implied that the test panel had not buckled up to DUL. The strain data in the failure load case showed divergence from linearity after DUL. Typical strain data for back-to-back strain gages in the test panel, are also shown later. The test panel had started to buckle only after DUL, as observed during the test. The test under hot/wet condition was terminated at 192.5% of DLL due to the failure of the test box between Ribs 3 and 4.

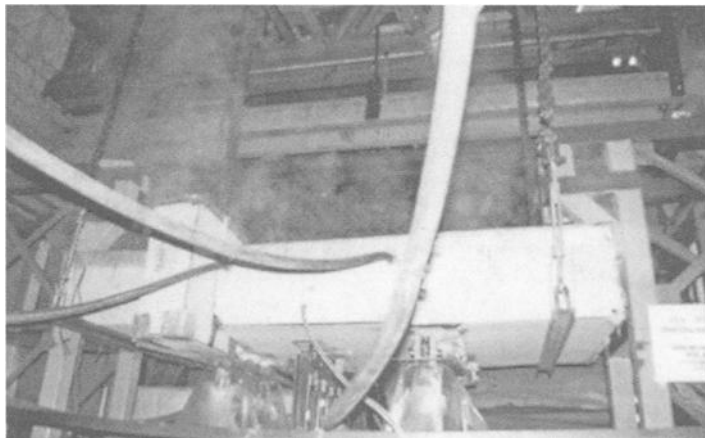


Figure 10 – A view of the CFC pressure test box undergoing full scale hot/wet test at component test rig at $100^{\circ}\text{C} \pm 5^{\circ}\text{C}$ and $> 85\%$ RH.

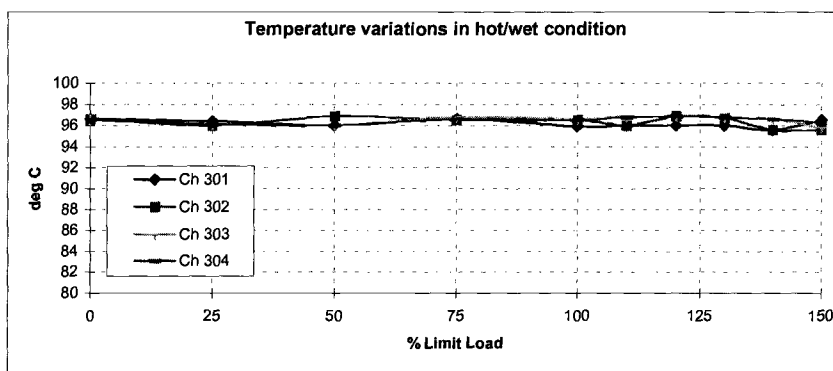


Figure 11 - Temperature variation during hot/wet environmental test for loading up to ultimate applied load and pressure. Thermocouple locations indicated in Figure 4.

Southwell Method of Buckling Load Analysis

In the case of hot/wet test, the strain output from back-to-back strain gages in the test panel exhibited divergence from linearity above DUL. It is also observed that the strain channels at different locations and along different orientations exhibited different nonlinear behavior after DUL. In order to draw an objective conclusion as regards the magnitude of critical elastic buckling load, "Southwell method" of buckling load analysis was carried out [6]. Figure 12 shows a typical Southwell plot of Strain versus Strain per unit load in percent DLL for strain channel No. 62, whose location is shown in Figure 3. The plot yields a critical buckling load of 170.138 % DLL. Similar Southwell plots for the other back-to-back strain channels in the buckled region of the test panel yielded the result of critical buckling load varying from 160.1 % to 173.7 % of DLL.

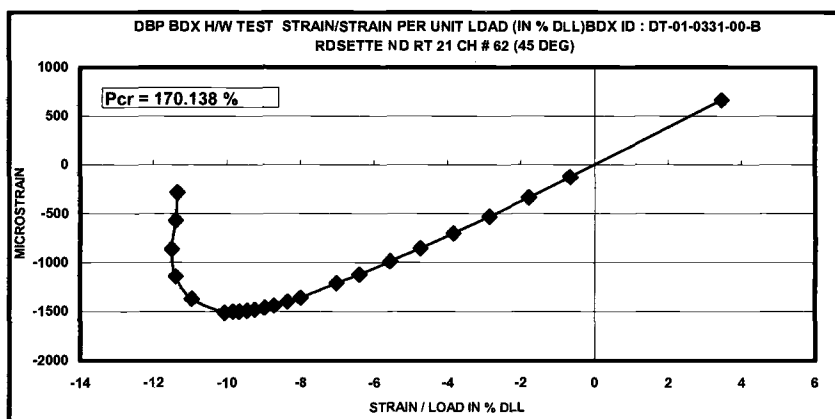


Figure 12 – Determination of critical buckling load by Southwell method from a typical strain gage output from hot/wet test without pressurization up to failure.

Comparison of Results from Test and Analysis

Loads and Reactions

The loads applied in the test and the reactions obtained were monitored through load cells. These are plotted in Figure 13 for a typical load case and are found to meet the design requirements.

Deflections

The deflections measured with the help of LVDTs during test were compared with those from the FEM analysis. Typical comparison is shown in Figure 14 for a hot/wet test. It may be noted that during the hot/wet test some LVDTs had shown very little or no deflections at the first step of loading due to the friction between the stem of LVDT and the bottom wall of the environmental test chamber. This was subsequently set right by allowing free movement of the stems of those LVDTs. The deflections obtained from tests compare well with the analysis up

to DLL. Beyond DLL, the deflections from test are on the higher side as compared to those obtained from linear FEM analysis, as shown in Figure 14.

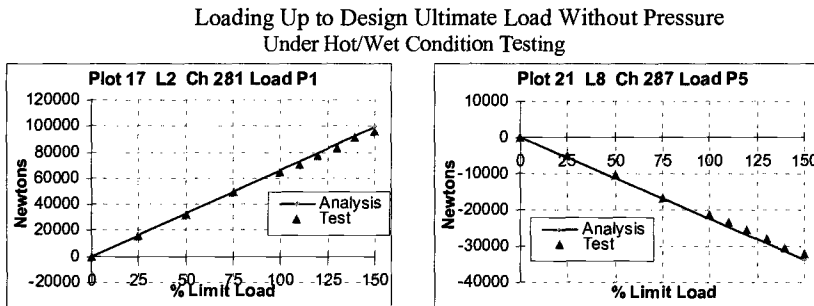


Figure 13 - Typical test loads compared with those from FEM analysis.

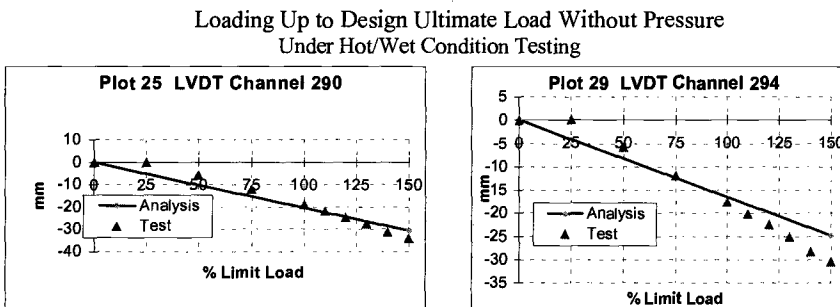


Figure 14 - Typical LVDT channel output data plotted against percentage limit load.
For Loading up to Design Ultimate Load without Pressure

Strains

The strain gage outputs in terms of micro-strains recorded during the tests have been compared with the FEM analysis results. Typical comparison for four channels of strain gages in the test panel is shown in Figure 15. Analysis of all the strain data of the gages in the test panel showed that for the RT test, the maximum variation between the strains at DLL recorded during the test and the strains obtained from finite element analysis (FEA) was around 5%. Similarly, for the hot/wet test, the variation in the strain values was generally around 10% and only at a few gage locations, the variation was up to 15 - 25%. From plot 7 of Figure 15, it is observed that at 150% of DLL the magnitude of strain from test is about 35% less than that of FEA value. From Figure 15, it is also seen that under room temperature condition the slopes of strain versus applied load curves obtained from FEA and test compare well up to DLL. However, under hot/wet conditions, the slopes of FEA data are higher than that obtained from the test data. This may be due to the variation between material properties of the composite test panel and those obtained from coupon-level tests.

The strains predicted by analysis in the case of test with internal pressure generally compared well with the test data.

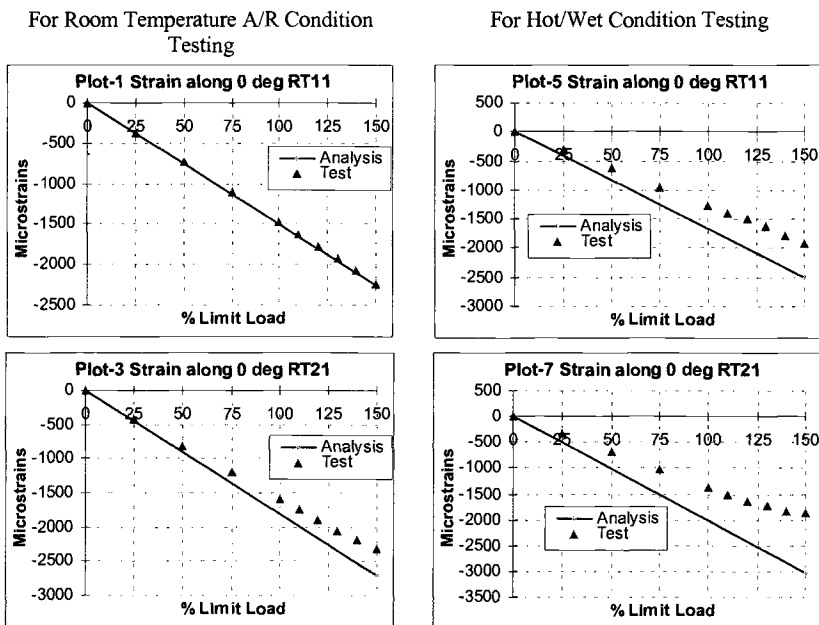


Figure 15 – *Typical test strain data comparison with those from FEM analysis.*

Buckling

The strain output of several pairs of back to back strain gages fixed to the test panel were analyzed with a view to ascertain the buckling load. Typical strain data for back-to-back strain gages in the test panel are shown in Figure 16.

For room temperature condition, the FEM analysis had predicted first mode buckling to be at 124.8% DLL (187.2% DLL). In tests, the test panel started exhibiting out of plane deformations around 150% of DLL and before the panel could develop a distinctly buckled (deformed) shape, the box experienced a secondary failure in the metallic loading bracket.

For the hot-wet condition, the FEM analysis predicted first mode buckling to be at 117.8% DLL (176.7% DLL). In tests, the test panel started exhibiting out of plane deformation at around 150% DLL. The test panel strain values also started showing divergence from linearity above 150% DLL. The critical buckling load obtained from use of Southwell method varies between 160.1% DLL and 173.7% DLL. The mode shapes predicted by the FEM analysis were also confirmed by the test.

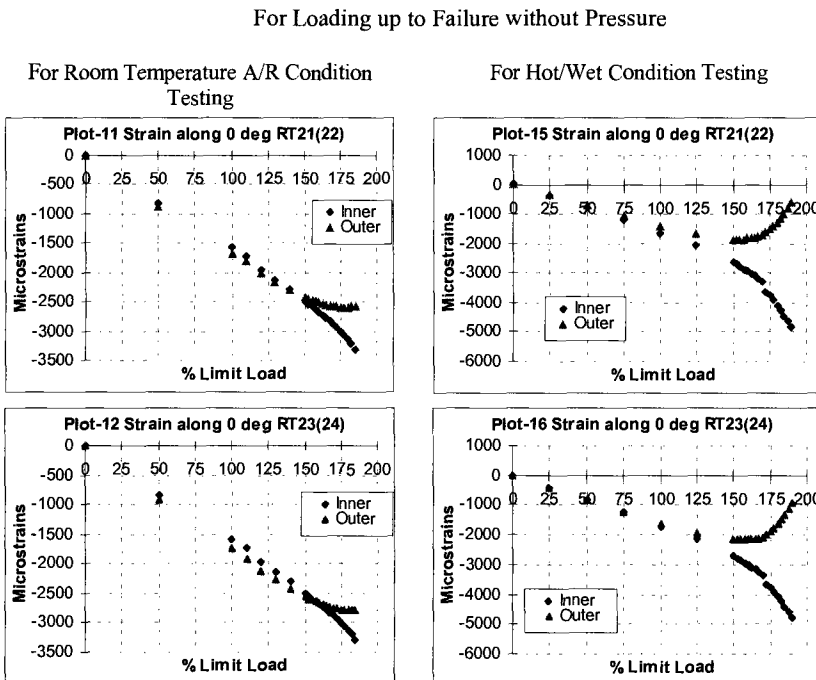


Figure 16 - Typical back-to-back strain channel data plotted to ascertain buckling of test panel.

Concluding Remarks

In this investigation, an attempt has been made to design, and test a carbon fiber reinforced composite test box representing a typical wing structure with a view to ascertain the following:

1. The structural integrity assessment of the composite test box up to design ultimate load;
2. The prediction capability of the FEM analysis employed in respect of displacements, strains, and critical buckling load, to be determined from actual full scale test of the CFC pressure box;
3. Effect of environmental degradation on the strength and buckling of the CFC skin through analysis and testing under both room temperature and hot/wet environmental conditions; and
4. Effect of internal pressure combined with external loading on the strain response of the CFC test panel.

From the FEM analysis and test results, it is observed that the structural integrity of the CFC test box has been ensured up to design ultimate load, both without and with internal pressure, as well as under room temperature and hot/wet environmental conditions. Comparison of strain data, as obtained from FEM analysis and from test, show reasonably good correlation with and without pressure under room temperature condition. However, under hot/wet environmental conditions, variation was seen between the strain data obtained from analysis and test in a few

strain channels, especially those close to the buckled region of the test panel. The prediction of critical buckling loads through FEM analysis have been found to be close to those, obtained from full scale test of CFC test boxes.

Acknowledgments

This study was supported by the National Team, CFC – Wing program. The authors would like to thank Dr. K. N. Raju, Program Director, National Team, Dr. T. S. Prahlad, Director, NAL, and Mr. Yogesh Kumar, General Manager (ARDC) for their encouragements and support. Thanks are also due to Mr. D. Dinakaran and his team for their test box design support and to Mr. Shama Rao and his team for fabrication of the test boxes. They would also like to acknowledge with thanks the meticulous strain-gaging support of Messers Selvamani Babu, K. M. Sathish, test rig design and testing efforts of Mr. M. V. Mukund, Mr. G. Sarvanan and all other SID and contract staff, Dr. R. M. V. G. K. Rao and his colleagues for environmental conditioning of one test box. They also thank Mr. P. Kishore for his help in preparation of the manuscript.

References

- [1] Anderson, B. W., "Factors for Designing of Military Aircraft's Structures in Carbon Fiber Reinforced Composites," *Advances in Fracture Research, Proceedings, ICF-6*, S. R. Valluri, D.M.R. Taplin, P. Rama Rao, J.F. Knott and R. Dubey, Eds., Pergamon Press, New York, 1984, pp. 607-622.
- [2] Sanger, K. B., Dill, H. D. and Kautz, E. F., "Certification Testing Methodology for Fighter Hybrid Structure," *Composite Materials: Testing and Design (Ninth Volume), ASTM STP 1059*, S. P. Garbo, Ed., American Society for Testing and Materials, West Conshohocken, PA, 1990, pp. 34-37.
- [3] Watanabe, R. T., and Scheumann, T. D., "Structural Integrity Criteria for Commercial Transport Aircraft," *Effects of Product Quality and Design Criteria on Structural Integrity, ASTM STP 1337*, R. C. Rice and D. E. Tritsch, Eds., American Society for Testing and Materials, 1998.
- [4] Flaggs, D. L. and Vinson, J. R., "Hygrothermal Effects on the Buckling of Laminated Composite Plates," *Fibre Science and Technology*, Vol. 11, 1978, pp. 353-365.
- [5] Collings, T. A. and Stone, D. E. W., "Hygrothermal Effects in CFRP Laminates: Strains induced by Temperature and Moisture," *Composites*, Vol. 16, No. 4, 1985, pp. 307-316.
- [6] Parida, B. K., Prakash, R. V., Ghosal, A. K., Mangalgiri, P. D., and Vijayaraju, K., "Compression Buckling Behavior of Laminated Composite Panels," *Composite Materials: Testing and Design, Thirteenth Volume, ASTM STP 1242*, S. J. Hooper, Ed., American Society for Testing and Materials, 1997, pp. 131-150.
- [7] Engineering Sciences Data Unit (ESDU), Data Item No. 91003, November, 1991
- [8] ELFINI Base Reference Manuals, Avions Marcel Dassault – Breguet Aviation, France, May 1989.
- [9] CATIA Reference Manuals, Avions Marcel Dassault – Breguet Aviation, France, May 1986.

Dan Ruffner¹ and Pierre Jouin¹

Qualification Using a Nested Experimental Design

Reference: Ruffner, D. and Jouin, P., "Qualification Using a Nested Experimental Design," *Composite Materials: Testing, Design, and Acceptance Criteria, ASTM STP 1416*, A. Zureick and A. T. Nettles, Eds., American Society for Testing and Materials International, West Conshohocken, PA, 2002.

Abstract: The general aviation approach was taken in these material qualifications, where it is assumed that a large portion of composite material property batch-to-batch variability can be reproduced in the laboratory through independent layup and cure of panels, termed a process lot. A nested experimental design was used to quantify the actual sources of variability for hot/wet tension and compression strengths, and dry and wet glass transition temperatures. Two large crossplied panels, each representing a process lot, were independently made from each of three qualification batches. Two subpanels, each representing a machine lot, were cut from each process lot panel, then independently machined into coupons, moisture conditioned, and tested. With these three nested experimental levels the batch-to-batch variability can be partitioned into true batch variability, laminate fabrication, coupon test, and within sample variability. Results indicate that true batch variability was a relatively minor contributor to material property variability as a whole.

Keywords: Composite, qualification, experiment, nest, regression

Introduction

Background

This composite material qualification work supports the development of a composite main rotor blade for the AH-64 Apache attack helicopter. Since A-basis allowables were desired, five batch qualifications were performed for the 250°F (120°C) curing glass/epoxy materials. A batch is defined as a unique combination of resin and fiber lots. Two preps were qualified in parallel to avoid second source qualification in the future, and to take advantage of dual sources during the development portion of the program. Efficiencies from using the regression approach for data layout and allowables calculation made this affordable.

¹ Materials Engineer and Project Manager, respectively, The Boeing Company, 5000 E. McDowell, Mesa, AZ, 85215.

As the glass tape qualifications for this program were being completed, design established the need for carbon reinforced materials to provide selective additional stiffness for portions of the blade. The data was urgently needed, but a carbon effort had not been planned or funded. Neither the blade program management nor the prepreg manufacturers expressed enthusiasm for the effort and calendar time required for fabrication of an additional five batches, but A-basis allowables of comparable quality to the just-completed glass qualifications were desired by design.

Regression Approach

The regression methodology was used for both layout of the data structure [1] and calculation of the allowables [2] for the glass/epoxy materials. For the critical environmental condition, typically hot/wet, all five batches were tested, with six coupons per batch. For less critical conditions, such as Room Temperature Dry (RTD), only two batches were sampled. This approach is diagrammed in Figure 1, showing the effect of not testing all five batches for the dry conditions. The dotted line in Figure 1 represents the true curve that would be obtained if all five batches were tested dry. The solid line reflects the inaccuracy that could result from sampling only two batches, which is seen as negligible compared to the substantially lower hot/wet values that drive design allowables. Spare panels were cured to allow additional testing should a dry condition become critical. For the glass qualifications this became necessary, and all five batches were tested cold/dry for tension as well.

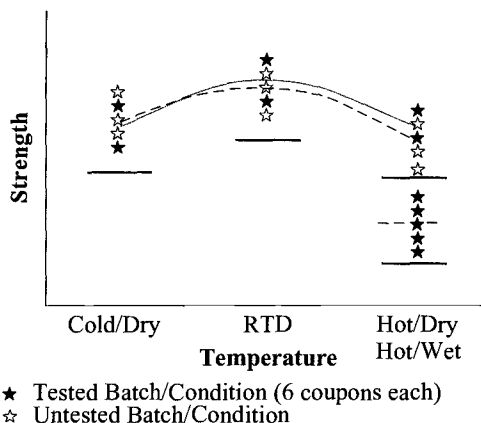


Figure 1 - *Regression qualification methodology.*

Nested Experiments

The general aviation community has done an excellent job of combining efforts across companies for composite material qualifications [3]. One of the most interesting aspects

of their methodology is the creation of multiple process lots from batches on the assumption that this will recreate in the test laboratory much of the variation associated with batch-to-batch variability. During calculation of the allowables these process lots are treated as if they were batches, allowing the development of much more stable allowables from a limited number of batches.

During the glass qualifications, a side effort had been planned to investigate the sources of observed batch-to-batch variation measured during a material qualification. Similar efforts have been discussed at MIL-HDBK-17 [4] working group meetings for some time. A nested experimental design [5] was laid out, aiming to partition variability between: "true" batch variability, variability induced in the process of laying up and curing panels, and variability induced by machining coupons from the panels then conditioning and testing them.

This effort was originally planned with two process lots, consisting of panels layed up and cured at independent times, being fabricated from each of two batches. From each process lot panel two subpanels for a given test would be cut. Each of these subpanels would be machined into coupons, conditioned, and tested at independent times, forming a machine lot. If there was no effect as a result of process lot, then the average of the process lots from the same batch would be expected to be very similar. In the same manner, if the machine lot did not have an effect, then machine lots from the same process lot would be expected to be close. This effort was planned but never performed due to program schedule and priorities.

Single Panel Testing

For the glass material qualifications, the basic multi-batch mechanical properties were 0° lamina tension and compression, and in-plane shear (IPS) strength. The combined loading compression (CLC) fixture [6] was used for compression strength testing, where crossplied laminates (without tabs) are tested and lamina strengths backed out for optimum compression values. A water boil flexural strength test was being used as a conditioned receiving inspection test [1]. Since ±45° preplied glass tape was being procured, this test had also been performed using crossplied laminates.

This left tension as the only mechanical test where crossplied laminate testing had not been performed during the glass qualifications. After a brief laboratory evaluation using carbon tape, it was apparent that crossplied tension [7-9] was as effective as the crossplied compression testing, and had the same advantage of eliminating tabs. The use of tabs brings into the composite variability assessment task a multitude of issues associated with tab and adhesive materials, and their properties, dimensions, surface preparation and bonding issues. If standardized composite materials are not possible without standardized tests, certainly standardized test results are problematic with the variety of factors introduced by the use of tabs.

Since IPS and flexural strength tests were already performed without tabs, all the carbon multi-batch mechanical property coupons could now be tested without tabs, and using the same [90, 0]4s layup. Consolidating the layups meant that the panels for individual tests could be combined into one panel. This one crossplied panel undergoes nondestructive inspection (NDI), then subpanels for tension, compression, in-plane shear,

and flexural strength are rough cut from it. If NDI shows the process lot panel to be uniform, then one set of physicals (degree of cure, resin content, void volume, etc.) can represent all of the machine lot subpanels. At least one unidirectional panel is fabricated and tested for each batch to determine the required elastic and 90° strength properties, again with tabs being unnecessary.

Carbon/Epoxy Qualification Approach

These various aspects were then combined in an attempt to qualify the IM7 carbon/epoxy unidirectional tape reinforced versions of the preprints in a manner that met the technical, schedule, and funding requirements of the program: desire for 5-batch type A-basis allowables, application of the regression methodology for data layout and allowables calculation, investigation into the sources of batch-to-batch variability such as through process lots, and single panel testing.

A three-batch qualification for the carbon tape form was envisioned, as seen in Figure 2, with the batches formed from three resin lots (A, B and C) and two fiber lots (1 and 2). From each batch two independent process lot panels would be fabricated, numbered 1 through 6. From each process lot panel two subpanels would be cut for tension (T1 through T12) and compression (C1 through C12) tests. The process and machine lot identification numbers in Figure 2 indicate the randomized run order.

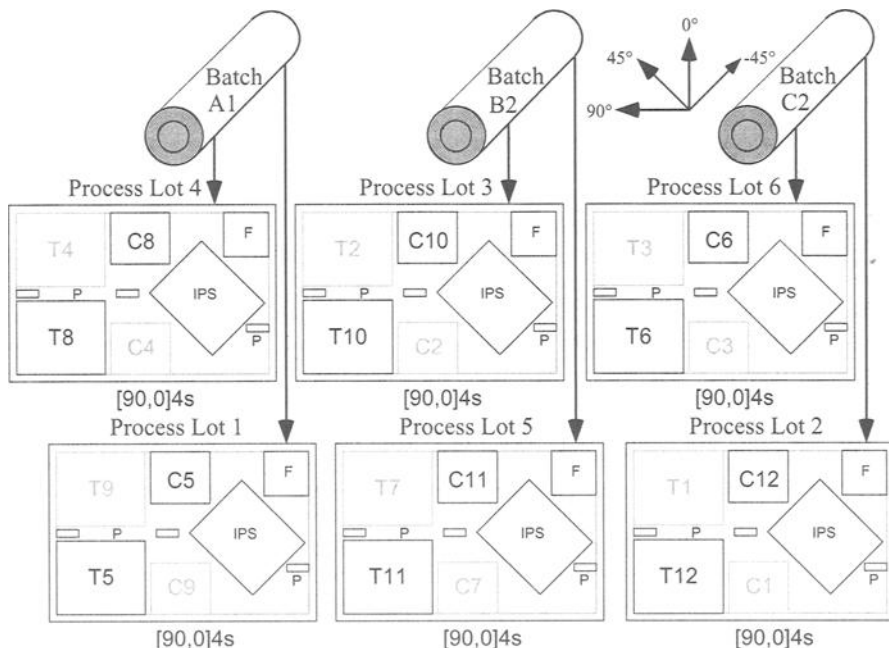


Figure 2 - Nested experimental design approach.

These machine lot panels would be machined into coupons, conditioned and tested at independent times. Three coupons per machine lot would be moisture conditioned at 70°C under more than 85% relative humidity for 30 days then tested at 70°C. The glass transition temperature (T_g) coupons were cut from compression panel trim. T_g s were run on both dry and moisture conditioned samples, two per machine lot.

While intervals between lots of at least two to three days was desired, in some cases they occurred on subsequent days. All the subpanels to be rough cut from each process lot panel were programmed into a waterjet cutter, allowing this process to be completed in a matter of minutes. Since the randomized run order for process and machine lots was established by the experimental design, this became the pacing item for the entire qualification. Although some additional planning was required in advance, once the qualification started scheduling, tracking, and management became minimal issues, rather than the substantial burden experienced in previous qualifications. All but the nested hot/wet tension and compression and the T_g coupons were machined, conditioned and tested at the lab's convenience between machine lots, allowing flexibility in the lab work load. As many coupons as possible were cut from each machine lot subpanel since the wafer saw setup had already been performed. This generated a spare coupon pool that was immediately available for retests, expanded testing for an emerging dry critical condition, and visual inspection of adjacent coupons in the event of an unusual failure.

Data Review

Once laminate strength values were obtained for the tension and compression coupons, the 0° lamina strengths were backed out and normalized [6]. The nested experimental data for the 3M and Hexcel materials are recorded in Tables 1 and 2, respectively. The tension data for both materials is plotted in Figure 3.

At the top of Figure 3, the average values for the three batches tested are plotted for both 3M and Hexcel. The horizontal lines connect: the three batches from a manufacturer, the two process lots from the same batch, or the two machine lots from a process lot. The point plotted for each batch is connected by a vertical line to the process lots making up the batch. Each process lot is in turn connected by a vertical line to the two machine lots making up the process lot. The machine lot points plotted are individual coupon values, with the coupons from the first machine lot slightly below the horizontal line, and the second slightly above the line, a total of 72 coupons.

From the plot it certainly appears that the averages for the two materials differ by about 240 MPa for tension strength. While there is no overlap in batch or process mean ranges, there is considerable overlap between the two material machine lots. Both materials have ranges spanning about 560 MPa, leading to an expected standard deviation of about 140 MPa. With a mean of 2 700 MPa, this would equate to a coefficient of variation of about 5%, which seems reasonable for tension testing.

For the compression data plotted in Figure 4, there is substantial overlap between batch, process lot, and machine lot ranges. For compression the range of values for each material is again about 560 MPa. With a mean of 1 400 MPa, this would equate to a coefficient of variation of about 10%, not unreasonable for compression testing.

Table 1 - 3M IM7/SP381 data.

Batch	Process Lot	Machine Lot	Replicate	70°C Wet Tensile Str., MPa	70°C Wet Compress. Str., MPa	Dry T _g , °C	Wet T _g , °C
1	1	1	1	2383	1470	147, 51	136, 98
1	1	1	2	2577	1463	145, 04	137, 89
1	1	1	3	2555	1611	--	--
1	1	2	1	2763	1462	144, 84	133, 68
1	1	2	2	2490	1519	143, 51	133, 69
1	1	2	3	2272	1375	--	--
1	2	1	1	2686	1154	150, 66	141, 09
1	2	1	2	2589	1213	151, 71	143, 31
1	2	1	3	2548	1185	--	--
1	2	2	1	2533	1130	147, 68	147, 69
1	2	2	2	2535	1180	146, 21	142, 39
1	2	2	3	2417	1355	--	--
2	1	1	1	2554	1641	151, 69	135, 28
2	1	1	2	2679	1626	150, 48	135, 09
2	1	1	3	2590	1635	--	--
2	1	2	1	2479	1546	150, 21	143, 69
2	1	2	2	2467	1434	150, 75	141, 99
2	1	2	3	2649	1401	--	--
2	2	1	1	2531	1328	151, 52	136, 41
2	2	1	2	2663	1476	153, 16	139, 77
2	2	1	3	2630	1433	--	--
2	2	2	1	2642	1292	150, 24	142, 00
2	2	2	2	2717	1552	150, 40	143, 27
2	2	2	3	2806	1460	--	--
3	1	1	1	2745	1388	150, 23	129, 98
3	1	1	2	2626	1381	150, 38	132, 38
3	1	1	3	2476	1441	--	--
3	1	2	1	2594	1558	148, 94	142, 27
3	1	2	2	2591	1664	150, 38	146, 32
3	1	2	3	2681	1361	--	--
3	2	1	1	2510	1526	149, 09	135, 06
3	2	1	2	2528	1418	148, 88	135, 04
3	2	1	3	2696	1485	--	--
3	2	2	1	2584	1644	148, 79	142, 05
3	2	2	2	2335	1490	147, 48	142, 02
3	2	2	3	2597	1516	--	--

Table 2 - *Hexcel IM7/R913 data.*

Batch	Process Lot	Machine Lot	Replicate	70°C Wet Tensile Str., MPa	70°C Wet Compress. Str., MPa	Dry T _g , °C	Wet T _g , °C
1	1	1	1	2717	1510	157, 63	154, 56
1	1	1	2	2642	1498	159, 93	157, 29
1	1	1	3	3000	1420	--	--
1	1	2	1	2814	1279	159, 12	155, 83
1	1	2	2	2869	1377	157, 41	149, 29
1	1	2	3	2844	1446	--	--
1	2	1	1	2510	1433	157, 51	156, 08
1	2	1	2	2865	930	158, 83	153, 74
1	2	1	3	2843	1399	--	--
1	2	2	1	2625	1388	157, 11	153, 53
1	2	2	2	2786	1262	157, 36	157, 18
1	2	2	3	2577	1283	--	--
2	1	1	1	2851	1274	160, 06	150, 32
2	1	1	2	2935	1498	159, 99	150, 68
2	1	1	3	2764	1493	--	--
2	1	2	1	2825	1193	160, 10	153, 32
2	1	2	2	2899	1381	157, 37	153, 12
2	1	2	3	2827	1594	--	--
2	2	1	1	2908	1215	158, 82	146, 08
2	2	1	2	2906	1473	160, 86	147, 85
2	2	1	3	2914	1474	--	--
2	2	2	1	2914	1441	158, 76	150, 40
2	2	2	2	2747	1383	158, 78	146, 23
2	2	2	3	2781	1327	--	--
3	1	1	1	2911	1413	160, 09	150, 41
3	1	1	2	2653	1264	158, 45	151, 83
3	1	1	3	2902	1259	--	--
3	1	2	1	2964	1120	162, 84	151, 63
3	1	2	2	2612	1074	160, 02	154, 37
3	1	2	3	2942	1050	--	--
3	2	1	1	2939	1222	160, 49	149, 01
3	2	1	2	2821	1049	161, 36	153, 04
3	2	1	3	2900	1386	--	--
3	2	2	1	2879	1509	159, 94	147, 61
3	2	2	2	2797	1199	159, 11	149, 19
3	2	2	3	2724	1275	--	--

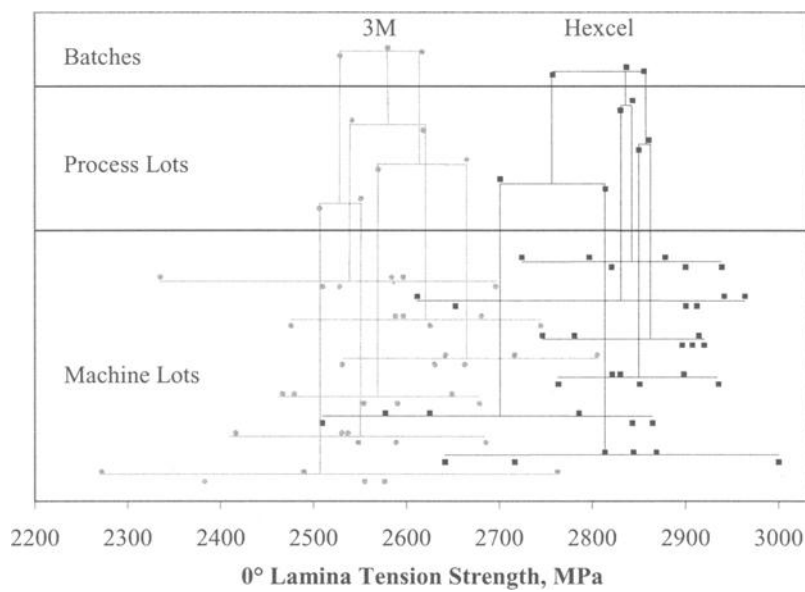


Figure 3 - 0° Lamina tension strength nested data (ASTM D 3039).

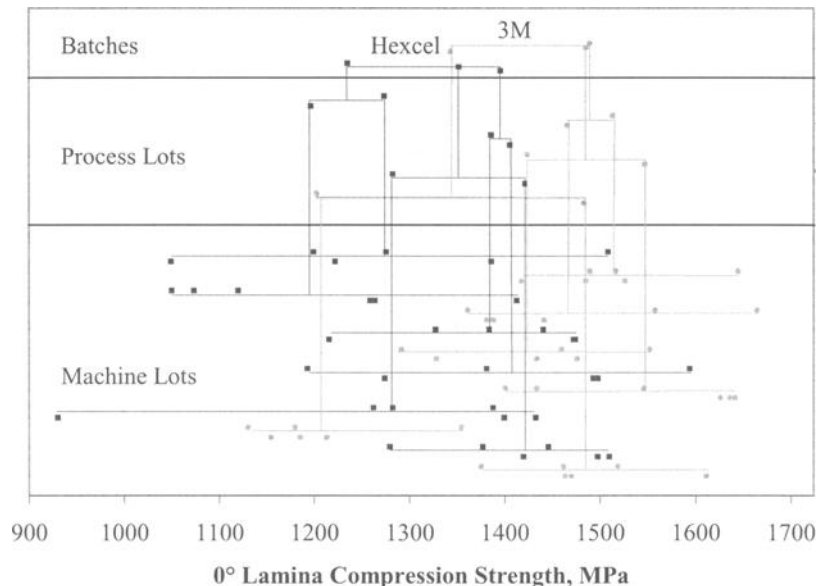


Figure 4 - 0° Lamina compression strength nested data (ASTM D 6641).

In addition, it is noted that in tension Hexcel material appears to provide higher values, while in compression the 3M material does. If both properties have comparable performance requirements, selecting one as the "best" material is problematic. If a specification requires both tests, then each material is much more likely to fail one test.

The dry glass transition temperature data can be seen in Figure 5. There is no overlap between values for the two materials, although the difference in mean values appears to be less than about 15°C. Differences between machine lots appear more pronounced compared to the prior mechanical data.

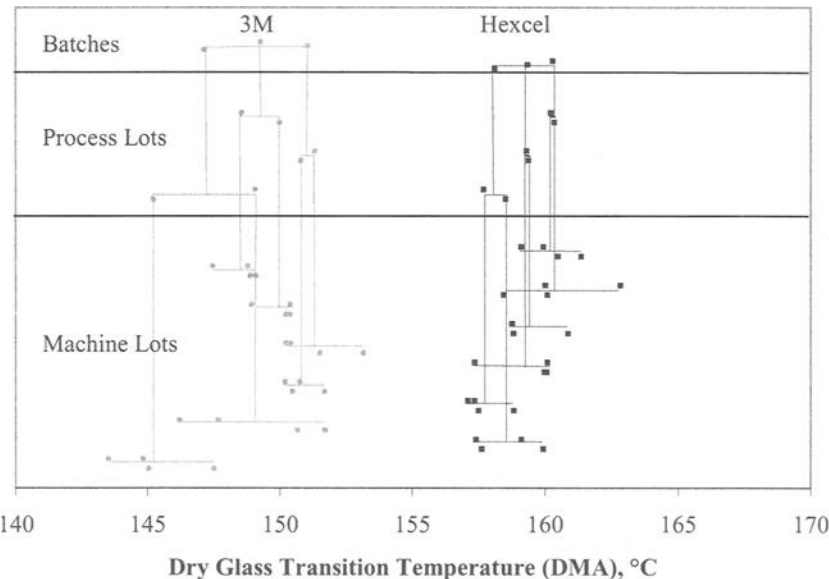


Figure 5 - *Dry glass transition temperature nested data (SACMA SRM 10R-94).*

The wet T_g data can be seen in Figure 6. The range for process and machine lot averages seems to have increased somewhat. While machining did not have a conceivable influence on T_g values, machine lot also encompasses the conditioning and test variability aspects.

Analysis

The nested experimental data from Tables 1 and 2 were statistically analyzed for each of the four sets of test values discussed [5, 10]. Basic regression model parameters and estimates of variance components are contained in Table 3. Various reviews of the residuals and other model checks did not indicate any problems with assumptions.

The mechanical property models explain at most two-thirds of the variation seen for those properties. Provided by the analysis is an assessment of the variance for each of the

random factors included in the experiment: batch, process lot, and machine lot. The residual variance not explained by any of the experimental factors is also included.

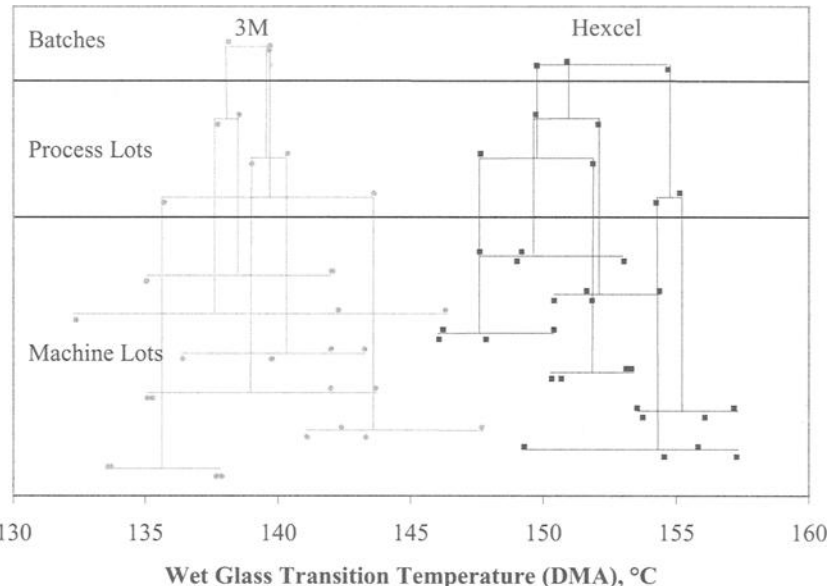


Figure 6 - *Wet glass transition temperature nested data (SACMA SRM 10R-94).*

Graphical displays of the results for the tension and compression mechanical properties can be seen in Figure 7. The comparative width of the distributions shown represents the variability estimated for each of the random factors, going from batch at the top of the figure to process lot, machine lot, then residual at the bottom. The scale is the same for the compression and tension distributions. The numerical value of the standard deviation represented is noted to the right of each distribution.

Tension

Figure 7 indicates that for a given vendor, the true batch-to-batch contribution to variability in tension values seen is represented by a standard deviation of 33 MPa. With about 95% of the variation in values contained within approximately two standard deviations, we would expect a range of about 132 MPa. For any given batch mean, represented by the point at the base of the batch distribution, there is a distribution of process lot averages about that batch mean similar in magnitude to the batch variation.

Since machine lot did not appear as statistically significant for the tension model, there is no standard deviation or distribution shown. For any given process lot average, there is variation from the individual coupons within the machine lots, represented by the residual distribution. We see that within machine lot there is substantially more variation compared to the batch or process lot contribution.

Table 3 – *Regression model parameters and estimates.*

	70°C Tension Strength	70°C Compression Strength	Dry T _g (DMA)	Wet T _g (DMA)
Model Parameters				
Rsquare	0.6672	0.6322	0.9810	0.9651
Rsquare Adj.	0.5077	0.4560	0.9629	0.9343
Root Mean Squ. Error	118.2	117.0	1.0526	1.9118
Mean, MPa	2696	1383	154.2025	145.2860
Source Prob>F				
Model	<0.0001	<0.0001	<0.0001	<0.0001
Vendor	0.0036	0.1753	0.0015	0.0012
Batch	0.2352	0.3496	0.0887	0.5313
Process Lot	0.1575	0.0298	0.1730	0.3935
Machine Lot	0.8633	0.2731	0.0128	<0.0001
Standard Deviation Estimates				
	MPa		°C	
Batch	32.96	42.82	1.33	N/A
Process Lot	34.68	85.36	0.82	1.03
Machine Lot	N/A	34.41	1.02	3.55
Residual	118.2	117.0	1.05	1.91

A conclusion that could be drawn from this is that while testing additional batches and/or process lots could provide a somewhat better assessment of material variability, just the act of making and testing more coupons regardless of batch, process lot, or machine lot is beneficial. For this test, this justifies the general aviation approach qualification methodology using process lots as a substitute for testing more batches.

Compression

For compression strength there is a similar story in Figure 7, although with some interesting differences. The contribution of batch is only slightly higher for compression compared to tension, but process lot seems to introduce substantially more variation. Perhaps compression is more vulnerable to the small variations in fiber direction compared to tension, since the coupons came from the same panel. Machine lot is seen as statistically significant for the compression test data, with a standard deviation of about 34 MPa. Finally, the residual or within machine lot variability is large and almost identical to that seen for the tension model. Again process lot appears as a good substitute for additional batches, with machine lot also contributing, but simply more coupons regardless of source lot provide a better assessment of variability.

It is very interesting, and somewhat unexpected, that such a large residual should remain for these mechanical property models. The residual represents the variability which remains unexplained by any of the model factors. In other words, after the effects

of batch (“true” batch-to-batch variation), process lot (panel layup and cure), and machine lot (coupon machining, conditioning and test) have been accounted for, more than a third of the variability remains unexplained.

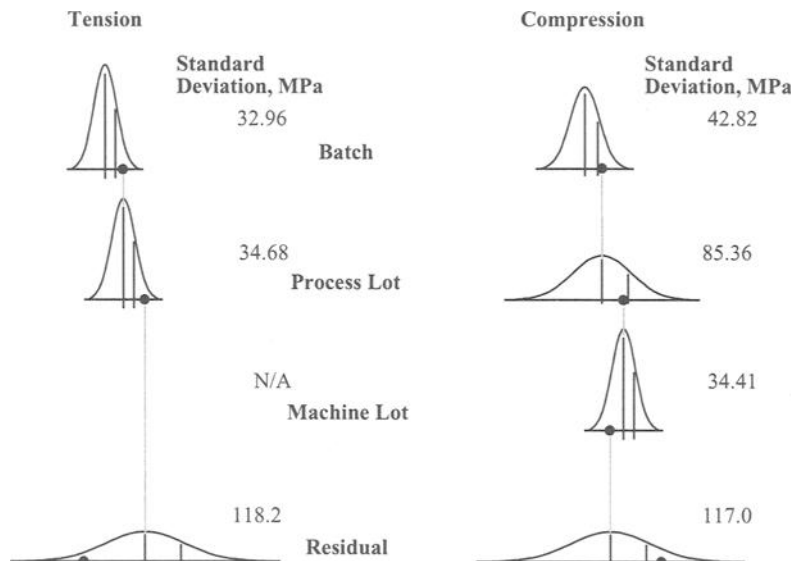


Figure 7 - Nested experiment statistical model variance estimates – tension and compression strength.

Glass Transition Temperature

The same type of plot is contained in Figure 8 for the dry and wet T_g data. The scale for the wet and dry distributions is the same, although it differs from that used in Figure 7 for clarity. For dry T_g there is a pattern similar to the mechanical testing for the batch, process lot and machine lot contributions to variability, with each having roughly the same contribution. Interestingly, the residual is also of about the same order, indicating that this dynamic mechanical analysis (DMA) test is much more reproducible than the mechanical tests.

While for the wet data the process lot and residual variability contributions are similar to that seen for the dry data, the batch effect is not statistically significant, and the machine lot contribution is substantially higher. While it doesn't seem reasonable that coupon machining is responsible for the difference in T_g values, the conditioning and test occurring as a part of the machine lot appear to be substantially influencing the results.

Correlation between the properties was evaluated. The only strong correlations were with the dry T_g values. With tension strength the correlation coefficient was 0.75. With wet T_g the correlation coefficient was 0.80. There were no strong correlations between compression values and the other three tests.

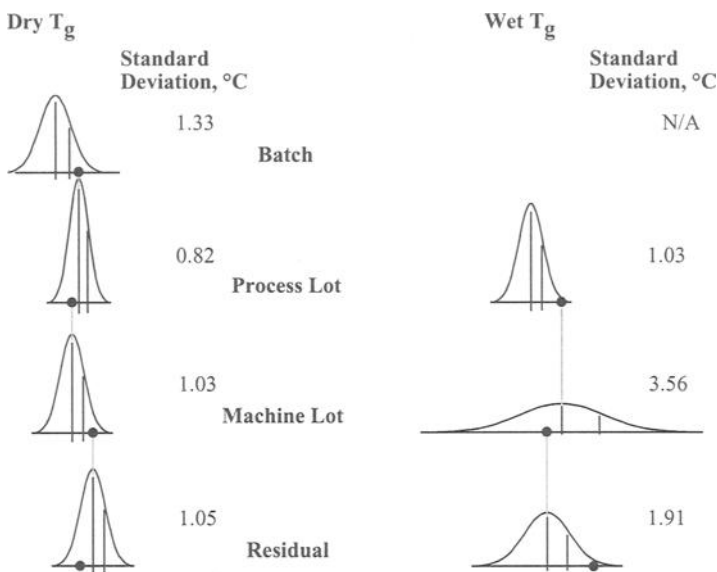


Figure 8 - *Nested experiment statistical model variance estimates – dry and wet glass transition temperature.*

Review

This qualification approach and evaluation has achieved several objectives. The nested experiment contained within the qualification allows assumptions made about variability sources used to lay out the qualification to be justified by the same qualification data. This makes the general aviation qualification approach “self-justifying” rather than an untested assumption. The nested experimental structure also plans and schedules the work, requiring little intervention or management, and allows completion of the effort in as little as a few months.

Basic multi-batch composite properties have been tested and variability well characterized through the fabrication of only six crossplied panels and three unidirectional panels. The reduction in physical, chemical, and nondestructive testing as a result of requiring substantially fewer panels alone makes this approach attractive.

This effort fits in well with the regression approach to allowables calculation. The approach generates an adequate number of adjacent spares that are immediately available for test or examination if required. Also, the entire effort can be completed without the use of tabs, which bring their own factors and associated variability. It is very interesting that different tests appear to respond differently to the sources of material variability, although for all the tests examined in this effort true batch to batch variability was a minor component.

Conclusions

1. The compression and tension mechanical tests respond differently to the components of variability compared to the dry and wet glass transition temperature physical tests.
2. For the mechanical tests, simply having more coupons, regardless of batch, process lot, or machine lot, provided the greatest contribution to characterizing variability.
3. The residual scatter for the T_g tests was much less than for the mechanical tests, implying better reproducibility.
4. True batch to batch variability was a minor component for all the mechanical and physical tests performed.

References

- [1] Ruffner, D., and Jouin, P., "Material Qualification Methodology for a Helicopter Composite Main Rotor Blade," American Helicopter Society 56th Annual Forum, Virginia Beach, Virginia, May 2-4, 2000.
- [2] Vangel, M., "Design Allowables from Regression Models Using Data from Several Batches," Composite Materials: Testing and Design (Twelfth Volume), ASTM STP 1274, R.B. Deo and C.R. Saff, Eds., American Society for Testing and Materials, West Conshohocken, PA, 1996, pp. 358-370.
- [3] Tomblin, J., Ng, Y., Bowman, K., Hooper, E., Smith, T., and Showers, D., "Material Qualification Methodology for Epoxy-Based Prepreg Composite Material Systems," Advanced General Aviation Transport Experiments (AGATE), February 1999.
- [4] MIL-HDBK-17E, "Polymer Matrix Composites," Naval Publications Office, Philadelphia, PA, January 23, 1997.
- [5] Montgomery, D., Design and Analysis of Experiments, John Wiley and Sons, 1991.
- [6] Wegner, P. and Adams, D., "Verification of the Wyoming Combined Loading Compression Test Method," UW-CMRG-R-98-116 under FAA Grant No. 94-G-009, September 1998.
- [7] Rawlinson, R., "The Use of Crossply and Angleply Composite Test Specimens to Generate Improved Material Property Data," 36th International SAMPE Symposium, San Diego, CA, April 15-18, 1991.
- [8] Zabora, R., "Allowables Assurance Plan for Composite Materials," 36th International SAMPE Symposium, San Diego, CA, April 15-18, 1991.
- [9] Hart-Smith, L.J., "Generation of Higher Composite Material Allowables Using Improved Test Coupons," 36th International SAMPE Symposium, San Diego, CA, April 15-18, 1991.
- [10] Box, G.E.P., Hunter, W.G., and Hunter, J.S., Statistics for Experimenters, John Wiley and Sons, 1978.

Peter Shyprykevich,¹ John S. Tomblin,² Mark G. Vangel³

The Development and Use of a Common Database for Composite Materials

Reference: Shyprykevich, P., Tomblin, J. S., and Vangel, M. G., “**The Development and Use of a Common Database for Composite Materials,**” *Testing, Design, and Acceptance Criteria, ATM STP 1416*, A. Zureick and A.T. Nettles, Eds., American Society for Testing and Materials International, West Conshohocken, PA, 2002.

Abstract: The development of a database and guidelines for its generation are described. The developed common database guidelines include types and number of mechanical tests, test methods, and environmental conditions. Methods to reduce the test data to the level of obtaining A- and/or B-basis values include statistical procedures that allow pooling across different environments for the same failure modes in order to increase sample sizes to estimate material variability. Either Weibull or normal distribution statistics can be used. For the normal distribution, knockdown factors from mean value to A-and B-basis material (lamina) allowables were developed that are based on a large sample size for variability and a small sample size for the mean. The concept of establishing large sample (population) variability for particular failure modes has implications for the statistical significance of design allowables for notched and unnotched laminates where the test samples are historically small. In order to utilize the database, each company must demonstrate that their processing of the identical composite material results in mechanical properties that are the same as in the database. Equivalency tests, along with statistical acceptance criteria, were developed that would perform that function. In addition, the developed acceptance criteria may be used by the manufacturing company to control the quality of the incoming material. This paper will also contain an example of a database for a carbon/epoxy material along with example equivalency tests and statistics.

Keywords: composite materials, databases, material allowables, statistical methods, pooling, equivalency tests, acceptance criteria

Introduction

A major barrier to lowering the cost of aircraft using composite structural materials has been the cost of certification. To a large extent, the high certification cost has been

¹R&D Program Manager for Advanced Materials/Structures AAR-430, Federal Aviation Administration, Atlantic City International Airport, NJ, 08405.

²Associate Professor, Department of Aerospace Engineering, Wichita State University, 1845 N. Fairmount, Wichita, KS, 67260-0093.

³Senior Statistician, Dept. of Biostatistical Science, Dana-Farber Cancer Institute, 44 Binney Street, Boston, MA, 02115.

due to the need for individual manufacturers to develop extensive and costly data on mechanical and chemical properties of the composite materials selected in aircraft construction. In the conventional approach, each company is required to develop a complete database. If several companies desire to apply the same material to a number of components, each company is required to develop the same database. Thus, the considerable effort involved in generating the database has to be duplicated several times.

The purpose of this work was to establish a database and guidelines for its generation and use. The database, in this case, was shared by a group of small aircraft companies in the Advanced General Aviation Technology Experiments (AGATE) consortium. Because the companies agreed to use a common material and qualification procedure for each of their applications, only one database development was required. The cost of generating the database was then shared, resulting in a sizeable saving to each of the partners. It is estimated that, after the development of a common database, the certification cost of each company was reduced from \$350 000 to \$50 000, with a concurrent reduction in time to complete the development of the property base from as much as 24 months to as little as 6 months. The developed methodology may also be used by material suppliers to qualify a material system to be used by future customers and not necessarily small aircraft builders.

In order to utilize the database, each company must demonstrate that their processing of the identical composite material results in mechanical properties that are the same as in the database. Equivalency tests, along with statistical acceptance criteria, were developed that would perform that function. In addition, the developed acceptance criteria may be used by the manufacturing company to control the quality of the incoming material that is being purchased.

Database

The database described here will be able to generate statistically based material allowables for both A- and B-basis applications. Specific test matrices and test methods are presented that produce lamina level composite material properties for various loading modes and environmental conditions. The database only covers the initial material qualification at the lamina level and does not include procedures for laminate or higher level building block tests. For brevity, only mechanical property values are discussed; methods to obtain other material data are contained in [1].

For a composite material system database to be viable, several batches of material must be characterized to establish the statistically based material property for each of the material systems. The definition of a batch of material for this database refers to a quantity of homogenous resin (base resin and curing agent) and fiber prepared in one operation with traceability to individual component batches as defined by the resin manufacturer.

In order to account for processing and panel-to-panel variability, the material system being qualified must also be representative of multiple processing cycles. For this database, each batch of prepreg material was represented by a minimum of two independent processing and curing cycles.

In order to substantiate the environmental effects with respect to the material properties, several environmental conditions are defined to represent extreme cases of

exposure. The conditions defined as extreme cases in this database are listed as follows:
Cold Temperature Dry (CTD) = -59 °C with an "as-fabricated" moisture content,
Room Temperature Dry (RTD) = ambient laboratory conditions with an as-fabricated
moisture content,

Elevated Temperature Dry (ETD) = 82 °C with an as-fabricated moisture content, and
Elevated Temperature Wet (ETW) = 82 °C with an equilibrium moisture weight gain in
an 85% relative humidity environment.

Two test matrices are presented, one that represents reduced sampling requirements and one that represents robust requirements. The former, Table 1, is suited for obtaining B-basis material allowables; the latter, Table 2, is for A-basis material allowables. The numbers of replicates in the tables are identified as such: the first number is the number of batches, the second number is the number of replicates per batch. A typical number of replicates per environmental condition are 18 in Table 1 and 55 in Table 2. The number of replicates is based on MIL-HDBK-17 but with number of batches reduced to three.

Table 1 – Reduced sampling requirements for cured lamina properties.

Test	Method	No. of Specimens Per Test Condition			
		CTD	RTD	ETW	ETD
0° (warp) Tensile Modulus, Strength and Poisson's Ratio*	ASTM D 3039	3x6	3x6	3x6	3x6
90° (fill) Tensile Modulus and Strength*	ASTM D 3039	3x6	3x6	3x6	3x6
0° (warp) Compressive Strength	SACMA SRM 1	3x6	3x6	3x6	3x6
0° (warp) Compressive Modulus	SACMA SRM 1	3x2	3x2	3x2	3x2
90° (fill) Compressive Strength	SACMA SRM 1	3x6	3x6	3x6	3x6
90° (fill) Compressive Modulus	SACMA SRM 1	3x2	3x2	3x2	3x2
In-Plane Shear Modulus and Strength*	ASTM D 5379	3x6	3x6	3x6	3x6
Short Beam Shear	ASTM D 2344	--	3x6	--	--

* Strain gages or extensometers used during testing for only two specimens per batch.

Table 2 – Robust sampling requirements for cured lamina properties.

Test	Method	No. of Specimens Per Test Condition			
		CTD	RTD	ETW	ETD
0° (warp) Tensile Modulus, Strength and Poisson's Ratio*	ASTM D 3039	5x11	5x11	5x11	5x11
90° (fill) Tensile Modulus and Strength*	ASTM D 3039	5x11	5x11	5x11	5x11
0° (warp) Compressive Strength	SACMA SRM 1	5x11	5x11	5x11	5x11
0° (warp) Compressive Modulus	SACMA SRM 1	5x4	5x4	5x4	5x4
90° (fill) Compressive Strength	SACMA SRM 1	5x11	5x11	5x11	5x11
90° (fill) Compressive Modulus	SACMA SRM 1	5x4	5x4	5x4	5x4
In-Plane Shear Modulus and Strength*	ASTM D 5379	5x11	5x11	5x11	5x11
Short Beam Shear	ASTM D 2344	--	5x11	--	--

* Strain gages or extensometers used during testing for only four specimens per batch.

Tables 1 and 2 can be used for both tape and fabric material although the specimen width for ASTM D 3039 will be different. The suppliers for the Advanced Composite Materials Association (SACMA) SRM 1 [2] test method for compression properties

requires two different specimens to be tested. Therefore, the two additional specimens needed to determine stiffness properties are reflected in these tables. The test methods cited are currently being used in general aviation industry. Other test methods, such as the combined loading compression [3], are preferable as they do not require separate test specimens for stiffness measurements. The number of replicates at each environmental condition can be considered a minimum: 18 for B-basis and 55 for A-basis. A much larger number is recommended in MIL-HDBK-17. However, the number of specimens chosen is representative of industry practice, primarily small aircraft manufacturers. As the number of replicates is small, there is a need to lessen the impact of low material allowables on the design of the structure.

Material Allowable Generation

Upon completion of the mechanical test program and data reduction, including normalization of fiber-dominated properties, the next step in the qualification procedure is to produce statistical material allowables for each mechanical property. B- or A-basis material allowables are determined for each strength property using the statistical procedures outlined in the following sections. In the case of modulus and Poisson's ratio, the average value of all corresponding tests for each environmental condition are used as design properties.

The general methodology described here is based on the methodology described in [4] that employed the Weibull distribution to characterize the data. Here, the methodology is extended to encompass a normal distribution. Either statistical distribution can be used, depending on the best fit to the data, although, in general, the use of the Weibull distribution will result in more conservative material allowables. In this data reduction method, the data from all environments, batches, and panels are pooled to obtain population variability factors for each test condition and failure mode, i.e., tension, compression, and shear. This approach allows the use of small data sets to grow the database and establish material basis numbers from this much larger data set.

The data reduction methodology presented in this section requires several underlying assumptions in order to generate a valid material allowable. By pooling the data sets in the analysis method, the variability across environments should be comparable and the failure modes for each environment should not significantly change. If the variability or failure modes significantly change, recourse should be taken in the traditional methods of MIL-HDBK-17.

Data Reduction Methodology

The methodology to produce a material allowable (based upon testing represented by the Tables 1 and 2) is presented through a stepwise process, which assumes that all testing data for each condition and testing environment has been reduced and is in terms of failure stress. An assumption of normality is used in the method to reduce and model the behavior. The stepwise process then proceeds as follows.

1. All relevant fiber-dominated property data is normalized via the procedures presented in MIL-HDBK-17-1E. This normalization procedure accounts for variations in the fiber volume fraction between individual specimens, panels, and/or batches of material.

2. For a single test condition (such as 0° compression strength), the data for each environment being tested is collected. The number of observations in each environmental condition is n_j where the subscript j represents the total number of environments being pooled. The sample mean \bar{x} and sample standard deviation s for each environment is then calculated by

$$\bar{x} = \frac{1}{n} \sum_{i=1}^n x_i \quad (1)$$

$$s^2 = \frac{1}{n-1} \sum_{i=1}^n (x_i - \bar{x})^2 \quad (2)$$

For each environment, the environmental groupings must be checked for any outliers as well as for the assumption of normality. In addition, the variances of each environmental grouping should be checked for equality. If any outliers exist within each environmental grouping, the disposition of each outlier should be investigated via the procedures given in MIL-HDBK-17. For the check of population normality, engineering judgment should be applied to verify that the assumption of normality is not significantly violated. If the variance of each environmental grouping is significantly different, as determined by the procedure described later, statistical methods of MIL-HDBK-17 should be used.

3. Strength data at each environment is then normalized by dividing the individual strength by the mean strength. This results in all data having a mean of 1.0. Next, all the normalized data from each environment is pooled together into one data set.
4. For the pooled, normalized data set, the number of samples N , the sample mean \bar{x} , and sample standard deviation s is calculated by Equations (1) and (2). For the pooled data set, a visual comparison of the best normal fit should be conducted. If the assumption of normality is significantly violated, the other statistical models should be investigated to fit the data. In general, the Weibull distribution provides the most conservative basis value.
5. The one-sided B- and A-basis tolerance factors are calculated for the normal distribution for each environment j that is based upon the number of samples in the pooled data set N and the number of samples in each environment n_j . The B-basis tolerance factor (number of standard deviations), $(k_B)_j$ may be approximated by [5]

$$(k_B)_j = z_B \sqrt{\frac{f}{Q}} + \sqrt{\frac{1}{c_B n_j} + \left(\frac{b_B}{2c_B} \right)^2} - \frac{b_B}{2c_B} \quad (3)$$

where n_j is the number of observations of the selected environment (a subset of N , the number of total pooled observations) and z_B is the standard normal random variable. In the case of a B-basis calculation, z_B is taken as 1.28115 (90% probability). The subscript j is used to indicate the tolerance factor for that specific environment. The coefficients b_B and c_B are given by the following relationships

$$b_B(f) = 1.1372 \frac{1}{\sqrt{f}} - 0.49162 \frac{1}{f} + 0.18612 \frac{1}{f\sqrt{f}} \quad (4)$$

$$c_B(f) = 0.36961 + 0.040342 \frac{1}{\sqrt{f}} - 0.71750 \frac{1}{f} + 0.1963 \frac{1}{f\sqrt{f}} \quad (5)$$

where $f = N-2$ is the degree of freedom for the variance. In the case $f \geq 3$, Q may be approximated by

$$Q = f - 2.327\sqrt{f} + 1.138 + 0.6057\frac{1}{\sqrt{f}} - 0.3287\frac{1}{f} \quad (6)$$

For $f = 2$, the exact value of Q may be used as $Q = 0.05129$. The above approximations are accurate within 1.2% of the tabulated values for B-basis calculations.

The A-basis tolerance factor, k_A , may be approximated by

$$(k_A)_j = z_A \sqrt{\frac{f}{Q} + \sqrt{\frac{1}{c_A n_j} + \left(\frac{b_A}{2c_A}\right)^2}} - \frac{b_A}{2c_A} \quad (7)$$

where n_j is the number of observations of the selected environment (a subset of N , the number of total pooled observations) and z_A is the standard normal random variable. In the case of an A-basis calculation, z_A is taken as 2.32635 (99% probability). The subscript j is used to indicate the tolerance factor for that specific environment. The coefficients b_A and c_A are given by the following relationships

$$b_A(f) = 2.0643\frac{1}{\sqrt{f}} - 0.95145\frac{1}{f} + 0.51251\frac{1}{f\sqrt{f}} \quad (8)$$

$$c_A(f) = 0.36961 + 0.0026958\frac{1}{\sqrt{f}} - 0.65201\frac{1}{f} + 0.011320\frac{1}{f\sqrt{f}} \quad (9)$$

where $f = N-2$ is the degree of freedom for the variance. In the case $f \geq 3$, Q may be approximated by

$$Q = f - 2.327\sqrt{f} + 1.138 + 0.6057\frac{1}{\sqrt{f}} - 0.3287\frac{1}{f} \quad (10)$$

For $f = 2$, the exact value of Q may be used as $Q = 0.05129$. The above approximations are accurate within 0.9% of the tabulated values for A-basis calculations.

6. The normal distribution B- and A-basis allowable is then calculated using the pooled (normalized by fiber volume) mean, standard deviation, and tolerance factors for each environment j via the equation

$$B_j = \bar{x} - (k_B)_j s \quad (11)$$

This number is essentially a knockdown factor less than 1. The A-basis value for each environment may be obtained similarly by

$$A_j = \bar{x} - (k_A)_j s \quad (12)$$

7. The pooled basis values obtained in step 6 are multiplied by the mean strength calculated for each environment obtained in step 2. These values then become the basis values (A and B) for each individual environmental condition.

Equality of Variance – The equality of variances between the different grouped data must also be checked using Levene's test [MIL-HDBK-17-1E]. This test determines whether the sample variances for "k" groups differ significantly, which is an important assumption that must be validated to substantiate pooling across environments. This test is usually performed at a significance level of 0.05. It should be noted that values less than 0.05 may also be used to assess equality of variances at different environments. These different significance values can be useful in establishing engineering judgment as to the degree of variance inequality and suggest possible problems with obtaining a representative pooled data set. In the case when the variances are not equal at the 0.05 level, engineering judgment should be used to determine the degree of inequality. Figure 1 provides guidance in the situation of unequal variances and describes procedures to obtain a conservative material allowable. Note that these procedures must be combined with engineering judgment and that the failure modes must remain the same across environments. In general, if variances are significantly different at the 0.01 level, the reason should be investigated and some corrective action may be required.

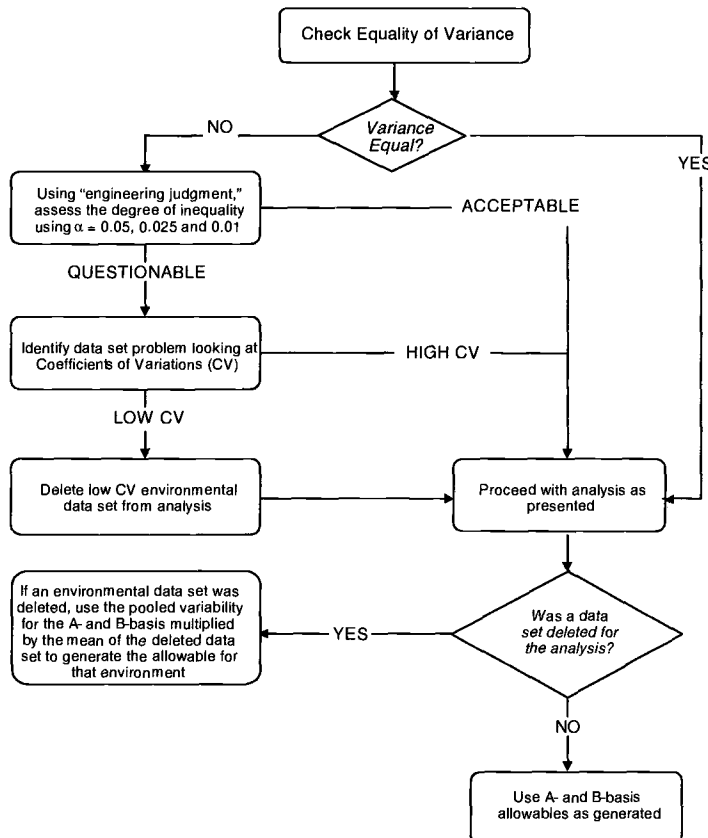


Figure 1 – Procedure to obtain material allowables in the case of variance inequality.

In general, a coefficient of variation between 4% to 10% is typical of composite materials. Experiences with large data sets have shown that this range is representative of most composite material systems. Lower coefficients of variation may be caused by the specimen fabrication and testing by a single laboratory while higher coefficients may point to lack of material and processing control. In cases where the coefficients of variation of the pooled data set are higher or lower than this range, the reason for the higher or lower coefficient of variation should be investigated before determining design allowable values from the pooled data set. For the coefficient of variation lower than 4%, an assigned value of 4% may be considered as an alternative engineering solution.

Example of B-Basis Calculation

This section illustrates the calculation of basis values according to the stepwise procedure presented using example mechanical property data (in the case of this specific example, for compression) that was generated according to the test matrix of Table 1 with some reduction in testing at CTD. The example data have been normalized to fiber volume fraction. The resulting mechanical property data (in MPa) are shown in Table 3. The sample mean, standard deviation, coefficient of variation, and number of observations are shown at the bottom of each column of data that is grouped by testing environment.

The next step in the data reduction procedure is to check the individually grouped environmental data for any outliers that may exist. Using MIL-HDBK-17 method, an outlier is detected in the ETD test data for the stress of 403.3 MPa. For the purpose of this example, the low outlier will be retained in the data set at this point.

Table 3 – *Example data set for each testing environment.*

CTD			RTD			ETD			ETW		
Batch	Panel	Data									
1	1	712.0	1	1	650.8	1	1	501.3	1	1	384.8
1	1	719.0	1	1	702.3	1	1	564.6	1	1	385.1
1	1	769.4	1	1	705.8	1	1	474.5	1	1	400.5
1	2	767.6	1	2	699.4	1	2	543.1	1	2	438.4
1	2	709.9	1	2	666.6	1	2	584.9	1	2	414.6
1	2	748.9	1	2	717.8	1	2	550.9	1	2	392.7
			2	3	705.8	2	3	403.3	2	3	434.3
			2	3	666.6	2	3	573.0	2	3	467.4
			2	3	671.8	2	3	552.7	2	3	447.8
			2	4	656.8	2	4	557.2	2	4	421.2
			2	4	720.4	2	4	583.9	2	4	453.2
			2	4	681.9	2	4	633.5	2	4	425.9
			3	5	646.4	3	5	524.8	3	5	428.2
			3	5	630.7	3	5	536.7	3	5	414.2
			3	5	647.1	3	5	574.4	3	5	410.6
			3	6	658.6	3	6	508.5	3	6	456.4
			3	6	669.4	3	6	580.7	3	6	392.8
			3	6	687.7	3	6	494.2	3	6	413.9
AVG : 737.8			AVG : 677.0			AVG : 541.2			AVG : 421.2		
STD : 27.60			STD : 26.77			STD : 51.78			STD : 24.95		
CV% : 3.74			CV% : 3.95			CV% : 9.57			CV% : 5.92		
n : 6			n : 18			n : 18			n : 18		

After the data is checked for outliers, visual and statistical checks should be performed on the environmentally grouped data to validate the assumption of normality. Figure 2 shows the data from Table 3 plotted against the standard normal curves for each environment tested. The Figure 2(a) plot is graphically represented on a normality scale, which reduces the distribution to a straight line. The identified outlier RTD is the only point that does not fit the normality criterion. This type of plotting is a graphical method for determining whether sample data conforms to a hypothesized normal distribution based on a subjective visual examination of the data. If the normal distribution adequately describes the data, the plotted points will fall approximately on a straight line. As seen in Figure 2(b), the normal model appears to closely represent the data across all represented environments and does not appear to cause any significant concerns.

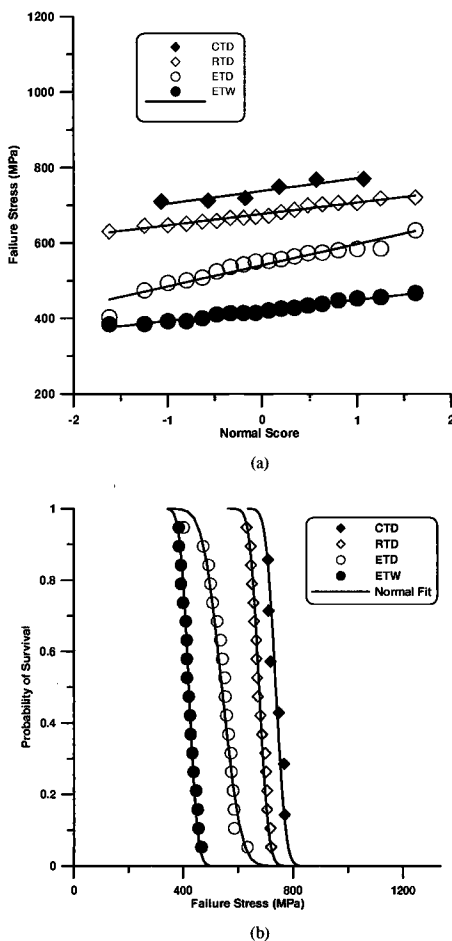


Figure 2 – Fit of experimental data for each environment [(a) normality scale – (b) probability scale].

In addition to a visual check on normality, an Anderson-Darling (A-D) test was performed to check the normality of the data at each environmental condition. The A-D test showed that the normality of the data at each environmental condition is not rejected.

The next step in the data reduction process is the pooling of data across environments. At this point, the equality of variance was performed using the F-test. This statistical test showed that at the 0.05 significance level the variances at the four environmental conditions cannot be ruled out to be different. The $F_{\text{calculated}}$ was equal to 1.88 which is below $F_{\text{critical}} = 2.93$. The data from each environment is normalized using the sample mean from each environmental condition. Table 4 shows the resulting normalized data pooling all environments together. As seen from this method, all strength values then take on a normalized value in the neighborhood of one. Also shown in Table 4 are the resulting mean, standard deviation, coefficient of variation, and number of observations. Using the pooled data, Figure 3 shows the visual check of the normal distribution with respect to the pooled data. As seen from Figure 3, the normal model appears to closely represent the data across all pooled data. Again, the only exception is the outlier.

After the pooled data have been collected, the pooled sample mean and standard deviation may be computed (see Table 4). Using these values, the B- and A-basis values may be calculated for the pooled data. Using Equations 3-10, the one-sided tolerance limits may be calculated for each environmental condition. The values of these tolerance limits for each environment are shown in Table 5. k_A and k_B , when combined with the pooled normal sample mean and standard deviation, yield B and A knockdown values for each by Equations (11) and (12) as shown in Table 6.

Table 4 – Resulting pooled data after normalization procedure.

CTD			RTD			ETD			ETW		
Batch	Panel	Data									
1	1	0.965	1	1	0.961	1	1	0.926	1	1	0.913
1.	1	0.975	1	1	1.037	1	1	1.043	1	1	0.914
1	1	1.043	1	1	1.042	1	1	0.877	1	1	0.951
1	2	1.040	1	2	1.033	1	2	1.003	1	2	1.041
1	2	0.962	1	2	0.985	1	2	1.081	1	2	0.984
1	2	1.015	1	2	1.060	1	2	1.018	1	2	0.932
			2	3	1.042	2	3	0.745	2	3	1.031
			2	3	0.985	2	3	1.059	2	3	1.110
			2	3	0.992	2	3	1.021	2	3	1.063
			2	4	0.970	2	4	1.029	2	4	1.000
			2	4	1.064	2	4	1.079	2	4	1.076
			2	4	1.007	2	4	1.171	2	4	1.011
			3	5	0.956	3	5	0.970	3	5	1.016
			3	5	0.932	3	5	0.992	3	5	0.983
			3	5	0.956	3	5	1.081	3	5	0.975
			3	6	0.973	3	6	0.939	3	6	1.084
			3	6	0.989	3	6	1.073	3	6	0.933
			3	6	1.016	3	6	0.913	3	6	0.983

Pooled Average :	1.000
Pooled Standard Dev. :	0.0649
Coeff. of Variation (%) :	6.494
Number of Observations :	60

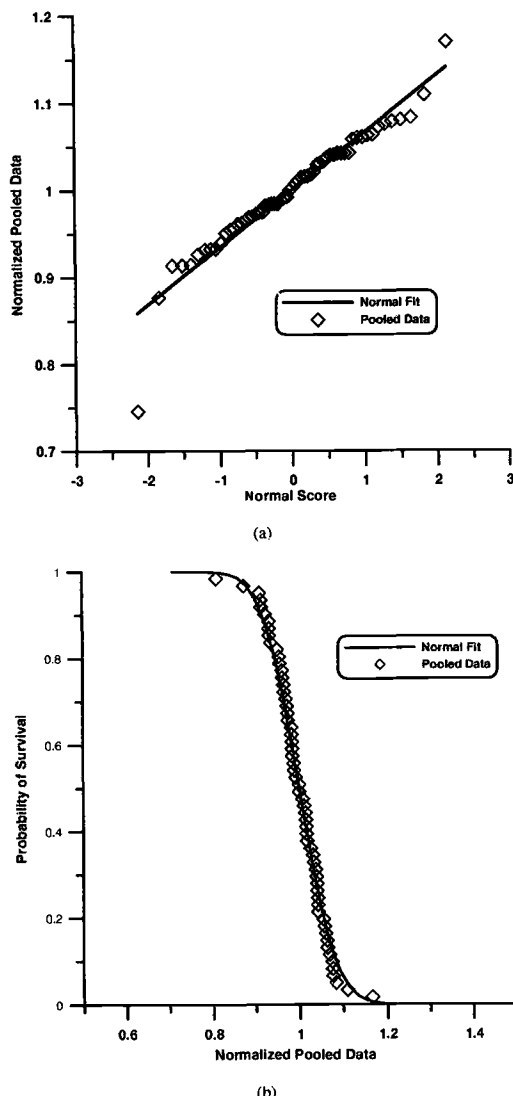


Figure 3 – Fit of pooled data [(a) normality scale – (b) probability scale].

Table 5 – Example tolerance limit values for each environment.

Statistic	CTD	RTD	ETD	ETW
k_B	2.0281	1.7585	1.7585	1.7585
k_A	3.1632	2.9250	2.9250	2.9250

Table 6 – Example knockdown values for each environment.

Statistic	CTD	RTD	ETD	ETW
B _{normal}	0.8683	0.8858	0.8858	0.8858
A _{normal}	0.7946	0.8100	0.8100	0.8100

Once these values are calculated, the B- and A-basis for each environmental condition are obtained using the mean of each environment and the pooled B- and A-basis values. Simple multiplication yields the B- and A-basis values for each of the environmental conditions as shown in Table 7.

Table 7 – Example basis values for each environment (in MPa).

Statistic	CTD	RTD	ETD	ETW
B-Basis Value	640	600	479	373
A-Basis Value	586	548	438	341

It should be noted that even though A-basis numbers were calculated for this example, the number of specimens was more in accordance with the number recommended for B-basis calculations. For a more robust A-basis allowable, the number of specimens can be increased to those given in Table 2.

Material Equivalence and Acceptance Testing

The methodology to demonstrate material equivalency and establish acceptance testing criteria is described next. Material equivalency programs are specified to assure that a follow-on material will produce material properties equivalent to those of the original qualification. Acceptance testing is a quality control procedure designed to detect large property variations or undesirably high or low properties in an incoming prepeg lot.

The procedures for material equivalency described in this document are only applicable to the following specific types of changes:

- Identical material fabricated by the same airframe manufacturer using identical fabrication process at a different location,
- Identical material fabricated by a different airframe manufacturer using a follow-on process that is equivalent to the original process,
- Identical material fabricated by the same airframe manufacturer using a follow-on process that is slightly different from the original process,
- Minor changes in the prepeg constituent(s) and/or constituent manufacturing process, or
- Combinations of the above.

The equivalence criterion that was chosen is based on a statistical test commonly known as test of hypotheses [6]. For strength properties, both the means and the minimum individuals are considered. As this is a joint or combined α for one-sided test, a low mean or low minimum individual, or both, will constitute a rejection. For modulus properties, only the means are considered.

When showing equivalency, engineering judgment should not be left behind. If some mechanical property at one temperature does not show statistical equivalence, the

importance of that property and the size of the discrepancy should be investigated before declaring that the materials are not the same or equivalent. For example, tensile strength and modulus and ETW compression strength and modulus are examples of properties that are usually design critical and therefore more importance should be placed on the statistical test results for these properties.

Acceptance testing is also known as material receiving inspection, incoming material inspection, or raw material quality control testing. It is designed to detect large variations or undesirably high or low properties in the incoming prepreg lot. The procedures and acceptance criteria described herein are intended as guidelines for developing material and process specifications for quality control purposes. The procedures for receiving inspection do not allow for any changes in the material system or manufacturing process. The material system and manufacturing process must be identical to that used in the original qualification, or if material equivalency has been substantiated, it must be identical to that used in the material equivalence exercise.

Testing Requirements for Material Equivalence

For mechanical properties, Table 8 describes the minimum number of tests required for each environmental condition along with the relevant test methods to establish material equivalence with respect to the original A- or B-basis design allowable. The temperature for each environmental condition was described previously. Specimen sampling and selection should be based on at least two independent processing or cure cycles. Thus, eight replicates in Table 8 represent four replicates for each processing or cure cycle. Table 8 is a reduced version of Table 1, otherwise there would be no benefit in trying to use the existing database if one has to duplicate it. For Table 8, the two most critical environments were selected. The number of batches were reduced to one, the number of processing cycles reduced to two, and the number of replicates reduced from 6 to 4.

Table 8 – *Material equivalence testing requirements for cured lamina properties.*

Test	Method	No. of Specimens Per Test Condition	
		RTD	ETW
0° (warp) Tensile Modulus and Strength ¹	ASTM D3039	8	8
90° (fill) Tensile Modulus and Strength ^{1,2}	ASTM D 3039	4	4
0° (warp) Compressive Strength	SACMA SRM 1	8	8
0° (warp) Compressive Modulus	SACMA SRM 1	4	4
90° (fill) Compressive Strength ²	SACMA SRM 1	8	8
90° (fill) Compressive Modulus ²	SACMA SRM 1	4	4
In-Plane Shear Modulus and Strength ¹	ASTM D 5379	8	8
Short Beam Shear	ASTM D 2344	8	--

¹ Strain gages or appropriate extensometers are to be used on four specimens.

² Only required for unidirectional (tape) material form when design relies on these properties.

Testing Requirements for Acceptance

Acceptance test requirements may vary from airframe manufacturer to airframe manufacturer. All of the mechanical tests described in Table 9 should be performed by a material vendor, airframe manufacturer, or both. For acceptance testing, it is not necessary to incorporate processing cycle or panel-to-panel variability as was required for the equivalency testing. All of the test panels for the test matrix in Table 9 may be processed in a single cure cycle.

Table 9 – *Acceptance testing requirements for cured lamina properties.*

Test	Method	No. of Specimens Per Test Condition	
		RTD	ETD
0° (warp) Tensile Modulus and Strength ¹	ASTM D3039	5	
90° (fill) Tensile Modulus and Strength ^{1,2}	ASTM D 3039	5	
0° (warp) Compressive Strength	SACMA SRM 1		5
0° (warp) Compressive Modulus	SACMA SRM 1		2
90° (fill) Compressive Strength ²	SACMA SRM 1		5
90° (fill) Compressive Modulus ²	SACMA SRM 1		2
In-Plane Shear Modulus and Strength ¹	ASTM D 5379	5	
Short Beam Shear	ASTM D 2344	8	8

¹ Strain gages or appropriate extensometers are to be used on four specimens.

² Only required for unidirectional (tape) material form when design relies on these properties.

Statistical Tests

This section provides test statistics related to material equivalency and acceptance testing. The test statistics are selected based on the material properties of interest. The test statistic for modulus requires that the mean value to be within an acceptable range, neither a high nor a low mean is desirable. The test statistics for these properties are designed to reject either a high or a low mean value. The test statistics for strength properties, on the other hand, will reject either a low mean or a low minimum individual value.

Failure for Decrease in Mean or Minimum Individual – The mean, \bar{x} , and standard deviation, s , are approximated by results from the individual test condition (environment) of the original qualification. The pass/fail thresholds for mean properties, W_{mean} , are determined by Equation (13). The mean values from experimental tests must meet or exceed

$$W_{mean} = \bar{x} - k_n^{\text{see footnote(4)}} \cdot s^4 \quad (13)$$

The pass/fail threshold for minimum individual properties, $W_{\text{minimum individual}}$, are determined by Equation 14. The minimum individual values from experimental tests must meet or exceed

⁴ See Table 20 of [I] for appropriate k_n .

$$W_{\text{minimum individual}} = \bar{x} - k_n^{\text{see footnote(5)}} \cdot s \quad (14)$$

Failure for Change in Mean - This statistical test assumes that the standard deviations of the original and follow-on data are equal but unknown. The pooled standard deviation, S_p , is used as an estimator of common population standard deviation.

$$S_p = \sqrt{\frac{(n_1 - 1) \cdot S_1^2 + (n_2 - 1) \cdot S_2^2}{n_1 + n_2 - 2}} \quad (15)$$

$$t_0 = \frac{\bar{x}_1 - \bar{x}_2}{S_p \cdot \sqrt{\frac{1}{n_1} + \frac{1}{n_2}}} \quad (16)$$

The test statistic is t_0 , and n is the number of specimens. Subscripts 1 and 2 denote follow-on and original, respectively. Since this is a two-sided t-test, $t_{a,n} = t_{a/2,n_1+n_2-2}$, $t_{a,n}$ is obtained from Table 22 of [1]. The passing range is between $-t_{a/2,n_1+n_2-2}$ and $t_{a/2,n_1+n_2-2}$. In other words, t_0 must be smaller than $t_{a/2,n_1+n_2-2}$ but larger than $-t_{a/2,n_1+n_2-2}$ to pass the criteria. For stiffness properties, modulus, and Poisson's ratio, variations of $\pm 5\text{-}7\%$ from the base material mean can be an acceptable practice if difficulties are encountered with the t-test.

Criteria Specific to Material Equivalence

For determining material equivalency, it is recommended to set the probability of rejecting a good property (α) to 0.05 or 5% for all test methods that utilize the test statistics. One retest is allowed for each property, reducing the actual probability to 0.0025 or 0.25%. As depicted in Table 8, a minimum of eight specimens is required for strength properties comparison (typically four specimens from each processing cycle). A minimum of four specimens is required for modulus comparisons (typically two specimens from each processing cycle). In the case where one or more properties fail the criteria, one may choose to test only those properties that failed the criteria. However, it is recommended that the entire material equivalence test matrix be repeated if more than half of the properties in Table 8 fail the criteria, so that a new qualification database may be generated.

Criteria Specific to Acceptance Testing

For determining material acceptance, it is recommended to set the probability of rejecting a good property to 0.01 or 1% for all the test methods that utilize the test statistics. Since one retest is allowed for acceptance testing, the actual probability of rejecting a good property is reduced to 0.0001 or 0.01%. Only those properties that fail

⁵See Table 21 of [1] for appropriate k_n .

the criteria need to be repeated. It is highly recommended that five or more specimens be used to reduce the probability of accepting a bad lot of prepreg material without increasing the probability of rejecting a good lot of material.

Concluding Remarks

The utility of a database that is based on a minimum number of specimen replication has been demonstrated using AGATE consortium database. The approach described here produced A- and B-basis material allowables that were sound statistically and made engineering sense. In this approach, advantage is taken of statistical procedures that allow pooling across different environments for the same failure modes in order to increase sample sizes in the estimate of material variability. Either Weibull or normal distribution statistics can be used, although only the use of a normal distribution was shown. For the normal distribution, equations are given that can be used to calculate knockdown factors from the means to A- and B-basis values based on a large sample size for variability and a small sample size for the mean. The concept of establishing large sample (population) variability for particular failure modes has implications for the statistical significance of design allowables for notched and unnotched laminates where the test samples are historically small.

Equivalency tests were developed that would permit usage of the database by new material users. Guidelines are given, in terms of mechanical and statistical testing, for what the company must demonstrate to show that their processing produces the same material as the original database. In addition, guidelines and criteria were provided for what mechanical and statistical tests should be used in the material acceptance activity that a manufacturing company could use to control the quality of the incoming material. For best results the equivalency and acceptance testing should mirror test methods and processing of the database with the criteria also derived from the database.

Acknowledgments

The authors gratefully thank Larry Ilcewicz, David Showers, and Lester Chang from the FAA for their leadership and support of this effort; Yeow Ng and Suresh Raju from Wichita State University for their technical and testing contributions; and the AGATE consortium for the financial support.

References

- [1] Tomblin, J.S., Ng, Y.C., and Raju, K. S., "Material Qualification and Equivalency for Polymer Matrix Composite Material Systems," DOT/FAA/AR-00/47, April 2001.
- [2] SRM 1-94, "Compressive Properties of Oriented Fiber-Resin Composites," Suppliers of Advanced Composite Materials Association (SACMA), 1994.
- [3] Wegner, P.M. and Adams, D.F., "Verification of the Combined Load Compression (CLC) Test Method," DOT/FAA/AR-00/26, August 2000.
- [4] Shpyrykevich, P., "The Role of Statistical Data Reduction in the Development of Design Allowables for Composites," *Test Methods for Design Allowables for*

- Fibrous Composites: 2nd Volume, ASTM STP 1003*, C.C. Chamis, Ed., American Society for Testing and Materials, Philadelphia, PA, 1989, pp. 111-135.
- [5] Scholz, F.W., "Approximation for Allowable k-Factors," Boeing Computer Services, The Boeing Company, Seattle, WA (internal paper).
 - [6] Vangel, M.G., "The Joint Distribution of the Mean and an Extremum of a Normal Sample, with Applications to Quality Control," *Proceedings of the Section on Physical and Engineering Sciences*, American Statistical Association, 1998, pp. 73-77.

Alan T. Nettles¹ and Michael J. Douglas²

A Comparison of Quasi-Static Indentation Testing to Low Velocity Impact Testing

Reference: Nettles, A. T. and Douglas, M. J., "A Comparison of Quasi-Static Indentation Testing to Low Velocity Impact Testing," *Composite Materials: Testing, Design, and Acceptance Criteria, ASTM STP 1416*, A. Zureick and A. T. Nettles, Eds., American Society for Testing and Materials International, West Conshohocken, PA, 2002.

Abstract: The need for a static test method for modeling low-velocity foreign object impact events to composites would prove to be very beneficial to researchers because much more data can be obtained from a static test than from an impact test. In order to examine if this is feasible, a series of static indentation and low velocity impact tests were carried out and compared. Square specimens of many sizes and thickness were utilized to cover the array of types of low velocity impact events. Laminates with a $\pi/4$ stacking sequence were employed because this is by far the most common type of engineering laminate. Three distinct flexural rigidities under two different boundary conditions were tested in order to obtain damage due to large deflections, contact stresses and to examine if the static indentation-impact comparisons are valid under the spectrum of damage modes that can be experienced. Comparisons between static indentation and low velocity impact tests were based on the maximum applied transverse load. The dependent parameters examined included dent depth, back surface crack length, delamination area and to a limited extent, load-deflection behavior. Results from this particular study showed that no distinct differences could be seen between the static indentation tests and the low velocity impact tests.

Keywords: composites, static indentation, impact, transverse loading rate

Low velocity impact events are expected to occur during the manufacturing and service life of composite parts and/or structures. Foreign body impact can occur during manufacturing, routine maintenance or use of a laminated composite part. This has led to an abundance of research on low-velocity impact damage to laminated composite plates. Typically, laminated plates are impacted by a "drop weight" method. This method usually consists of an instrumented striker (tup) that is secured to a carriage that falls along guideposts and collides with the plate. After an impact event has been performed, ultrasonic C-scans, X-radiography and cross sectional photo-microscopy are some of the common techniques used to document the damage area. Post impact strength testing (mostly compression) is often performed to evaluate a material's or structure's damage tolerance.

¹ Composite Materials Engineer, NASA Marshall Space Flight Center, ED34, MSFC, AL 35812.

² Design Engineer, International Construction Equipment, 301 Warehouse Dr., Matthews, NC 28104.

It would be very beneficial to simulate an impact event using a "quasi-static" loading test. By using this test, damage initiation and propagation can be more easily detected, deflection can be directly measured with great accuracy, and maximum transverse force can be better controlled. Thus it is the focus of the work in this study to examine if drop weight impact tests and quasi-static loading tests give the same size, shape, and location of damage for a given maximum transverse load.

In the present study, all tests were conducted on laminated plates made from an intermediate modulus carbon fiber with a toughened epoxy resin in prepreg form. The plates tested were quasi-isotropic with a stacking sequence of $[+45, 90, -45, 0]_n$, with n equal to 1, 2, 4, or 6, and a per ply areal density of 0.0194 g/cm^2 .

Previous Work

Background

The need for a static (or more commonly referred to as quasi-static) test method for modeling low-velocity foreign object impact events would prove to be very beneficial to researchers since much more data can be obtained from a quasi-static test than from an impact test. Standard Test Method for Measuring the Damage Resistance of a Fiber-Reinforced Polymer-Matrix Composite to a Concentrated Quasi-Static Indentation Force (ASTM Standard D6264-98) has been proposed for transverse quasi-static loading of composite laminates, although the standard stops short of claiming to represent low-velocity impacts. Since a "low-velocity" impact event lasts approximately 6-10 milliseconds there is debate as to whether or not a quasi-static indentation test truly represents a low velocity impact event.

First it is important to determine whether or not an impact event is considered "low-velocity" and can thus be subject to further analysis as a quasi-static event. It has been clearly shown that projectile-type impacts in the ballistic range are governed by dynamic events and therefore could never be represented by a quasi-static test [1,2,3]. Some research efforts have been focused on defining the bound between "low-velocity" and "dynamic" impact events. One study suggested that the impactor to target frequency ratio governs the type of event with a low (much less than unity) ratio implying a quasi-static event [4]. A simpler method was obtained by Swanson [5] in which a rule has been established that if the impactor mass is more than ten times the "lumped mass" of the target, then the impact event will be quasi-static in nature. The "lumped mass" is a function of the target shape and boundary conditions but is generally about one-half the mass of the entire target. However, for most practical purposes it is fairly clear if an impact event is "low-velocity" or not. High-velocity/large mass impacts are little concern because the part will be so heavily damaged by such an event that an analysis is not needed and conversely a low velocity/low mass impact is of little concern because no visible damage will form.

Once an impact event is deemed to be "low-velocity" the question remains as to whether or not a static indentation test can be performed that will duplicate certain aspects of the impact. Some of these aspects include permanent indentation, maximum displacement and most importantly, amount and type of damage formed. All of these parameters must be compared against an independent variable that will be common to

both tests. It has been suggested that this independent variable be the maximum transverse load [3,6,7].

Permanent indentation after an impact or quasi-static loading test has been examined in a few studies [8,9,10]. The one common feature to all of these studies is the large amount of scatter in indentation depth data to the point of rendering this measurement useless. Nevertheless, it was decided to examine this parameter in this study to see how much scatter would exist.

For load-deflection correlation it is imperative to have an instrumented impact apparatus. The interpretation of the signals has been greatly simplified with the use of commercially available systems that filter the load signals to reduce unwanted noise. Care must be taken to ensure that the filter being used does not mask important load events. A complete analysis of instrumented impact testing is beyond the scope of this study, but two excellent references are noted for the reader [11,12].

The amount of damage formed by an impact event can be measured in a number of ways. Destructively, the impacted specimen can be sectioned and examined under high magnification, or a residual property can be measured (termed "damage tolerance"). Non-destructively, ultrasonic or X-radiography can give a planar indication of the type and extent of damage. Ultimately the amount of damage formed by an impact event is of the most concern to the engineer investigating such an occurrence and because the impacted part may still be useable, nondestructive techniques are preferred. Thus the major portion of this study will deal with the resulting damage as detected via nondestructive evaluation, and whether or not the damage formed for a given transverse load is similar in low-velocity impact and quasi-static testing.

Impact versus Quasi-Static Testing

Several studies [3,6,8,13,14] show a similarity between quasi-static indentation and drop weight impact testing. While other studies, [7,15,16] have shown a limit to the applicability of using quasi-static indentation to represent impact events, it must be noted that there are many variables involved in these tests such as boundary conditions, specimen size, specimen thickness, stacking sequence, impactor size, impactor shape and type of fiber/resin system. The amount of impact damage formed in a laminated composite has been shown to be very sensitive to stacking sequence, regardless of thickness [17]. As plies are grouped together, larger areas of delaminations tend to form. It has been conventional wisdom in the composites industry to disperse the ply orientations in order to increase damage resistance. For example, a stacking sequence of $[+45_2, -45_2, 90_2]_{2S}$ is preferable to one of $[+45_2, 0_2, -45_2, 90_2]_S$ in order to increase the damage resistance of the laminate.

Experimental Procedure

The intent of this study was to compare quasi-static indentation testing to drop weight impact testing based on the maximum transverse load. In order to ensure a complete analysis of the two events, the testing was divided into two different categories based on the boundary conditions. These two categories were then

subdivided into three additional groups based on the composite laminate's transverse (flexural) stiffness. To ensure the repeatability of the experimental procedure each impact test was performed on approximately four different specimens, while the quasi-static indentation tests were performed on two different specimens. Because of the inherent scatter in data of the drop-weight impact testing, it was decided that portions needed to be repeated numerous times. However, the repeatability became so constant during the latter stages of the testing that the number of impacted specimens for repeatability assurance was reduced.

The rate of the quasi-static indentation test was also investigated to find if there was any time dependency involved in quasi-static indentation testing. The two rates used were 0.02 mm/s and 0.42 mm/s.

Boundary Conditions

The main two categories of test depended on the boundary conditions. Specimens were either clamped on all four edges or simply supported (also called free) on all four edges. This was done to determine if the boundary conditions would have a major influence on the damage introduced due to impact or quasi-static loading.

To perform the simply supported test, the specimens were placed on machined plates made from a 5.08 cm thick aluminum plate with an outside square dimension of 40.64 cm. A total of four plates were made with a square cutout in the center. These cutouts had sizes of 5.08 cm, 10.16 cm, 15.24 cm, and 30.48 cm. This was done to explore the effects of the transverse flexural properties of the composite panels.

In order to perform the test with clamped boundary conditions the plates had a series of 0.64 cm holes drilled and tapped into the aluminum plate 3.81 cm from the edge of the opening. The holes were spaced 2.54 cm on center. A 1.27 cm thick steel plate was machined with holes placed in the same location as those in the aluminum plate. The laminated composite panel to be tested was placed between the aluminum plate and the steel plate. Socket head bolts were then used to secure the specimen and a uniform torque of 5.65 N·m was applied to each bolt.

Flexural Rigidity of Specimens

The three subgroups of tests involved the transverse stiffness of the composite plates. The stiffness was a function of the ratio of the support opening size versus the laminate thickness. The specimens were divided into three categories under this assumption: Flexible, Medium, and Stiff, with ratios of 150, 50, and 25 respectively. During an impact event this transverse stiffness characteristic changes the mode of damage. For stiff laminates the contact forces caused the majority of damage, which was more confined to the side of the plate hit by the impactor. For flexible laminates the damage was most severe on the side opposite the impact site. This is characteristic of the materials used in advanced composites.

Specimen Preparation

The quasi-isotropic laminated panels were layed-up by hand from the carbon/epoxy prepreg material, placed in a vacuum bag and autoclave cured using the manufacturer's cure cycle. The panels were fabricated into 61.0 X 91.4 cm plates. In order to obtain a large variety of flexural stiffnesses of laminates the following four thicknesses (based on number of plies) were used, 8, 16, 32, and 48-ply. The panels were fabricated utilizing the quasi-isotropic $\pi/4$ stacking sequence of $[+45, 90, -45, 0]_{ns}$, where 'n,' was given the value of 1, 2, 4, or 6 respectively in order to obtain the desired number of plies.

Impact Testing Procedure

The impact testing was performed using a drop-weight impact tester. The specimens were placed on the platens with the desired opening size. Table 1 lists the opening (or span) size used depending on the laminate plate thickness. This divided the tests up into the proper flexural rigidity ratios being examined.

Table 1 — *Opening and laminate thickness ratios.*

	Number of Plies	Thickness (mm)	Opening (Specimen Size) (mm)
Flexible	8	1.02	152.4
	16	2.04	304.8
Medium	8	1.02	304.8
	16	2.04	101.6
	48	6.1	304.8
Stiff	16	2.04	50.8
	32	4.06	101.6
	48	6.1	152.4

Specimens were then impacted with a hemispherical tipped steel tup. The drop height and mass of the impactor were adjusted to give the desired damage level. The damage level desired was very little visual damage to the top of the specimen while achieving a measurable crack on the bottom surface. This level of damage was chosen since the onset of visual damage is such a critical state for an impact event. If penetration is allowed, boundary conditions and rate effects will not be as noticeable and if too low of an impact level is used, damage may not form at all. Table 2 lists the height, max load, boundary condition and mass for each subgroup that was finally chosen for impact testing.

Table 2—*Maximum load and drop height for the impact specimens tested.*

	Number of Plies	Mass (kg)	Impact Force (N)	Drop Height (cm)	Boundary Condition
Flexible	8	2.4	1930	30.5	Clamped
	16	2.4	7108	121.9	Clamped
	8	2.4	1873	44.5	Free
	16	2.4	5400	148.6	Free
Medium	8	2.4	1036	12.7	Clamped
	16	2.4	3728	35.6	Clamped
	48	13.3	26823	119.4	Clamped
	8	2.4	974	5.7	Free
	16	2.4	3728	49.5	Free
Stiff	16	2.4	3100	33.0	Clamped
	32	2.4	7268	71.1	Clamped
	48	13.3	23100	63.5	Clamped
	16	2.4	2922	52.7	Free
	32	2.4	9853	124.5	Free

Quasi-Static Indentation Testing Procedure

Once the impact testing was completed, the maximum impact force obtained for each of the different subgroups (listed in Table 2) was used as the independent variable for the quasi-static indentation testing. Figure 1 shows the test fixture used for all of the quasi-static indentation tests performed. The platen rested on top of the 5.08 cm thick aluminum uprights and could be removed without taking the fixture out of the test frame. The aluminum uprights were bolted to a 5.08 cm thick steel plate. The indentor was placed in the upper crosshead of the servo hydraulic load frame. In a limited number of tests, transverse deflection of the center point of the laminate, directly under the hemispherical tup, was measured using a linear voltage displacement transducer (LVDT). Figure 1 shows the location of the LVDT. The tests were run in stroke control at load rates of 0.02 and 0.42 mm/s.

Nondestructive Analysis

Once the impact and quasi-static testing were completed the specimens underwent three types of nondestructive analysis to document internal and external damage. These consisted of measuring dent depth on the impacted surface, crack lengths on the non-impacted surface and internal damage as determined from X-radiography.

After the specimens were impacted or subjected to quasi-static indentation testing, they were set aside for at least 24 hours so that the resulting dent would have time to relax to its equilibrium state. Any visible cracks on the non-impacted surface of the specimens were measured.

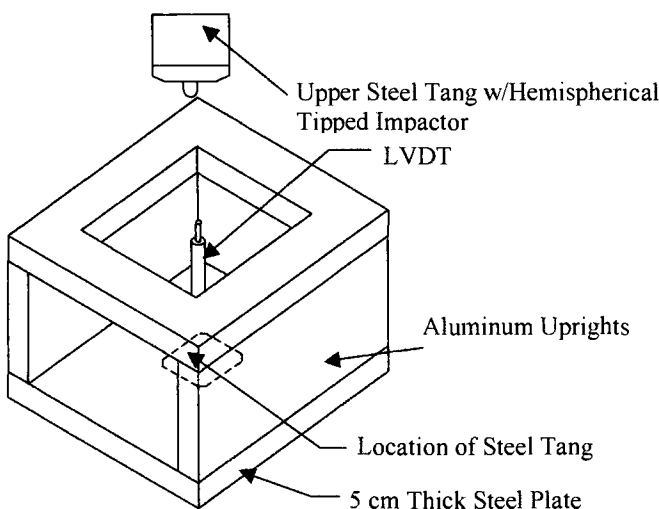


Figure 1 — *Test fixture for quasi-static indentation testing.*

After all dent depths and crack lengths were measured the specimens were then subjected to radiographic techniques to document the internal damage. The specimens were soaked on both sides with a zinc iodide penetrant solution for 24 hours and then X-rayed using a Faxitron™ X-ray machine. A piece of photographic film was placed directly under the specimen to capture the image of the internal planar damage in the form of a negative. From the negatives positives were made so that the planner damage area could be calculated. This was accomplished by superimposing a grid of 4 mm^2 squares over the picture and then counting squares that were within the damage area. Figure 2 illustrates the process used.

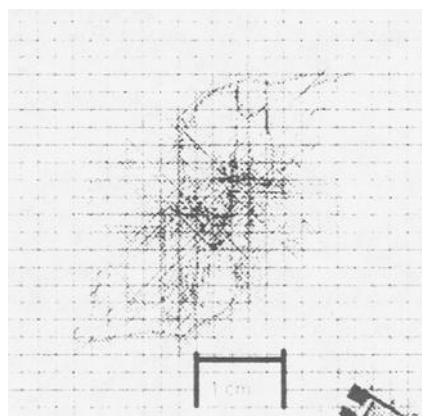


Figure 2 — *X-ray of impact specimen with 4 mm^2 grid superimposed.*

It should be noted that this is only a planar calculation and does not take into consideration the thickness of the specimen. The planar area of delamination was the most important variable used in this study and was the main factor in determining if an impact event can be represented by a quasi-static indentation test.

Results and Discussion

Introduction

Because the main purpose of the research being presented was to establish if quasi-static indentation testing was a true representation of a low velocity impact event, this section will address this issue by comparing the experimental results obtained. Table 2 lists the maximum transverse loads used for comparison between impact and quasi-static testing. Once the specimens were tested, comparisons were made on the following; dent depth, crack length, delamination area, and to a limited extent, load-deflection data.

Dent Depth

Plots of dent depth versus maximum transverse load demonstrate the vast amount of scatter that exists in the dent depth measurements, thus making trends difficult to identify. There appears to be no difference between the dent depth of an impacted specimen versus that of a quasi-statically loaded one. Two examples of these types of plots are shown in Figure 3. The clamped and free boundary conditions are shown together for comparison.

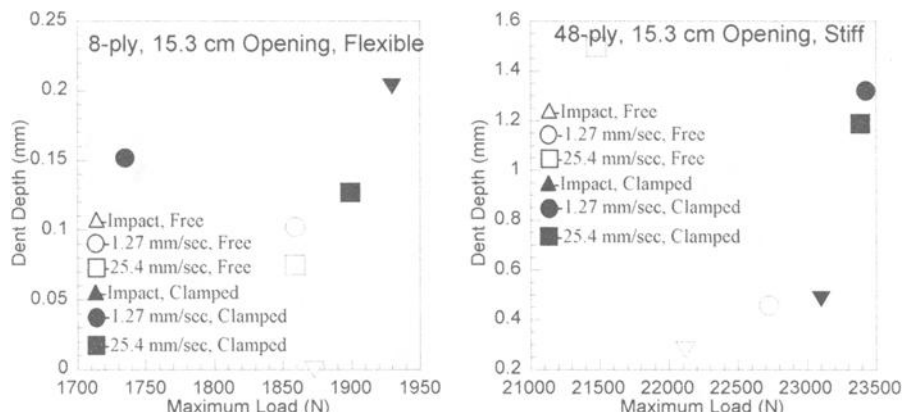


Figure 3 — Plots of dent depth versus maximum transverse load.

Crack Length

The length of the crack, or split, on the opposite side from the impact site also demonstrated a large amount of scatter. For the specimens that were impacted, the split length was longer than an equivalently load quasi-static specimen. Two examples of data are presented as they were for dent depth and are shown in Figure 4.

Delamination Area

Figures 5-12 present delamination area as a function of applied transverse load for both low-velocity impacts and quasi-static loads of two rates. Each figure contains data for both clamped and simply supported (free) specimens.

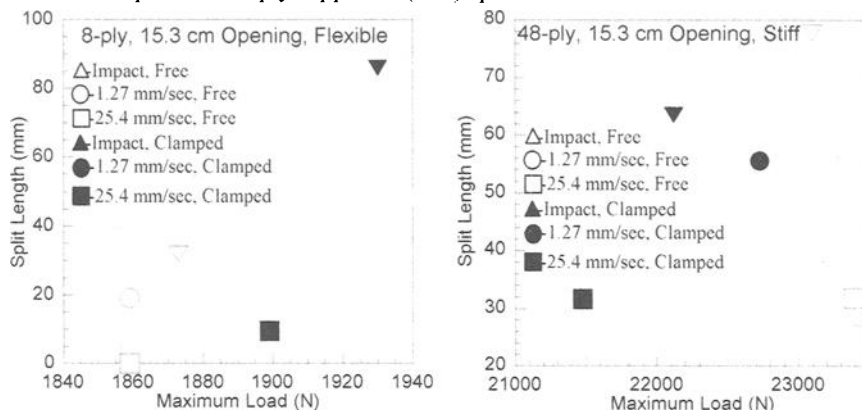


Figure 4 — Plots of split length versus maximum transverse load.

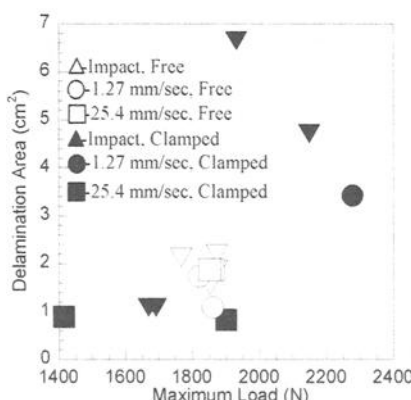


Figure 5 — Delamination area versus transverse load, 8-ply specimen over 152.4 mm opening, flexible.

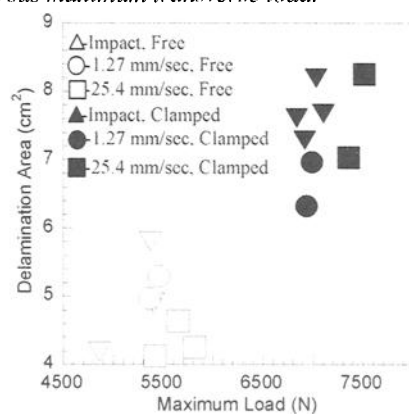


Figure 6 — Delamination area versus transverse load, 16-ply specimen over 304.8 mm opening, flexible.

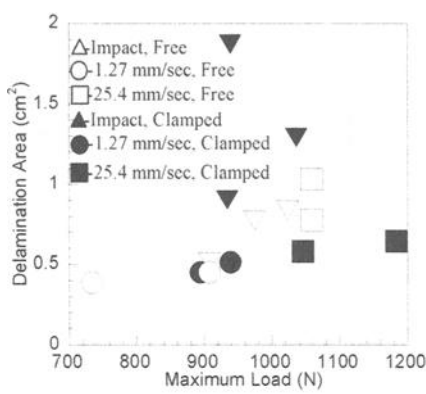


Figure 7—Delamination area versus transverse load, 8-ply specimen over 50.8 mm opening, medium.

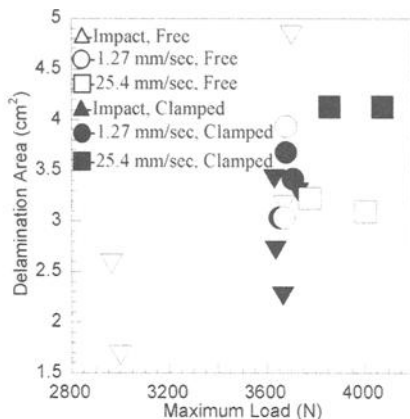


Figure 8—Delamination area versus transverse load, 16-ply specimen over 101.6 mm opening, medium.

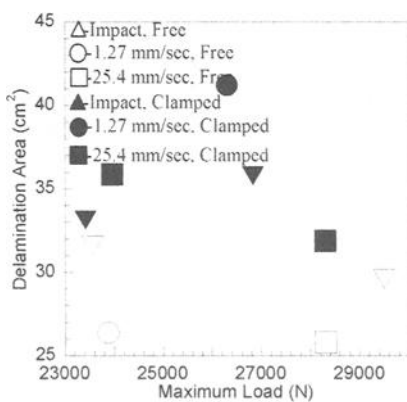


Figure 9—Delamination area versus transverse load, 48-ply specimen over 304.8 mm opening, medium.

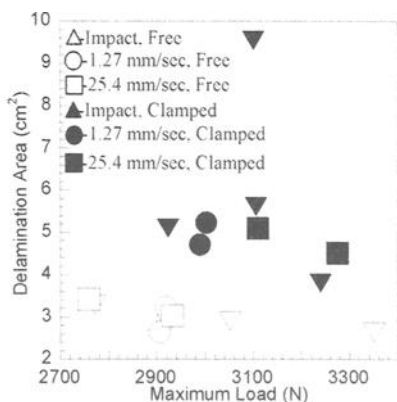


Figure 10—Delamination area versus transverse load, 16-ply specimen over 50.8 mm opening, stiff.

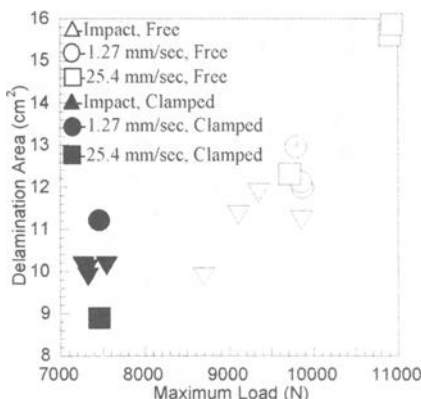


Figure 11—Delamination area versus transverse load, 32-ply specimen over 101.6 mm opening, stiff.

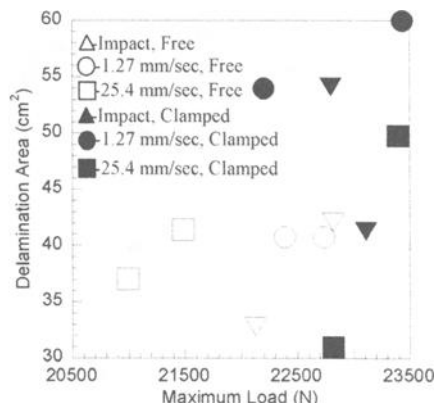


Figure 12—Delamination area versus transverse load, 48-ply specimen over 152.4 mm opening, stiff.

Figures 5 and 6 present data for the case of “flexible” laminates (support/thickness ratio of 150). Figures 7-9 present data for the case of “medium” laminates (support/thickness ratio of 50). Figures 10-12 present data for the case of “stiff” laminates (support/thickness ratio of 25).

For the “flexible” laminates there is no distinct difference between the impacted specimens and the ones tested quasi-statically at either rate. The effects of the boundary conditions show no difference for the 8 ply specimens supported over the 152.4 mm opening whereas a distinct difference is seen for the 16 ply specimens supported over the 304.8 cm opening. This difference is due to the clamped specimens being loaded to a higher level resulting in a larger delamination area.

The “medium” specimens have no distinct trends between boundary conditions or rate of loading. The impact test results fall in well with the static indentation tests in Figures 7, 8, and 9.

Figures 10, 11, and 12 represent the opposite extreme from the “flexible” specimens in that the contact damage dominates. Again there is no discernable difference between impact and static indentation results. In Figure 10, the simply supported specimens show slightly less damage for the same magnitude of maximum load than the clamped specimens, however this difference is slight.

Overall the low velocity impact tests can be represented by static indentation testing at rates of .02 and 0.42 mm/sec, regardless of specimen rigidity and boundary conditions. There is enough inherent scatter in both types of tests that all data fall within this scatter.

It must be kept in mind that these results are only valid for laminates of the $\pi/4$ type and laminates with different lay-ups or clumped plies may yield different results.

Load-Deflection Data

As another check of the validity of using static indentation tests to represent impact tests, a comparison of the load/deflection data can be made.

Figures 13-18 show static indentation load/deflection data superimposed over impact load/deflection data. A circle represents the static data, while the impact data are represented by a triangle. Static load/deflection data was not available for all of the static tests since a faulty LVDT was used, thus only the valid data are presented.

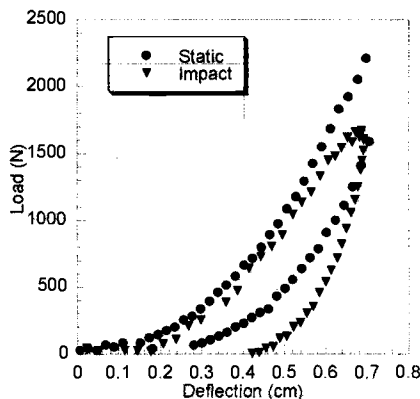


Figure 13 — Static and Impact Load-Deflection Data for 8-ply Specimen Over 152.4-mm Opening; Clamped.

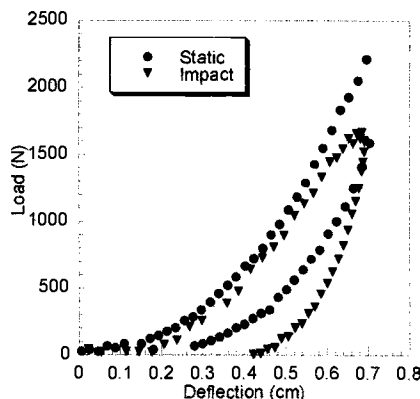


Figure 14 — Static and Impact Load-Deflection Data for 16-ply Specimen Over 101.6-mm Opening; Clamped.

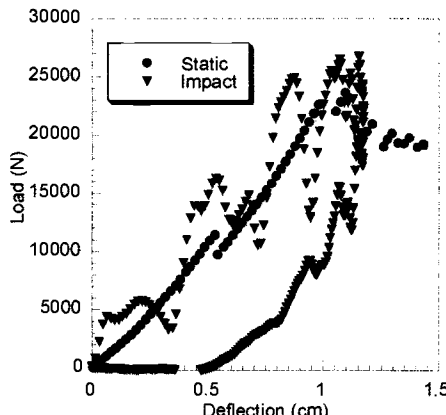


Figure 15 — Static and Impact Load-Deflection Data for 48-ply Specimen Over 304.8 mm Opening; Clamped.

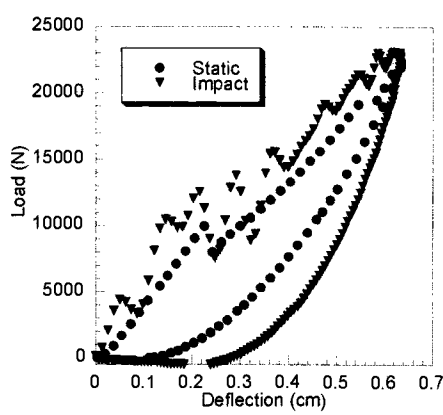


Figure 16 — Static and Impact Load-Deflection Data for 48-ply Specimen Over 152.4-mm Opening; Clamped.

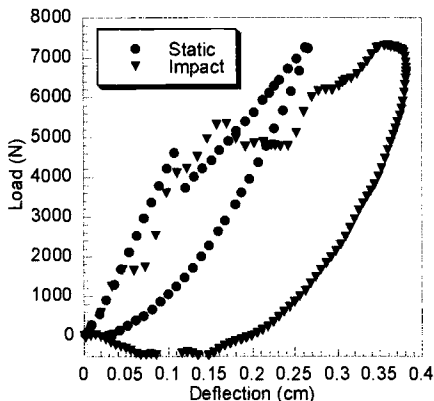


Figure 17—*Static and Impact Load-Deflection Data for 32-ply Specimen Over 101.6 mm Opening; Clamped.*

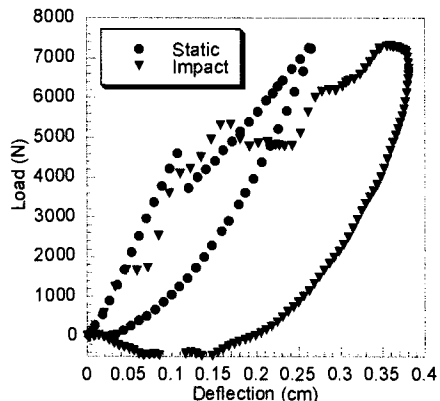


Figure 18—*Static and Impact Load-Deflection Data for 32-ply Specimen Over 101.6 mm Opening; Free.*

On the loading portion of the curves, the data agree well, except for the undulations in load seen on the specimens that experience a relatively high load. However, for the unloading portion of the curves the impact data usually indicate that more energy was lost during the event because there is a much larger hysteresis in the impact curves. However, from the delamination area data it was anticipated that the energy loss should be about the same. It has always been suspected that most of the energy lost in this type of impact testing is lost due to vibrations within the impact apparatus, not in damage to the specimen. When the falling crosshead and tup impact the composite plate, the head will tend to rebound at an angle that is not parallel to the guideposts. Thus a sideways force is exerted on the guideposts, which causes them to vibrate and interfere with the "natural" rebound of the impactor had the guideposts not been a factor.

Figures 14, 16 and 17 represent this erroneous "loss of energy" data quite well. Figure 13 is a flexible specimen and the loading portions of the curves agree well for both the static and impact cases. However, for unloading, the impact data shows a larger deflection than the static data for a given load on the rebound.

Figure 15 does not have unloading data for the static case, but the loading portions of the curves agree quite well. Figure 15 is unique in that during the static indentation test, the maximum load as determined from the impact tests could not be reached since the impactor began penetrating through the plate before this load was obtained. This is a result of selecting the onset of "easily" visible damage as the point at which the impact tests were carried out. For a relatively thick plate, the load at which a back surface split appears is not much below the load needed to begin penetration because so much volume of material needs to be damaged to cause the back surface split.

Conclusions

The following are the major conclusions of this study.

1. Static indentation tests *can* be used to represent low velocity impact events when the damage is compared by maximum transverse force. This is true of plates that experience flexural type damage, contact type damage, and a combination of the two. Lay-ups other than of the $\pi/4$ type may not yield these same results.
2. Much non-linear behavior is observed in the load-deflection curves for flexible laminates. As the laminate becomes stiffer, more linearity is seen and a distinct drop in load due to delamination becomes more pronounced.
3. Load-deflection plots of static indentation and low velocity impact are similar for the loading portion of the curve. The impact plots tend to show that more energy is lost.
4. Dent depth results produce a great deal of scatter, which makes any conclusions concerning this parameter difficult.
5. The only difference in damage between statically loaded and impacted specimens may be the split length that forms on the underside of the specimen, although this difference is small and does not seem to affect the delamination area.

References

- [1] Cantwell, W.J. and Morton, J., "Comparison of the Low and High Velocity Impact Response of CFRP," *Composites*, Vol. 20, No. 6, November 1989, pp. 545-551.
- [2] Wu, E. and Chang, L., "Loading Rate Effect on Woven Glass Laminated Plates by Penetration Force," *Journal of Composite Materials*, Vol. 32, No. 8, 1998, pp. 702-721.
- [3] Jackson, W.C. and Poe, C.C., "The Use of Impact Force as a Scale Parameter for the Impact Response of Composite Laminates," NASA Technical Memorandum 104189, January, 1992.
- [4] Bucinell, R.B., Nuismer, R.J., and Koury, J.L., "Response of Composite Plates to Quasi-Static Impact Events," *Composite Materials: Fatigue and Fracture (Third Volume)*, ASTM STP 1110, American Society for Testing and Materials, West Conshohocken, PA, 1991, pp. 528-549.
- [5] Swanson, S.R., "Limits of Quasi-Static Solutions in Impact of Composite Structures," *Composites Engineering*, Vol. 2, No. 4, pp. 261-267.
- [6] Kwon, Y.S. and Sankar, B.V., "Indentation-Flexure and Low-Velocity Impact Damage in Graphite Epoxy Laminates," *Journal of Composites Technology and Research*, Vol. 15, No. 2, Summer 1993, pp. 101-111.
- [7] Lagace, P.A., Williamson, J.E., Wilson Tsang, P.H., Wolf, E., and Thomas, S., "A Preliminary Proposition for a Test Method to Measure (Impact) Damage Resistance," *Journal of reinforced Plastics and Composites*, Vol. 12, May 1993, pp. 584-601.

- [8] Kaczmarek, H. and Maison, S., "Comparative Ultrasonic Analysis of Damage in CFRP Under Static Indentation and Low-Velocity Impact," *Composites Science and Technology*, Vol. 51, 1994, pp. 11-26.
- [9] Wardle, B.L. and Lagace, P.A., "On the Use of Dent Depth as an Impact Damage Metric for Thin Composite Structures," *Journal of Reinforced Plastics and Composites*, Vol. 16, No. 12, 1997, pp. 1093-1110.
- [10] Nettles, A.T., Douglas, M.J., and Estes, E.E., "Scaling Effects in Carbon/Epoxy Laminates Under Transverse Quasi-Static Loading," NASA Technical Memorandum 209103, March 1999.
- [11] Cheresh, M.C. and McMichael, S., "Instrumented Impact Test Data Interpretation," *Instrumented Impact Testing of Plastics and Composite Materials, ASTM STP 936*, American Society for Testing and Materials, West Conshohocken, PA, 1987, pp. 9-23.
- [12] Found, M.S., Howard, I.C., and Paran, A.P., "Interpretation of Signals from Dropweight Impact Tests," *Composite Structures*, Vol. 42, 1998, pp. 353-363.
- [13] Lee, S.M. and Zahuta, P., "Instrumented Impact and Static Indentation of Composites," *Journal of Composite Materials*, Vol. 25, Feb. 1991, pp. 204-222.
- [14] Sjoblom, P.O., Hartness, T.J., and Cordell, T.M., "On Low-Velocity Impact Testing of Composite Materials," *Journal of Composite Materials*, Vol. 22, Jan. 1988, pp. 30-52.
- [15] Elber, W., "Failure Mechanics in Low-Velocity Impacts on Thin Composite Plates," NASA Technical Paper 2152, 1983.
- [16] Highsmith, A.L., "A Study of the Use of Contact Loading to Simulate Low Velocity Impact," NASA Contractor Report 97-206121, Jan. 1997.
- [17] Abrate, S., "Impact on Laminated Composites: Recent Advances," *Applied Mechanics Review*, Vol. 47, No. 11, 1994, pp. 517-544.

James L. Walker,¹ Samuel S. Russell,¹ and Matthew D. Lansing²

Detection and Characterization of Imperfections in Composite Pressure Vessels

Reference: Walker, J. L., Russell, S. S., and Lansing, M. D., "Detection and Characterization of Imperfections in Composite Pressure Vessels," *Composite Materials: Testing, Design, and Acceptance Criteria, ASTM STP 1416*, A. Zureick and A. T. Nettles, Eds., American Society for Testing and Materials International, West Conshohocken, PA, 2002.

Abstract: Interpreting the information given in a thermogram can be a difficult task under ideal circumstances and extremely challenging in a real world setting. The work discussed in this paper illustrates how the microstructure of several commonly found defects in composite structures relate to their thermographic image counterpart. Two test cases are studied herein, including a large graphite/epoxy RP-1 fuel tank and a graphite composite cryogenic fuel feedline. The structures used in this study were designed to serve as manufacturing proof of concept specimens and to undergo hydroburst testing to verify manufacturing practices and structural design. Prior to hydrostatic testing the structures underwent 100% thermographic evaluation to ensure that no manufacturing or handling damage was present. Due to a large inclusion found in the feedline, it was pulled from service and dissected without performing the hydroproof. The thermographic indications found in the RP-1 tank were below critical limits so it underwent a complete hydroproof loading series and finally a hydroburst. Following the hydroburst samples were cut from the tank in regions where thermography had located damage before the test. These regions were re-evaluated thermographically and then were cross-sectioned and photomicrographed.

Keywords: thermography, composite materials, microstructure

Introduction

The thermographic evaluation of composite structures for delaminations, disbonds, inclusions, porosity, and microcracking has proven to be a valuable asset in the field of nondestructive testing. Coupling large area coverage, variable sensitivity, and minimal surface contact with a photographic type image representation of structural anomalies thermography has become a primary inspection method for composite structures. Thermography works well for locating both surface and subsurface defects in most composite systems ranging in thickness of up to 0.25 inch (0.64 cm) or more.

¹ Materials Engineers, Nondestructive Evaluation Team ED32, and ² Materials & Structures Engineer, Nonmetallic Materials Group ED34, respectively, Marshall Space Flight Center, Alabama 35812.

The thermographic method for inspection of composite structures typically involves applying an external source of heat to the structure, either from the camera side or back surface, and then recording the changes in the surface temperature. The heat source may be a hot air gun, flash lamp, standard "shop type" high intensity quartz lamps, or any other source that provides a uniform initial surface heating to the structure. The structure then responds to this heating and variations in the material property manifest themselves as changes in the surface heat profile of the structure. If these temperature variations are large enough and a camera with sufficient sensitivity is used, then the material or structural abnormality can be detected and referred back to its source. The problem though is determining just what created the thermal indication. Variables, including depth, thermal conductivity, orientation, and size of the abnormality can all have a great influence on how its heat pattern will be seen by the imager.

In this paper the problem with interpreting thermographic images "thermograms" will be addressed by conducting several destructive tests. Samples will be cut from real defects in real structures, then polished and photographed under low power magnification to determine the true nature of the defect. Two structures will be investigated for this study including a full scale thin walled composite tank, designed and fabricated for the storage of pressurized RP-1 rocket fuel, and a prototype rocket motor cryogenic fuel feed line designed to transport liquid hydrogen.

Numerous anomalies were detected and mapped in both structures prior to proof testing, some along bond lines and some scattered throughout the acreage. After testing was completed coupons were cut from the regions including thermographic anomalies, and these coupons were again inspected thermographically to document the growth of any indications due to proof testing. The sections were then dissected and micrographed so that the relationships between the thermograms and the physical nature could be determined.

RP-1 Fuel Tank

The RP-1 fuel tank evaluated in this study was manufactured in three primary sections (forward and aft cylinder/dome, and skirt) by hand placing sheets of woven graphite/epoxy prepreg over an aluminum mold, vacuum bagging, then curing in an autoclave. The finished tank measured nearly 13.8 ft (4.2 m) long with a 6.1 ft (1.9 m) diameter. The forward and aft sections were joined by way of a stepped "bellyband" overwrap applied to the inner and outer surface of the tank. The skirt was attached to the transition of the cylinder and dome on the aft tank half by a stepped overwrap applied just to the outer surface of the tank.

The primary sections were inspected thermographically prior to being combined to form the final tank as well as after final assembly. Each inspection utilized a highly sensitivity infrared camera and flash heat source applied to the outer "viewed side" of the tank. In this manner variations in the quality of the tank would be manifested as a thermal abnormality in the resulting thermograms. The thermographic system consisted of an Amber Radiance 1t thermal camera run under Thermal Wave Imaging (TWI) software. Heat was supplied by a TWI flash hood, which uses a bright flash of light generated by two Xenon flash tubes to impart approximately 6.4 kJ of energy to the tank surface. To produce each thermogram 10 frames were averaged. Each frame was

acquired at a frame rate of 60 Hz over an 11 second period. The field of view was kept at 11 inch (28 cm) square, the face area of the flash hood. The image map shown in Figure 1a illustrates the number of individual shots (zones) that were required to inspect the acreage of the tank. The domes were inspected in a similar manner, with the aft dome being inspected from inside the tank, accessed through the manhole in the forward dome. The inner band of the belly overwrap was also inspected from the inside of the tank.

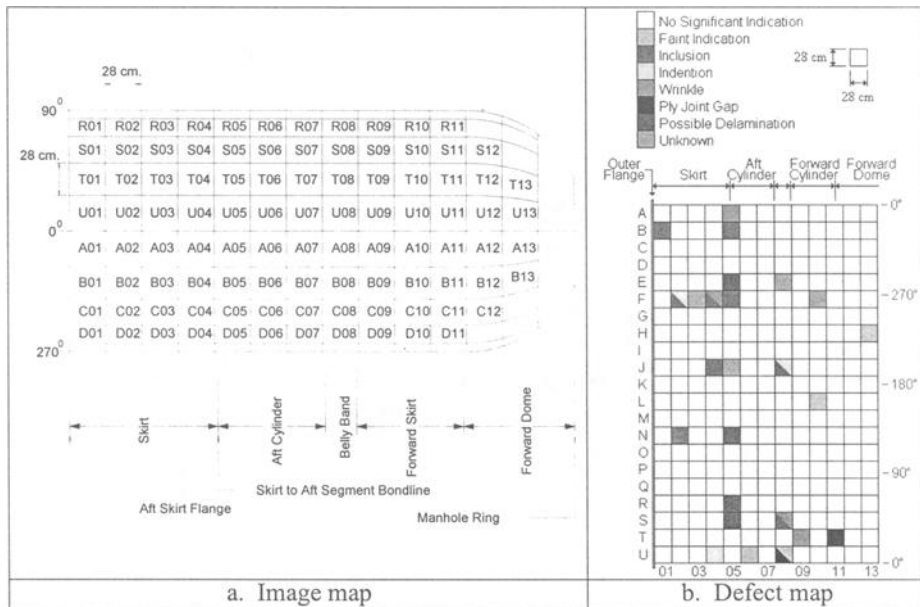


Figure 1 - RP-1 tank image/defect maps.

The defect map shown in Figure 1b indicates how the thermal indications were distributed around the tank. Without standards to work from it was impossible to identify the unique nature of each indication. Based upon the thermal duration, magnitude and sharpness of each indication the character of indication mechanism was estimated. Since, none of the defects were found to be above acceptable limits for the test, it was decided to complete the hydroproof test series without attempting any repair. Ultimately the tank performed as, or better, than planned with the noted thermal indications having little bearing on the final burst pressure.

Sections of the failed tank where the original thermal indications had been located were removed and re-inspected. Little or no growth was detected for these indications. After carefully marking the boundaries of each indication, sections were cut, mounted in acrylic holders, and polished with successively finer emery cloth down to 1200 grit. The sections were then viewed under a low power microscope and photographed with a CCD camera. Except for the inclusion defects it was difficult if not impossible to detect any variations in the cross-sections between good and damaged material. To enhance fine details in the cross-sections a fluorescent die penetrant was applied to the sample. After soaking for two minutes, excess die was flushed from the surface and the samples were

dried. Due to the highly porous nature of the composite material an abnormal amount of bleedout was present. The excess die was wiped from the sample with a soft lint free cloth, leaving just the die that was trapped inside the cracks of the sample.

The first defect, shown in Figure 2, is that of a piece of sand that was trapped under the outermost ply of the tank at location B5. The indication was very pronounced on the thermogram yielding a 0.25 inch (0.64 cm) diameter hot spot. This hot spot indicated that a void was present due to the inability of the material to transmit the flash heat into the thickness as fast as the surrounding material. The micrograph taken from a slice though the edge of the thermal indication clearly shows the sand particle, which measures 0.06 inch (0.15 cm).

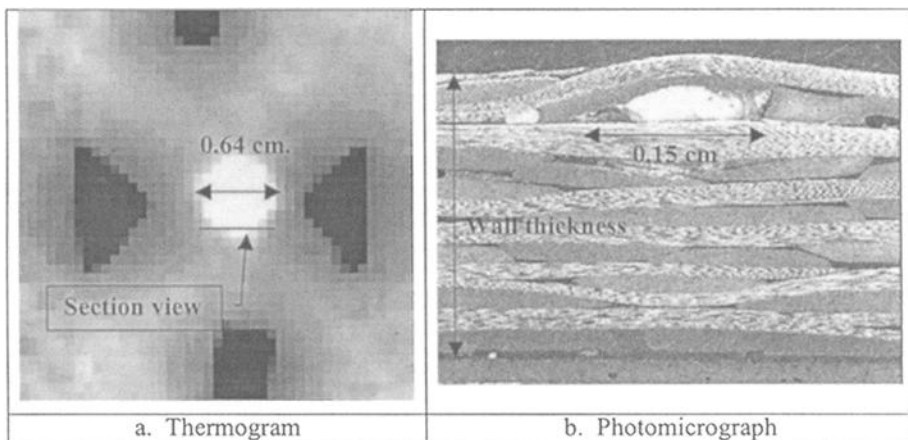


Figure 2 - *Inclusion at Zone B5.*

The second indication shown (A5) is that of a delamination at the build-up region of the skirt overwrap. On the tank surface a slight ridge could be seen and thermally a portion of that ridge remained hotter than the surrounding material after the flash was initiated. The thermal indication appeared sharp and well defined, showing up immediately after the flash (Figure 3a). The micrograph shown in Figure 3b clearly shows a delamination at two levels, both near the surface. The surface-breaking feature appears to be resin pocket that is poorly bonded to the surrounding fibers and is linked to a second delamination, between the outermost and second ply. The dimensions of the two closely approximate the size of the thermal indication.

Another type of indication found on the tank occurred at positions E5, N5, R5 and S5 appearing to be a site of impact related damage. The indication in the thermal image sequence appeared to spread slightly with time and last for almost the entire capture duration. The questionable feature of the indication was the dark band that passed circumferentially through its middle. A ridge found on the inside of the tank directly below these indications was thought to be the culprit by possibly causing localized bending during a post cure process which initiated the delamination. The photomicrograph, as shown in Figure 4, support these findings in that a series of delaminations can be seen to exist though the thickness of the sample on either side of the inner surface ridge.

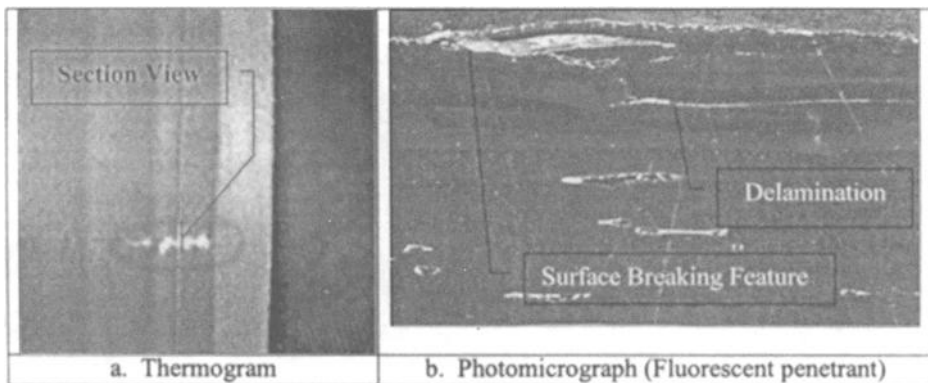


Figure 3 - Wrinkle at Zone A5.

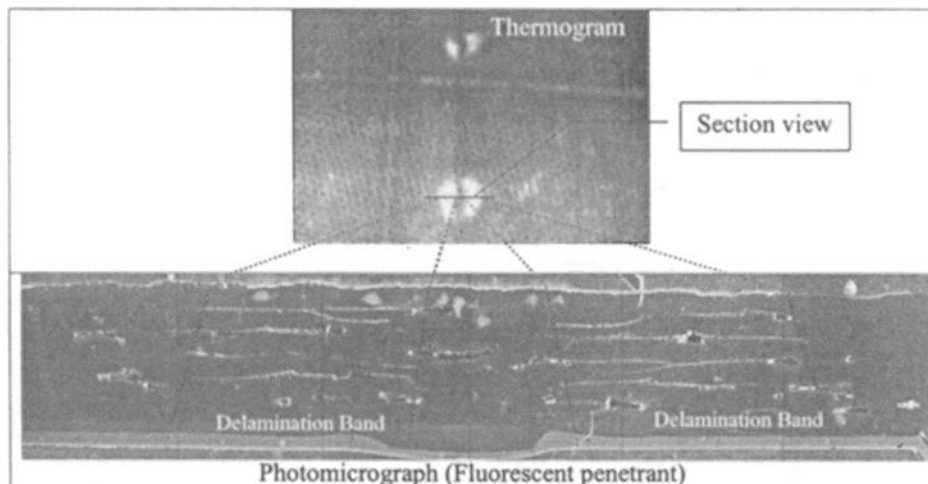


Figure 4 - Delaminations at Zone S5.

Cryogenic Feedline

A graphite composite feedline intended for cryogenic, liquid hydrogen, service was thermographically evaluated for manufacturing or handling defects just before it was to undergo extensive structural testing. The 8 inch (20.3 cm) diameter feedline was thermographically inspected with a combination of front surface flash heating (Figure 5a) and rear surface lamp heating (Figure 5b) using a highly sensitivity infrared camera. The long duration lamp heating was required to get full thickness coverage of the thick flanges and build up regions on each end of the tube. The same infrared imager and flash heating unit were used on the feedline as used on the tank. A TWI flash hood capable of generating approximately 6.4 kJ of energy supplied the flash heat. However, long duration heating was supplied by a 1000W IR lamp. Frame averaging produced each

thermogram as previously discussed. The field of view was kept at 11 inches (28 cm) square, the face area of the flash hood by placing 0.25 inch (0.64 cm) square foil squares in a grid pattern as shown in Figure 6.

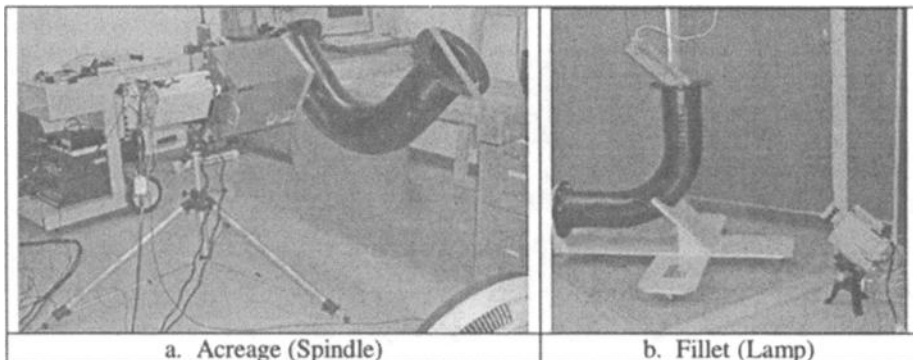


Figure 5 - Feedline thermographic inspections.

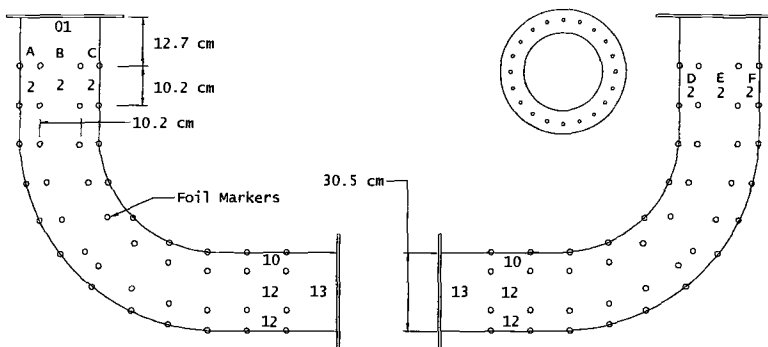


Figure 6 - Feedline image map.

During the thermographic scan of the feedline a large indication (Figure 7) was found which caused it to be pulled from the test pool of tubes. The large thermal indication spanned a length of nearly 9 inches (22.9 cm). Due to its sharply defined edges, uniformity and quick arrival time the indication was classified as a piece of tape or paper below the first or second ply. Foil markers were used to help define the location of the indication on the tube and a sketch of the boundaries of the indication made on the tube. Based upon these sketches precision sectioning with a diamond band saw blade was made exposing cross-sections as shown in Figure 8.

View number one was taken of the cross-section at the "thinner" end of the indication. The edge was polished with 800 grit silica carbide paper. The indication can be seen to be a piece of plastic tape that was left on the top of the third ply as the fourth and final ply was being applied. View number two was taken at the other end of the indication at a point where the indication began. In this view the edge of the tape is clearly visible.

A second indication (Figure 9) was found in the same feedline, which had similar features except that the edges were not as clearly defined and the time of maximum thermal signal occurred later in the image sequence. Upon dissection this indication was also found to be caused by a piece of plastic tape. At this indication the tape is between the first and the second plies.

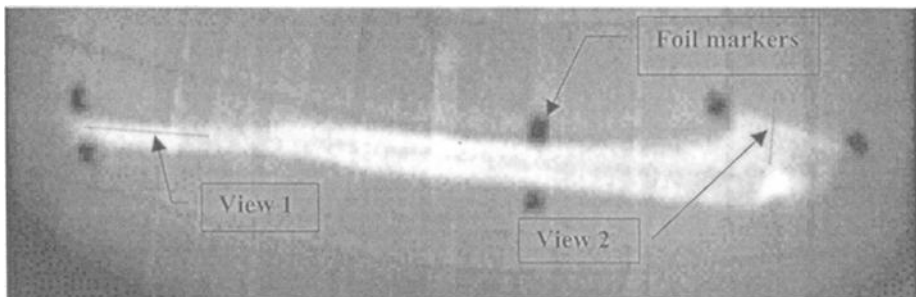


Figure 7 - Thermographic indication of inclusion.

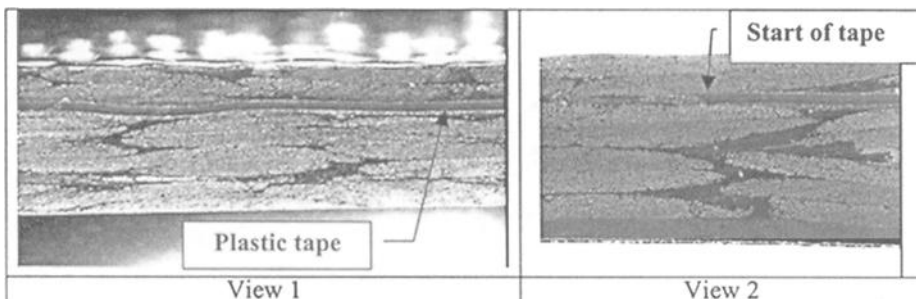


Figure 8 - Photomicrographs of Teflon tape inclusions.

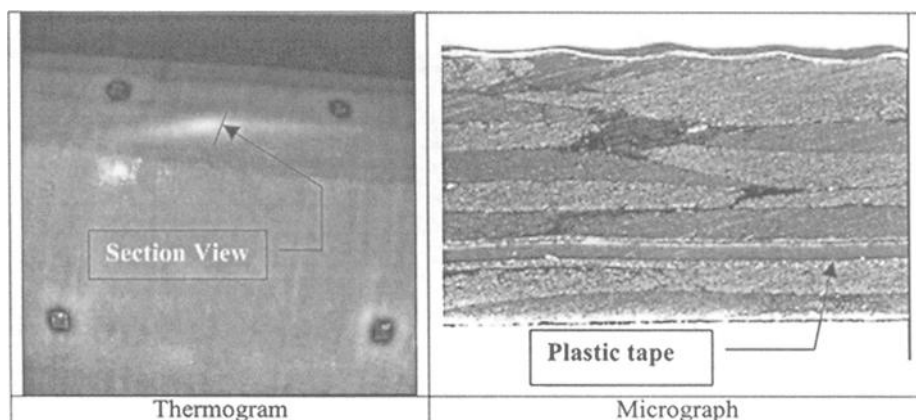


Figure 9 - Deeply embedded plastic tape inclusions.

The third set of indications found on the feedline bore no resemblance to the inserts found elsewhere in the tube. The indications were dark "colder" than the surrounding material and their boundaries were not clearly definable. Based upon these thermal findings it was suspected that these indications were resin rich zones. A set of examples of two of these indications is given in Figure 10. The cross-sections of these regions showed that large resin pockets were present. The left most indication appears to have been caused by a small piece of plastic being left between the spliced materials.

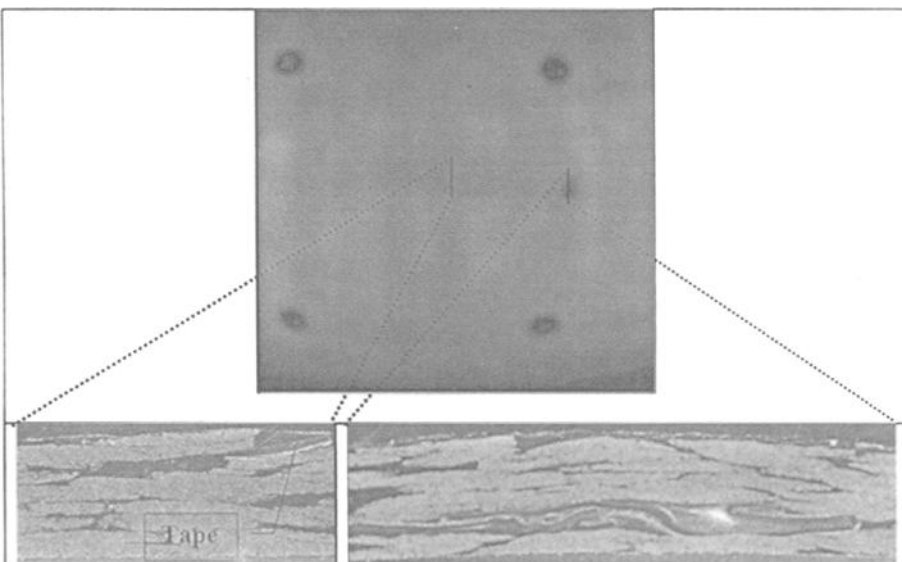


Figure 10 - Defect at position A4.

Conclusions

Identification and characterization of manufacturing and service-related defects/damage by thermographic methods pose two entirely different challenges to nondestructive testing personnel. While much research has been placed on developing alternative ways for performing thermographic inspections to locate and identify abnormalities, it is the interpretation of such findings that ultimately determine the usefulness of such testing. The work discussed in this paper has shown how the microstructure of several commonly found defects in composite structures relate to their thermographic image counterpart. By analyzing two test cases, a large graphite/epoxy RP-1 fuel tank and a graphite composite cryogenic fuel feedline, defects that can impact the performance of a structure were compared. The results clearly show the challenges a thermographer faces when trying to evaluate defects, determining the type, size, and location of irregularities in a material.

R. Prabhakaran,¹ M. Saha,² M. Douglas,³ and A. T. Nettles⁴

Damage Resistance and Damage Tolerance of Pultruded Composite Sheet Materials

Reference: Prabhakaran, R., Saha, M., Douglas, M., and Nettles, A. T., "Damage Resistance and Damage Tolerance of Pultruded Composite Sheet Materials," *Composite Materials: Testing, Design, and Acceptance Criteria, ASTM STP 1416*, A. Zureick and A. T. Nettles, Eds., American Society for Testing and Materials International, West Conshohocken, PA, 2002.

Abstract: The damage resistance of pultruded composites to quasi-static transverse indentation is characterized, and the damage tolerance of transversely indented composites under subsequent compression is assessed. Two specimen thicknesses are investigated. In each case four specimens are transversely indented to failure. Five load levels are selected and sets of five specimens are loaded up to each of these load levels and then unloaded. Extensive data are gathered: load-central displacement, back surface crack length, damage area obtained from X-radiography, optical photomicrographs obtained for specimens sectioned in different orientations, etc. This information is analyzed to develop the damage initiation and progression in pultruded composites. Open hole compression tests are performed on specimens of the two thicknesses, with seven hole sizes. The specimens damaged at five load levels, during transverse indentation, are tested in compression (simulating compression after impact). From the measured compressive strengths, the concept of an 'equivalent hole diameter' for damaged specimens is explored. The strain distributions are also compared.

Keywords: pultruded composites, transverse indentation, damage resistance, damage tolerance, compression, equivalent hole diameter

Damage resistance of composites is usually studied under either low velocity impact loading or static (quasi-static) transverse indentation loading. The former is more difficult and expensive to perform. Damage tolerance of composites is usually assessed by testing composite specimens, with prior damage, in tension or compression. Compression after impact (CAI) is a common method of assessing damage tolerance. An overwhelming majority of damage resistance and damage tolerance studies have been conducted with aerospace composites, such as carbon-polymer (thermoset or thermoplastic) composites.

¹ Eminent Professor, Department of Mechanical Engineering, Old Dominion University, Norfolk, VA, 23529.

² Assistant Professor, Department of Mechanical Engineering, Tuskegee University, Tuskegee, AL, 36088.

³ Senior Engineer, International Construction Equipment, Matthews, NC, 28104.

⁴ Senior Research Engineer, Marshall Space Flight Center, AL, 35812.

The present investigation deals with damage resistance of pultruded composites under quasi-static indentation and subsequent damage tolerance under compression.

Instrumented impact and static indentation tests of graphite-epoxy composites, with comparisons based on damage width rather than damage area, have been reported [1] to show large scatter due to vibrations in the drop-weight crosshead, absorbing significant energy. The influence of indentor size and laminate stacking sequence on the response of graphite-epoxy composites to contact loads and low velocity impact was investigated [2]. Some investigations [3-5] have shown that there is a correlation between quasi-static indentation and drop-weight impact testing, while some others [6, 7] have concluded that quasi-static indentation tests can not be used to simulate impact tests. More recently, it has been reported [8], on the basis of extensive experimentation with a carbon fiber reinforced epoxy composite, that static indentation can be used to represent a low-velocity impact event. The impact research on laminated composites has been reviewed [9].

Considerable work has been done in the area of compressive strength of composite plates containing cutouts or prior impact damage. The use of hole strength data to predict impact damage strength has been questioned [10]. The compressive failure mechanisms of 45° ply dominated carbon epoxy laminates with circular holes or impact damage have been investigated [11]. Very limited information is available regarding impact damage, transverse indentation, or compressive strength degradation due to cutouts/damage in pultruded composites. The low-velocity impact response of a complex geometry pultruded glass fiber reinforced polyester matrix composite box section has been studied [12].

Test Material

The material tested in this investigation was an E-glass fiber reinforced polyester pultruded composite. The composite consisted of layers of unidirectional roving fibers in the pultrusion direction sandwiched between layers of continuous strand mats (CSM). The pultruded composite is available in different thicknesses and in different shapes. In this investigation, pultruded sheets of 6.3 mm and 12.7 mm thicknesses were used to prepare all the specimens. The lay-up configuration and percentage of glass were slightly different for the two thicknesses. The 6.3 mm thick sheet had two roving fiber layers sandwiched between five CSM layers, while the 12.7 mm thick sheet had four roving layers sandwiched between nine CSM layers. Both sheets had approximately 60% by volume of glass; the 6.3 mm thick sheet had 58% of the glass in the form of CSM, while 64% of the glass in the 12.7 mm thick sheet was in the form of CSM. It may also be mentioned here that the outer layers of all the pultruded sheets were made of CSM.

Quasi-Static Transverse Indentation Test

This section describes the damage resistance part of the investigation. All the specimens were tested in the simply supported boundary condition in a test fixture that is commonly used for indentation tests [8].

Specimen Configuration

Plate specimens of 6.3 mm and 12.7 mm thicknesses were tested under transverse indentation. Specimens with a length of 152 mm and width of 102 mm were prepared from the 6.3 mm thick pultruded sheet and specimens with a length of 254 mm and width 178 mm were machined from the 12.7 mm thick pultruded sheet. A total of 30 specimens were prepared for each thickness.

Testing Procedure

The quasi-static indentation tests were performed on an 89 kN servo-hydraulic Tinius-Olsen testing machine. A square aluminum platen, 51 mm thick, with an outside dimension of 406 mm, was located on top of a 51 mm thick steel base plate. The composite specimens were placed on the aluminum platen, with a square cut-out, for the simply supported boundary condition on all four edges. The specimens with 6.3 mm thickness were loaded by a 19 mm diameter spherical steel indentor on a supporting platen with a 51 mm square cut-out. The specimens with 12.7 mm thickness were loaded by a 38 mm diameter spherical steel indentor on a supporting platen with a 102 mm square cut-out. Two direct current differential transformers (DCDTs) were used to measure the indentor movement and the central plate displacement directly under the indentor. The tests were conducted in a stroke control mode at a rate of 1.27 mm per minute. The load and the displacements were recorded using a data acquisition system.

Damage Evaluation

Four types of measurement were performed on each specimen after the quasi-static indentation test. These were: measurement of the permanent (or residual) dent depth, measurement of the back surface crack length, X-radiography photographs, and photomicrographs of sectioned surfaces. Dent depth measurements were made 24 hours after the indentation test, with a DCDT. The DCDT was traversed along the length and width directions across the dent and the data (maximum depth) were averaged. A digital caliper was used to measure the visible crack length on the back surface.

The X-radiography technique provides a through-thickness integrated view of delamination and matrix cracking. The specimens were soaked on both sides with a zinc iodide penetrant solution for 24 hours and were then X-rayed using a Faxitron™ X-ray machine. A piece of photographic film was placed directly under the specimen to capture the image of the internal damage in the form of a negative. Some specimens did not show any damage, especially at low force levels; in such cases, a small hole of 0.8 mm diameter was drilled near the damage area, the dye-penetrant was injected through a syringe into the hole, and the specimen was X-rayed again. Prints from the negatives were viewed against a transparent grid with small squares and the damaged area was measured.

In the fourth damage evaluation method, quasi-statically loaded specimens were sectioned along the longitudinal and transverse directions and the sectioned specimens were examined under a stereo microscope with a camera attachment.

Repeatability Tests

As the study involved evaluation of damage in specimens transversely indented to different percentages of the failure load and the comparison of compressive behavior of specimens with different damage levels with specimens having circular holes, tests were conducted to establish the repeatability in pultruded composites. Four identical specimens of each thickness were tested under quasi-static indentation. Each specimen was loaded up to the maximum indentation force and was unloaded once the indentation force started dropping. The indentation force-central displacement curves for the 6.3 mm thick specimens and the 12.7 mm thick specimens are shown in Figures 1, and 2, respectively.

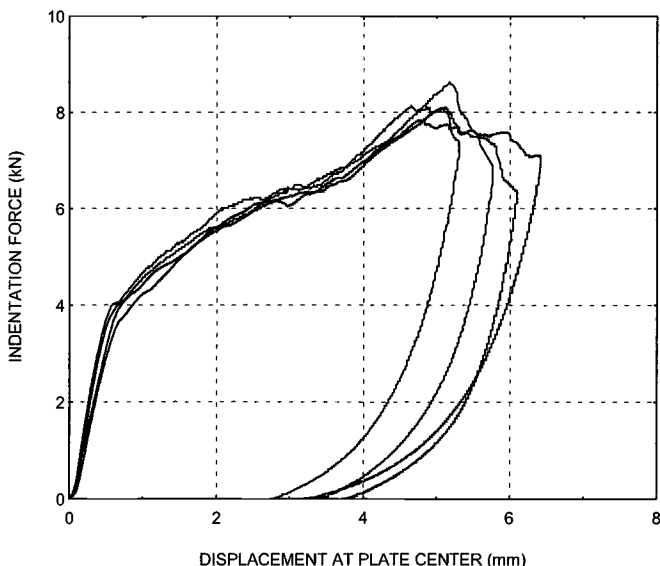


Figure 1 – *Indentation force as a function of the plate center displacement for the repeatability test (6.3 mm thick).*

These figures show that the indentation force-displacement curves are very close to each other for each thickness. The repeatability tests were also performed in terms of damage parameters, such as maximum deflection, back-surface crack length, energy absorption, and damage area. These results are summarized in Table 1 for the 6.3 mm thick specimens and in Table 2 for the 12.7 mm thick specimens. These tables show that considering the inherent material variability in civil engineering infrastructure pultruded composites, the repeatability is good.

Tests for Damage Characterization and Tolerance

After the repeatability tests, damage resistance of the pultruded composite was investigated. Damage was introduced at various transverse indentation force levels, selected from the force-displacement curves up to failure. The selected load levels are

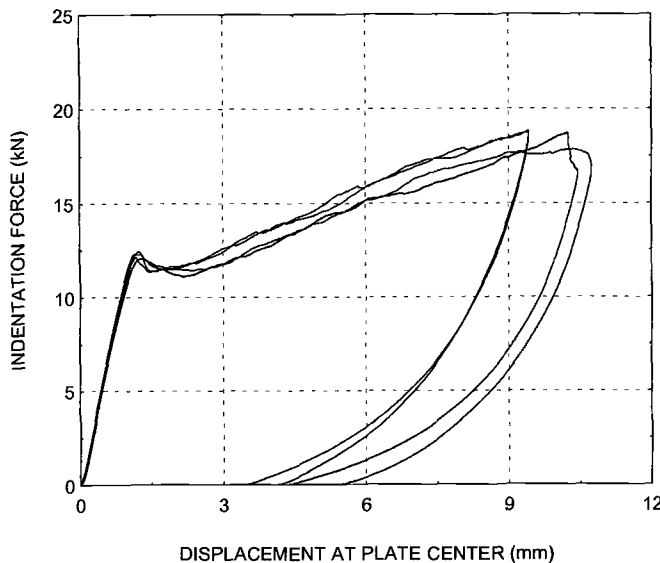


Figure 2 – *Indentation force as a function of the plate center displacement for the repeatability test (12.7 mm thick).*

Table 1 – *Summary of repeatability test results for the 6.3 mm thick specimens.*

Specimen Number	Max. Deflection (mm)	Max. Indentation force (kN)	Damage area (cm ²)	Back surface crack length (mm)	Energy absorbed (N-m)
1	5.8	6.9	17.0	51.3	30.5
2	5.3	7.3	17.6	43.2	26.0
3	6.1	6.3	15.3	47.2	32.1
4	6.5	7.1	16.6	50.5	32.2

shown in Figure 3 for the 6.3 mm thick composite and in Figure 4 for the 12.7 mm thick composite. At each load level, five identical specimens were loaded and unloaded. The surface damage was measured for all the five specimens. Two specimens at each load level were sectioned along the longitudinal and transverse directions following the X-radiography examination. The rest of the specimens were reserved for the compression tests to characterize the damage tolerance.

Table 2 – Summary of repeatability test results for the 12.7 mm thick specimens.

Specimen Number	Max. Deflection (mm)	Max. Indentation force (kN)	Damage area (cm ²)	Back surface crack length (mm)	Energy absorbed (N-m)
1	10.7	17.9	65.4	96.5	123.1
2	10.4	18.7	68.3	73.7	115.2
3	9.4	18.9	-	81.3	99.6
4	9.4	18.6	-	97.3	101.4

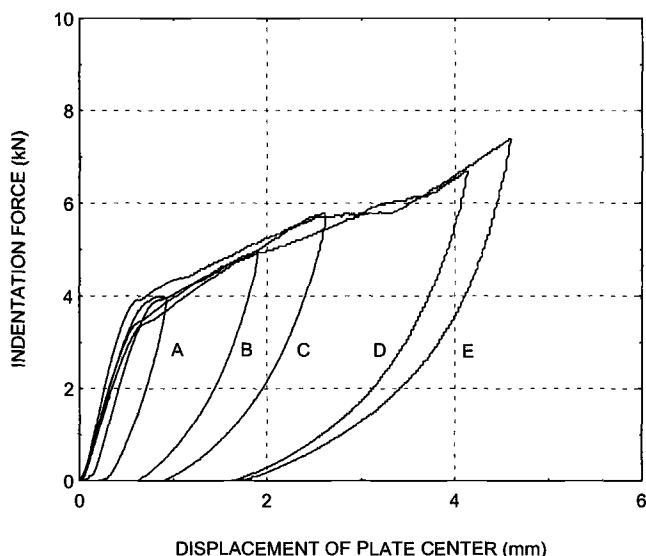


Figure 3 – Indentation force as a function of plate center displacement of various unloading states for 6.3 mm thick specimen.

The back-surface crack was mostly in the form of an s-shaped crack, as shown in Figure 5 for a 12.7 mm thick specimen. A typical X-radiograph showing the internal damage in a 12.7 mm thick specimen is shown in Figure 6.

Compression Tests

This section describes the damage tolerance part of the investigation. Specimens with circular holes of different diameters were tested under compression in a compression fixture [13]. Specimens subjected to transverse indentation at different load levels were

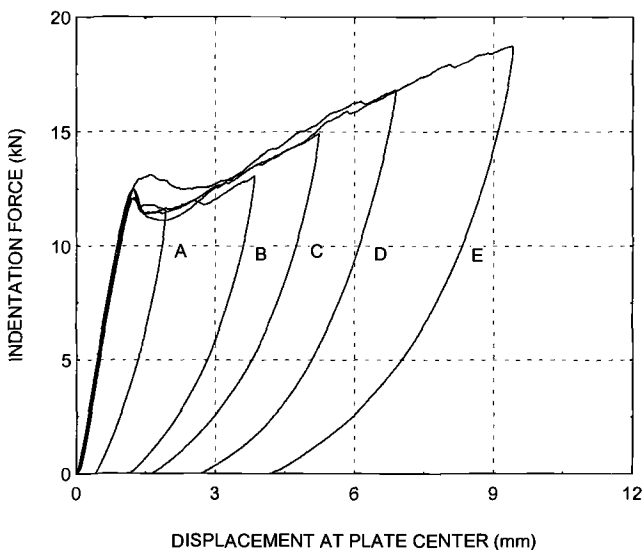


Figure 4 – *Indentation force as a function of plate center displacement of various stages for a 12.7 mm thick specimen.*

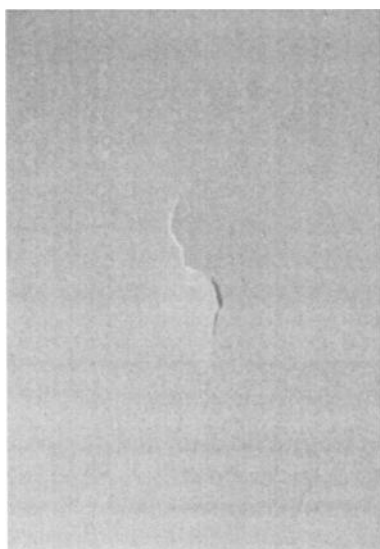


Figure 5 – *Photograph showing back surface crack at static indentation load of 16.8 kN (12.7 mm thick).*

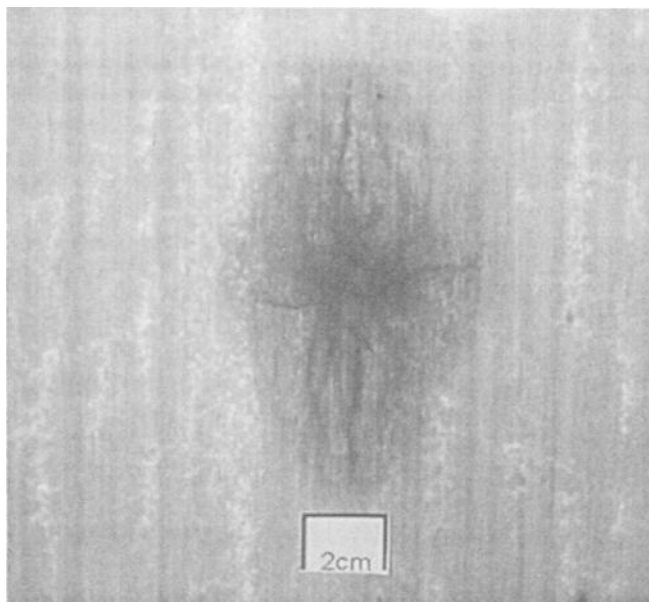


Figure 6 – Typical X-radiograph showing the internal damage due to quasi-static indentation loading up to failure (12.7 mm thick).

also tested under compression. These results were compared to establish the concept of an ‘equivalent hole diameter’ for damaged specimens.

Specimen Configuration

The dimensions for the compression specimens, of both the thicknesses, were chosen so that a strength failure would more likely occur than a buckling mode failure. Specimens of 152 mm length and 102 mm width were prepared from the 6.3 mm thick pultruded composite sheet, while specimens of 254 mm length and 178 mm width were made from the 12.7 mm thick sheet. The length direction of all the specimens was oriented parallel to the pultrusion direction. A total of 30 specimens for each thickness was prepared. Circular holes of different diameters were machined in these specimens to give a wide range of diameter to width ratios of 0.075 to 0.75. The holes were machined with special tools and by following careful procedures so as to minimize the influence of machining.

Some of the specimens were instrumented with strain gages. Back to back strain gages were used to minimize bending effects. Strain gages, away from the hole and along the specimen width, verified the uniformity of the compressive loading. In addition, strain gages on the inside surface of the holes captured strain concentrations, while strain gages along the width across the minimum cross section were used to record the strain gradients.

Testing Procedure

The end-gripped compression test fixture was used in this investigation. This fixture has two pairs of adjustable grips to accommodate specimens of different thicknesses. Two side fixtures with knife-edge restraints attached were placed along the specimen sides. Thus clamped boundary conditions were applied at the loaded ends, while simply supported boundary conditions on the sides prevented column buckling. All the compression specimens were loaded quasi-statically using a Tinius Olsen 1.78 MN capacity hydraulic testing machine. During the tests, two DCDTs were used: one at the specimen center and oriented transverse to the specimen to measure the out-of-plane displacements (specimens with a hole had the DCDT offset) and one along the loading direction to measure the end shortening. The load, the DCDT signals, and the strain gage data were all recorded using a data acquisition system. The specimens with prior indentation damage were also instrumented with strain gages and tested in compression following the same procedure.

Results

This section summarizes some of the important results from the damage resistance and damage tolerance tests.

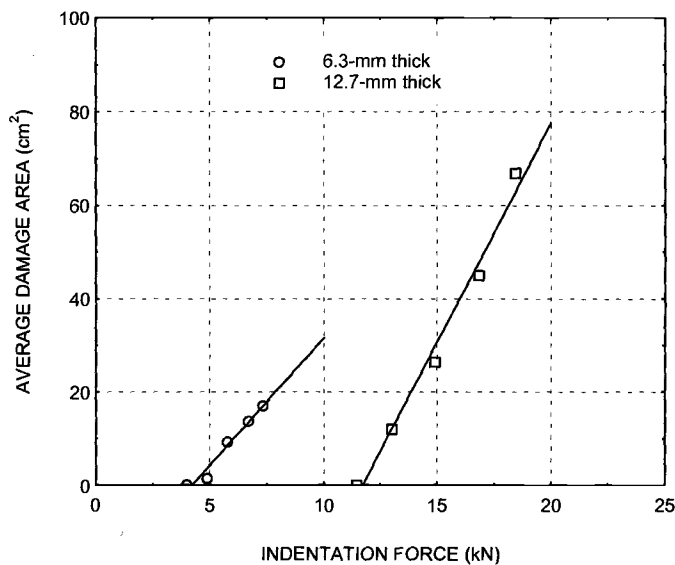
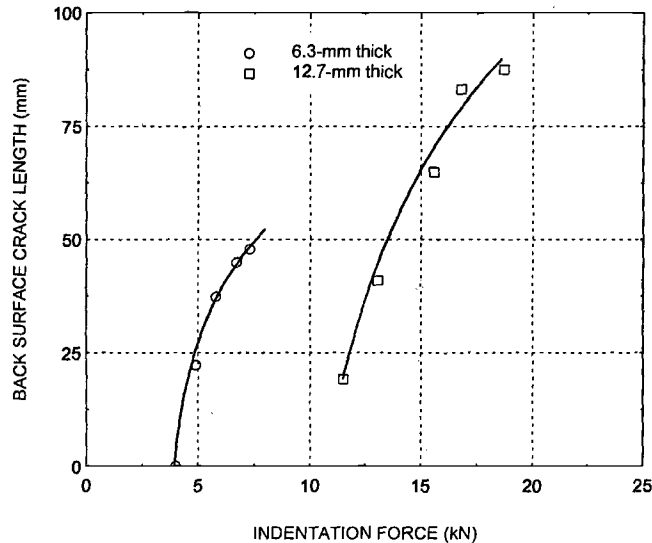
Damage Resistance

As mentioned earlier, the damage parameters were assessed in terms of back surface crack length, damage area by X-radiography and photomicrographs after sectioning, at five load levels for each thickness. The average damage area as a function of the indentation force is shown in Figure 7 for the 6.3 mm and 12.7 thick specimens. This figure shows a linear relationship between the damage area and the indentation force. The figure also shows that the thicker material withstands larger forces, with correspondingly larger damage areas. The back surface crack length is shown as a function of the indentation force in Figure 8. It is clear that the back surface crack length and the damage area both increase as the indentation force increases.

Photomicrographs, taken at different load levels, of the longitudinal (along the pultrusion direction) and transverse sections through the center of the specimens showed the progressive failure mechanisms. At lower load levels (for instance 4 KN for the 6.3 mm thickness), there was no visible damage. At higher load levels, matrix cracks begin to form; then delamination between the roving and CSM layers on the tension side begins. Then extensive delamination spreads across the thickness, accompanied by fiber breakage in the roving layers. Extensive delamination and failure in the 6.3 mm thick specimen at the failure load are shown in Figure 9.

Damage Tolerance

The damage tolerance of the pultruded composite was evaluated in terms of the compressive strength of specimens that were subjected to different levels of transverse indentation loading. The measured compressive strengths of these damaged specimens were compared with the compressive strength of similar specimens with a circular hole.

Figure 7 – *Damage area as a function of indentation force.*Figure 8 – *Back surface crack length as a function of indentation force.*

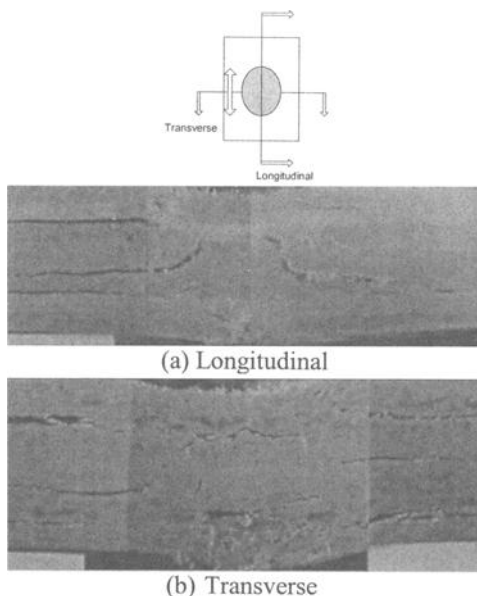


Figure 9 – Photomicrographs showing extensive delamination and fiber breakage at failure load of 7.3 kN (6.3 mm thick).

Compression Strength of Specimens with Holes

The strength results for the compression specimens with holes of different diameters are summarized for the two thicknesses in Figure 10. This figure shows the compression strength based on the net section; each point represents the average strength of at least three specimens. The 6.3 mm thick specimens exhibited higher compressive strengths compared to the 12.7 mm thick specimens, probably because of more internal flaws observable in the thicker material. As the ratio of hole diameter to specimen width increased, the differences between the two thicknesses became less significant. As explained later, this figure was used as a master curve to compare the damaged specimens with the specimens with circular holes to arrive at an ‘equivalent hole diameter’.

As mentioned earlier, many of the compression specimens were instrumented with electrical resistance strain gages. The axial strain distribution in the vicinity of the hole for several hole sizes is shown in Figure 11 for the 12.7 mm thick composite. Such plots provided information for determining the strain concentration factors as well as for comparison with the behavior of specimens with indentation damage.

Compression Strength of Specimens with Damage

Specimens of both thicknesses, damaged at different transverse indentation loads, were tested in subsequent compression. A number of these specimens were also instrumented with strain gages on both surfaces, to capture the strain gradients. The strain

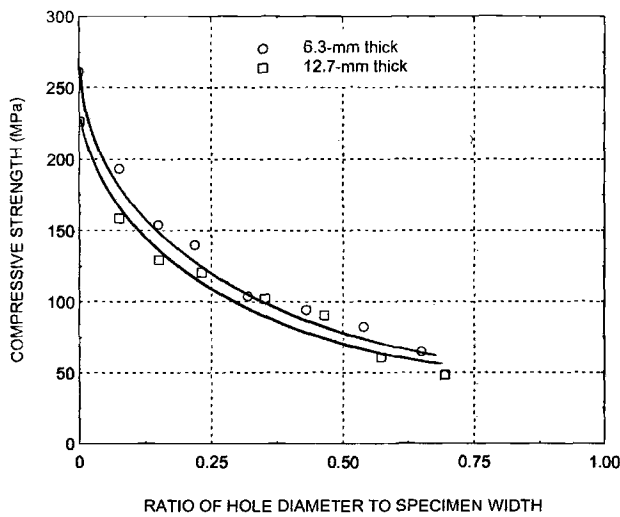


Figure 10 – *Compressive strength as a function of the hole diameter to specimen width ratio for 6.3 mm and 12.7 mm thick plate specimens.*

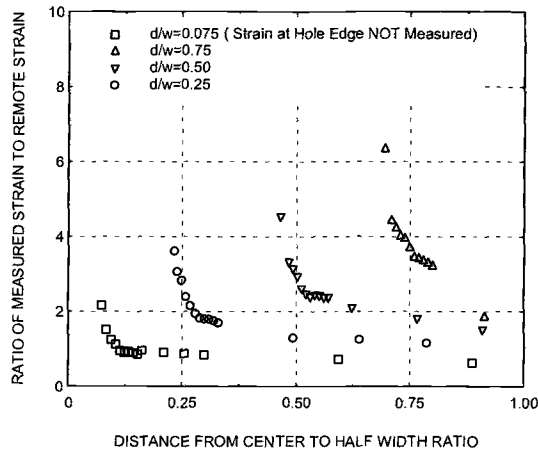


Figure 11 – *Axial strain distribution in the vicinity of a hole for several hole diameters in 178 mm wide plate specimens of 12.7 mm thickness.*

gages were located close to the damaged region. Typical strain variations for a 6.3 mm thick specimen at a prior indentation load of 7.3 kN are shown in Figure 12. This figure

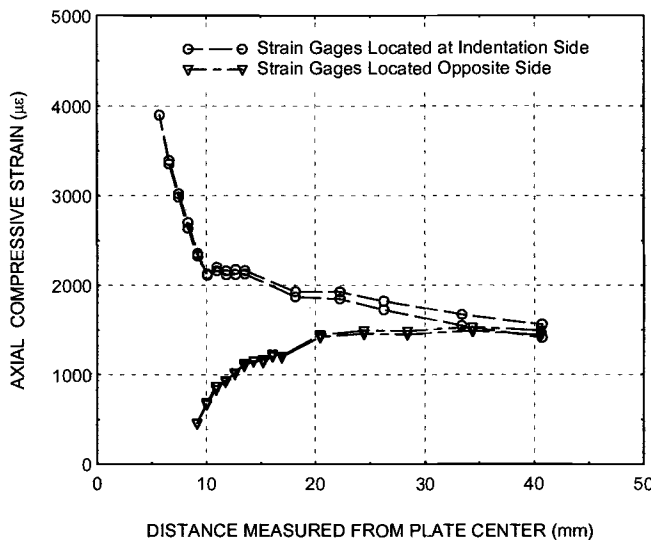


Figure 12 – *Axial strain distribution in the vicinity of the damage region for 6.3 mm thick plate specimen at a load of 7.3 kN.*

shows the strain variations on the indentation side as well as the backside, for two different specimens. The measured strains for the two specimens agree very well. The figure shows that on the backside (where tension occurs during the transverse indentation) the strains increase away from the damage zone, while on the indentation side, there is a strain concentration due to the damage zone. It can also be noticed that the strain on both sides merge together away from the damage region.

The residual compressive strength (compression after damage) is shown as a function of the back surface crack length for both thicknesses in Figure 13. It is interesting to note that the curve for the smaller thickness is above that for the larger thickness for relatively short back surface cracks, but the two curves cross over around a 20 mm long crack. Earlier, in Figure 10, it was shown that the thicker composite exhibited a compressive strength closer to that of the thinner composite for relatively larger holes. Thus the 12.7 mm thick composite appears to be more damage tolerant.

The residual compressive strength is shown as a function of the indentation force for both the thicknesses in Figure 14. The corresponding undamaged compressive strength is also included in the figure. The figure shows that the damaged specimens did not show any degradation of compressive strength unless the threshold indentation force was exceeded. This threshold was 10 kN for the 12.7 mm thickness and about 4 kN for the 6.3 mm thickness.

The compression strength measured for the damaged specimens was used in conjunction with the compression strength of specimens with holes (Figure 10) to arrive at

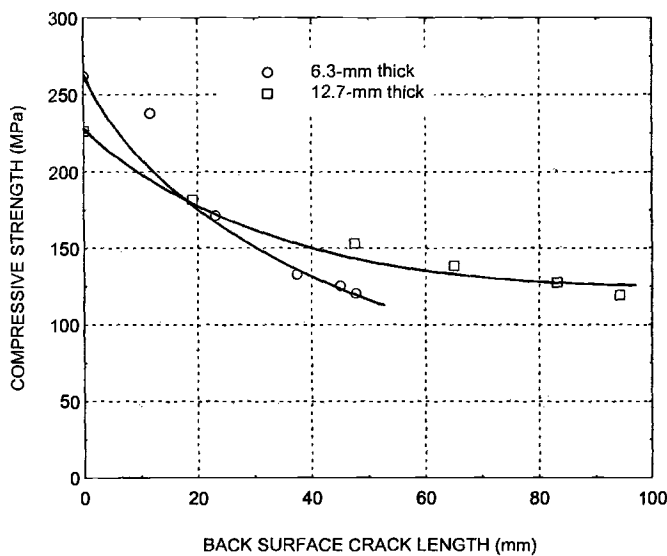


Figure 13 – Compressive strength as a function of back surface crack length.

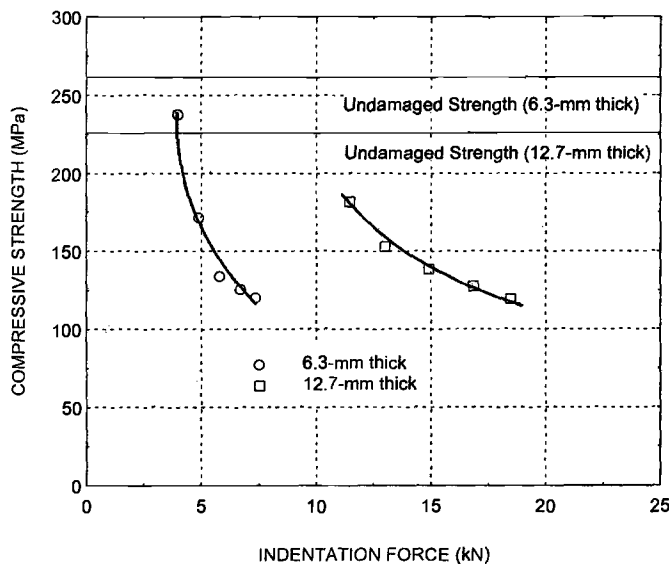


Figure 14 – Compressive strength as a function of indentation force.

an ‘equivalent hole diameter’. Such an ‘equivalent hole diameter’, determined for the 6.3 mm and 12.7 mm thicknesses, is shown as a function of the back surface crack length in Figure 15. Consistent with the results shown in Figure 13, the ‘equivalent hole diameter’ for the smaller thickness materials is observed to be larger.

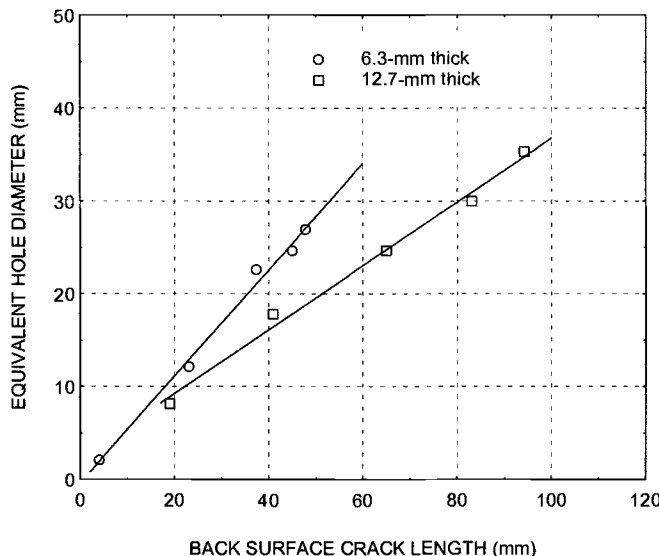


Figure 15 – Relationship between the equivalent hole diameter of the damaged specimens and the back surface crack length.

Finally, the variation of the ‘equivalent hole diameter’ with the damage size (measured from X-radiography images) is shown in Figure 16 for the two materials. Again, it is seen that the ‘equivalent hole diameter’ for the smaller thickness composite is larger for a given damage size.

Conclusions

The damage resistance and damage tolerance behavior of a fiberglass-epoxy pultruded composite material, in two thicknesses, has been investigated. The damage parameters were determined from X-radiography, back surface crack length and cross-sectional photomicrographs, after different levels of transverse indentation loads. The repeatability of the experimental results was good, especially in view of the inherent material variability. It may be mentioned here that many investigators have tried, with varying degrees of success, to correlate the results from transverse indentation tests and from low velocity impact tests; most of these investigations have involved aerospace composites containing carbon fibers.

The second phase of this investigation parallel the compression after impact (CAI) studies aerospace composites. Specimens with damage caused by different levels

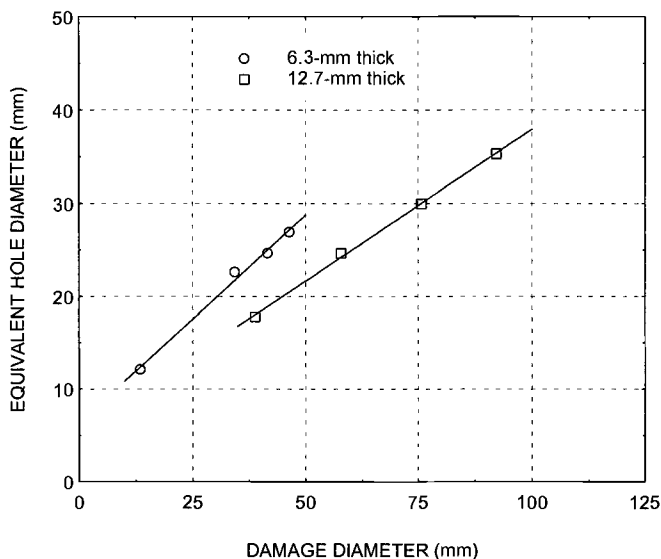


Figure 16 – Relationship between the equivalent hole diameter of the damaged specimens and the average damage diameter.

of transverse indentation force were subjected to compression. The compressive strengths and the strain distributions were compared with the corresponding characteristics of specimens with circular holes. Based on this comparison, ‘equivalent hole diameters’ were determined for some of the damage parameters such as the back surface crack length and the damage area (given by X-radiography).

Acknowledgment

This work was supported by NASA grant number CA NCC-1-389.

References

- [1] Lee, S. M. and Zahuta, P., “Instrumented Impact and Static Indentation of Composites,” *Journal of Composite Materials*, Vol. 25, 1991, pp. 204-222.
- [2] Wu, E. and Shyu, K., “Response of Composite Laminates to Contact Loads and Relationship to Low-Velocity Impact,” *Journal of Composite Materials*, Vol. 27, 1993, pp.1443-1464.
- [3] Jackson, W. C. and Poe, C. C., “The Use of Impact Force as a Scale Parameter for the Impact Response of Composite Laminates,” NASA Technical Memorandum 104189, 1992.

- [4] Kaczmarek, H. and Maison, S., "Comparative Ultrasonic Analysis of Damage in CFRP Under Static Indentation and Low-Velocity Impact," *Composites Science and Technology*, Vol. 51, 1994, pp. 11-26.
- [5] Sjolom, P. O., Hartness, T. J. and Cordell, T. M., "On Low-Velocity Impact Testing of Composite Materials," *Journal of Composite Materials*, Vol. 22, 1988, pp. 30-52.
- [6] Lagace, P. A., Williamson, J. E., Wilson Tsang P. H., Wolf, E. and Thomas, S., "A Preliminary Proposition for a Test Method to Measure (Impact) Damage Resistance," *Journal of Reinforced Plastics and Composites*, Vol. 12, 1993, pp. 584-601.
- [7] Highsmith, A. L., "A Study of the Use of Contact Loading to Simulate Low-Velocity Impact," NASA Contractor Report 97-206121, 1997.
- [8] Nettles, A. and Douglas, M. J., "A Comparison of Quasi-Static Indentation to Low-Velocity Impact," NASA Technical Publication 2000-210481, 2000.
- [9] Abrate, S., "Impact on Laminated Composites: Recent Advances," *Applied Mechanics Review*, Vol. 47, 1994, pp. 517-544.
- [10] Starnes, J. H., Jr., Rhodes, M. D. and Williams, J. G., "Effect of Impact Damage and Holes on the Compressive Strength of a Graphite/Epoxy Laminate," *Nondestructive Evaluation and Flow Criticality for Composite Materials*, ASTM STP 696, American Society for Testing and Materials, 1979, pp. 145-171.
- [11] Shuart, M. J. and Williams, J. G., "Compression Behavior of 45° Dominated Laminates with a Circular Hole or Impact Damage," *AIAA Journal*, Vol. 24, 1986, pp. 115-122.
- [12] Wisheart, M. and Richardson, M. O. W., "Low Velocity Response of a Complex Geometry Pultruded Glass/Polyester Composite," *Journal of Materials Science*, Vol. 34, 1999, pp. 1107-1116.
- [13] Saha, M., "Elastic Properties, Strength and Damage Tolerance of Pultruded Composites," Ph.D. Dissertation, Department of Mechanical Engineering, Old Dominion University, Norfolk, 2001.

Johannes F. Neft,¹ Karl Schulte,² and Peter Schwarzer¹

Mechanical Degradation of Continuous Glass Fibre-Reinforced Thermoplastics under Static and Cyclic Loading:

A Prepreg Laminate - Technical Textile Comparison

Reference: Neft, J. F., Schulte, K., and Schwarzer, P., "Mechanical Degradation of Continuous Glass Fibre-Reinforced Thermoplastics under Static and Cyclic Loading: A Prepreg Laminate - Technical Textile Comparison," *Composite Materials: Testing, Design, and Acceptance Criteria, ASTM STP 1416*, A. Zureick and A. T. Nettles, Eds., American Society for Testing and Materials International, West Conshohocken, PA, 2002.

Abstract: The mechanical degradation of continuous glass fibre-reinforced thermoplastics (GFRT) was analysed considering differences in the semifinished products of the laminates. The investigated laminates were produced from prepgres and technical textiles (commingled thermoplastic and glass fibres stitched together with a polymeric yarn) with isotactic polypropylene (iPP) as matrix material. E-glass fibres were used as reinforcement in both systems. Static transverse and longitudinal tensile, compression and bending tests were performed. Fatigue tests were made in tension-tension ($R=0.1$). The matrix morphology varied due to different manufacturing procedures. The results showed a significant influence on the mechanical degradation of the semifinished products.

Keywords: glass/polypropylene, microstructure, morphology, prepgres, technical textile, mechanical degradation, fatigue, failure mechanisms

Introduction

The advantage of continuous fibre reinforced polymers (FRP), high specific strength and stiffness, superior fatigue and corrosion resistance, are adequately known from the aircraft applications [1]. Carbon fibre reinforced polymers (CFRP) allow the greatest weight savings when compared to metals. However, due to high material costs and a

¹ Lab Engineer and Manager of the polymer analytics group at Volkswagen AG, Central Laboratory 1437, 38436 Wolfsburg, Germany.

² Professor, Polymer and Composites Section, Technical University Hamburg-Harburg, 21073 Hamburg, Germany.

complicated processing, they are mainly used in the air- and space industry. In order to have their positive properties also available in other industries, mainly the automotive industry, new fibre/matrix combinations and processing methods have been developed [2-4]. Continuous glass fibre-reinforced thermoplastics (GFRT) are one of the most promising new material combinations. They offer a very good price to payment relationship. Besides the exceptional mechanical properties they have a good damping behaviour and they are easy to reuse, respectively recycle, what is, at least in Europe, an important property [5-7]. They have an unlimited shelf life. For the part production near net shape manufacturing technologies, as hot pressing or diaphragma forming etc. can be used, which are well-known from the sheet metal deformation technologies [8, 9]. Pre-impregnated fibres, or new methods derived from textiles allow the manufacture of favourable and cost effective semifinished products [10]. Comingled yarns consisting of reinforcement and polymer(matrix) fibres, are stitched together with a polymeric binding yarn to form a flat weft inserted warp knitted structure, in which during the hot pressing process the polymer(matrix) fibres melt to form the matrix, while the binding yarn remains unaffected.

For the future application of this group of materials it is of great importance to understand their mechanical properties and damage behaviour. As this is a relatively new group of materials there is still a lack of understanding and the numerous examples for their industrial application has not yet lead to serious production [11].

It is the aim of this paper to give an overview of the property / damage characteristic of various manufactured glass fibre-reinforced thermoplastics. Two different thermoplastic laminate systems with E-glass fibres as reinforcement and isotactic polypropylene (iPP) as matrix were used. Static tensile, three-point bending, compression, tests and fatigue tests under tension-tension load ($R = 0.1$) were performed.

Materials and Experimental

Laminate Systems

The laminate systems investigated were the Plytron® prepgres from Borealis Comp. (Stathelle, Norway) in which the fibres are already impregnated with the matrix before they are processed to the final component and a new technical textile Twintex® from Vetrotex (Chambery, France). Twintex® fibres of polypropylene (PP) which will later form the matrix, are commingled together with the reinforcement fibres and a binding yarn of polyethylenterephthalate (PET) was used to form a textile.

Both laminate systems had a commercially available E-glass fibre as reinforcement and isotactic polypropylene (iPP) as matrix. The characteristics of the components are summarised in Table 1.

Processing and Laminate Structure

The manufacturer of the semifinished products also produced the sheets from which the test coupons were taken.

The prepreg systems had a thickness of approx. 0.2 mm. Consolidation of the test plates was carried out in an autoclave for 30 minutes with a cooling rate of 13°C/min.

In the technical textiles the impregnation with the matrix and the consolidation of the fabrics to test plates was carried out in a two step process. In a first press the textile was heated, under the low pressure of 4 bar to a temperature of 220°C, which was held for 3 minutes. Immediately after this it was consolidated in a second press in a cold tool (30°C) at 10 bar for more than 3 minutes. The transport between the two presses needed less than 5 seconds. The cooling rate in the second press corresponded to 66°C/min.

Table 1 – *Materials characteristics.*

	Tensile strength [MPa]	Tensile strain [%]	Young's modulus [GPa]	Density [g/cm³]	Fibre diameter [μm]	Coefficient of thermal expansion [$10^{-6}/\text{K}$]
Prepreg						
PP ¹	34.7	7.4	1.5	0.90	-	150
E-glass ¹	3400	4.5	73	2.6	17	5.4 ²
Tech. Textile						
PP ¹	37	8.6	1.9	0.90	-	150
E-glass ¹	3400	4.5	75	2.6	18.5	5.4 ²

¹ from the manufacturers Borealis and Vetrotex

² [12]

The sheet laminates produced were different in the fibre volume fraction, the matrix crystallinity and the stacking sequence (number of layers) (compare Table 2). The fibre volume fraction v_F was 34% for the prepreg and 44% for the technical textile according to ASTM Test Method for Fibre Volume Determination (D792 86). The matrix crystallinity K_0 was analysed with a DSC (Mettler Toledo DSC 821e/700). K_0 depends on the processing conditions [13]. Due to the long processing cycle and low cooling rate the prepreg system reached a higher matrix crystallinity with 53% compared to the technical textile with 42%. For the technical textile it had to be taken into account that during the heating of the specimens in the DSC an exothermic recrystallisation of the PET binding yarns took place besides the endothermic melt reaction of the polypropylene. As both reactions overlapped they could not be analysed separately. Therefore the crystallinity measurements of the technical textiles had to be repeated with a textile from which the binding yarn had been diminished (Table 2). It could be proved that with the help of a temperature modulated DSC the superimposed effects can be evaluated separately.

Table 2 - *Fibre volume fraction v_F , crystallinity K_0 of the matrix and stacking sequences of the laminate systems.*

	v_F [%]	K_0 [%]	Stacking sequence
Prepreg	34 ± 0.7	53.5 ± 1.2	[0] ₁₄
Tech. Textile	44 ± 0.8	$41.6 \pm 2.8^*$	[0] ₁₀

* tech. textile without PET binding yarns

Test plates with a thickness of approx. 3 mm were manufactured from both laminate systems, from which test coupons were machined with the help of a diamond saw. The edges were carefully ground to minimise preparation influences.

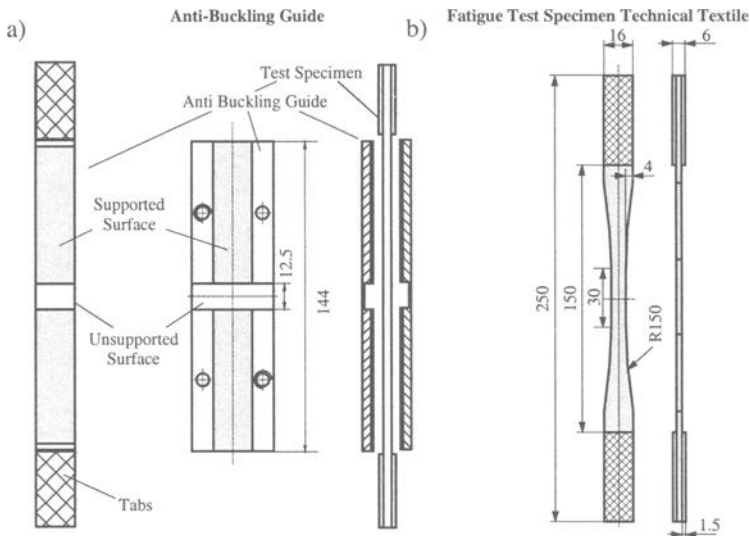


Figure 1 - a) Anti-buckling guide for compression tests; b) Tailored test specimens for the technical textile fatigue tests.

Test Conditions and Specimen Geometry

Static tension, compression and three-point-bending tests were carried out in a computer-controlled universal test machine (Zwick 1485, 100 kN) following DIN EN ISO 527 (tension), DIN 65380 (compression) and DIN EN 63 (bending). The ultimate strength σ_{ULTi} , the ultimate strain to failure ϵ_{ULTi} and the Young's modulus E_i were measured, with i indicating the fibre orientation compared to the load direction (0° or 90°). The used geometries of the test coupons are listed in Table 3. The test coupons were provided with 1.5 mm thick and 50 mm long glass fibre polyester tabs at the sample ends except for the bending tests. A special ethyl-cyanacrylat adhesive was used together with a primer (Loctite 406/770) to affix the tabs.

For compression tests of FRP several standards exist. The most frequent test configurations used are the so-called Celanese test according to ASTM D3410 and the IITRI test method [14]. Both methods have in common that the test coupons have only in the middle of the sample a short gauge length for scheduled buckling. In this work a simple anti-buckling guide with Teflon foils to minimise the possible influences by friction was used for the compression tests [15]. This anti-buckling-guide allows the test specimens to fail in the centre at a length of 12.5 mm, comparable to the Celanese test. A principle outline

is shown in Figure 1a. An extensometer with a measurement range of 45 mm was fastened on the test specimens to monitor the strain.

Table 3 – *Geometry of test coupons.*

[mm]	Thickness	Width	Length	Measuring length
Tension [0°]	3	16	250	150
Tension [90°]	3	16	250	150
Compression [0°]	3	16	250	12.5
Bending [0°]	3	10	150	--
Fatigue [0°]				
R = 0.1	3	16	250	150

Fatigue tests were carried out in a servo hydraulic machine (Schenck: $F_N = 10 \text{ KN}$) under sinusoidal tension control at a frequency of 10 Hertz and an R-value of $R=0.1$. The specimen geometry was identical with those for the static tension tests (Table 3). Only for the technical textiles tailored specimens were used to avoid failure in the clamping area (Figure 1b) [16].

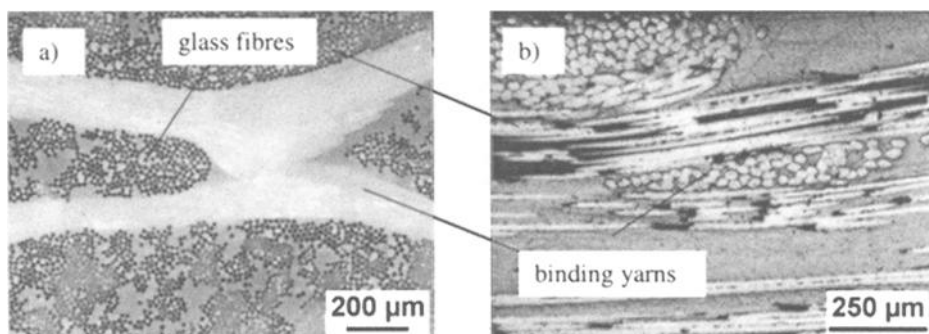


Figure 2 – *Technical Textile: a) Inhomogeneous fibre distribution vertical to the fibre direction; b) Wavy deflection of the fibres in fibre direction.*

Results and Discussion

Microstructure

The PP/glass fibre prepreg had a homogeneous fibre distribution over the complete sample cross-section, which can be compared with unidirectional thermosetting prepgs. The technical textiles, however, had an inhomogeneous fibre distribution. Zones with PET binding yarns and matrix rich regions with the polypropylene matrix, followed by fibre rich regions (Figure 2a) due to the textile structure of the semifinished products. The reinforcement fibres and the matrix fibres were stitched together by the PET binding

yarns to form the fabric. The hot pressing temperature of 220°C is not high enough to melt the PET binding yarns, which have a melting temperature of about 250°C. Additionally the fibre bundles showed some waviness, which results from the textile process (Figure 2b). Similar laminate structures are known from earlier examinations on glass fibre-reinforced technical textiles [17].

Static Properties

Transverse Tension - Transverse tensile tests give information about matrix properties and the bond strength between fibre and matrix. Figure 3a shows characteristic σ - ϵ -diagrams of both laminate systems.

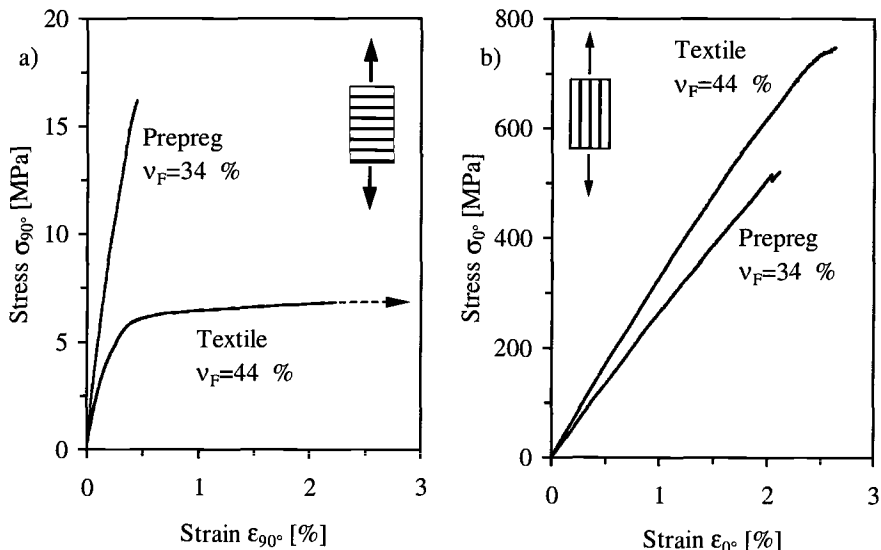


Figure 3 - Characteristic σ - ϵ -diagrams: a) Transverse tension; b) Longitudinal tension.

The prepreg laminates had a predominantly elastic deformation with only a small deviation from the linear behaviour until failure with the onset of the first continuous transverse crack. The specimen failed abruptly. The technical textile showed distinctive plastic deformations. It failed at about 8% of strain, which is not shown in the diagram, and therefore indicated by an arrow at the end of the curve. From about 0.5% of strain on, no further stress increase occurred, with a continuous development of transverse cracks took place. This is schematically shown in Figure 4. At the intersection of the tangents for the totally elastic respectively totally plastic deformation of the σ - ϵ -diagram an approxima-

tion for the actual ultimate strength (σ_{ULT90°) and strain (ϵ_{ULT90°) can be obtained (see also Table 4) and is used in this work for better comparison of mechanical data between both laminates. In Region 1 of the σ - ϵ -diagram in the beginning a totally elastic deformation took place. With increasing strain plastic deformation can be observed. At the end of Region 2 a first transverse crack developed, bridged by the binding yarns. At this stage the laminate was regarded as failed. Further loading (Region 3) led to the development of further transverse cracks and the specimen was only held together by the binding yarns until also their ultimate strength was reached.

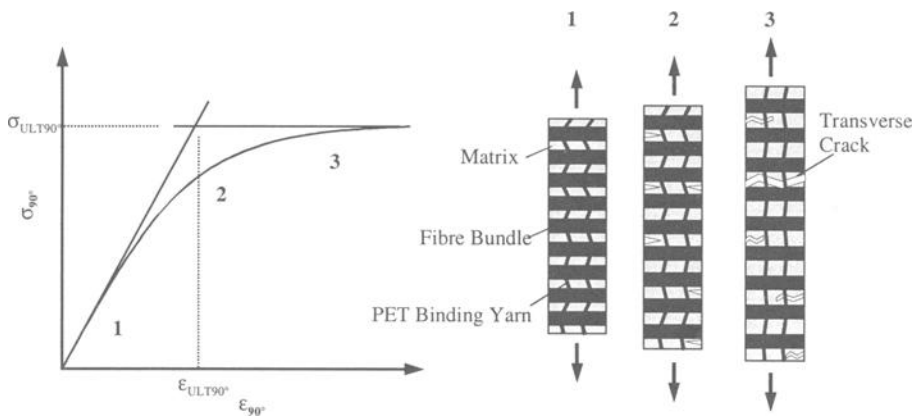


Figure 4 - *Transverse tensile failure and schematics of material property determination in the technical textile.*

The ultimate properties of both laminates are summarised in Table 4. The ultimate transverse tensile strength of 15 MPa for the prepreg system was comparable to the values determined by Davies [18] and Rijstdijk [19] at unidirectional glass/PP. The ultimate tensile strength of the technical textile was approximately 60% lower. One reason for this can be related to the higher fibre volume fraction of the technical textile which leads to locally higher internal stresses in the laminate and stress concentrations in the matrix. Due to the high transverse modulus of the fibres and the comparably low modulus of the matrix, the matrix has to deform to an extremely high content in between the fibres, which will lead to early failure and has been described by Puck [20] with the so-called strain extension factor

$$f_e = \frac{1}{1 - \left(\frac{2}{\sqrt{\pi}} \sqrt{V_F} \left(1 - \frac{E_M}{E_F} \right) \right)} \quad (1)$$

with E_M and E_F as the Young's modulus of the matrix and the fibre respectively and v_F as the fibre volume fraction (in weight per cent).

Table 4 - *Tension, compression and three-point-bend properties.*

Test		Prepreg ($v_F=34\%$)	Tech. Textile($v_F=44\%$)
Tension			
σ_{ULT90°	[MPa]	15 ± 1.3	5.9 ± 0.7
σ_{ULT0°	[MPa]	548 ± 42	763 ± 51
ϵ_{ULT90°	[%]	0.41 ± 0.06	0.28 ± 0.01
ϵ_{ULT0°	[%]	2.24 ± 0.09	2.66 ± 0.44
E_{90°	[GPa]	3.97 ± 0.04	1.56 ± 0.04
E_0°	[GPa]	26.71 ± 2.57	33.52 ± 0.46
Compression			
σ_{ULT0°	[MPa]	266 ± 3	148 ± 5
ϵ_{ULT0°	[%]	1.18 ± 0.13	0.43 ± 0.05
E_0°	[GPa]	25.10 ± 0.94	34.6 ± 0.51
Bending			
σ_{ULT0°	[MPa]	608 ± 38	266 ± 11
ϵ_{ULT0°	[%]	2.96 ± 0.34	0.93 ± 0.10
E_0°	[GPa]	26.09 ± 1.08	33.44 ± 1.39

The calculated strain extension factor f_e amounted to 2.71 for the prepreg system and to 3.79 for the technical textile, which corresponds to an increase of 40%. The differences in the ultimate strength, however, are clearly higher than the calculated 40% increase in the strain extension factor. It is well-known that the fibre volume and distribution also influences the stress conditions within the laminate [20]. The strain extension factor increases with increasing fibre density. This is the case for the technical textile. Due to the binding yarn the glass fibres are held to bundles in the laminate with locally higher fibre volume fractions.

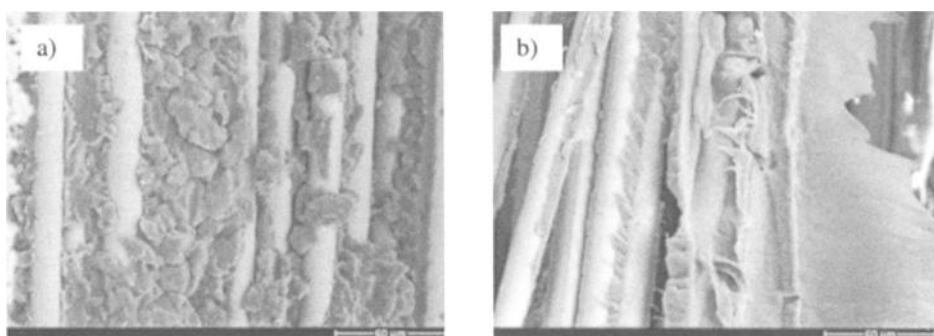


Figure 5 - *Characteristic fracture morphologies after transverse tension tests:*
a) Prepreg system; b) Technical textile.

The transverse Young's modulus of the technical textiles was lower as in the prepreg system (Table 4). This can be related to the inhomogeneous fibre distribution in the technical textile where the matrix-rich zones reduce the overall stiffness of the laminate. Differences in the matrix crystallinity in both laminates have an effect on the transverse Young's modulus as well. A lower matrix modulus corresponds to a lower laminate modulus.

In the prepreg system the fibres are poorly wetted with matrix as naked fibres can be observed (Figure 5a). The matrix was highly crystalline, which was due to the long processing cycles and low cooling rates. The crack propagation partly proceeded intercrystalline in the matrix and partially along the fibre/matrix-interface. Within the laminates the spherulitic boundaries represented weak points due to the high initial crystallinity [21]. The morphology of the technical textile was characterised by a ductile matrix with low crystallinity (Figure 5b). The crack propagation proceeded transcrystalline with good fibre/matrix-adhesion.

Longitudinal Tension – A characteristic σ - ϵ -diagram of both laminate systems under longitudinal tensile load is shown in Fig 3b. The technical textile reached a higher strength and modulus (Table 4). Failure is in both laminates characterised by longitudinal intralaminar cracks. A brush-like fracture appears. Bader first described this failure behaviour on the example of carbon fibre reinforced epoxy resins [22]. Starting from statistically distributed ruptures of single fibres due to Mode II (shear loads) longitudinal intralaminar cracks propagate and connect the fibre breaks with each other. A stress redistribution from the broken fibres into the unbroken fibres occurs with a stress rise until final failure. In the prepreg system the longitudinal cracks can develop along the entire specimen. In the technical textile the longitudinal cracks are stopped at the next binding yarn. Therefore the damage area is limited to a few centimetres of the free sample length.

Table 5 – Normalised tensile strength and Young's modulus ($v_F = 40\%$.).

	Prepreg System	Tech. Textile
σ_{ULT0°	[MPa]	645
E_0°	[GPa]	31.42
		695
		30.47

The different fibre volume fractions of both laminate systems did not directly result in the properties achieved. The strength and modulus were normalised to a characteristic fiber volume fraction of $v_F = 40\%$ for easier comparison. The results are listed in Table 5. The prepreg system showed a lower normalised ultimate tensile strength compared to the technical textile. Obviously the fiber waviness and the inhomogenous fiber distribution did not have a significant influence to the ultimate tensile strength. The normalised Young's modulus was not affected.

Axial Compression - Under compression load the technical textile had a higher Young's modulus (Figure 6a) due to the higher fiber volume fraction (Table 4). The ultimate compressive strength of the technical textile was, clearly lower as in the prepreg

system. The fibre waviness led to an early microbuckling with an initiation of shear stresses in the matrix and a dramatic reduction of the ultimate compression strength. [23].

The failure mechanisms of the different laminate systems were differently. Failure in the technical textile appeared by the formation of kink-bands induced by the PET binding yarns (Figure 7 and 8a).

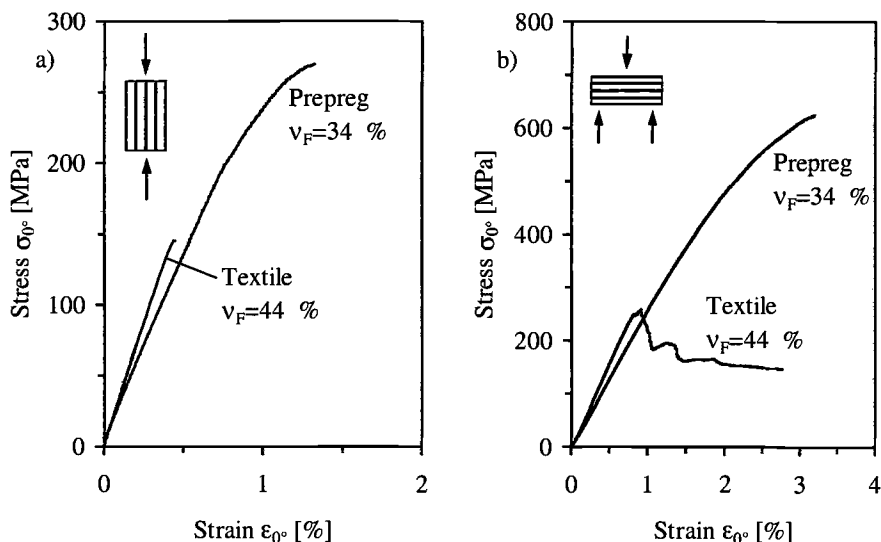


Figure 6 - Characteristic σ - ϵ -diagrams: a) Axial compression; b) three-point bending.

In the prepreg system two compression failure mechanisms could be observed: shear failure was 45° to the load direction and an indication for the formation of kink-bands (Figure 7 and 8b). Both mechanisms are well-known from tests with carbon fibre reinforced epoxy resins, in which under shear failure higher strength results were reached [24-26]. This could not be corroborated with the prepreg system. Both failure mechanisms showed equal compression strengths within small scatter. Also, the appearance of longitudinal intralaminar cracks could not be found, as they have been observed by Rijsdijk [18] in unidirectional glass/PP.

Three-Point-Bending – The stress-strain response in a three point bending test of both laminates is shown in Figure 6b. The prepreg system deformed linearly to approx. 80% of the ultimate strength. First failure in the form of fiber breaks started and the σ - ϵ -slope declined until final failure of the test specimens. The technical textile again showed a higher Young's modulus due to the higher fiber volume fraction, however it did not even reach 50% of the ultimate bending strength of the prepreg system. It failed abruptly followed by a stepwise strength decrease.

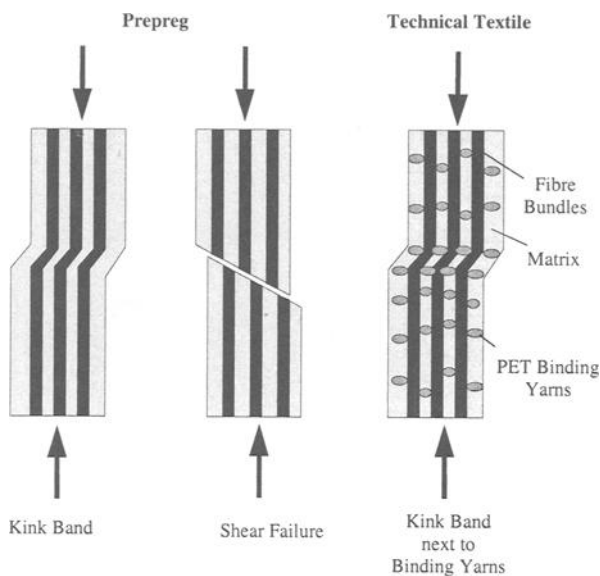


Figure 7 - *Characteristic failure mechanisms for axial compression.*

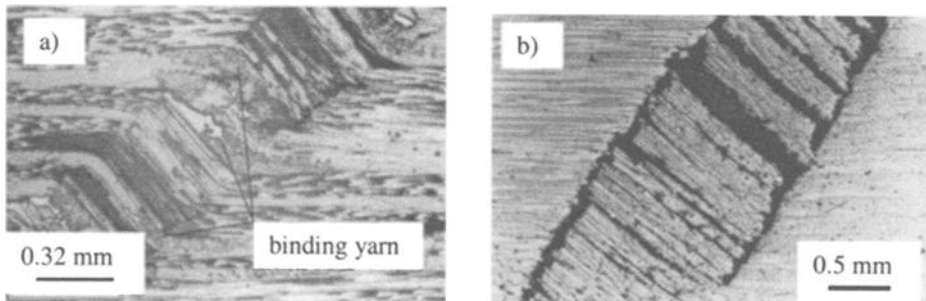


Figure 8 - *Characteristic failure under axial compression; a) Kink-bands initiated at binding yarns in the tech. textile; b) Kink-bands in the prepreg.*

Both laminate systems failed under compression. In the technical textile a kink-band was formed at the first load decrease. The specimen had not failed yet, and further fibre failure with the development of kink-bands followed (Figure 9). First ply failure did not arise under the bend stamp but at the nearest binding yarn. The PET binding yarns caused a stress concentration and an out of axis waving of the glass fibres and led to early microbuckling kink-band formation and failure of the laminates. The failure under three-point-bending could not be compared to the failure in a simple compression test, as in a three-point-bending test the compressive stresses are continuously reduced from the sam-

ple top side towards the neutral zone. Therefore the bending strength in a three-point-bend test is normally higher than the corresponding compressive strength in a unidirectional laminate [27] like it was the case in the prepreg system. The technical textile showed an opposite behaviour.

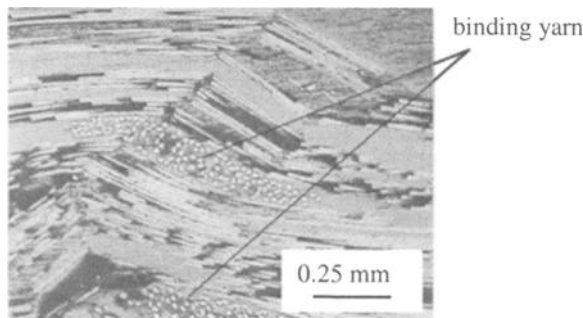


Figure 9 - Technical textile: Kink-bands initiated at binding yarns under three-point-bending.

Fatigue Behaviour

Tension-Tension Fatigue ($R = 0.1$)

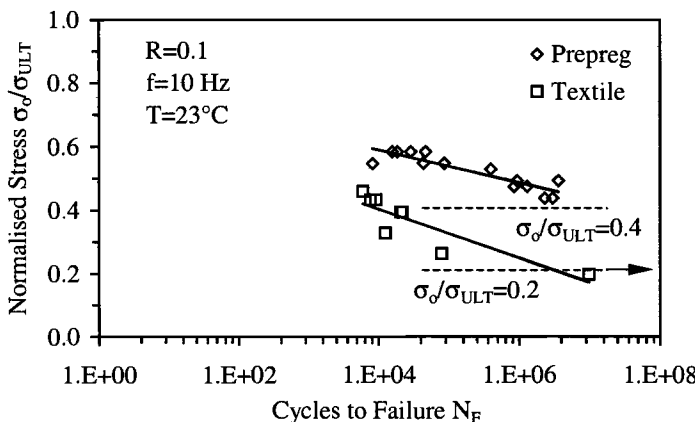
Fatigue loading can lead to a temperature increase, due to the dissipation of energy as a result of internal friction [28]. The temperature development was monitored with a thermocouple during the fatigue tests. A temperature increase of max. 4°C could be measured, therefore a temperature dependence of the fatigue results could be excluded. The results achieved were plotted in a normalised fatigue diagram with the normalised maximum stress in each consecutive fatigue cycle on the y-axis and the number of cycles to failure plotted in a logarithmic scale on the x-axis (Figure 10). Equation (2), proposed by Reifsnider et al [29] describes the fatigue behaviour

$$\frac{\sigma_o}{\sigma_{ULT}} = m * \log N_F + b \quad (2)$$

with σ_o - maximum stress in the fatigue load cycles; σ_{ULT} – maximum fracture stress from the static tensile test; N_F – number of fatigue load cycles until failure and m and b as regression parameters (compare Table 6). m describes the slope of the curve. Because of the few tests only a low correlation coefficient R_K could be expected. It was the aim of this investigation to obtain just a qualitative comparison of the different laminate systems.

Table 6 - Parameters from the logarithmic equation.

Prepreg System	<i>m</i>	<i>b</i>	R_K
Prepreg	-0.022	0.8	0.815
Textile	-0.035	0.78	0.784

Figure 10 - Normalised fatigue life-diagrams under $R = 0.1$.

Hahn defined a fatigue ratio [30] σ_0/σ_{ult} at 10^6 load cycles. This value helps to compare different laminates. Typical values of unidirectional glass fibre-reinforced laminates with thermoset matrices have values between 0.6 and 0.4 [31, 32]. Oever et al. [33] calculated for glass fibre-reinforced polypropylene the fatigue strength value to 0.4, which is comparable to that of the prepreg laminates, which had in our tests a value of 0.45. The technical textile, however, had a fatigue strength value of only 0.2. Both, the fatigue ratio and the slope of the curve in Figure 10 showed the significantly lower fatigue properties of the technical textile.

Damage Mechanisms - A particularly appropriate method sensitive to the fatigue damage degradation of a fibre reinforced polymer is the response of the secant modulus [34]. Figure 11 shows the variation of the secant modulus, normalised to the initial modulus in the very first load cycle, plotted versus the fatigue life. The prepreg laminates showed the typical decrease in the secant modulus (stiffness reduction) for unidirectional laminates. After the initial decrease in stiffness one can observe two further reduction steps, which can be correlated to fibre and fibre bundle rupture. The technical textile, however, showed a continuous decrease of the secant modulus, which can be compared to that of woven fabrics [35]. After a first stiffness reduction (Region I) which occurs within the first 20% of fatigue life one can observe a continuous further stiffness reduction (Region II). In Region III, at the very end of the fatigue life, an accelerated stiffness reduction can be observed.

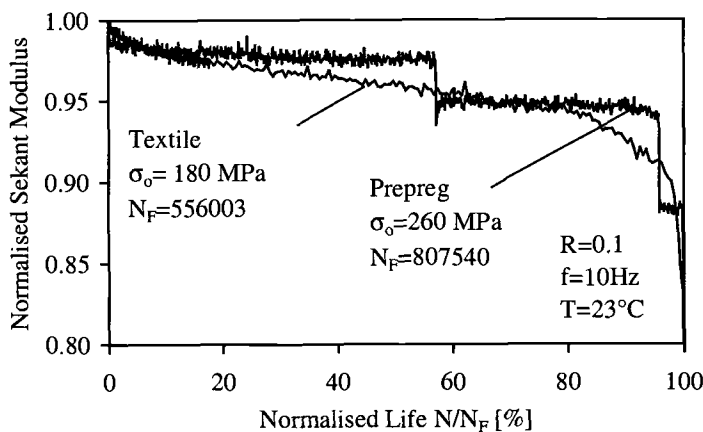


Figure 11 - Secant modulus (normalised) versus fatigue life under $R = 0.1$.

The dominating damage mechanism in the prepreg laminates was the formation of transverse cracks starting from the beginning of fatigue loading. With increasing number of load cycles further transverse cracks developed. The cracks propagated either through the matrix or along the fibre matrix boundaries. At some locations the rupture of fibre bundles occurred, which resulted in the stepwise stiffness reduction. Therefore, after failure of the specimen it had a brush-like appearance.

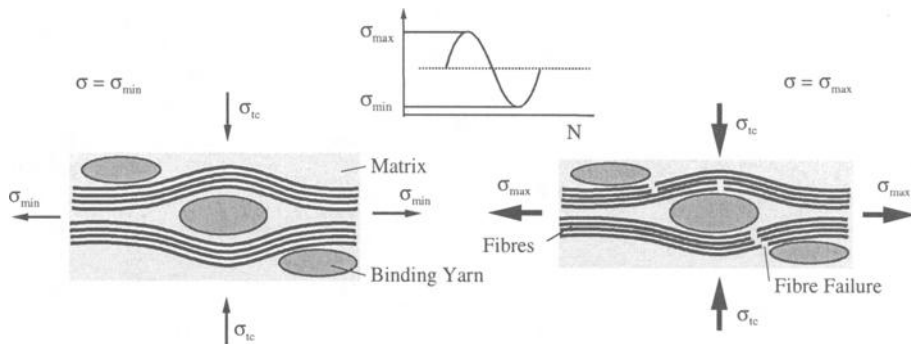


Figure 12 - Schematic of fatigue damage degradation in unidirectional technical textiles.

In the technical textile we observed (as in the prepreg laminates) with the first fatigue load cycles the initiation of transverse cracks in the matrix. However, these cracks initiated near the PET binding yarns. Fibre fracture occurred from the very first beginning as

well. The binding yarns constrained the fibre bundles. This led to normal stresses (in fibre direction) and additionally transverse stresses to the glass fibres and therefore to a local stress increase (Figure 12). A load transfer from the broken fibres into the unbroken fibres occurs, and with further fatigue load cycles a further (Region II) and accelerated stiffness reduction (Region III) can be observed. This is a self accelerating process, so at the very end of fatigue life we have an extremely rapid stiffness reduction.

Conclusions

The influence of two different semifinished products (Plytron® and Twintex®) on the static and fatigue degradation behaviour of a glass fibre-reinforced polypropylene was investigated. Plytron® is a prepreg system and Twintex® a technical textile with glass and polypropylene fibres stitched together with a PET binding yarn. The two materials essentially differ in their microstructure and unidirectional fibre arrangement. While the prepreg system had a homogeneous fibre distribution, the technical textile had a more bundle-like arrangement with an inhomogeneous fibre distribution and matrix rich zones due to the textile fabrication. This microstructure also influenced the static mechanical properties. While the tensile properties were not as much influenced, significant differences on the compressive stresses could be found, because the binding yarns already initiated a small fibre deformation which could easily lead to kinking under the compressive load.

Under fatigue loading the technical textile showed an early fatigue damage initiation. Therefore, it was not as fatigue resistant as the prepreg material. The results showed the important influence of the semifinished products on the mechanical degradation behaviour of continuous fibre-reinforced polymer composites. Designers should consider the differences in tensile properties under static and fatigue loading as well as the differences in compressive properties.

Acknowledgments

The support of materials by Borealis and Vetrotex is gratefully appreciated. The help of graduate students in performing the tests is gratefully acknowledged: Mrs. H.-Q. Lu, Mr. T. Jung, Mr. O. Schulz and Mr. S. Himmel

References

- [1] Räckers, B.: "Faserverbundwerkstoffe, Entwicklungstrends am Beispiel des Airbus," in: *Verbundwerkstoffe und Werkstoffverbunde*, DGM Informationsgesellschaft, 1997, pp. 3-14.
- [2] Brandt, J., Drechsler, K. and Strachauer, F.: "Kostengünstige und großserienfähige Herstellung von Verbundwerkstoffen mit textilen Faserstrukturen," in: *Kunststoffe im Automobilbau: Zukunft durch neue Anwendungen*, Mannheim, VDIK, Düsseldorf, 1998, pp. 227-246.

- [3] Taylor, C.: "PNGV materials accomplishments," *Automotive Engineering*, December 1996.
- [4] Stumpf, H.: "Study on the manufacture of thermoplastic composites from new textile preforms," Ph-D Thesis, Technical University Hamburg-Harburg; TUHH Technologie GmbH, 1998.
- [5] Sato, N., Takahashi, H. and Kurauchi, T.: "Bumper Recycling Technology," in: *Polypropylene: An A-Z Reference*, J. Karger-Kocsis, ed., Kluwer Publisher, Dordrecht, 1999, pp. 68-75.
- [6] Marissen, R.: "Some Environmental Aspects of the Application of Fibre Reinforced Plastics in Structures," Delft University of Technology, 1993, LTM 998.
- [7] Friedrich, K. and Reinicke, R.: "Verbundwerkstoffe mit Thermoplastmatrix, Herstellung, Struktur, Eigenschaften," *VDI-Berichte* Nr. 1420, 1998, pp. 97-113.
- [8] Brandt, J., Drechsler, K., Vullriede, S.: "Leichtbau mit Faserverbundwerkstoffen in der Flugzeugindustrie - ein technologischer Ansatz für den Fahrzeugbau?," in: *Kunststoffe im Automobilbau: Trends, Technologien, Anwendungen*, VDI-Gesellschaft Kunststofftechnik, 1997, pp. 221-237.
- [9] Zepf, H.-P.: "Faserverbundwerkstoffe mit thermoplastischer Matrix," Expert Verlag, 1997.
- [10] Stumpf, H., Mäder, E., Baeten, S., Pisanikovski, T., Zäh, W., Eng, K., Andersson, C.-H., Verpoest, I. and Schulte, K.: "New thermoplastic composite preforms based on split-film warp-knitting," *Composites Part A*, Volume 29 A, 1998, pp. 1511-1523.
- [11] Brüdgam, S., Henkelmann, H.: "Anforderungsprofil an Faser-Kunststoff-Verbundhalbzeuge für Kfz-Leichtbaukomponenten," *Kunststoffe im Automobilbau*, VDIK-Tagung, 1996, pp. 21-43.
- [12] Thomason, J. L., Hartman, D. R.: "Properties of glass fibres for polypropylene reinforcement," in: *Polypropylene: An A-Z Reference*, J. Karger-Kocsis, ed., Kluwer Publisher, Dordrecht, 1999, pp. 678-685.
- [13] Varga, J.: "Review supermolecular structure of isotactic polypropylene," *Journal of Materials Science*, Volume 27, 1992, pp. 2557-2579.
- [14] Carlsson, L. A. and Pipes, R. B.: "Experimental Characterisation of Advanced Composite Materials," Second Edition, Technomic Publishing, Lancaster, 1997.
- [15] Schulte, K.: "Compressive Static and Fatigue Loading of Continuous Fibre-Reinforced Composites," *Compression Response of Composite Structures, ASTM STP 1185*, S. E. Groves and A. L. Highsmith, Eds., Philadelphia, 1994, pp. 278-305.
- [16] Maier, G. and Ott, H.: "Damage development in composite laminates with brittle matrix in fatigue loading," *Cryogenics*, Volume 28, 1988, pp. 278-280.
- [17] Mäder, E. and Skop-Cardarella, K.: "Textile Hybridkordelstrukturen für langfaserverstärkte Thermoplaste," *Technische Textilien*, Volume 39, 1996, pp. 124-126.
- [18] Rijsdijk, H. A., Contant, M. and Peijs, A. A.: "Continuous-Glass-Fibre-Reinforced Polypropylene Composites: I. Influence of Malein-Anhydride-Modified Polypropylene on Mechanical Properties," *Composites Science and Technology*, Volume 48, 1993, 161-172.
- [19] Davies, P., Pomies, F. and Carlsson, L.: "Influence of Water Absorbtion on Trans-

- verse Tensile Properties and Shear Fracture Toughness of Glass/Polypropylene," *Journal of Composite Materials*, Volume 30, 1996, pp. 1004-1019.
- [20] Puck, A.: "Zum Deformationsverhalten und Bruchmechanismus von unidirektionalem und orthogonalem Glasfaser/Kunststoff," *Sonderdruck Kunststoffe*, 55, 1965.
 - [21] Friedrich, K.: "Strength and fracture of crystalline isotactic polypropylene and the effect of molecular and morphological parameters," *Prog. Colloid & Polymer Science*, Volume 66, 1979, pp. 299-309.
 - [22] Bader, M. G.: "Modelling fibre and composite failure," in: *European Symposium on Damage Development and Failure Processes in Composite Materials*, Leuven, Belgium, 1987, pp. 8-19.
 - [23] Wisnom, R.: "The effect of fibre misalignment on the compressive strength of unidirectional carbon fibre/epoxy," *Composites*, Volume 21, 1990, pp. 403-407.
 - [24] Drzal, L. T. and Madhukar, M.: "Fibre-matrix adhesion and its relationship to composite mechanical properties," *Journal of Materials Science*, Volume 28, 1993, pp. 569-610.
 - [25] Hahn, H. T. and Williams, G.: "Compression failure mechanisms in unidirectional composites," *Composite Materials: Testing and Design, ASTM STP 893*, J. M. Whitney, Ed., 1986, pp. 115-139.
 - [26] Nakanishi, Y., Hana, K. and Hamada, H.: "Fractography of failure in CFRP under compressive load," *Composites Science and Technology*, Volume 57, 1997, pp. 1139-1147.
 - [27] Chen, F., Bazhenov, S., Hiltner, A. and Baer, E.: "Flexural failure mechanisms in unidirectional glass fibre-reinforced thermoplastics," *Composites*, Volume 25, 1994, pp. 11-20.
 - [28] Neubert, H., Schulte, K. and Harig, H.: "Anwendung der Thermometrie bei der Prüfung von Faserverbundwerkstoffen," *Werkstoffprüfung 1985*, DVM, 1985, pp. 373-382.
 - [29] Reifsnider, K. L., Schulte, K. and Duke, J. C.: "Long-term fatigue behaviour of composite materials," *Long-term Behaviour of Composites, ASTM STP 813*, T. K. O'Brien, Ed., 1983, pp. 136-159.
 - [30] Hahn, H. T.: "Fatigue behaviour and life prediction of composite laminates," *Composite Materials: Testing and Design, ASTM STP 674*, S. W. Tsai, Ed., 1979, pp. 383-417.
 - [31] Hashin, Z. and Rotem, A.: *Journal of Composite Materials*, Volume 7, 1973, pp. 448-464.
 - [32] Dharan, C. K. H.: "Fatigue failure in graphit fibre and glass fibre-polymer composites," *Journal of Materials Science*, Volume 10, 1975, pp. 1665-1670.
 - [33] Oever, M. van den and Peijs, T.: "Continuous-glass-fibre-reinforced polypropylene composites; II. Influence of maleic-anhydride modified polypropylene on fatigue properties," *Composites A*, Volume 29, 1998, 227-239.
 - [34] Baron, Ch. and Schulte, K.: "Fatigue damage response of CFRP with toughened matrices and improved fibres," *Proc. ICCM-VI/ECCM-2*, London/UK, 1987, pp. 4.54-4.64.
 - [35] Schulte, K., Reese, E. and Chou, T. W.: "Fatigue behavior and damage development in woven fabric and hybrid fabric composites," *Proc. ICCMVI/ECCM-2*, London/UK, 1987, pp. 4.89-4.99.

Scott W. Case,¹ Kenneth L. Reifsnider,¹ and John J. Lesko¹

Philosophies for Assessing Durability of Commercial and Infrastructure Composite Systems

Reference: Case, S. W., Reifsnider, K. L., and Lesko, J. J., "Philosophies for Assessing Durability of Commercial and Infrastructure Composite Systems," *Composite*

Materials: Testing, Design, and Acceptance Criteria, ASTM STP 1416, A. Zureick and A.T. Nettles, Eds., American Society for Testing and Materials International, West Conshohocken, PA, 2002.

Abstract:

A key need for the commercial acceptance and viability of composite structural material systems is a methodology for reliability and lifetime predictions. In this paper, we present a philosophy in which the residual strength of the composite material is calculated as a function of applied loading conditions, environment, and resulting failure mode. Two specific example applications are considered: the assessed and verified performance of fiber wound composite tubes and pultruded shapes. We attempt to demonstrate the understanding of the controlling damage mechanisms and the degradation processes that contribute to the loss in stiffness and strength under simulated service conditions.

Keywords: durability, life prediction, residual strength

Introduction and Motivation

Many groups have made the claim that fiber reinforced plastic (FRP) composites will offer improved durability and corrosion resistance over metallic materials for infrastructure and commercial applications. However, these claims have not been substantiated in the open literature. The group on International Research on Advanced Composites for Construction (IRACC) stated that the understanding and mechanistic description of composite durability is the primary obstacle to routine use of these material systems in civil infrastructure. Properties such as stiffness may change by more than 40% during the life of a component. These property changes are integrally coupled to the damage and failure modes that control remaining strength and life, the critical features of such materials and structures. Unfortunately, many of the operative mechanisms and processes that cause these changes are highly nonlinear in response to stress, temperature, time, or aggressive environments, and especially so in response to combinations of those applied conditions. A clear understanding of the overall response of composites subjected to multiple mechanisms of degradation/physical change is a challenging problem with critical consequences.

¹ Assistant Professor, Professor, and Associate Professor, respectively, Department of Engineering Science and Mechanics, Mail Code 0219, Virginia Tech, Blacksburg, VA, 24061.

The prediction of this composite damage and life prediction for composite materials has been the subject of many investigations during recent years. An excellent review of work in this area of fatigue life predictions has been given by Liu and Lessard [1]. In this paper, they divided the models used to predict fatigue life into three classes: residual strength degradation, modulus degradation, and damage tolerance approaches. In our current work, we will focus on the residual strength approach.

In the residual strength degradation approach, fatigue failure is typically assumed to occur when the residual strength becomes equal to the applied maximum stress amplitude. Such an approach was used by Broutman and Sahu [2], who proposed a cumulative damage theory based on a linear strength degradation approach to explain the fatigue damage of fiberglass reinforced composites. Using this approach, they were able to make predictions for the residual strengths of laminates which were subjected to high-low stress tests and of laminates which were subjected to low-high stress tests. These predictions were compared with the experimentally measured residual strengths.

Reifsnider and his coworkers [3-6] proposed a nonlinear residual strength prediction based on the critical element model. In this approach, a representative volume was selected which was typical of the material in question. This representative volume may contain damage, such as matrix cracks, delaminations, microbuckles, or fiber fractures, but some part of it still retains the ability to carry load. It is the failure of this part of the representative volume, the "critical element," which determines the fracture of the entire representative volume. The remaining strength of the critical element was calculated by using a nonlinear damage evolution equation that accounts for the changing stress amplitude in the critical element. The predictions of the model were compared with laboratory data for polymeric as well as ceramic composite systems.

In this paper, we present a philosophy by which the residual strength approach may be applied to the analysis of composite materials subjected to complex environmental and mechanical loadings.

Life Prediction Philosophy

We begin our analysis by postulating that remaining strength may be used as a damage metric. We next assume that the remaining strength may be determined (or predicted) as a function of load level and some form of generalized time. For a given load level, a particular fraction of life corresponds to a certain reduction in remaining strength. We claim that a particular fraction of life at a second load level is equivalent to the first if and only if it gives the same reduction in remaining strength, as illustrated in Figure 1. In the case of Figure 1, time t_1 at an applied stress level S_a^1 is equivalent to time t_2^0 at stress level S_a^2 because it gives the same remaining strength. In addition, the remaining life at the second load level is given by the amount of generalized time required to reduce the remaining strength to the applied load level. In this way, the effects of several increments of loading may be incorporated into the analysis by adding their respective reductions in remaining strength. The process by which this may be accomplished will be described later in this work.

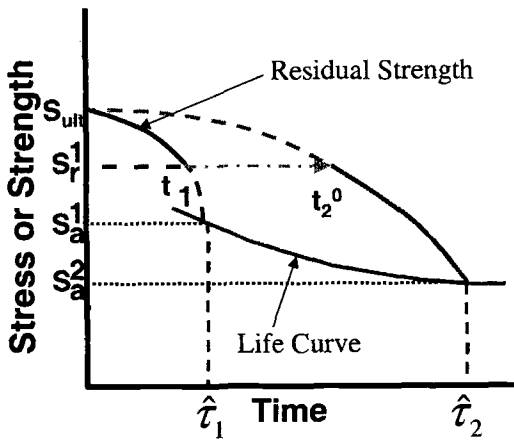


Figure 1—The use of remaining strength as a damage metric.

Our next step in the analysis is select an appropriate failure criterion (such as maximum stress or Tsai-Wu) which is a scalar combination of the principal material strengths and applied stresses in the critical element. In this way we are able to consider a single quantity rather than the individual components of the strength tensor. We denote this failure function by Fa . We next define a generalized time, τ , so that

$$\tau = \frac{t}{\hat{\tau}} \quad (1)$$

and $\hat{\tau}$ is the characteristic time for the process at hand. This characteristic time could be a creep rupture life, a creep time constant, or even a fatigue life, in which case

$$\tau = \frac{n}{N} \quad (2)$$

where n is the number of fatigue cycles and N is the number of cycles to failure at the current applied loading conditions.

For the case in which Fa is constant, we assume that the residual strength is given by

$$Fr = 1 - (1 - Fa)\tau^j \quad (3)$$

For a detailed discussion of the motivation for Eq. (3), the reader is referred to references [3-5]. A special case of Eq. (3) is that of initial fatigue loading at constant amplitude in which

$$\begin{aligned} \tau &= \frac{n}{N} \\ Fa &= \frac{S_a}{S_{ult}} \\ Fr &= \frac{S_r}{S_{ult}} \end{aligned} \quad (4)$$

where S_a is the applied fatigue stress level, and S_{ult} is the initial ultimate strength.

Substituting into Eq. (3), we arrive at

$$\frac{S_r}{S_{ult}} = 1 - \left(1 - \frac{S_a}{S_{ult}} \right) \left(\frac{n}{N} \right) \quad (5)$$

However, for cases in which $Fa(\tau)$ is not continuous (such as in the case of block loading) we use a slightly modified approach based on the idea of remaining strength as a damage metric. To explain our implementation of these ideas, we will consider the case of creep loading at a level Fa_1 for a generalized time τ_1 , resulting in a remaining strength Fr . This loading is followed by loading at a level Fa_2 . The question then is how to determine the equivalent amount of time, t_2^0 , that would have been necessary to cause an equivalent amount of damage (reduction in residual strength) at the level Fa_2 . We will call a time “pseudo-time” because it does not refer to actual time. Substituting into Eq. (3) and using the idea of equivalent remaining strength, we obtain

$$Fr = 1 - (1 - Fa_1) \tau_1^j = 1 - (1 - Fa_2) (\tau_2^0)^j \quad (6)$$

Eq. (6) may then be solved for the generalized pseudo-time to yield

$$\tau_2^0 = \left(\frac{1 - Fr}{1 - Fa_2} \right)^{\frac{1}{j}} \quad (7)$$

The equivalent pseudo-time, t_2^0 (unnormalized), is given by

$$t_2^0 = \hat{\tau}_2 \tau_2^0 = \left(\frac{1 - Fr}{1 - Fa_2} \right)^{\frac{1}{j}} \hat{\tau}_2 \quad (8)$$

Making use of Eq. (3) the change in remaining strength, ΔFr , over the interval $(t_1, t_1 + \Delta t)$ which corresponds to an interval $(t_2^0, t_2^0 + \Delta t)$ in pseudo-time is then given by

$$\Delta Fr = -(1 - Fa_2) \left\{ \left[\frac{t_2^0 + \Delta t}{\hat{\tau}_2} \right]^j - \left(\frac{t_2^0}{\hat{\tau}_2} \right)^j \right\} \quad (9)$$

In general, such an approach may be carried out for any number of blocks of loading having an applied stress level Fa_i so that the remaining strength is given by

$$Fr = 1 - \sum_{i=1}^{N_{blocks}} \Delta Fr_i \quad (10)$$

where N_{blocks} is the number of blocks of loading. For cases in which more than one damage mechanism acts, this process may be repeated for each of the mechanisms (e.g. [7-8]).

To illustrate practical applications of the residual strength approach, we will consider two cases: a hoop wound pipe subjected to internal pressure due to water and a pultruded composite beam subjected to cyclic bending loads.

Example Application: Composite Pipe

The life prediction analysis for the composite pipe consists of four separate subanalyses: the axisymmetric stress analysis, the axisymmetric moisture diffusion analysis, the residual strength analysis, and the progressive failure analysis. The first two

analyses make use of standard techniques. The stress analysis is an elasticity solution for a multi-layer composite pipe similar to that presented by Hyer and Rousseau [9]. Each of the constituent layers is assumed to be linearly-elastic and orthotropic. The moisture diffusion is assumed to obey Fick's law, and the resulting axisymmetric diffusion problem is solved using the alternating-direction explicit (ADE) finite-difference method [10].

In the residual strength calculations, we actually consider two different modes of failure. The first failure mode is a bursting failure mode characterized by rupture of the hoop direction glass. For this fiber-controlled failure, we use a maximum stress failure criterion, so that

$$Fa_{burst} = \frac{\sigma_1}{X_t} \quad (11)$$

We assume that a Tsai-Wu failure criterion may be used to predict the cracking behavior of the plies. This criterion takes the form of

$$Fa_{cracking} = \sqrt{F_{11}\sigma_1^2 + F_{22}\sigma_2^2 + F_{12}\sigma_1\sigma_2 + F_1\sigma_1 + F_2\sigma_2 + F_{66}\sigma_{12}^2} = 1 \quad (12)$$

where the values for F_{ij} and F_i are constants. These values may be related to the principal composite strengths as follows:

$$\begin{aligned} F_{11} &= \frac{1}{X_t X_c} & F_1 &= \frac{1}{X_t} - \frac{1}{X_c} \\ F_{22} &= \frac{1}{Y_t Y_c} & F_2 &= \frac{1}{Y_t} - \frac{1}{Y_c} \\ F_{66} &= \frac{1}{S^2} \end{aligned} \quad (13)$$

Different approaches have been suggested to determine the value of F_{12} . For our purposes, we assume that F_{12} may be calculated as

$$F_{12} = -\frac{1}{2} \sqrt{F_{11}F_{22}} \quad (14)$$

Since these phenomenological representations of the strength versus combined loading conditions seem to represent the observed behavior well, it seems reasonable to assume that this Tsai-Wu failure criterion can be used to predict the failure of layers made from these materials. The question then is how to predict the strength of these layers that are made from different percentage compositions of these materials. As a first estimate, we may assume that the strengths in each of the principal directions for the layers may be determined using micromechanical models. The Tsai-Wu parameters are then determined using the expressions given in Eqs. (13) and (14).

These expressions relate only to the initial properties of the layers. For the pipe lifetime prediction, it is also necessary to include the manner in which those properties change with time, and due to environmental effects. To introduce the effects of moisture, we use the approach suggested by Springer [11]—the material properties can be reduced using a linear function of the moisture content. The properties are reduced linearly according to the maximum moisture content, the maximum percentage of reduction so that

$$X = X_o \left(1 - \frac{\text{Max_reduction_ \% } \times \text{moisture_ content}}{\text{moisture_ content}_{\max}} \right) \quad (15)$$

where X_o is the initial value, and X is the reduced value. The maximum reduction in properties as well as the corresponding maximum moisture content are then determined experimentally.

In addition to the moisture effects, it is also necessary to introduce the information that describes the lifetime of the plies as a function of rupture and fatigue stresses. This information is obtained from previous results cited in the literature. For the rupture case, we assume that Zhurkov's theory of rupture [12] may be applied. This implies that, for 1-D loading

$$\frac{S}{S_{ult}} = A_r + B_r \log t_{rupture} \quad (16)$$

or that in terms of the failure criterion

$$Fa = A_r + B_r \log t_{rupture} \quad (17)$$

Based upon tests conducted on chopped strand mat laminates in air by Phillips [13], we assume values of

$$\begin{aligned} A_r &= 1.00 \\ B_r &= -0.05 \end{aligned} \quad (18)$$

For the fatigue loading situation, we make use of the work of Schutte [14] who collected previous work of Mandell. From this work, we find that for glass fiber composites, *regardless of the fiber architecture*, the fatigue lifetime may be expressed in the form of

$$\frac{S_a}{S_{ult}} = A_n - 0.1 \log N \quad (19)$$

or, written in terms of the failure criterion

$$Fa = A_n - 0.1 \log N \quad (20)$$

A separate residual strength quantity (Fr_{burst} or $Fr_{cracking}$) is then calculated for each of the failure modes (burst failure or cracking). When the residual strength for a particular failure mode is equal to the corresponding failure criterion, failure by that mode is assumed to occur. In the case of hoop failure, bursting of the pipe occurs immediately. In the case of cracking, a progressive damage analysis is employed. The progressive damage involves two aspects: discounting the transverse and shear stiffness values of the cracked layer by a factor of ten, and increasing the diffusivity of the cracked layers by a factor of one hundred.

The general procedure employed in the life prediction scheme for the case of weeping failure (pipe leakage) is shown in Figure 2 (for burst failure, no progressive damage analysis is used). To illustrate the applicability of the approach, we consider the composite pipe subjected to internal pressurization studied by Bodin [15]. The geometry and initial material properties are identical to those employed by Bodin in his study. For convenience, the analysis models described above have been incorporated into a user-friendly analysis code with a graphical user interface. The results of the application of the analysis to the prediction of the pipe lifetime (due to either burst or weeping failures) are shown in Figure 3.

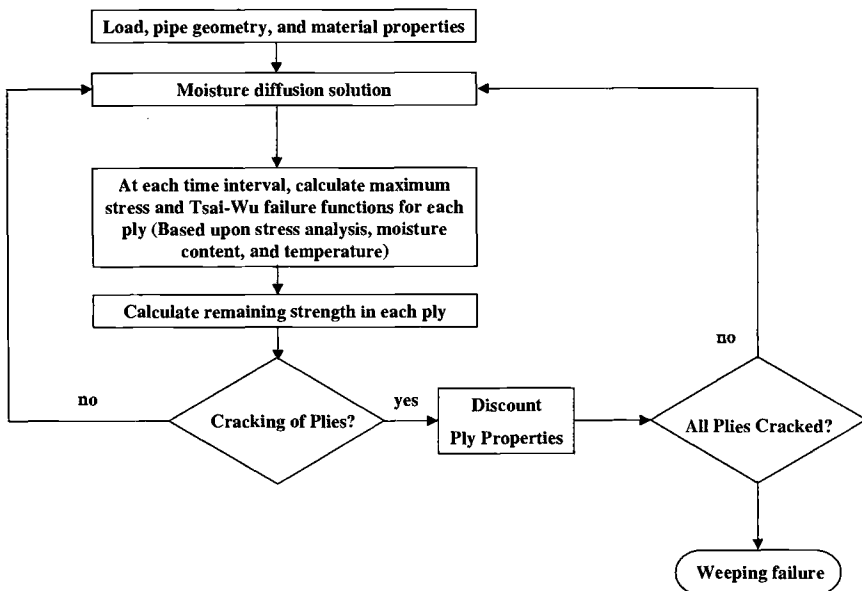


Figure 2—Flowchart for life prediction approach used for weeping failure.

Example Application: Pultruded Composite Beam

Life Prediction for Thick Section Composites

Much of the prior work for composite life prediction has focused on in-plane, fiber failure dominated damage controlled process. The structural members used in the civil infrastructure are often of thick section and fail due to out-of-plane or matrix dominated damage. Thus the work presented here is based on testing and analysis of the 20.3 cm (8 in) double-web beam (Extren DWBTM) manufactured by the Strongwell Corp [16], and used in the Tom's Creek Bridge in Blacksburg, VA [17]. The beam is a pultruded hybrid section, consisting of unidirectional carbon in the flanges and stitched mat E-glass in a vinyl-ester resin, where the failure of the girder is controlled by delamination buckling in the top flange at the location of the hybridization.

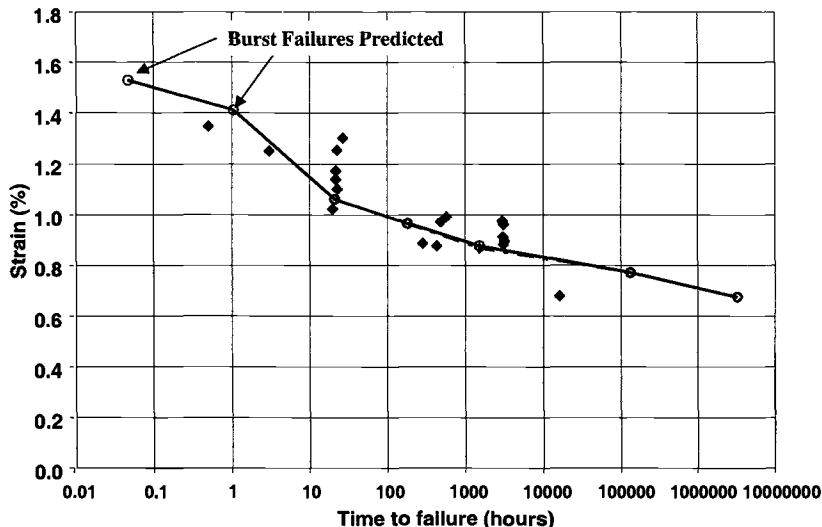


Figure 3—Predicted and measured lifetimes for composite pipe. Experimental results are given by solid symbols. Burst failures are predicted for the highest two applied strain levels; weeping failures for all others.

Methodology Assumptions

We consider the case where the DWB is subjected to four-point bending fatigue loading. The model employs the idea that initially stiffness reduction only occurs in the tensile flange. As the stiffness of the bottom/tensile flange is reduced, there is a redistribution of strain to the compressive flange and an inherent shift in the neutral axis. The remaining strength approach, in conjunction an iterative stress analysis is then used to determine the onset of delamination and the crack growth to failure. The assumptions employed in the residual strength model include the following.

- Reduction in tensile stiffness of the beam will be evaluated, based on tensile coupon data of similar material conducted by Phifer [18] which focuses on off-axis plies.
- The unidirectional carbon plies do not experience any stiffness reduction.
- Strength reduction is uniform for both the tensile and compression flanges and is related to the in-plane strength reduction of the tensile flange.
- The carbon acts stiffer in tension than in compression, therefore the neutral axis is initially offset toward the tensile flange but during loading shifts toward the compressive side.
- The tensile out-of-plane strength (Z_t) is calculated from the M_{ult} found from quasi-static failure testing.
- Once delamination initiates, stiffness reduction must be accounted for in the compression flange in addition to the tensile flange.
- Crack growth, once delamination is initiated, is symmetric from each side of the beam, across the width of the beam (in the y-direction)

- Failure occurs when the crack propagates across the width of the beam or if the in-plane remaining strength matches the loading.

The flowchart in Figure 4 graphically describes the process required to assess life. The process begins by inputting the geometry, layup, and loading. Using this information the stresses and strains are evaluated. The free edge stresses are then compared to the strength of the top flange. If the stress exceeds the in-plane strength, delamination is assumed. If the stress does not exceed the strength, the stiffness in the tensile flange is reduced based on a maximum strain criterion. The neutral axis shift corresponding to the stiffness reduction is then calculated. The new stiffness and neutral axis location are used in laminated beam theory to determine the new EI_{eff} and curvature. The κ_x^0 becomes the new loading condition for the stress evaluation. The process is continued until delamination initiation.

Stiffness Reduction of the Tensile Flange

Prior tensile fatigue testing of pultruded, E-glass, vinyl ester laminates is used to characterize the stiffness reduction of the bottom flange. The dynamic stiffness reduction was monitored in the tests; and indicates a linear reduction in stiffness occurs with respect to cycles at a given load [18], following an initial drop off. The flange is divided into sublaminates that mimic the cross-ply and quasi-isotropic coupons tested, and the stiffness reduced on a sub-laminate basis.

For modeling the beam, it seems that the initial coupon degradation is similar to what occurs in the beam itself, therefore the data was fit to a logarithmic curve to capture the initial area, and then flatten out. The resulting curve fits were

$$\text{Quasi-Isotropic: } \frac{E_x}{E_o} = -0.0124 \ln\left(\frac{n}{N}\right) + .8281 \quad (21)$$

$$\text{Cross-Ply: } \frac{E_x}{E_o} = -0.0118 \ln\left(\frac{n}{N}\right) + .8933 \quad (22)$$

The reduction of the quasi-isotropic laminates is more severe initially, but both have similar attributes thereafter due to the nature of the logarithmic curve fit. In the analysis, the effective modulus of a sublamine is found from a rule of mixtures approach

$$E_{eff} = \frac{\sum E_{x,i} t_i}{\sum t_i} \quad (23)$$

where $E_{x,i}$ is the equivalent modulus in the axial direction for a ply of any orientation and t_i is the thickness of the respective ply. This effective stiffness was then used in the same manner to determine the stiffness of the entire flange. For the entire flange the $E_{x,i}$ and t_i are the sublamine E_{eff} and thickness, respectively.

Neutral Axis Shift

Initially, the neutral axis shift is toward the tensile flange, as carbon acts stiffer in tension than in compression. As the stiffness of the flanges change, there is a shift in the neutral axis. This shift inherently changes the strain distribution across the section and will influence the in-plane stiffness reduction. Initially, the neutral axis moves toward the

compression flange, and once delamination occurs, it begins to shift toward the bottom flange. The location of the neutral axis is simply found by considering the effective E_x for the top and bottom flanges, in the standard mechanics of materials calculation

$$NA = \frac{\sum E_{x,i} t_i \bar{y}_i}{\sum E_{x,i} t_i} \quad (10)$$

The influence of the neutral axis shift on the inertia properties is negligible and is not accounted for in the analysis. A .635 cm (0.25 in) shift, representing the carbon acting 76% less stiff in compression, results in a less than 1% change in inertia values.

Out-of-Plane Strength Properties

The quadratic delamination theory proposed by Brewer and Lagace [19] predicts delamination initiation, based on the out-of-plane stresses and strengths. Failure is assumed to occur when

$$\left(\frac{\tau_{xz}}{Z_{xz}} \right)^2 + \left(\frac{\sigma_z}{Z_t} \right)^2 \geq 1 \quad (24)$$

where τ_{xz} and σ_z are interlaminar stresses calculated using variational mechanics. In terms of a failure criterion, Eq. (24) may be expressed as

$$Fa_{out-of-plane} = \sqrt{\left(\frac{\tau_{xz}}{Z_{xz}} \right)^2 + \left(\frac{\sigma_z}{Z_t} \right)^2} \quad (25)$$

The value of τ_{xz} is negligible in this analysis when compared to the matrix strength, allowing the Eq. (25) to be simplified as

$$Fa_{out-of-plane} = \frac{\sigma_z}{Z_t} \quad (26)$$

The out-of-plane strength in the z-direction (Z_t) is assumed to be the maximum calculated σ_z at the critical glass carbon interface at failure in the quasi-static test.

In the fatigue situation, we must predict changes in the residual through-thickness strength. To do so, we employ the failure criterion given in Eq. (26) with the residual strength calculation approach outlined in [3]. Delamination is predicted to initiate when the residual strength calculated in this fashion is equal to the value of the failure criterion calculated using Eq. (26).

Crack Growth

Following the onset of delamination, stiffness reduction of the compressive flange must also be considered with the tensile in-plane effects. These effects are also coupled with the crack growth and propagation to predict the ultimate failure of the beam. The reduction scheme is shown schematically in Figure 4. This stiffness reduction is used with the continued modulus reduction in the bottom (tensile) flange to determine the neutral axis shift. The new stiffness values and neutral axis location are then used to determine EI_{eff} and κ_x^0 that allow for calculation of the stress state. The drop in stiffness and increase in curvature will inherently raise the stresses and may cause additional failures. The initial crack, and any newly formed cracks, are then monitored and continue through this evaluation cycle until failure. The process used to calculate the stiffness

reduction in the compression flange as well as the rate of delamination growth is outlined below.

Compressive Flange Stiffness Reduction

The new modulus of the compression flange is determined through a rule of mixtures approach developed by O'Brien [20]

$$E_x = (E^* - E_{lam}) \frac{a}{b} + E_{lam} \quad (27)$$

In Eq. (27), a is the crack length of the largest crack in the laminate, b is the half width of the laminate, E^* represents the effective modulus of the laminate if the layers are completely delaminated from each other, and E_{lam} is the initial effective modulus value of the laminate. The rule of mixtures is also used to determine E^* :

$$E^* = \frac{\sum E_{x,i} t_i}{t} \quad (28)$$

where $E_{x,i}$ and t_i represent the effective modulus and thickness of the sublaminates formed by the cracks.

Crack Growth

Once delamination initiates, crack growth is considered symmetric from each free edge of the beam. O'Brien has shown a good estimation of crack growth is based on the relation [20, 21]

$$\frac{da}{dn} = \left(\frac{b}{E^* - E_{LAM}} \right) \left(\frac{dE}{dn} \right) \quad (29)$$

where dE/dn is the change in modulus over the step size, and all other terms are consistent with their definitions above. The crack growth rate (da/dn) is not constant, since it is dependent on the number of layers that have delaminated at a given time, thus as more layers delaminate, the rate of crack growth increases.

Determining Failure of the Beam

The model predicts failure due to in-plane effects and also delamination. Failure is assumed when either of the following criteria are met:

1. Delamination initiates and the crack completely propagates across the width of the beam, or
2. The in-plane remaining strength of the beam matches the loading ($F_a = F_r$).

These criteria are met when the remaining strength curve intersects the respective loading curve intersection of the remaining strength curve and the applied load curve.

Predicted S-N Curve Compared to Experimental Data

An S-N curve was created for the beam considering no neutral axis shift and using the overall average ultimate moment data to determine the strength of the beam. The experimental points and the predicted S-N curve are plotted in Figure 5, normalized to the average ultimate moment of all of the hybrid beams tested from both batches. The beam failure at 53% is about six orders of magnitude from the prediction. The two beams which experienced runout at 8 and 10 million cycles were under the predicted failure.

The beam that failed after 370 000 cycles at 71% of the average ultimate moment agrees well with the prediction of 300 000 cycles at the same load. Without further data, the validity of the model overall cannot be determined.

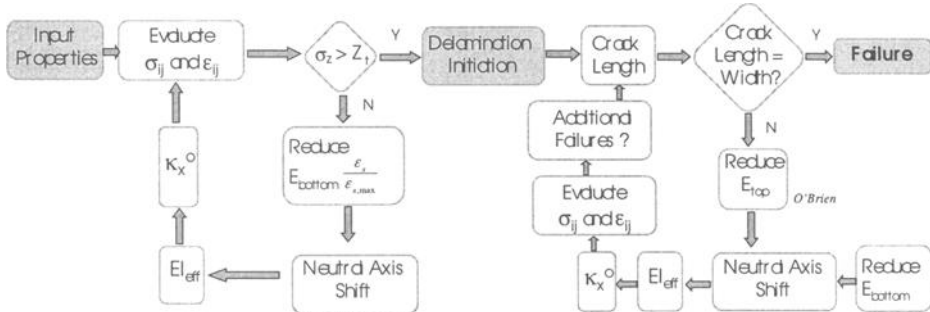


Figure 4—Flowchart of Stress Analysis and Stiffness reduction, delamination determination, and stress redistribution following delamination.

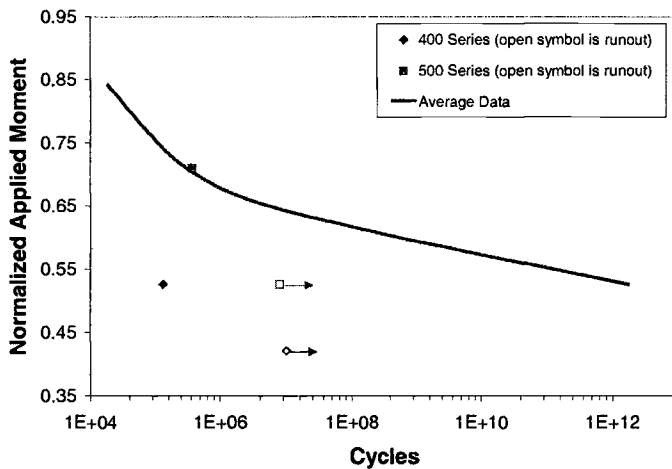


Figure 5—Comparison of predicted S-N curve for beam fatigue loading to experimental data.

Summary and Future Directions

In this work, we have outlined a philosophy based upon the residual strength approach that may be used to predict the lifetime of commercial composite systems. This philosophy may incorporate multiple damage modes such as those due to environmental and mechanical loads. A key feature of this philosophy is that the stress analysis resulting

from the design and the predicted performance are coupled with one another, thus it is possible to adjust the design based upon recognizing the influences of material and geometry on durability. Two examples were considered: a composite pipe and a hybrid composite beam. For the pipe, two different types of failure were recognized: burst failure and weeping failure. Burst failure is controlled by the hoop strength layer whereas the weeping failure is controlled by the ability of the layers to resist cracking. In the case of the beam, degradation in through-thickness strength of the hybridized region controls the initiation of delamination. Subsequently, this delamination grows rapidly, leading to failure of the beam. As a result, by improving the resistance to delamination, we may improve the service life of the beam.

References

- [1] Liu, B. and Lessard, L. B. "Fatigue and Damage Tolerance Analysis of Composite Laminates: Stiffness Loss, Damage Modelling, and Life Prediction," *Composites Science and Technology*, Vol. 51, 1994, pp. 43-51.
- [2] Broutman, L. J. and Sahu, S. "A New Damage Theory to Predict Cumulative Fatigue Damage in Fiberglass Reinforced Plastics," *Composite Materials: Testing and Design (Second Conference)*, ASTM STP 497, American Society for Testing and Materials, Philadelphia, PA, 1972, pp. 170-188.
- [3] Reifsnider, K. L., Iyengar, N., Case, S. W. and Xu, Y. L. "Damage Tolerance And Durability Of Fibrous Material Systems: A Micro-Kinetic Approach," *Durability Analysis of Structural Composite Systems*, A. H. Cardon, ed., A. A. Balkema, Rotterdam, 1996, pp. 123-144.
- [4] Reifsnider, K., Iyengar, N., Case, S. and Xu, Y. "Kinetic Methods for Durability and Damage Tolerance Design of Composite Components," Keynote Address, Conference on Composite Materials, Japan Society for Mechanical Engineers, June 26, 1995, Tokyo.
- [5] Reifsnider, K., Lesko, J., and Case, S. "Kinetic Methods for Prediction of Damage Tolerance of High Temperature Polymer Composites," Composites '95: Recent Advances in Japan and the United States, I. Kimpara, H. Miyairi, and N. Takeda, eds., Proceedings Japan-U.S. CCM-VII, Kyoto, 1995, pp. 49-55.
- [6] Reifsnider, K., Case, S. and Iyengar, N. "Recent Advances in Composite Damage Mechanics," *Proc. of Conference on Spacecraft Structures, Materials & Mechanical Testing* (ESA SP-386), Noordwijk, The Netherlands, June 1996, pp. 483-490.
- [7] Case, S., Iyengar, N. and Reifsnider, K. "Life Prediction Tool for Ceramic Matrix Composites at Elevated Temperatures," *Composite Materials: Fatigue and*

Fracture, Seventh Volume, ASTM STP 1330, R. B. Bucinell, ed., American Society for Testing and Materials, Philadelphia, PA, 1998, pp. 165-178.

- [8] Loverich, J. S., Russell, B. E., Case, S. W., and Reifsnider, K. L. "Life Prediction of PPS Composites Subjected to Cyclic Loading at Elevated Temperatures," *Time Dependent and Nonlinear Effects in Polymers and Composites, ASTM STP 1357*, R. A. Schapery and C. T. Sun, Eds., American Society for Testing and Materials, Philadelphia, PA, 2000, pp. 310-317.
- [9] Hyer, M. W., and C. Q. Rousseau, "Thermally-Induced Stresses and Deformation in Angle-Ply Composite Tubes," *Journal of Composite Materials*, Vol. 21, No. 5, 1987, pp. 454-480.
- [10] Anderson, D. A., Tannehill, J. C., and Pletcher, R. H., *Computational Fluid Mechanics and Heat Transfer*, Hemisphere Publishing Corporation, 1984, pp. 119-120.
- [11] Springer, G. S. "Effects of Temperature and Moisture on Sheet Molding Compounds," *J. of Reinforced Plastics and Composites*, Vol. 2, 1983, pp. 70-89.
- [12] Zhurkov, S. N, *Int. J. of Fracture Mechanics*, Vol. 1, pp. 311-322, 1965.
- [13] Phillips, M. G. "Prediction of Long-Term Stress-Rupture Life for Glass Fibre-Reinforced Polyester Composites in Air and Aqueous Environments," *Composites*, , July 1983, pp. 270-275.
- [14] Schutte, C. "Environmental Durability of Glass-fiber Composites," *Mat. Sc. & Eng.* 1994.
- [15] Bodin, J.-M., *Life Prediction of Composite Pipes in Sewage-Type Environments*, M. S. Thesis, Virginia Polytechnic Institute and State University, August 1998.
- [16] *Extren DWB Design Guide: 8"x6" Double Web Beam (DWB) Hybrid and All-Glass Material Configurations*, Strongwell, Corp. Bristol, VA, 2000.
- [17] Hayes, M. D., Lesko, J. J., Haramis, J., Cousins, T. E., Gomez, J., Massarelli, P., "Laboratory and Field Testing of Composite Bridge Superstructure," ASCE, *Journal of Composites for Construction*, Vol. 4, No. 3, 2000, pp. 1-9.
- [18] Phifer, S.P., *Quasi-Static and Fatigue Evaluation of Pultruded Vinyl Ester/E-Glass Composites*, M.S. Thesis, Virginia Polytechnic Institute and State University, May 1999.

- [19] Brewer, J.C. and Lagace, P.A. "Quadratic Stress Criterion for Initiation of Delamination," *Journal of Composite Materials*, Vol. 22, Dec 1988, pp. 1141-1155.
- [20] O'Brien, T.K., "Generic Aspects of Delamination in Fatigue of Composite Materials," *Journal of the American Helicopter Society*, Vol. 32, Jan 1987, pp 13-18.
- [21] O'Brien, T.K., "Stacking Sequence Effect on Local Delamination Onset in Fatigue", *International Conference on Advanced Composite Materials*, The Minerals, Metals & Materials Society, 1993, pp. 399-406.

Guillaume Terpant,¹ Prakash Krishnaswami,¹ and Youqi Wang¹

Computational Prediction of Yarn Structure of 3D-Braided Composites

Reference : Terpant, G., Krishnaswami, P., and Wang, Y. Q., “**Computational Prediction of Yarn Structure of 3D-Braided Composites,**” *Composite Materials: Testing, Design, and Acceptance Criteria, ASTM STP 1416*, A. Zureick and A. T. Nettles, Eds., American Society for Testing and Materials International, West Conshohocken, PA, 2002.

Abstract: In order to design braiding sequences for three-dimensional braided components, a method to predict the yarn structure is necessary, because the mechanical properties of the component are dependent on the yarn structure. Satisfactory methods for predicting yarn structure based on braiding sequence are presently unavailable, although recent efforts [1] based on a finite element approach have yielded some positive results. In this paper we present a relatively efficient method based on an optimization approach. In our approach, the basic idea is to exploit the fact that the yarn structure of the braid must be the one that minimizes the total yarn length in the braid. Thus, the yarn structure can be predicted by minimizing the yarn length, subject to the condition that the yarns cannot intersect each other.

Keywords: optimization, 3D-braided composites, preform, yarn structure

Introduction

Three-dimensional braided composites have recently emerged as a promising class of high-tech materials for use in the aviation industry and have many potential applications in other sectors as well [2]. This type of material has two main advantages as compared to traditional two-dimensional reinforced composites. First, they are more robust because there is no risk of delamination failure; second, the braiding sequence and the yarn structure can be chosen to meet specific design requirements. Indeed, investigations have shown that the mechanical properties of three-dimensional braided composites depend mainly on the yarn structure [3-5]. A method to generate a 3D model of the yarn structure in a braided preform for a given braiding sequence is therefore necessary to support the design of 3D braided composite structures. This model must be accurate for both the macro and microstructure level. A large amount of work has been done using experimental and/or analytical methods in the last ten years

¹ Research Assistant, Professor, and Associate Professor, respectively, Department of Mechanical and Nuclear Engineering, 302 Rathbone Hall, Kansas State University, Manhattan, KS 66506.

[6-10]. These methods yielded results on the topology of the braid but do not give detailed information about the yarn shape inside the preform.

Precise analytical models are difficult to build due to the complexity of the process and the large number of parameters that have to be taken into account. Experimental characterization is very expensive and only provides information on one preform. The constantly increasing power of the computer now allows us to consider numerical methods to compute a complete model of a preform. A recent attempt [1] using a finite element approach has given interesting results on the four-step braiding process.

This paper presents a new approach that uses numerical optimization to predict the yarn structure of three-dimensional braided composites. Two optimization methods are presented here, each of which has its advantages and disadvantages. In general, it appears that the suggested approach is capable of generating solid models of preform geometry with reasonable accuracy and reliability.

The braids studied are made of yarns that are assumed to be of circular cross-section. The sequence of braiding steps (called the *braiding sequence*) is known, as well as the number of pitches on the braid considered for each sample. It is assumed that there is no friction and that pulling the yarn along the braiding axis direction tightens the braid. The tension in each yarn is assumed to be the same. If the braid axis is taken to be in the vertical direction, the problem can be seen as the minimization of the potential energy of weights hanging at the extremities of each yarn. As there is no friction, we can restate this problem as the minimization of the total length of the yarns in the braid. Of course, some non-intersection constraints are needed to avoid the solution in which all the yarn hangs straight down, which would be the minimal potential energy solution without constraints.

For the present study, we are mostly concerned with the four-step braiding sequence shown in Figure 1, however any other braiding sequence can be studied using the same method. This braiding sequence was chosen because it is simple and has been

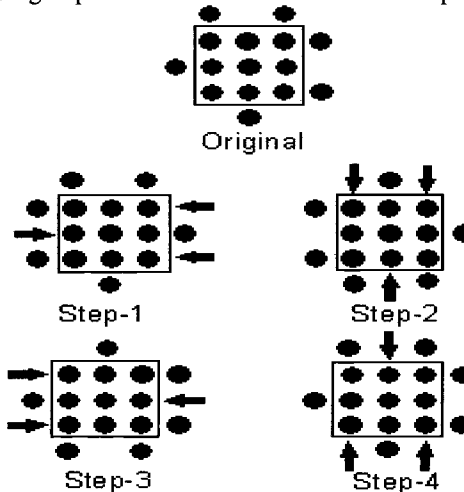


Figure 1 - *The four-step braiding sequence.*

studied in other papers, which was important in providing confirmation of our final results. If n is the number of yarn on one side of the central square (Figure 1), then the number of yarn is $n*(n+2)$. Samples for $n=2$ or $n=3$, i.e. 8 or 15 yarns were studied.

The Optimization Problem

As mentioned above, this paper presents two methods that were tested to predict the yarn structure of 3D-braided composite. Those two methods, although different, have a lot in common and share the same general idea. In both cases, the problem of obtaining the yarn structure is formulated as a nonlinear programming problem (NLP).

A NLP is a standard formulation of an optimization problem that consists of three distinct parts: the design variables, the objective function and the constraints. The problem is to minimize the objective function $f(\mathbf{X})$ where \mathbf{X} is the design vector, $\mathbf{X} = [X_1, X_2, \dots, X_n]^T$, containing the n design variables, subjected to m constraints. The constraints can be of two types:

- $h_j(\mathbf{X}) = 0$ $j = 1, 2, \dots, k$ are the equality constraints
- $g_j(\mathbf{X}) \leq 0$ $j = k, k+1, \dots, m$ are inequality constraints.

In this problem we used only inequality constraints to check for non-intersection of the yarns. It is clear that once the design variables, objective function, and constraints are defined, the NLP is fully specified; once this is done, several numerical methods are available to solve the NLP.

The Design Variables

For this problem, the design variables are the (x, y, z) coordinates of points belonging to the yarn itself or of points defining its shape (e.g., control vertices of B-Splines). The yarns were modeled as flexible solid cylinders. The number of design variables considered is fairly high, in the range of 300 to 2000, depending on the accuracy required and the method used. Of course, increasing the number of design variables leads to greater accuracy. Indeed, as the number of design variables increases, the yarns become more "flexible," which allows for tighter control over the yarn shape.

The Objective Function

In the models considered, it was assumed that there was no friction between the yarns. Furthermore, the only constraints are the non-intersection of the yarns and the geometric constraints at the endpoints of the yarns. Therefore the objective function is just taken as being the sum of the length of the yarns.

The Constraints

The two methods presented later in this paper – the linearization approach and the check points method - differ mostly in the formulation of the constraints. The idea is that the yarns should not intersect or, if they do, the intersection should be small and controlled. Indeed, jamming may occur in an actual braid because the yarns deform as the braid gets tighter because the yarns are not truly solid cylinders.

Moreover, the study relates only to a small sample and one of the assumptions here is that we are looking at the steady state of the braid (i.e. where the braid has a cyclic pattern, after the initial start-up phase). Hence, it was necessary to put constraints on the end points of the yarns to ensure the cyclic behavior was enforced between extremities of the braid.

The Optimization Method

We chose a numerical optimization method that uses an exterior penalty function with a directed grid search for unconstrained minimization. The idea is to minimize a pseudo-objective function, which is given by the sum of the objective function and a set of penalty functions. Each penalty function is a constraint violation multiplied by a high penalty factor. When minimizing the pseudo-objective function, the constraints tend to zero and the objective function is minimized subject to the constraints. The directed grid search method is an unconstrained optimization method which is relatively slow, but very robust. It was adopted because our major concern was to test and prove the proposed methods and not to tune them for efficiency. Thus, throughout this paper, when computational time is mentioned, it has to be remembered that moving to faster optimization methods such as derivative methods could improve efficiency dramatically. The optimization code used is adapted from the Sandia Mathematical Program Library developed at Sandia Laboratories, Albuquerque, New Mexico. The version used is Version 8.1 (August 1980).

Display and Analysis of Results

To analyze the results, we used Excel plots of the center of the yarn, but there was also a need for a powerful 3D modeler to do the solid display. We used ACIS 6.0 for this purpose. All the figures showing solid models of the braid are a screen capture of the 3D model displayed with ACIS 6.0.

First Method: The Linearization Approach

The Yarn Model

This is the first model that was implemented. At first, the natural idea when discretizing the yarn is to use a piecewise linear discretization. This first try, simple to implement, was essential to check if the length minimization approach was reasonable. In this case, the yarn was modeled as an assembly of short cylinders connected at the extremities of their axes.

The Optimization Problem

Clearly, the objective function is the sum of the length of all the short cylinders composing the braid. To simplify the problem, the design variables are only the x and y coordinates of the extremities of each cylinder's axes. The z-coordinates of those points are set constant.

The only constraint applied is that on each $z = \text{constant}$ plane that is considered, the distance between any two cylinder center points should be greater than or equal to one diameter. The diameter minus the distance between the two points is the constraint in case of a constraint violation.

Results and Discussion

The sample studied here is a 15-yarn four-step braiding sequence considered over five pitches. For an optimization problem, generating the initial guess on the design variables can be a major issue. This initial guess (Figure 2 and Figure 3) was generated manually. Each step in Figure 1 (which corresponds to a $z=\text{constant}$ plane) was placed two diameters (in the z direction) from the previous step. Two intermediate points were added on the linear approximation between each plane for each yarn. Thus, we have 15 yarns and five pitches of a four-step braiding sequence (i.e., 20 steps) and two intermediate points between each step. Each point has two associated design variables, x and y . Therefore the number of design variables is $15*2*20*3=1800$. The simulation required 30 minutes on a 450Mhz Pentium II computer, and the final predicted shape of the braid that was obtained is shown in Figure 4 and Figure 5.



Figure 2 - *First guess from the side.*

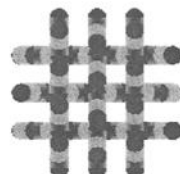


Figure 3 - *First guess from the top.*



Figure 4 - *Predicted shape from the side.*



Figure 5 - *Predicted shape (section).*

With this example, we can see that the general behavior agrees with past experiments; the braid free volume decreases when the total length of the braid is minimized. Moreover, the predicted braid pattern is cyclic as expected and as checked experimentally. Figure 6 shows also that the (x, y) plot of a yarn agrees with the pattern predicted by recent FEM methods [1].

However, this model is not completely satisfactory. We wanted to know with precision the inner structure of the braid without yarn intersection. Figure 5 shows that the yarns intersect and Figure 7 shows that the yarn shape is not very smooth. To get a smoother final shape as well as better control on non-intersection, we would need many more design variables (i.e., a better piecewise linear approximation), however this would lead to a very large NLP problem. It should also be noted that this method, even with a very large number of design variables, will never be exact. Even if the angle of braiding is not very large, the intersection of the cylindrical yarn with a plane perpendicular to the angle of braiding is an ellipse. The way the constraints are implemented, those ellipses are assumed to be circles, which is not the case.

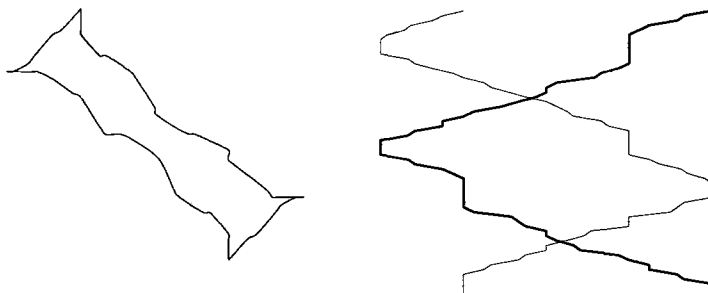


Figure 6 - *Projection of single
yarn on x-y plane.*

Figure 7 - *x (z) and y (z) plot of one
yarn.*

Second Method: The Check Points Method

After the encouraging results obtained from the linearization method, a more efficient and accurate method was necessary to ensure non-intersection and giving better control over the yarn shape. The idea here was to use parametric B-splines. This kind of curve gives good control over the yarn shape with relatively few control vertices and the check for non-intersection of the yarns is possible. This check can be done by generating a large number of random check points inside the braid and checking to see if any of these points falls inside more than one yarn. The number of points belonging to more than one yarn is taken to be the constraint violation.

The Yarn Model

In order to model the yarns, we chose second order non-uniform rational B-splines of the form

$$p(u) = \left(\sum_{i=0}^n h_i \cdot p_i \cdot N_{i,k}(u) \right) / \left(\sum_{i=0}^n h_i \cdot N_{i,k}(u) \right), \text{ with } k=3 \text{ for second order} \quad (1)$$

Here, $p(x, y, z)$ is position vector to the point, u is the parameter, n is the number of control vertices, p_i is the position (x_i, y_i, z_i) of the i^{th} control vertex and h_i its corresponding weight.

$N_{i,k}(u)$ is defined as follows:

$$N_{i,k}(u) = 1 \text{ if } t_i \leq u \leq t_{i+k}$$

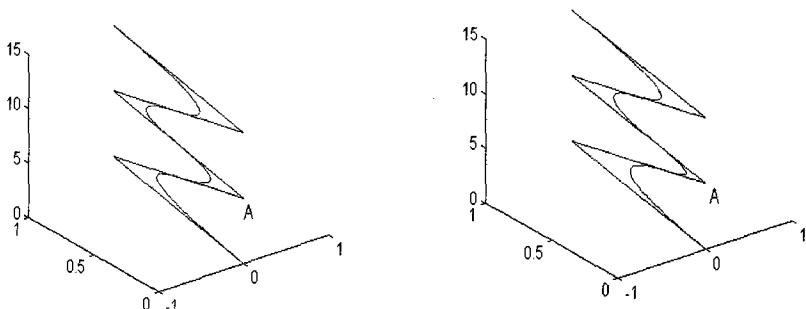
$$N_{i,k}(u) = (u - t_i)^k N_{i,k-1}(u) / (t_{i+k-1} - t_i) + (t_{i+k} - u)^k N_{i+1,k-1}(u) / (t_{i+k} - t_{i+1}) \text{ otherwise}$$

$$\text{where } t_i = 0 \quad \text{if } i < k$$

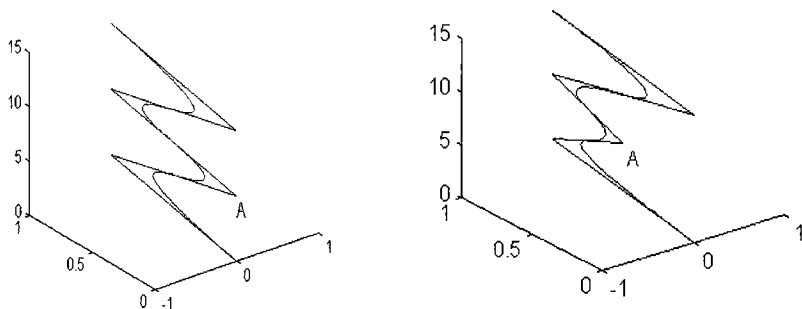
$$t_i = 1-k+1 \quad \text{if } k \leq i \leq n$$

$$t_i = n+k+2 \quad \text{if } i > n$$

This kind of curve is suitable for our purposes for several reasons. First, the curve is easily controlled with just a few control vertices. Moreover, the control vertices of non-uniform rational B-splines can be weighted, changing the shape of the curves as shown in Figures 8 and 9. The curves also have the property of local control (Figures 8 through 11). This means that changes in a control vertex will only affect a small segment of the curve near that vertex. This is important because during the optimization process, the weights and positions of the control vertices vary, and we want the modification of the yarn shape to be limited to a small region. Finally, we used locally quadratic B-splines in order to be able to manipulate the equations conveniently. For instance the inverse calculation to get the value of the parameter t , given a particular value of z (the yarn is monotonic in z), can be done very easily for this type of B-spline, whereas it would be much more complicated and long with a cubic B-spline.



Figures 8 and 9 - Influence of doubling the weight of the control vertex A on the yarn shape.



Figures 10 and 11 - *Influence of moving the control vertex A on the yarn shape.*

The Optimization Problem

Here again, the objective function is the sum of the length of all the yarns. We created a function that computes the length of a B-spline by piecewise linear discretization. The design variables are the (x, y, z) coordinates of the control vertices. A check is made at each step to ensure that the function $z(t)$ is monotonic. The weight of the control vertices can either be set as constant or treated as design variables.

To detect intersections, we first tried a method that generated random points inside the braid and checked each point to see if it fell inside more than one yarn. The number of points belonging to more than one yarn was taken as the value of the constraint violation. To ensure having a cyclic pattern at the ends of the sample, we first tried putting equality constraints to enforce the equality of the x and y values at the two endpoints of each yarn. This idea was rejected and replaced by design variable linking; we found that using the same design variable for both endpoints would be more efficient and reduce the number of control vertices. The z coordinate of the endpoints of each yarn is fixed. If they were treated as design variables, the minimization of the total length of the braid would lead to yarns reduced to a point, which is not what we want.

A few tries using random points showed that there were some difficulties with this method.

- With too few points, the design quickly became infeasible due to the particular random distribution of points; after this, it was often impossible to go back to the feasible region.
- When increasing the number of points, the computational time increased substantially and as the precision required for convergence was increased, the same problem was encountered. The convergence behavior near the solution was also poor.

In fact, with this technique of random points, the boundary of the feasible region is not clearly defined, which adversely affects the performance of the optimization algorithm. It is also better to have a routine that gives the same result for two different runs, which is not the case with the random points. We therefore abandoned the random

point distribution in favor of a fixed, uniform grid of points in the braid region and did the same kind of checking as described above.

The sample studied here is an eight yarn, four-step braiding sequence considered over four pitches. A computer program was written to generate the initial design (Figure 14). The spatial positions of the yarn carriers at each step are generated for a given sequence, given the move sequence and the initial position of the carriers at the start of the braiding process. Using these positions, the program computes a piecewise linear approximation and scales it with a factor $k > 1$ to avoid intersections. Finally, the scaling factor is increased until the B-splines fitting these piecewise linear approximations are all non-intersecting. As mentioned earlier, we have eight yarns with four pitches of a four-step braiding sequence, i.e., 16 steps. Each yarn is defined by 16 control vertices, each of which have three degrees of freedom (i.e., three associated design variables), x , y and z . The number of design variables is therefore equal to $16 \times 3 \times 8 = 384$.

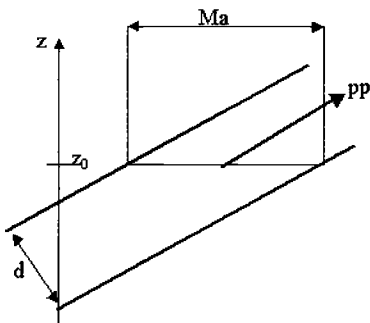


Figure 12 – Ellipse Computation (1).

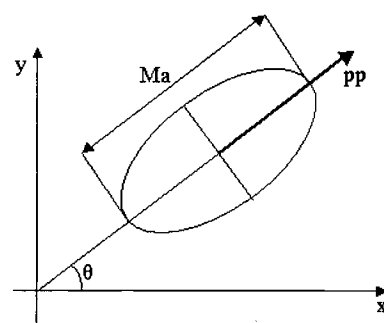


Figure 13 - Ellipse Computation (2).

The first guess can be enclosed in a parallelopiped of size $4 \times 4 \times 16$ units. The diameter of the yarn was taken to be 0.5 units. We chose for this example a regular grid spacing of 0.2 units, so that the number of check points is $4 \times 4 \times 16 / (0.2)^3 = 32\,000$ points. For each new design generated by the optimization algorithm, the following steps were followed for each of the 32 000 points:

- Computation of the value of the parameter t_i corresponding to the z coordinate, z^* , of the grid point for the i^{th} yarn. $z(t)$ is assumed to be monotonic, therefore the t_i is unique.
- Computation of the coordinate $p_i(x(t_i), y(t_i), z^*)$ of the center of the yarn at $z = z^*$.
- Computation of $pp_i(x'(t_i), y'(t_i), z'(t_i))$ at these points; pp_i are the tangent vectors to the yarns at $z = z^*$.
- Computation of major axes of ellipses of intersection of the yarns and the plane $z = z^*$

$$Ma_i = \frac{d \cdot \sqrt{x'(t_i)^2 + y'(t_i)^2 + z'(t_i)^2}}{2 \cdot z'(t_i)}$$

- First check: If the distance between the grid point and the center of the yarn is greater than the major axis of the ellipse, then the grid point is not inside the yarn.
- If the first check is inconclusive, the ellipse equation has to be computed for the final check:

The orientation of the ellipse is obtained by

$$\cos(\theta_i) = \frac{x'(t_i)}{\sqrt{x'(t_i)^2 + y'(t_i)^2}} \quad \sin(\theta_i) = \frac{y'(t_i)}{\sqrt{x'(t_i)^2 + y'(t_i)^2}}$$

And the equation of the ellipse is then given by

$$x(t_i)^2 \cdot \left(\frac{\cos^2(\theta_i)}{b_i^2} + \frac{\sin^2(\theta_i)}{a_i^2} \right) + 2 \cdot x(t_i) \cdot y(t_i) \cdot \cos(\theta_i) \cdot \sin(\theta_i) \cdot \left(\frac{1}{a_i^2} + \frac{1}{b_i^2} \right) + y(t_i)^2 \cdot \left(\frac{\cos^2(\theta_i)}{a_i^2} + \frac{\sin^2(\theta_i)}{b_i^2} \right) = 1$$

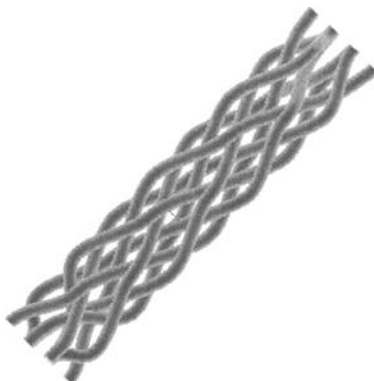
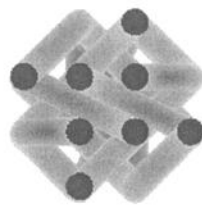
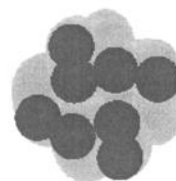
Where b_i is the semi-major axis of the i^{th} ellipse ($b = \text{Mai} / 2$) and a_i its semi-minor axis (in this case, the radius of the yarn). This allows us to obtain knowledge on whether a grid point belongs to zero, one or more than one yarns, enabling evaluation of the constraints. Figure 12 and Figure 13 illustrate the computation of the ellipse.

Results and Discussion

Plots similar to Figure 6 and Figure 7 are not useful in this case, as there are only eight yarns. However, due to the nature of the B-spline yarn model, the predicted yarn structure is smoother and much more realistic. This is shown in Figure 14 and in Figure 16. Examination of the 3D ACIS model from which Figure 16 is taken showed us that the final design was quite reasonable. The computation for this example required 15 hours on a 450Mhz Pentium II computer.

The results given by this method are generally better than those obtained by the linear method. First, the shape of the yarn is much more in agreement with what has been observed in real samples. More importantly, as we increase the number of control vertices and the fineness of the grid, the solution appears to converge quite well. This is an important advantage over the linear method, but here again the limit is the computational time.

It should be noted that the yarn structure obtained after 15 hours still has some discrepancies. Figure 17 shows clearly that there are some small intersections between yarns inside the braid. This could be caused by that fact that the optimization process tends to adapt to the fixed grid by favoring solutions in which yarn intersections occur between grid points, i.e., the intersections are not detected and therefore do not contribute to the constraint violations. Our research efforts are currently directed towards rectifying this problem by modifying the method presented here while retaining computational viability.

Figure 14 - *First guess from the side.*Figure 15 - *First guess (top view).*Figure 16 - *Predicted structure (side view).*Figure 17 - *Predicted structure (section).*

Conclusion

The determination of yarn structure for a given braiding sequence is a crucial step in designing three dimensional structural components. At present there is no satisfactory method for solving this problem in a general manner. The methods presented in this paper are intended to address this need by predicting the yarn structure through the use of numerical optimization. The results obtained up to this point are very encouraging, and the general approach appears to be capable of predicting braid geometry with reasonable precision and reliability. This is particularly true of the second method proposed, which uses B-splines to represent yarn shape in conjunction with a uniform fixed grid of check points for detecting yarn intersection. Another attractive feature of the proposed methodology is its generality and flexibility. The method can be directly applied to different braid geometries and braiding sequences. With suitable modifications, it can be used to model yarns of non-circular cross-section, as well as

cases where the yarn tension and cross-section vary from one yarn to the next. The method does involve substantial computing time, but is still much more efficient than the approach presented in [1]. Further work is needed to enhance computational efficiency by improving on the optimization algorithm used. The use of derivative-based optimization could lead to a significant reduction in the computing time. While the issue of computing time remains a concern, the underlying methodology presented here seems to work quite well.

References

- [1] Wang, Y., and Sun, X., "Determining the Geometry of Textile Preforms Using Finite Element Analysis," *Proceedings of the American Society for Composites Fifteenth Annual Conference*, College Station, TX, September 2000.
- [2] Mouritz, A.P., Bannister, M.K., Falzon, P.J., Leong, K.H., "Review of Applications for Advanced Three-dimensional Fiber Textile Composites," *Composites Part A*, Vol. 30 ,1999, pp. 1445-1461.
- [3] Wang, Y.Q., and Wang, A.S.D., "Microstructure/Property Relationships in Three-dimensionally Braided Fiber Composites," *Journal of Composites Science and Technology*, Vol. 53, 1995, pp. 213-222.
- [4] Sun, H.Y., and Qiao, X., "Prediction of the Mechanical Behavior of Three-dimensionally Braided Composites," *Journal of Composites Science and Technology*, Vol. 57, 1997, pp. 623-629.
- [5] Chen, L., Tao, X.M., and Choy, C.L., "Mechanical Analysis of 3-D Braided Composites by the Finite Multiphase Element Method," *Journal of Composites Science and Technology*, Vol. 59 ,1999, pp. 2383-2391.
- [6] Li, W., Hammad, M., and Sheikh, A., "Structural Analysis of 3-D Braided Preforms for Composites," *Journal of Textile Institute*, Vol. 81, 1990, pp. 491-514.
- [7] Wang, Y.Q., and Wang, A.S.D., "On the Topological Yarn Structure of 3-D Rectangular and Tubular Braided Preforms," *Journal of Composites Science and Technology*, Vol. 51, 1994, pp. 575-586.
- [8] Wang, Y.Q., and Wang, A.S.D., "Geometric Mapping of Yarn Structure Due to Shape Change in 3-D Braided Composites," *Journal of Composites Science and Technology*, Vol. 54, 1995, pp. 395-370.
- [9] Wang, Y.Q., and Wang, A.S.D., "Spatial Distribution of Yarns and Thermo-mechanical Properties in 3-D Braided Tubular Composites," *Journal of Applied Composite Materials*, Vol. 4, 1997, pp. 121-132.
- [10] Chen, L., Tao, X.M., and Choy, C.L., "On the Microstructure of Three-dimensional Braided Preforms," *Journal of Composites Science and Technology*, Vol. 59, 1999, pp. 391-404.

Youqi Wang,¹ Changjie Sun,¹ Xuekun Sun,¹ and Nicholas J. Pagano²

Principles for Recovering Micro-Stress in Multi-Level Analysis

Reference: Wang, Y. Q., Sun, C. J., Sun, X. K., and Pagano, N. J., "Principles for Recovering Micro-Stress in Multi-Level Analysis," *Composite Materials: Testing, Design, and Acceptance Criteria, ASTM STP 1416*, A. Zureick and A.T. Nettles, Eds., American Society for Testing and Materials International, West Conshohocken, PA, 2002.

Abstract: Multi-level stress analysis is widely used to recover the micro-stress of the stress concentration area in composite structures. One common approach is firstly to consider the composite material as a homogeneous material. Effective properties are employed to predict the effective stress and effective displacement fields (or called the macroscopic stress and macroscopic displacement fields). Then, a local domain, which includes the area of interest (normally the stress concentration area), is selected for local microscopic stress analysis, in which the effective stress and/or effective displacement along the local domain boundary are used as boundary conditions. Thus a question arises: can the micro-stress field in the area of interest found from multi-level stress analysis match that from full-field micro-stress analysis? In this paper, two principles and a "local domain test", which is based upon the two principles, are established for multi-level stress analysis. It is shown that micro-stress in the area of interest will be recovered accurately with multi-level analysis if the selected local domain passes the "local domain test." These two principles and the "local domain test" elevate multi-level stress analysis into a more powerful tool.

Keywords: Micro-mechanics, multi-level analysis, homogenization

Introduction

Composite failure often emanates from stress concentration areas. In order to estimate severity of stress concentration and possible failure consequences, it is necessary to investigate microstress distribution. However, a full-field micro-stress analysis would require a huge amount of human and computer resources. It is, in fact, unrealistic to conduct full-field micro-stress analysis for structural design. Instead, the most common method employed is multi-level stress analysis. Figure 1 illustrates it. The shaded area represents the area of interest. It normally is the stress concentration area. Firstly, the composite material is considered as a homogenous material. Effective properties are employed to predict the effective stress and effective displacement fields. Then, a local

¹ Associate professor and corresponding author, graduate student, and research associate, respectively, Mechanical and Nuclear Engineering, Kansas State University, Manhattan, KS 66506.

² Senior Scientist, Nonmetallic Material Division, AFRL/MLBC, Wright-Patterson AFB, OH 45433.

domain, which includes the area of interest (normally the stress concentration area), the shaded area in the figure, is selected for local microscopic stress analysis. Effective stress and/or effective displacement along the boundary of the local domain are used as boundary conditions.

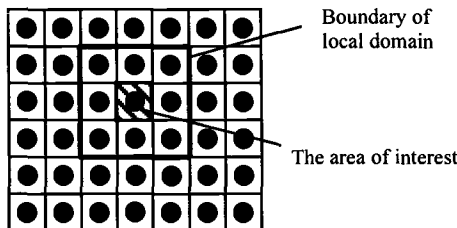


Figure 1 - *Illustration of two-level analysis.*

Thus, two critical issues arise.

1. Can we recover micro-stress distribution in the area of interest using multi-level analysis? The word "recover" is used because knowledge of micro-stress was lost during the employment of the homogenization step (The effective-level analysis).
2. How do we estimate the error of multi-level stress analysis without undertaking a full field microstress analysis?

The purpose of the paper is to establish criteria for an accurate recovery of the micro-stress field in the area of interest. Error mechanisms of multi-level analysis are discussed first. Based upon these discussions, two principles are established to quantify the required size of the local domain for multi-level analysis. These two principles are as follows.

1. There is no severe effective stress concentration along the boundary of the selected local domain.
2. The boundary of the local domain must be far enough from the area of interest.
The required minimum distance can be determined by a "local domain test," which will receive detailed elaboration in the body of this paper.

Finally, a numerical example is given. In this example, a two-level analysis was conducted. First, an effective stress analysis was conducted. A local domain based upon the first principle was selected. Then, a "local domain test" was applied to the local domain. The test was successful. The effective boundary conditions were applied to the local domain for a micro-stress analysis. Micro-stress in the area of interest was thus recovered from the two-level analysis. Micro-stress in the area of interest, derived from the two-level analysis, was compared to the results from full-field micro-stress analysis. The results coincided.

Error Mechanisms

Let us return to the example illustrated in Figure 1. During the first step of the multi-level analysis, the composite is considered as a homogeneous material. Effective

boundary stress conditions are calculated based upon the effective stress analysis. However, the effective boundary stress condition is different from the actual micro-stress boundary. Figure 2 illustrates the difference. Domain **A** is subjected to an effective boundary stress, which is derived from the effective stress analysis. Domain **B** is subjected to an actual boundary micro-stress that is derived from a full field micro-stress analysis. Subtracting micro-boundary stress from the effective boundary condition derives boundary conditions applied to Domain **C**. Therefore, the micro-stress field in Domain **C** is equal to the difference of the microstress fields of Domain **A** and **B** (Stress field of Domain **A** – Stress field of Domain **B**). It is, in fact, the error stress field of the multi-level analysis. If the micro-stress in the area of interest (not the entire selected local domain) of Domain **C** approaches zero, the same micro-stress field in the area of interest of Domains **A** and **B** will be achieved. This means microstress in the area of interest will be accurately recovered from the micro-stress analysis of Domain **A**.

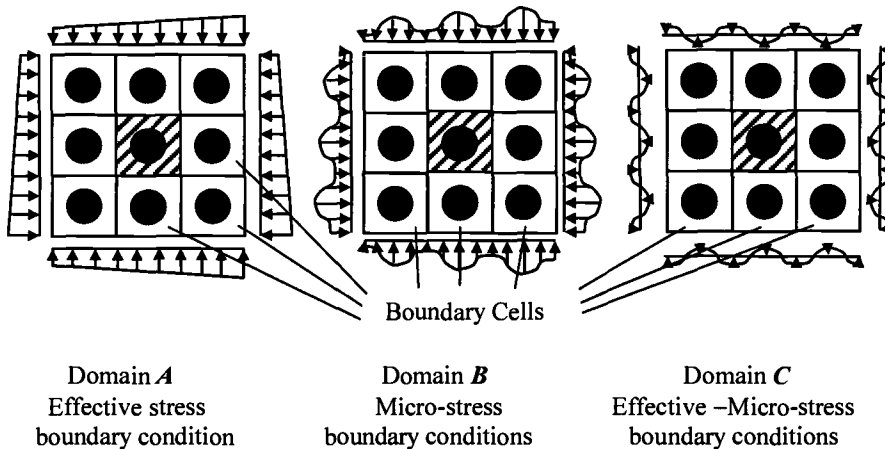
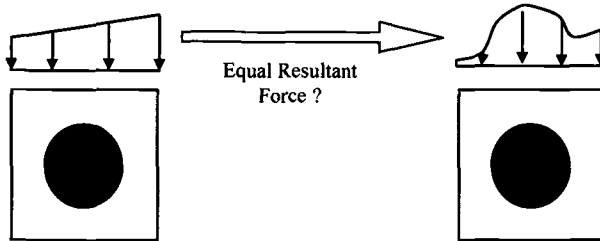


Figure 2 - Boundary stresses applied to the selected local domain.

Micro-stress in the area of interest of Domain **C** will approach zero if the following two conditions are satisfied.

1. The boundary along each side of the area of interest is under an oscillating load. The resultant forces of the oscillating load along the external edge of each boundary cell of Domain **C** equals zero.
2. The area of interest must be far enough from the boundary of the local domain. In multi-level stress analysis, the actual micro-stress condition applied to the boundary of the selected local domain is replaced by the effective stress. If the first condition is satisfied, the difference between the effective boundary stress and the micro-boundary stress is an oscillating stress with a zero-resultant force on the edge of each boundary cell. Such a boundary load only affects stress distribution in the vicinity of the boundary. If the area of interest is far enough from the boundary, the oscillating boundary load will not affect the micro-stress

field there. As such, the micro-stress recovered from multi-level stress analysis would be the same as results from full-field micro-stress analysis.



3-a: Effective boundary stress

3-b: Micro-boundary stress

Figure 3 - *Boundary stress applied to the boundary cell of the selected local domain.*

Therefore, multi-level analysis error can arise from two sources:

1. The resultant force of effective stress along the external edge of the each boundary cell is not equal to the resultant force of the micro-stress.

Refer to Figure 3, the cell shown in 3-a is a boundary cell in the middle of the first row of Domain A. The cell shown in 3-b is the corresponding boundary cell at the same location in Domain B. The effective boundary load must be equivalent to the micro-boundary load in order to avoid errors.

2. The local domain is too small. As a result, the distance between the area of interest is not far enough from the boundary of the local domain.

Error from the first source depends on validation of the homogenized effective stress analysis. If homogenization is effective, the error brought by the first source can be neglected. The error from the second source can be examined by a “local domain test.” Both are discussed forthwith.

Validation of Homogenized Effective-Stress Analysis

During effective stress analysis, the composite is considered as a homogenous material. The process is called homogenization.

Mathematically, if the size of the unit cell (or representative volume element), denoted as ε , approaches zero, the effective stress on the unit cell will approach the average value of the microstress over the unit cell, i.e.,

$$\sigma_{ij}^e \rightarrow \frac{\int \sigma_{ij}'' dV}{\Delta V} \quad \text{if} \quad \varepsilon \rightarrow 0 \quad (1)$$

where σ_{ij}^e denotes effective stress and σ_{ij}'' denotes microstress, respectively. ΔV is the volume of the unit-cell.

For most elastic materials, such as metal, glass, and plastic, their microstructures are so small compared to the entire material domain that the variation of effective stress over a unit cell is negligible. Effective stress approaches the average value of the microstress over the unit cell. Therefore, the homogenization approach has been traditionally accepted. The material domain is always assumed to be a continuum domain with effective properties.

For composite materials, the unit cell has a finite size. The effective stress cannot be considered as a constant stress over the unit-cell. Let $\overline{\sigma}_{ij}^e$ be the average value of the effective stress over a unit cell and $\overline{\sigma}_{ij}^m$ the average value of micro-stress over a unit cell.

The absolute error from homogenization can be measured by $|\overline{\sigma}_{ij}^e - \overline{\sigma}_{ij}^m|$, which is denoted as δ_{ij} . If the error is negligible, the effective stress field is macro-static equivalent to the micro-stress field. Under this circumstance, we say that the homogenization process is valid.

Strictly speaking, the effective stress equals the average stress of the micro-stress only under a constant effective stress condition. However, error over a unit cell becomes negligible if the following two conditions are satisfied.

1. The frequency of the effective stress in the vicinity of the unit cell is much lower than the frequency of the micro-stress. Under this condition, micro-stress oscillation is carried on the effective stress curve as shown in Figure 4. Micro-stress can be characterized by effective stress plus a micro-oscillation. For composite structures, the frequency of effective stress is usually much lower than that of the micro-stress. A fast-oscillating effective stress with a frequency of a similar order with the microstructure of the composite rarely occurs inside the composite structure. If this occurs, a coupling effect of the macro-(the effective-) stress and the micro-stress may occur. The homogenization approach would be invalid.

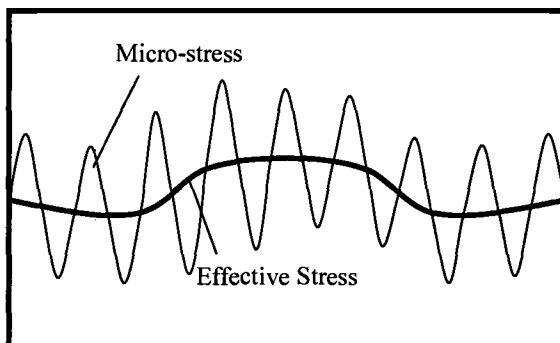


Figure 4 - *Effective stress and micro-stress distribution.*

2. There is no severe effective stress concentration in the unit cell. If the stress concentration occurs in a very small region, and, if the size of the region is comparable to the size of the unit cell, error can not be neglected. The average value of the effective stress over a unit cell might not be close to the average value of the micro-stress in the unit cell.

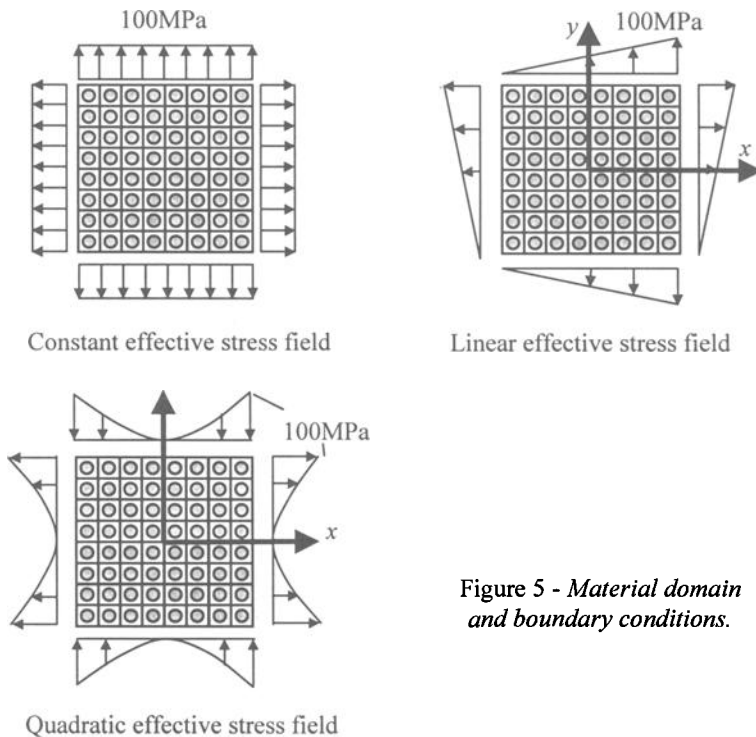


Figure 5 - Material domain and boundary conditions.

The purpose of this paper is not to establish the relationship between error and stress gradient mathematically. That is outside the scope of this paper. Instead, three numerical examples are given to demonstrate the effectiveness of homogenization. The material domain employed in these three examples is shown in Figure 5. It is a cross-section of a fibrous reinforced composite. 64 unit cells are included. Silicon carbide fibers and epoxy resin are employed. The properties of the fiber and matrix are

$$E_f = 325 \text{ GPa}, \quad \nu_f = 0.15, \quad V_f = 30.7\%$$

$$E_m = 3.45 \text{ GPa}, \quad \nu_m = 0.35$$

Three boundary conditions are applied to this material domain, respectively. These create three different effective stress fields. In the first example, a constant load of 100 MPa is applied to the boundary of the material domain. This creates a constant stress field of

100MPa. In the second example, linear load is applied. This creates a linear effective stress field, which can be expressed as

$$\sigma_x = \frac{100}{l}(y - l/2) + 50, \quad \sigma_y = \frac{100}{l}(x - l/2) + 50, \quad \tau_{xy} = 0 \quad (2)$$

where l is the length of the material domain.

In the third example, a quadratic boundary load is applied, creating a quadratic stress field that can be expressed as

$$\sigma_x = \frac{100}{l^2} y^2, \quad \sigma_y = -\frac{100}{l^2} x^2, \quad \tau_{xy} = 0 \quad (3)$$

0.1	0.5	0.7	0.7	0.7	0.7	0.5	0.1	0.1
0.1	0.1	0.0	0.0	0.0	0.0	0.1	0.1	0.1
0.1	0.2	0.2	0.2	0.2	0.2	0.2	0.1	0.1
0.5	0.2	0.1	0.0	0.0	0.1	0.2	0.5	0.5
0.0	0.1	0.1	0.2	0.2	0.1	0.1	0.0	0.0
0.7	0.2	0.1	0.1	0.1	0.1	0.2	0.7	0.7
0.0	0.0	0.1	0.1	0.1	0.1	0.0	0.0	0.0
0.7	0.2	0.2	0.1	0.1	0.2	0.2	0.7	0.7
0.0	0.0	0.4	0.1	0.1	0.1	0.0	0.0	0.0
0.7	0.2	0.2	0.1	0.1	0.2	0.2	0.7	0.7
0.0	0.1	0.1	0.2	0.2	0.1	0.1	0.0	0.0
0.7	0.2	0.1	0.1	0.1	0.1	0.2	0.7	0.7
0.1	0.2	0.2	0.2	0.2	0.2	0.2	0.1	0.1
0.5	0.2	0.1	0.0	0.0	0.1	0.2	0.5	0.5
0.1	0.5	0.7	0.7	0.7	0.7	0.5	0.1	0.1
0.1	0.1	0.0	0.0	0.0	0.0	0.1	0.1	0.1

δ in each cell of material domain
(Constant stress field)

0.4	1.1	0.7	0.5	0.3	0.3	0.2	0.0	0.0
0.3	0.3	0.1	0.1	0.0	0.0	0.0	0.0	0.0
0.4	0.2	0.2	0.4	0.3	0.1	0.0	0.0	0.0
0.6	0.1	0.2	0.1	0.1	0.1	0.0	0.0	0.2
0.1	0.3	0.3	0.0	0.1	0.1	0.1	0.0	0.0
0.0	0.6	0.0	0.1	0.1	0.1	0.1	0.1	0.3
0.1	0.1	0.2	0.1	0.0	0.1	0.1	0.0	0.0
0.3	0.6	0.2	0.0	0.0	0.1	0.3	0.3	0.3
0.0	0.1	0.2	0.1	0.0	0.1	0.1	0.1	0.1
0.4	0.5	0.3	0.1	0.1	0.0	0.4	0.5	0.5
0.0	0.1	0.2	0.3	0.2	0.0	0.2	0.1	0.1
0.4	0.4	0.2	0.2	0.2	0.3	0.2	0.2	0.7
0.1	0.2	0.4	0.5	0.6	0.5	0.0	0.3	0.3
0.3	0.2	0.1	0.1	0.1	0.3	0.2	0.2	1.1
0.1	0.3	0.4	0.4	0.3	0.0	0.6	0.3	0.3
0.1	0.1	0.0	0.0	0.1	0.1	0.4	0.4	0.4

δ in each cell of material domain
(Linear stress field)

1.5	2.5	1.7	1.2	1.2	1.7	2.5	1.5
1.5	0.4	0.1	0.1	0.1	0.1	0.4	1.5
0.4	0.0	0.9	1.2	1.2	0.9	0.0	0.4
2.5	0.0	0.6	0.5	0.5	0.6	0.0	2.5
0.1	0.6	0.4	0.2	0.2	0.4	0.6	0.1
1.7	0.9	0.4	0.8	0.8	0.4	0.9	1.7
0.1	0.5	0.8	0.8	0.8	0.8	0.5	0.1
1.2	1.2	0.2	0.8	0.8	0.2	1.2	1.2
0.1	0.5	0.8	0.8	0.8	0.8	0.5	0.1
1.2	1.2	0.2	0.8	0.8	0.2	1.2	1.2
0.1	0.6	0.4	0.3	0.2	0.4	0.6	0.1
1.7	0.9	0.4	0.8	0.8	0.4	0.9	1.7
0.4	0.0	0.9	1.2	1.2	0.9	0.0	0.4
2.5	0.0	0.6	0.5	0.5	0.6	0.0	2.5
1.5	2.5	1.7	1.2	1.2	1.7	2.9	1.5
1.5	0.4	0.1	0.1	0.1	0.1	0.2	1.5

δ in each cell of material domain
(Quadratic stress field)

Figure 6 - The error of homogenization.

Figure 6 shows errors from the homogenization approach in the material domain for these three examples. The material domain is divided into 64 squares. Each square represents a unit cell. There are two numerals in each cell. The top one is $|\overline{\sigma}_x^e - \overline{\sigma}_x^m|$ over the unit cell, i.e. δ_x , and the bottom one is $|\overline{\sigma}_y^e - \overline{\sigma}_y^m|$, i.e. δ_y . The unit of the error is MPa.

Referring to example one, error approaches zero in the middle of the material domain under a constant stress field. There is a boundary effect, which creates a small error between 0.1% and 1%. Error remains small under a linear stress condition. It would not be so small if the unit-cell were not a symmetric-cell, or, if a non-linear stress field were applied. The third example gives us a more general picture. Absolute error becomes slightly larger in an area with large stress variations (outside of the shaded area). In all three cases, error is insignificant compared to the magnitude of either effective stress or micro-stress in the material domain. More examples were calculated. The general conclusion is that error δ_{ij} will be negligible if there is both no oscillating effective stress and no singularity of effective stress inside the unit cell. This holds even when only a limited number of unit cells are included in the material domain. If the two conditions mentioned in this section are satisfied, the homogenization approach will be valid and the effective stress field will be statically equivalent to the micro-stress field.

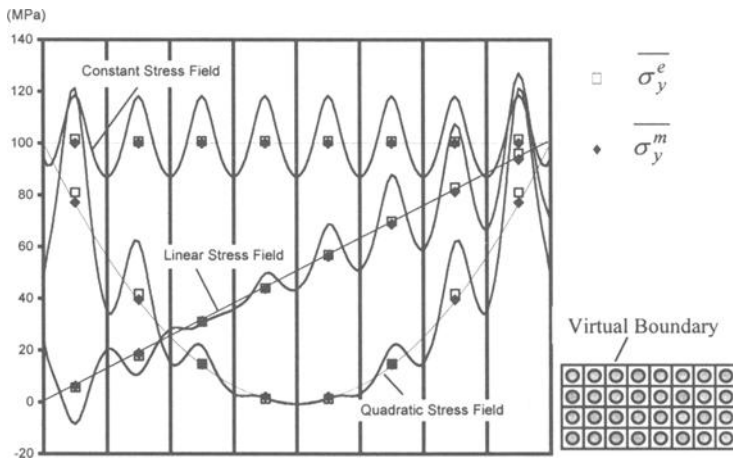


Figure 7 - Macro-(effective) and micro-stress distribution along the virtual boundary.

The next step is to examine the resultant forces of micro-stress and effective stress along the edge of each unit cell. Refer to Figure 5. Let us make a virtual cut along the middle line $y = 0$. A virtual boundary is thus created, as shown in Figure 7. The only boundary stress component is the normal stress σ_y . Figure 7 shows the distribution of σ_y along the new boundary. There are six curves in the figure. They are the effective-stress curves and the micro-stress curves for the above three examples. Also, the average value of both micro-boundary stress and effective boundary stress along the edge of each cell is

calculated and shown in the figure by symbol "□" and "◆", respectively. One can see the following.

1. The micro-stress curves are carried on the effective-stress curves.

2. The cell averages of effective stresses are very close to that of the micro-stress.

Small errors occur in the area where stress changes more rapidly, such as the high stress region of the quadratic stress field. Subtracting effective-stress from the microstress, one can derive three oscillating boundary stress curves. The resultant forces of boundary stress along the edge of each unit cell are insignificant.

Generally speaking, if homogenization is valid, the effective stress will be statically equivalent to the micro-stress over the external edge of each boundary cell of a selected local domain.

"Local Domain" Test

In this section, we will answer the following question: If homogenization is valid, how can we accurately recover the micro-stress in the area of interest?

Refer to Figure 3. If homogenization is effective in the boundary cell, the resultant force of oscillating boundary stress applied to each boundary cell of Domain *C* vanishes. This oscillating stress only affects the stress in the vicinity of the boundary. In order to test the effect of the oscillating stress in the area of interest, a "local domain test" can be conducted. Figure 8 is an illustration of the "local domain test." A periodical load, modeling the oscillating micro-stress, will be applied to the local domain as shown in Figure 8. Then, the stress in the area of interest is examined. This ratio of the stress in the area of interest to the boundary stress will be the relative error of the two-level analysis if this domain is selected. If the stress in the area of interest is very small, the domain selected for the two-level analysis is sufficient. Otherwise, one must increase the domain size and retest until a near-zero stress is achieved. This process is named the "local domain test." In order to achieve an accurate micro-stress recovery, the local domain used in two(multi)-level analysis must pass this test.

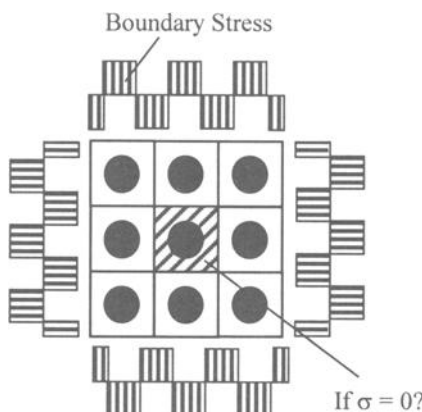


Figure 8 - "Local domain" test.

Application of the "Local Domain" Test in Multi-Level Analysis

Based upon the two principles and the "local domain test", we successfully recovered the microstress in an enlarged Pagano-Rybicki boundary value problem (Pagano and Rybicki 1974, Rybicki and Pagano 1976, Pagano and Yuan 2000).

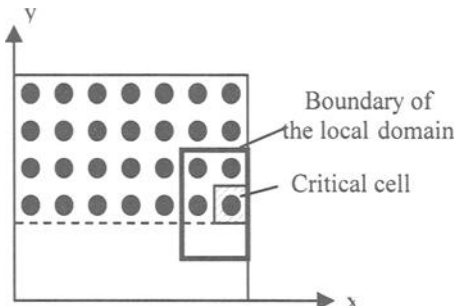
Figure 9-a is the material domain for the enlarged Pagano-Rybicki boundary value problem. At the top part of the material domain, sixteen silicon carbide fibers are embedded in an epoxy matrix. The properties of fibers and matrix are

$$E_f = 325 \text{ GPa}, \quad v_f = 0.15, \quad V_f = 30.7\%$$

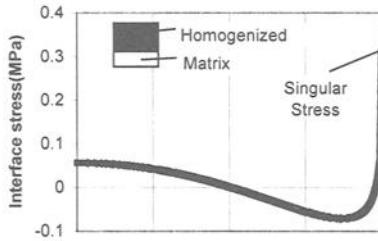
$$E_m = 3.45 \text{ GPa}, \quad v_m = 0.35$$

Both x- and y-axes are symmetric axes. The bottom part is made only of matrix. An axial strain of 0.002 is applied in the axial direction (z-direction).

The material domain is considered to consist of two homogenous materials. The upper part is a fiber reinforced composite with effective properties of $E_L = 102.11 \text{ GPa}$, $E_T = E_z = 7.27 \text{ GPa}$, $v_{LT} = v_{LZ} = 0.277$, $v_{TZ} = 0.440$, $G_{LT} = G_{LZ} = 2.39 \text{ GPa}$, $G_{TZ} = 1.99 \text{ GPa}$. The lower part is the pure epoxy matrix. Thus, an interface is formed between these two materials. Figure 9-b shows the effective stress distribution along the interface. There is a singular point on the edge of the interface. Therefore, it is critical to investigate the micro-stress in the critical cell, as shown in the figure.



9-a Material Domain



9-b Effective-stress along the interface

Figure 9 - Enlarged Pagano-Rybicki problem .

First, a local domain was selected for a two-level stress analysis, as shown in Figure 9-a. It is composed of six unit cells (four composite cells and two matrix cells). Results from an effective stress analysis showed that there was no singular stress or severe stress concentration occurring on the boundary cell. Therefore, the effective stress would be valid on the boundary of the domain.

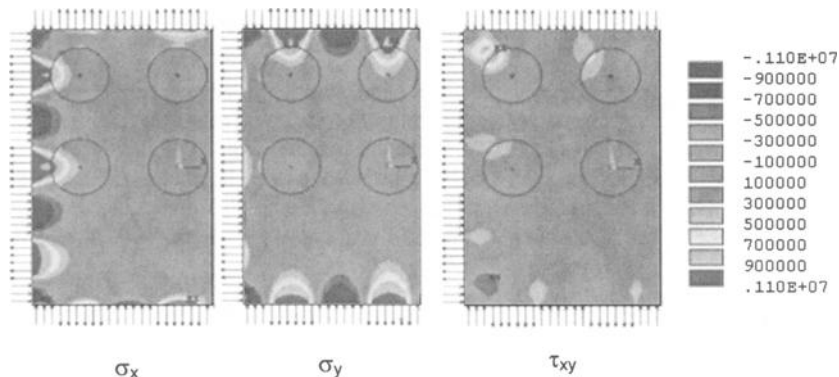


Fig.10 "Local Domain Test" Results

Then, a periodic normal stress of ± 1 MPa was applied to the boundary of the local domain. Figure 10 shows the stress contours of the local domain. One can see that the periodic load only creates stress in the boundary area. The stress over the critical cell is far smaller than 0.05 MPa, i.e., 5% of the external load. Similarly, a periodic shear stress was applied to the local domain. Similar phenomena was observed. Therefore, the "local domain test" was passed. The selected local domain was big enough for a two-level stress analysis.

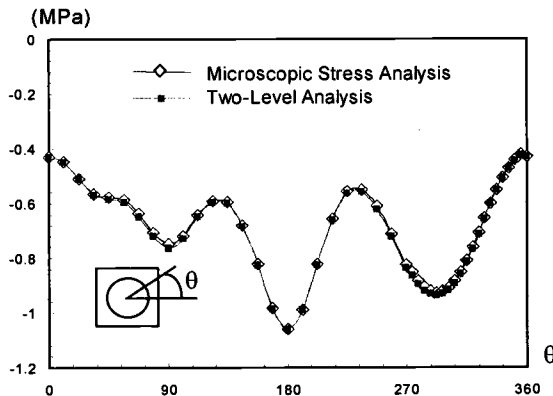


Figure 11 - Comparison of radial stresses along the fiber-matrix interface from full-field micro-stress analysis and two-level analysis.

Then, the effective-boundary displacement was applied to the local domain for a micro-stress analysis. It was found that the micro-stress field inside the critical cell resulting from two-level analysis was almost identical to the stress field resulting from a full field micro-stress analysis. Figure 11 shows normal stresses (σ_r) along the fiber-

matrix interface. One curve characterizes the result from two-level analysis and the other from a full-field microstress analysis. Both curves almost coincide. The micro-stress in the area of interest is accurately recovered.

Conclusions

In this paper, two principles have been proposed for selection of a local domain for multi-level analysis. They are as follows.

1. **Effective stress** does not oscillate along the boundary of the local domain and there is no severe stress concentration along the boundary of the selected local domain.
2. The selected local domain must pass the "local domain test."

If the above two principles are followed, the micro-stress in the area of interest (or stress concentration area) can be accurately recovered without a full field micro-stress analysis.

A numerical example, an enlarged Pagano-Rybicki problem, is given. Following these two principles, the micro-stress in the area of interest is accurately recovered by using two-level stress analysis.

Acknowledgments

Financial support from the Air Force Office of Scientific Research is acknowledged.

References

- [1] Pagano, N.J. and Rybicky, E.F., "On the Significance of the Effective Modulus Solutions for Fibrous Composites," *Journal of Composite Material*, Vol. 8, 1974, pp.214-228.
- [2] Rybicki, E.F. and Pagano, N.J., "A Study of the Influence of Microstructure on the Modified Effective Modulus Approach for Composite Laminates," *Proceedings of the 1975 International Conference on Composites Materials*, Vol.2, 1976, pp. 198-207.
- [3] Pagano, N.J. and Yuan F.G., "Significance of Effective Modulus Theory (Homogenization) in Composite Laminate Mechanics," *Composites Science and Technology*, Vol. 60, 2000, pp. 2471-2488.

Han Zhu,¹ Wen-Ying Li,¹ Ampere A. Tseng,² and Patrick Phelon²

Measurement of CTE at Reduced Temperature for Stressed Specimens

Reference: Zhu, H., Li, W., Tseng, A. A., Phelon, P., "Measurement of CTE at Reduced Temperature for Stressed Specimens," *Composite Materials: Testing, Design, and Acceptance Criteria, ASTM STP 1416*, A. Zureick and A. T. Nettles, Eds., American Society for Testing and Materials International, West Conshohocken, PA, 2002.

Abstract: The coefficient of thermal expansion (CTE) is one of the critical parameters in determining material behaviors. This article presents a study for developing a new method in measuring CTE at reduced temperature. The machine used in the measurement is a micro mechanical tester. Measured specimens are stressed, and at least one characteristic dimension of specimens is in the order of mm, sub mm or microns. CTE values are determined based on their relation with the measured magnitude of stress jump resulting from the change in temperature. Their comparison with the CTE values reported by other sources is also presented. It is interesting to notice that CTE values measured by the method may vary depending on the level of applied stresses for the same amount of temperature change. Advantages of this method with respect to high sensitivity, easy operation, short testing time and others are also discussed.

Keywords: Coefficient of thermal expansion (CTE), micro mechanical test, stress, strain, reduced temperature

Introduction

Quantitative description of the volume expansion caused by the change in temperature can be characterized by the coefficient of thermal expansion (CTE), or for all practical purposes, the linear CTE. Most work in the area of measuring CTE are performed by utilizing the instrument called Thermal Mechanical Analyzer (TMA) (ASTM E831-2000, "Standard Test Method for Linear Thermal Expansion of Solid Materials by¹ Thermomechanical Analysis,"), or by employing the method of electric resistance strain gages (ASTM D5335-1999, "Standard Test Method for Linear Thermal Expansion of

¹ Assistant professor and graduate student, respectively, Department of Civil and Environmental Engineering, Arizona State University, Tempe, AZ 85287-5306.

² Professor and associate professor, Department of Mechanical and Aerospace Engineering, Arizona State University, Tempe, AZ 85287-6106.

Rock Using Bonded Electric Resistance Strain Gages.”). The physics of this type of measurement performed by TMA is based on the free body expansion mechanism (stress-free status) that the expansion/shrinkage taking place in materials is proportional to the temperature change. CTE values can be determined based on the information of volume change. The mechanism for the electric strain gage method is to use the strain gage, which is bonded to specimens, to gauge the thermal deformation.

In this study, a new method is proposed in measuring CTE. There are a few features about this new method. The first one is that specimens are stressed when they are undergoing the temperature change. The second one is that specimens are small in size. At least one characteristic dimension of specimens is in the order of mm, sub mm or microns. Typical specimens are thin films, fibers, etc. The third one is that CTE values are related to the stress drop/jump upon change in temperature when specimens are under stress.

A microthermal mechanical tester is employed in this method. Since the tester can only work on small specimens, the time needed to reach the status of thermal equilibrium in specimens upon the change in temperature is short [1]. Also, measurement is recorded by the tester directly and no strain gage attachment to specimens is required. This will eliminate many errors in operating a test [2]. Mechanical testing on small specimens is a research area of much activity, particularly in characterizing electronic packaging materials like solders and solder joints, etc. [3]. One topic is to use the mechanical fatigue scheme in simulating the thermal cyclic loading for the reliability analysis of solder joints [4]. It is also reported for the experiments on NicalonTM fibers by using the micro testing method [5] that so individual fibers can be characterized mechanically to observe its failure pattern under various conditions [6].

CTE data obtained by TMA indicates the phenomenon of stress-free-body thermal expansion. The question asked here is whether CTE may change for the case of stressed-body thermal expansion. For example, if a material under normal working condition will bear a load at its 10% of the failure strength, it may seem to be preferable to have the CTE data at this particular stress status. Whether there is a difference between free-body CTE and stressed-body CTE is an issue of investigation in this study.

Micro Mechanical Tester

The machine used in this study is a micro thermo-mechanical two-axis tester made by Wisdom Technology Inc. It has one linear motor stage and one DC motor rotary stage, assembled with a six-axis load cell and a small environment chamber. The tester has a high load and displacement resolution, which is 2 grams in force and 0.1 micron in length respectively. The maximum load is 20 kg for tension and compression, and 20N·m for torsion. The maximum range is 100 mm for translation and 360° for rotation. The translation speed varies from 0.0005 mm/s to 10 mm/s. The environment chamber can provide a temperature range from -100°C to 300°C. Liquid nitrogen is used as cooling source. The tester is capable of performing two-axial loading modes: the uni-axial mode and the torsion mode. Four loading configurations are available: static, fatigue, creep and relaxation. Control of the tester and the data manipulation is fully computerized.

Testing Procedure

In this study, only the mode of tension load is considered. The steps in this procedure can be described as a five-step scheme. Step 1 is to load a specimen in tension to a certain force level in a displacement control mode at a given temperature, say T1. The recorded force-displacement response by the tester will be displayed in the computer running the M.S. Windows 98 software that controls the tester. The force level is pre-set so when the load cell detects the load that meets the pre-specified force magnitude, the tester stops. At this stage, the specimen is deformed. Step 2 is to hold the deformation steady (no further deformation is allowed), and reset (increase) the maximum load. Step 3 is to change the temperature in the environmental chamber from T1 to another level, say T2, for a time period that allows the thermal equilibrium status to be reached in the specimen. Step 4 is to re-start loading the specimen at T2 also in the displacement control mode. At the moment of starting Step 4, a stress jump will be observed in the recorded force-displacement response when $T_2 < T_1$. Step 5 is to stop the test by imposing a prescribed termination condition on the machine or the condition of specimen ultimate failure. The scheme can be repeated to test a specimen under multiple temperature changes.

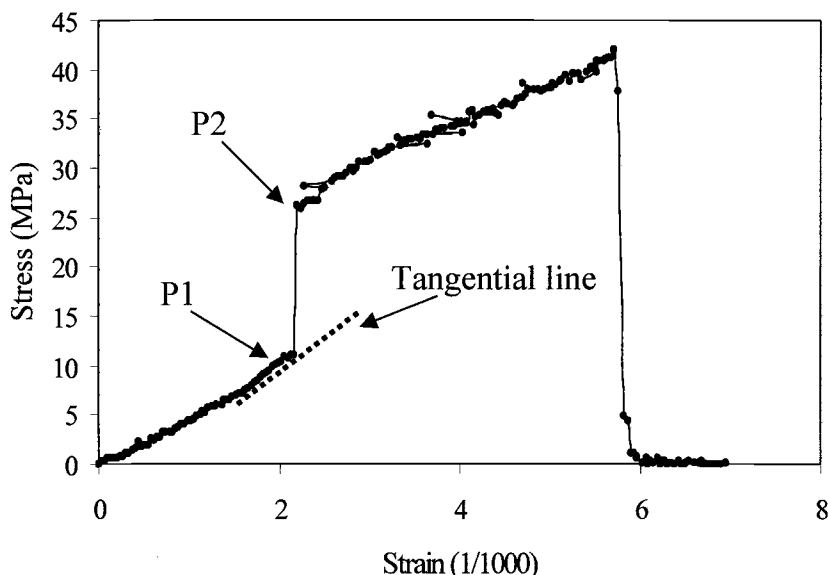


Figure 1 *Stress jump caused by the change in temperature.*

Results

The end result after completing the testing procedure is the force-displacement curve. This curve can also be easily converted to the stress-strain response provided specimen sizes are known. Figure 1 shows one typical stress-strain response obtained in the study. It is easily observed that there is a stress jump in the stress-strain curve that corresponds to the temperature change. If $\Delta\sigma$ is used to denote the stress jump, its definition is: $\sigma_2 - \sigma_1$. Here, σ_1 and σ_2 are the stress magnitude at P1 and P2 respectively (see Figure 1). Temperature at the point of P1 and P2 is T1 and T2, respectively. It is also noticed that the Young's modulus, denoted by E, is defined as the tangential ratio to the stress-strain curve, which can be graphically determined by using the software that controls the tester. Since the stress-strain curve is not linear, E's values vary. For example, E's value at the P1 can be obtained on the basis of the tangential line indicated in Figure 1.

CTE Equation

In this section, the relation between $\Delta\sigma$ and CTE will be analyzed. The foundation for the analysis sits on the linear theory of thermal-elasticity that the stress-strain relation in describing a specimen's thermo-mechanical behavior including the thermal strain effect is defined by

$$\sigma = E(\varepsilon - \varepsilon_{th}), \quad \varepsilon_{th} = \alpha(T - T_0) \quad (1)$$

where, σ and ε are the stress and strain, respectively. E is the Young's modulus. ε_{th} is the thermal strain. α is the linear coefficient of thermal expansion (from now on, α is the same as CTE). T is the current temperature, and T0 is a reference temperature at which the material remains at the status of zero residual stress.

The differential form of Eq. 1 is also available, which states

$$d\sigma = Ed\varepsilon - Ed\varepsilon_{th} \quad (2)$$

Since the mechanical strain ε is zero during the time period when temperature is changing as described in Step 3 in the section of **Testing Procedures**, the following equation is obtained

$$d\sigma = -E(T - T_0)d\alpha - E\alpha dT \quad (3)$$

$\Delta\sigma$ is defined as the stress jump: $\sigma_2 - \sigma_1$. Here, σ_1 and σ_2 are the stress magnitude at P1 and P2 respectively (see Figure 1). $\Delta\sigma$ then can be expressed by

$$\Delta\sigma = \int_{T1}^{T2} d\sigma = \int_{T1}^{T2} -E(T-T_0)d\alpha - \int_{T1}^{T2} E\alpha dT \quad (4)$$

Equation 4 requires further simplification, and three cases of simplifications are considered here.

Case 1

In Case 1, E and α are assumed to remain unchanged in the temperature range $[T1, T2]$. α then can be easily determined by

$$\alpha = \frac{-\Delta\sigma}{E\Delta T} \quad (5)$$

where ΔT is $T2-T1$. Since all the quantities in the r.h.s. of Eq. 5 are known either as input or a measured quantity, computing CTE is straightforward.

Case 2

In Case 2, only α is assumed to remain unchanged in the temperature range $[T1, T2]$. If the dependence of E, the Young's modulus, on temperature is further assumed to be linear, the calculation on CTE is governed by

$$\alpha = \frac{-2\Delta\sigma}{(E1+E2)\Delta T} \quad (6)$$

where $E1$ and $E2$ are the Young's modulus at the point $\sigma=\sigma1$ and $\sigma=\sigma2$, respectively.

Case 3

In Case 3, α is assumed to vary linearly with temperature in the temperature range $[T1, T2]$, while E remains unchanged. The corresponding equation is

$$1.5\alpha2 - 0.5\alpha1 = \frac{-\Delta\sigma}{E\Delta T} \quad (7)$$

where, $\alpha1$ and $\alpha2$ are the coefficient of thermal expansion of measured specimen at $T1$ and $T2$, respectively. $\alpha1$ and $\alpha2$ can not be computed by Eq. 7 alone. It appears that determining a spectrum of α 's values based on Eq. 7 may require a series of measurements on $\Delta\sigma$ with a multiple temperature changing scheme.

A natural extension of above three cases is to analyze the case when both α and E are linear function of temperature in $[T1, T2]$. However, such an analysis takes a long

mathematical derivation. Since this study focuses on the experimental work side of CTE measurement, we will not include the analytic derivation here.

Cooling Time

As stated in the section of **Testing Procedures**, Step 3 involves the change in temperature from T₁ to T₂. Now the question is raised about how to determine the time needed to let the specimen reach its temperature equilibrium status. Here, the following equation is employed to provide a time estimate[6]

$$0.5h = \sqrt{\beta\Delta t} \quad (8)$$

where h is the specimen thickness, β is the thermal diffusivity for the material with the unit being cm^2s^{-1} . s is the time unit in seconds, cm is centimeter, and Δt is the time estimate for reaching equilibrium temperature. Therefore, when values for h and β are known, Δt can be computed by using Eq. 8. It appears that, for a fixed h, the smaller β is, the bigger Δt becomes.

Tensile Test

The curve shown in Figure 1 is the stress-strain response for a polyimide specimen with a temperature drop when an applied stress level at about 12.% of the tensile failure strength is reached. The specimen is in the shape of thin film. Its thickness is 30 microns. However, before this test is carried out, a regular tensile test has to be done to determine the tensile failure strength, so the information of appropriate stress levels can be obtained

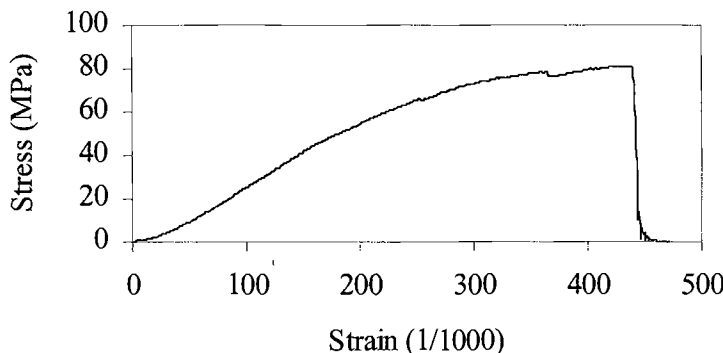


Figure 2 *Tensile stress-strain response for a polyimide specimen at room temperature.*

for designing the follow-up temperature drop tests. Here, the tensile test result is also included and shown in Figure 2.

CTE Data

The testing procedure for having a temperature drop is to first stretch the specimen in tension at room temperature at a rate 0.5 microns per second, which is extremely slow. When the load cell reacts to a force level at 400 grams, which is about 12% of the failure strength at the room temperature, the tester stops. At this moment, no displacement is allowed, but the load cell is free to register any change. Then the temperature in the environmental chamber is cooled down from the room temperature to -20°C . For typical polymer materials, β is of the order 0.0001 to 0.001 [7]. Based on Eq. 8 and using the value $\beta = 0.0001 \text{ cm}^2\text{s}^{-1}$, the computed value for Δt is only a fraction of a second. In the test, a 2-minute cooling time was enforced. After that, the tester continues to elongate the specimen at the same rate set in Step-1 till the specimen fails at -20°C . Measured Young's modulus is 5.11 GPa at P1 and is 5.03 GPa at P2. The data on stress jump due to the temperature change is recorded by the machine control software. So based on Eq. 5, CTE value is easily calculated. Three tests are done and their average is given in Table 1. Table 1 also includes two CTE values that are the case of applied stress level is at 4% and 8% of the tensile failure strength, respectively. In addition, the reported CTE value from the specimen provider is also listed in Table 1.

Table 1 - *Measured and reported CTE values.*

CTE	applied stress at 4% strength level	Applied stress at 8% strength level	applied stress at 12 % strength level	Reported
$(10^{-3}/^{\circ}\text{C})$	0.0854	0.0838	0.0774	0.026

Summary and Future Work

The paper presents a new experimental method in measuring CTE. The first issue concerning the validity of this method is whether the measured quantities have adequate sensitivity so as to provide meaningful data. For the experimental method presented in this paper, this issue appears to be well addressed with the following three considerations. Firstly, it can be seen from Eq. 1 that the stress jump is proportional to the Young's modulus. Young's modulus is usually a big number for most engineering materials. This means that the measured quantity in this method, which is the stress jump, is amplified. So a tiny change in CTE will lead to a 'sizeable' change in the stress jump. Secondly, because the tester is of very high force resolution that assures an accurate measurement in stress, this provides another mechanism to contribute the 'good' sensitivity for this testing method. So far a number of tests have been done in measuring CTE by this

experimental method, intuitively the results show a quite consistent and repeatable pattern.

There are other advantages about this method. Since specimens are small, it takes a relatively short period of time, typically a few minutes, to complete a test. Such a quick testing time may be attractive. For example, if a "regular sized" specimen is to be tested that may take hours or days to finish, it may be wise to conduct micro-testing first as a screen process for the purpose of increasing the success assurance for the test on regular sized specimens. In this way, losing time may be avoided. In addition, little gripping, mounting, adjusting, calibrating is needed when operating this tester. This eliminates many operational errors.

It is interesting to notice that, based on the results from using this method and shown in Table 1, the level of applied stress does have an effect on CTE. Upon all other conditions remaining the same, it appears that CTE decreases as the level of applied stress is increased. Also, in comparison with the reported value of CTE given by the specimen provider, the CTE values measured by this method are high. It is believed that the reported value is an estimate. Including this reported value in Table 1 is just for the purpose of presenting more CTE information about this particular material, and caution has to be exercised when the comparison is to be made between the reported value and the measured ones.

The work presented here is for the case of temperature decrease. A few tests also have been done in which the temperature increase is conducted. As expected, a stress drop is observed in those tests that follow the similar procedure as given in the section on Testing Procedures.

There are many issues that require further studies in relating this method. Since this paper aims to introducing this method, only the 'basic building blocks' in the method are discussed here. On the other hand, introduction of this new experimental method in measuring CTE presents an opportunity to consider and/or investigate a number of interesting topics. For example, single continuous fibers used in reinforcing composites are very small in diameter. Smallest ones can be in the order of 10 microns. It may be possible to use the quantity of stress jump described in this paper to back calculate the fiber diameter. Another important topic is the CTE measurement for composites which is a very important area. But it appears that the scope of experimental work in this area is relative small. Whereby, extending the micro testing into this area is very attractive. The progress on these topics will be reported separately when it is available.

Acknowledgment

The authors are thankful for the equipment funding provided by Arizona State University, College of Engineering and Applied Sciences.

References

- [1] Zhu, H., Guo, Y., Li, W. and Tseng, A. A., "Mechanical Characterization of Solder Mask Materials in Electronic Packaging Applications," *The Seventh Intersociety Conference on Thermal and Thermomechanical Phenomena in Electronic Systems*, Las Vegas, Nevada, USA, May, 2000.
- [2] Zhu, H., Guo, Y., Li, W. and Martin B., "Micro-Mechanical Characterization of Solder Mask Materials," *The Third Electronic Packaging Technology Conference*, Singapore, December, 2000.
- [3] Qian, Z., Lu, M., Ren, W., and Liu, S., "Fatigue Life Prediction of Flip-Chips in terms of Nonlinear Behaviors of Solder and Underfill," *Proceedings of the 49th Electronic Components and Technology Conference (ECTC)*, San Diego, CA, 1999.
- [4] Yu, Q. and Shiratori, M., "Fatigue-Strength Prediction of Microelectronics Solder Joints Under Thermal Cyclic Loading," *IEEE Transactions on Components, Packaging, and Manufacturing Technology Part A*, Vol. 20, No. 3, 1997.
- [5] Zhu, H. and Li, W. "Micro Testing on Individual Nicalon Fibers," *Seventh Pan American Congress of Applied Mechanics*, Temuco, Chile, January, 2002.
- [6] Mikhailov, M.D. and Özisik, "M.N. Unified Analysis and Solutions of Heat and Mass Diffusion," Wiley, New York, 1983.
- [7] Thermophysical Properties of Matter, The TPRC Data Series, Volume 10, 1970.

Emile S. Greenhalgh¹ and Sunil Singh¹

The Effect of Moisture, Matrix and Ply Orientation on Delamination Resistance, Failure Criteria and Fracture Morphology in CFRP

Reference: Greenhalgh, E. S. and Singh, S., "The Effect of Moisture, Matrix and Ply Orientation on Delamination Resistance, Failure Criteria and Fracture Morphology in CFRP," *Composite Materials: Testing, Design and Acceptance Criteria, ASTM STP1416*, A. Zureick and A. T. Nettles, Eds., American Society for Testing and Materials International, West Conshohocken, PA, 2002

Abstract: The objective of this work was to relate damage mechanisms, gleaned through electron microscopy, to delamination loci generated using fracture toughness (Mixed-Mode Bend) tests. From this, mixed-mode criteria were ranked using the χ^2 method (goodness of fit). The shapes of the failure loci (G_T versus $\%G_I$) were related to the damage mechanisms, and to the moisture content, fibre type and ply orientation. Due to cusp formation, the delamination toughness increased as the proportion of Mode II increased. A further finding was that a 'hump' which was observed in the failure loci under Mode I dominated loading was due to fibre bridging. Ply orientation also had a significant effect on the toughness: $0^\circ/90^\circ$ interface was about 45% tougher than the $0^\circ/0^\circ$ interface due to secondary matrix cracking parallel to the crack front. The presence of such additional mechanisms indicates that delamination toughness is not a material property but is dependent on ply orientation.

Keywords: Delamination, fractography, mixed-mode bend, failure criteria, moisture, ply interface, mechanisms

Nomenclature

χ^2	Goodness of fit
G_T	Total strain energy release rate, Jm^{-2}
G_I	Mode I strain energy release rate, Jm^{-2}
G_{II}	Mode II strain energy release rate, Jm^{-2}
G_{IC}	Critical Mode I toughness, Jm^{-2}
G_{MC}	Critical Mode II toughness, Jm^{-2}
m	Index in the Power Law criterion
n	Index in the Power Law criterion
ρ	Parameter in the Yan criterion

¹Principal scientist and engineer respectively, Structures and Materials Centre, QinetiQ, Farnborough, Hants, GU14 OLX, UK.

τ	Parameter in the Yan criterion
η	Index in the Exponential K criterion
β	Parameter in the General Interaction criterion
Φ	Parameter in the General Interaction criterion
Ω	Parameter in the Hackle criterion
γ	Index in the Exponential Hackle criterion
N	Index in the Exponential Hackle criterion
q	Index in the Benzeggagh criterion
G_0	Induced critical Mode I component in Kinloch criterion, Jm^{-2}
ω	'Surface roughness' in Kinloch criterion
ϕ_0	Phase angle due to elastic mismatch in the Kinloch criterion
ϕ	Phase angle, where $\cot^2 \phi = \frac{G_I}{G_{II}}$ in the Kinloch criterion
s_I	Standard deviation of the G_I component
s_{II}^P	Standard deviation of the G_{II} component
G_I^P	Predicted Mode I strain energy release rate, Jm^{-2}
G_{II}^P	Predicted Mode II strain energy release rate, Jm^{-2}
A,B & C	Arbitrary parameters
t	Ratio of G_I/G_{II}

Introduction

Although composites are now being utilised in a wide range of applications, they have yet to deliver the cost-savings expected. This is mainly attributed to the difficulty in predicting their behaviour, particularly when containing damage or delaminations. Consequently, expensive and time-consuming testing is required to qualify and certify composite structures containing damage. Sensitivity to delamination is widely recognised as one of the key limitations for using composites in primary (safety-critical) applications. Simplified or closed-form solutions for delamination are limited, and numerical methods, such as finite elements, are required for predicting growth. Accurate modelling of delamination requires issues such as large deflections, local buckling and contact between the delaminated layers to be addressed [1]. Through using a numerical approach, the forces and deflections at a defect boundary are determined, from which the Mode I and Mode II strain energy release rates (G_I and G_{II} respectively) are calculated. These are then input into a failure criterion, to ascertain whether delamination growth has occurred at each point around the defect boundary.

A wide range of failure criteria have been proposed to predict delamination growth, but most are empirical with little physical basis [1]. The objective of the work described here was to relate the mixed-mode delamination loci for CFRP with the delamination micro-mechanisms, gleaned through fractographic analysis, and to identify the best delamination criteria to use for design. Eleven delamination failure criteria were fitted and ranked using the toughness data from two carbon-fibre/epoxy materials, at two moisture conditions, at $0^\circ/0^\circ$ and $0^\circ/90^\circ$ ply interfaces. Failure criteria were ranked according to goodness of fit and their prediction of the critical Mode I (G_{IC}) and Mode II (G_{IIC}) toughnesses.

Experimental Details and Data Reduction

Table 1 - Mixed-mode delamination failure criteria from the literature.

Criterion	Failure Criterion as $f(G_I, G_{II})$	Parameters	Eqn
Linear	$\frac{G_I}{G_{IC}} + \frac{G_{II}}{G_{IIC}} \geq 1$	2	1
Power Law	$\left[\frac{G_I}{G_{IC}} \right]^m + \left[\frac{G_{II}}{G_{IIC}} \right]^n \geq 1$	4	2
Yan	$G_I + G_{II} \geq G_{IC} + p \left(\frac{G_{II}}{G_I} \right) + r \left(\frac{G_{II}}{G_I} \right)^2$	3	3
K	$G_I + G_{II} \geq G_{IIC} - (G_{IIC} - G_{IC}) \sqrt{\frac{G_I}{G_{IC}}}$	2	4
Exponential K	$G_I + G_{II} \geq (G_{IIC} - G_{IC}) e^{\eta \sqrt{\frac{G_I}{G_{II}}}} + G_{IC}$	3	5
General Interaction	$\left[\frac{G_I}{G_{IC}} - 1 \right] \left[\frac{G_{II}}{G_{IIC}} - 1 \right] + \left[\beta + \Phi \frac{G_I}{(G_I + G_{II})} \right] \frac{G_I G_{II}}{G_{IC} G_{IIC}} \geq 0$	4	6
Ramkumar	$\left[\frac{G_I}{G_{IC}} \right]^2 + \left[\frac{G_{II}}{G_{IIC}} \right]^2 + \frac{G_I G_{II}}{G_{IC} G_{IIC}} \geq 1$	2	7
Hackle	$G_I + G_{II} \geq G_{IC} - \Omega + \Omega \sqrt{1 + \frac{G_{II}}{G_I} \sqrt{\left(\frac{E_{11}}{E_{22}} \right)}}$	4	8
Exponential Hackle	$G_I + G_{II} \geq (G_{IC} - G_{IIC}) e^{\gamma(l-N)} + G_{IIC}$	4	9
Benzeggagh	$G_I + G_{II} \geq G_{IC} + (G_{IIC} - G_{IC}) \left(\frac{G_{II}}{G_I + G_{II}} \right)^q$	3	10
Kinloch	$G_0 \leq [G_I + G_{II}] [\cos^2(\phi - \phi_0) + \sin^2 \omega \sin^2(\phi - \phi_0)]$	3	11

To generate the toughness data, mixed-mode bend (MMB) tests were conducted on two different Hexcel materials; T800/5245 and T800/924. These matrix systems are a bismaleimide and a modified epoxy respectively. The laminates were tested at two different moisture conditions; *dry* (as received with negligible moisture content) and *wet* (equilibrium moisture content from conditioning at 60°C, 84% RH). The latter resulted in moisture contents of 0.7% (T800/5245) and 1.4% (T800/924) by weight.

Both these materials were tested as unidirectional laminates, but one material (T800/924) was additionally tested in the dry state to characterise a multidirectional ply interface ($0^\circ/90^\circ$). This used a stacking sequence of $[(90^\circ/-45^\circ/+45^\circ/0^\circ)_S(90^\circ/+45^\circ/-45^\circ/0^\circ)_S]I(0^\circ/+45^\circ/-45^\circ/90^\circ)_S(0^\circ/-45^\circ/+45^\circ/90^\circ)_S$ where 'I' is the location of the insert; this lay-up was chosen [1] to minimise the stiffness coupling terms in the arms of the coupon. All the laminates were tested using conventional DCB type specimens [1] except the $0^\circ/90^\circ$ ply interface specimens, which were tested using the modified specimen developed by Robinson and Song [2]. Five identical specimens were tested per parameter; the subsequent graphs shown in this paper are the averaged values. Further details of the experimental method are given elsewhere [1,3,4].

All the laminates contained 10 μm thick PTFE inserts, from which a 5mm precrack was grown under 75% Mode I loading; the precrack was accurately measured after the test. The laminates were tested at five different mixed-mode ratios, ranging from 0% mode I to 100% Mode II. However, the $0^\circ/90^\circ$ ply interface laminates could not be tested under pure Mode I loading due to problems with crack jumping under these conditions [1]. In all the tests the cracks were grown under displacement control and the data was reduced using the 'load only' method [5]. Selected fracture surfaces were examined using scanning electron microscopy to deduce the detailed failure processes. The data generated were used as the basis for assessing the failure criteria shown in Table 1; further details of these are given elsewhere [1]. For each mixed-mode ratio, the average G_I and G_{II} were determined for each data set at a given crack length, as well as the standard deviations, s_I and s_{II} , of the Mode I and Mode II components. The goodness of fit between the predicted data set from each criterion (G_I^P and G_{II}^P) and the experimental data (G_I and G_{II}) was given by χ^2 , where $n=5$; the number of data points:

$$\chi^2 = \frac{1}{n} \sum \left[\frac{(G_I - G_I^P)^2}{s_I^2} + \frac{(G_{II} - G_{II}^P)^2}{s_{II}^2} \right] \quad (12)$$

Consider a criterion $G_{II}^P=f(G_I^P, A, B, C)$, which has arbitrary parameters A, B and C. The optimum values of these parameters were determined by minimising χ^2 ; that is values of A, B and C were chosen to give values of G_I^P and G_{II}^P closest to G_I and G_{II} . However, since there was inherent uncertainty in both G_I and G_{II} , using the criterion in the form $G_{II}^P=f(G_I^P)$ was problematic. Therefore, where possible, each criterion was converted into the form $G_T=f(t)$ where $t=G_I/G_{II}$ and $G_T=G_I+G_{II}$, since the experimental values of t had minimal uncertainty. This optimisation method could be used if G_T was an explicit function of t . However, for criteria in which the expression was implicit (*i.e.* not solvable as $G_T=f(t)$), the Newton-Raphson iteration method was used [1]. It should be noted that the criteria did not all have the same number of parameters and thus the greater the number of parameters, the better the expected goodness of fit.

The curve fitting was conducted by minimising χ^2 using a quasi-Newton gradient search method [1]. Once the optimum values of the parameters and the minimum χ^2 for each criterion had been determined for a data set, the criteria were ranked. Two forms of ranking were used; the minimum χ^2 values, which indicated how well each criterion fitted the overall shape of the failure locus, and comparison between the predicted and measured values of Mode I and II toughness (G_{IC} and G_{IIC}) from each

criterion. In addition to ranking for each data set, the criteria were also ranked overall. These were determined by assigning each criterion with a ranking number (*e.g.* best fit=1, *etc.*) and summing these values over all the data sets; the lowest number = best overall fit. It should be noted that a four-parameter criterion (such as the General Interaction) requires more data than a two-point criterion (such as the Linear).

Experimental Results

The averaged failure loci for the 0°/0° ply interfaces are shown separately in Figure 1 for the effect of crack length and moisture. For clarity, the scatter in the data has not been shown, but this was generally below 10%. In general, the toughness was greatest under pure Mode II loading and fell as the proportion of Mode I increased. The shape of the failure loci were dependent on the material; T800/924 exhibited a fairly smooth locus whilst T800/5245 exhibited a hump at about 87% Mode I loading.

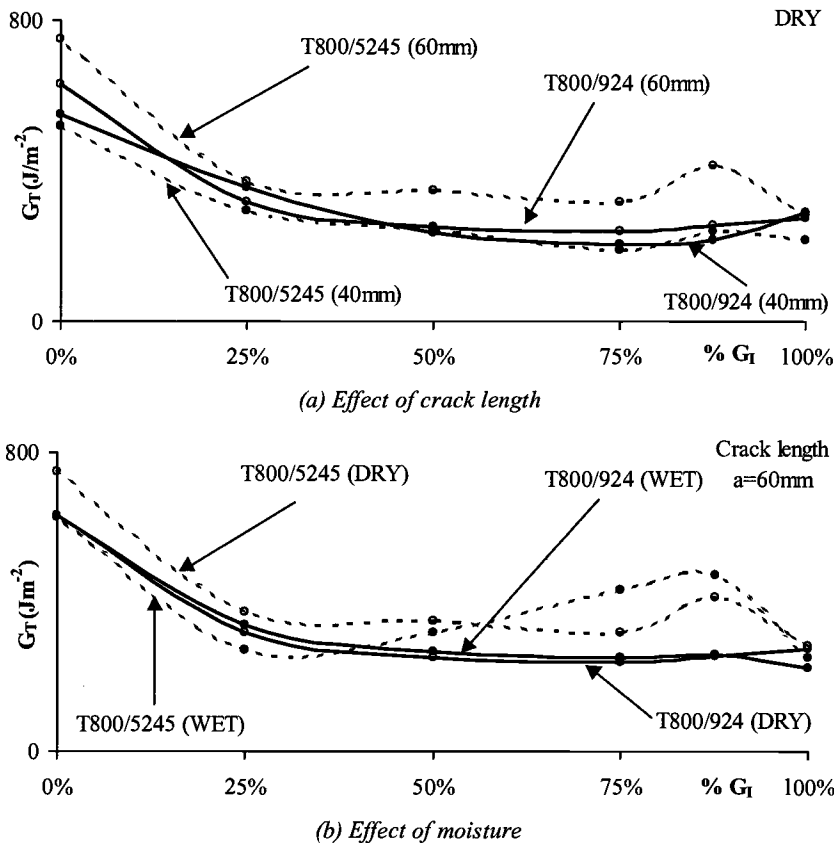


Figure 1 - Mixed-mode failure loci (experimental data) for 0°/0° ply interfaces.

As shown in Figure 1a, for a given mixed-mode ratio, the overall toughness increased and the hump became more exaggerated with increasing crack length in T800/5245. However, for T800/924 there was little evidence of a hump and negligible effect of crack length on the toughness. The toughness of T800/924 over most of the spectrum of mixed-mode conditions was similar to that of T800/5245 at short crack lengths, but was lower at larger crack lengths. This difference in toughness with crack length is further illustrated in Figure 2 which shows the toughness versus crack length from individual tests conducted at 75% Mode I loading for dry unidirectional T800/5245 and T800/924. At short crack lengths the toughnesses of the two materials were similar whilst at longer crack lengths the toughness of T800/5245 was significantly higher.

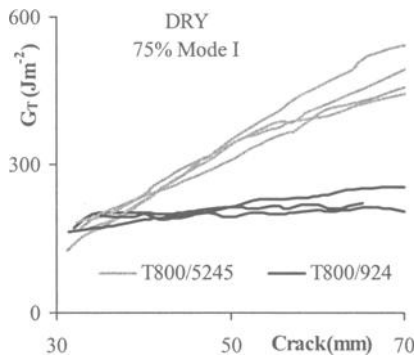


Figure 2 – Toughness versus crack length for T800/5245 and T800/924.

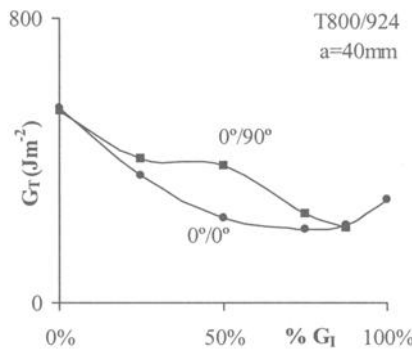


Figure 3 - Failure loci for 0°/0° and 0°/90° ply interfaces.

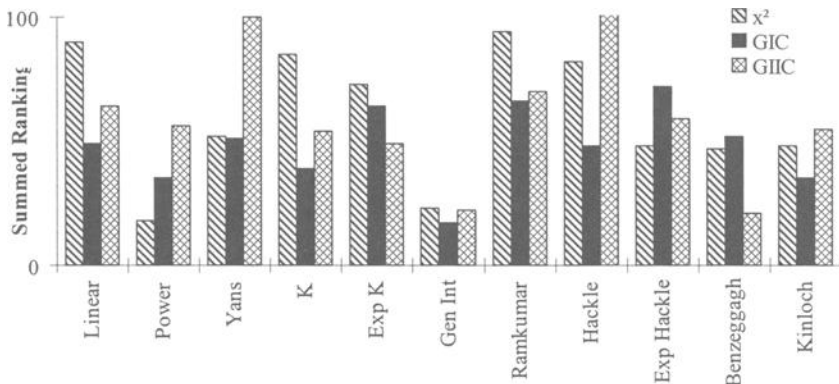


Figure 4 - Rankings for mixed-mode failure criteria summed for all materials.

The effect of moisture (Figure 1b) was dependent on the material. Although both materials had been conditioned to the same equilibrium level, the moisture contents differed significantly. This could be attributed to a difference in the resin chemistry.

However, since the environmental conditions were the same, it was felt that comparisons could be made between the materials. For T800/5245, under Mode II dominated loading, moisture reduced the toughness whilst under Mode I dominated loading, moisture increased the toughness and significantly increased the size of the hump. However, for T800/924, moisture had a negligible effect on the toughness over the whole spectrum of mixed-mode conditions studied.

As shown in Figure 3, there was a clear effect of ply interface on the toughness for T800/924. The shape of the $0^\circ/0^\circ$ and $0^\circ/90^\circ$ loci were very different. Although the toughnesses were similar under pure mode loading, there was a shallow hump in the $0^\circ/90^\circ$ failure locus; the toughness of the $0^\circ/90^\circ$ ply interface was 45% higher at 50% Mode I loading.

Overall rankings of the criteria are shown in Figure 4 and the goodness of fits (χ^2) are shown in Table 2. The optimum values of the parameters and the values of χ^2 , G_{IC} and G_{IIC} for each criterion and rankings are tabulated elsewhere [1]. In general, there were no clear trends or consistency in the goodness of fit and ranking for many of the criteria. However, if one was to select a criterion, the General Interaction criterion would be recommended since it ranked best for most of the data (Figure 4).

Firstly, for T800/5245, the best fits were for the Power and General Interaction criteria and the poorest for the Linear and Ramkumar criteria. There were no clear trends in the criteria with crack length, except that the minimum value of χ^2 increased as the crack length increased, particularly when the hump was significant. Similarly, the presence of moisture, particularly at large crack lengths, gave a poorer fit for most of the criteria. For the prediction of G_{IC} , the Power and General Interaction criteria gave the best results whilst for the prediction of G_{IIC} , the General Interaction and Benzeggagh criteria gave the best results. There was little consistency in the rankings as the crack length or moisture changed.

Table 2 - *Goodness of fit (χ^2) of mixed-mode criteria (best fit shown in black).*

χ^2 Interface a (mm)	T800/5245				T800/924				T800/924	
	(0°/0°) DRY		(0°/0°) WET		(0°/0°) DRY		(0°/0°) WET		(0°/90°) DRY	
	40	60	40	60	40	60	40	60	40	60
Linear	3.90	7.82	8.98	26.10	4.53	6.35	1.95	4.46	1.10	4.20
Power	0.74	1.56	1.18	14.83	0.14	0.11	0.06	0.68	0.11	0.41
Yans	1.74	2.24	1.65	19.76	2.57	0.76	0.17	0.66	2.77	7.03
K	2.35	4.55	5.10	24.65	3.55	3.16	0.62	1.60	2.82	8.77
Exp K	1.76	4.26	7.51	64.83	2.94	0.68	5.20	14.46	0.26	0.46
Gen Int	0.79	1.63	0.62	23.46	0.01	0.03	0.05	0.62	0.02	1.98
Ramkumar	7.37	11.5	14.38	26.75	6.21	10.9	4.62	9.14	0.69	1.49
Hackle	12.7	3.69	1.93	20.19	3.16	1.86	2.55	4.63	9.71	22.3
Exp Hackle	1.81	1.72	1.66	20.25	2.64	0.76	0.20	0.66	0.49	0.93
Benzeggagh	1.37	2.61	1.49	20.24	2.05	0.38	0.13	0.99	0.83	2.34
Kinloch	1.34	3.89	3.45	22.86	0.94	0.13	0.08	1.44	0.82	1.29

For the other $0^\circ/0^\circ$ ply interface laminates (T800/924) the ranking exhibited better consistency with changes in crack length or moisture than those for T800/5245. For the χ^2 rankings, the General Interaction criterion consistently gave the best predictions while the Ramkumar, Hackle and Linear were the poorest. The General Interaction,

Power and Kinloch criteria gave the closest predictions to G_{IC} and G_{IIC} whilst the Ramkumar, and Linear criteria gave the poorest predictions. There was no clear effect of moisture or crack length on the value of χ^2 .

For T800/924 (0°/90°) the criteria that best fit were the General Interaction and Power criteria whilst the Hackle and K criteria were the poorest and could not model the hump in the locus. For the G_{IIC} rankings, the Ramkumar and Benzeggagh criteria gave the closest predictions whilst the Power and K criteria gave the poorest.

The different behaviour of the materials, moisture contents and ply interfaces made recommending the best overall criterion problematic. The results indicated that data is required from a range of mixed-mode loading conditions (at least five conditions; 0%, 25%, 50%, 75% and 100% Mode I) to generate a detailed failure locus. The General Interaction criterion (Equation 6) gave the best overall predictions but most of the other criteria did not model the experimental results well, particularly at large crack lengths or high moisture contents.

Fracture Morphology

After testing, the fracture morphology was studied to develop an understanding of the delamination growth processes and their impact on the failure loci. Figure 5 shows the fracture surfaces of T800/924 (0°/0° ply interface) at different mixed-mode ratios. Under pure Mode I loading the surface was undulated with some bundles of loose and broken fibres (fibre bridging). The matrix fracture was quite plastic, exhibiting only limited brittle features such as riverlines; 'river-like' fracture morphology in the matrix [6]. As the proportion of Mode II increased, aligned scarps, and shallow flattened shear cusps developed [6]. Under 50% Mode I loading the fracture surface was flatter with only small regions of fibre bridging. The matrix failure was dominated by more upright cusps and some cleavage features. As the proportion of Mode II fracture increased (25% Mode I), the failure of the matrix was dominated by thicker cusps which were more upright. There were also loose pieces of matrix and fibres covering the surface. Under pure Mode II loading, the amount of debris had increased significantly and the surface was dominated by shear cusps tilted almost normal to the fibres.

Figure 6 shows the fracture morphology of T800/5245 and T800/924 at a loading condition of 50% Mode I; it can be seen that fracture morphology of T800/5245 was significantly different to that of T800/924. In the dry case, the fracture surface was more brittle with numerous distinct features such as riverlines. There was also an increase in the amount of fibre/matrix fracture in T800/5245, which manifests itself as an increase in fibre bridging, particularly at large crack lengths. Although it was difficult to quantify the degree of fibre bridging, careful inspection and comparison of the surfaces indicated that the maximum amount of bridging occurred under Mode I dominated loading (but not under pure Mode I loading).

Figure 6 also illustrates the effect of moisture on the fracture morphology in these two materials. For T800/5245 there was a clear effect on the fracture morphology; when moisture was present the fracture morphology became rougher and more dimpled, which was indicative of increased plasticity. Under Mode II dominated loading, the shear cusps became more irregular and more loosely attached to the surface. The presence of moisture also led to an increase in fibre bridging, which was particularly evident at large crack lengths.

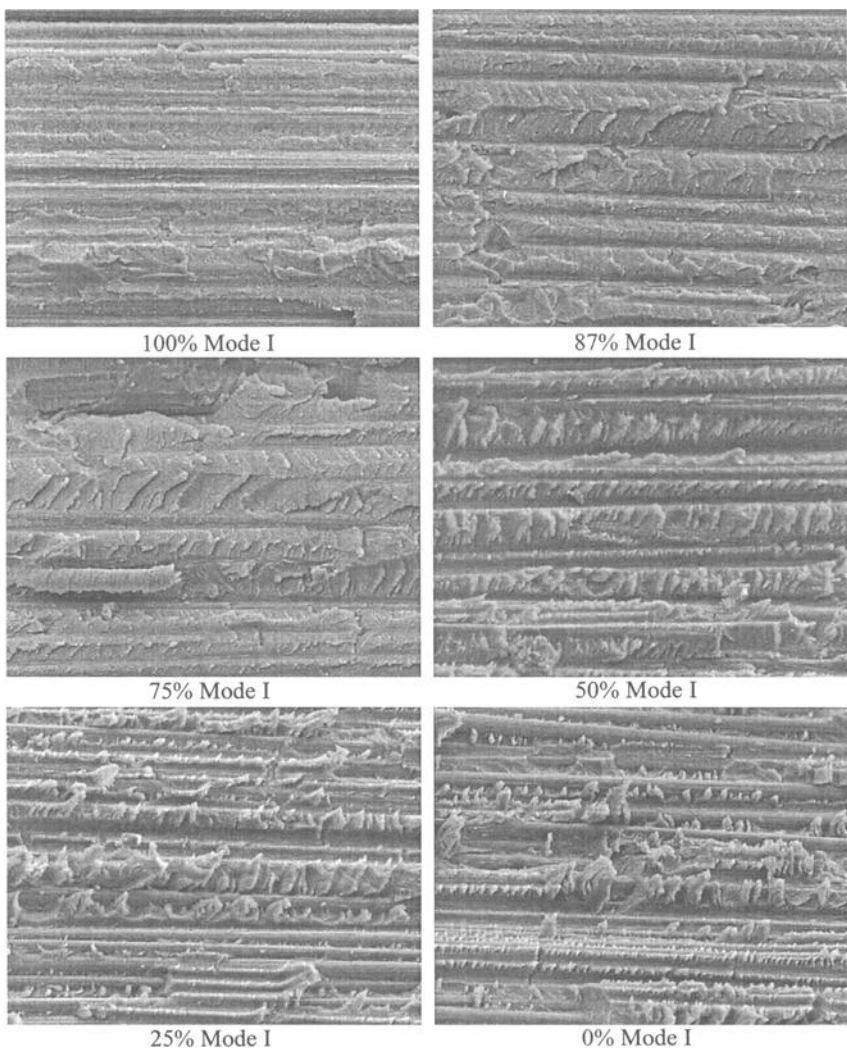


Figure 5 - *Fracture morphology (0/0° ply interface) for T800/924 (3000x, 30° tilt).*

The effect of moisture and crack length on the fracture morphology of T800/924 was limited. Moisture may have made the fracture morphology less brittle because features such as riverlines were less prevalent than in the dry case. However, there was no significant increase in the degree of fibre bridging or fibre/matrix failure in this material.

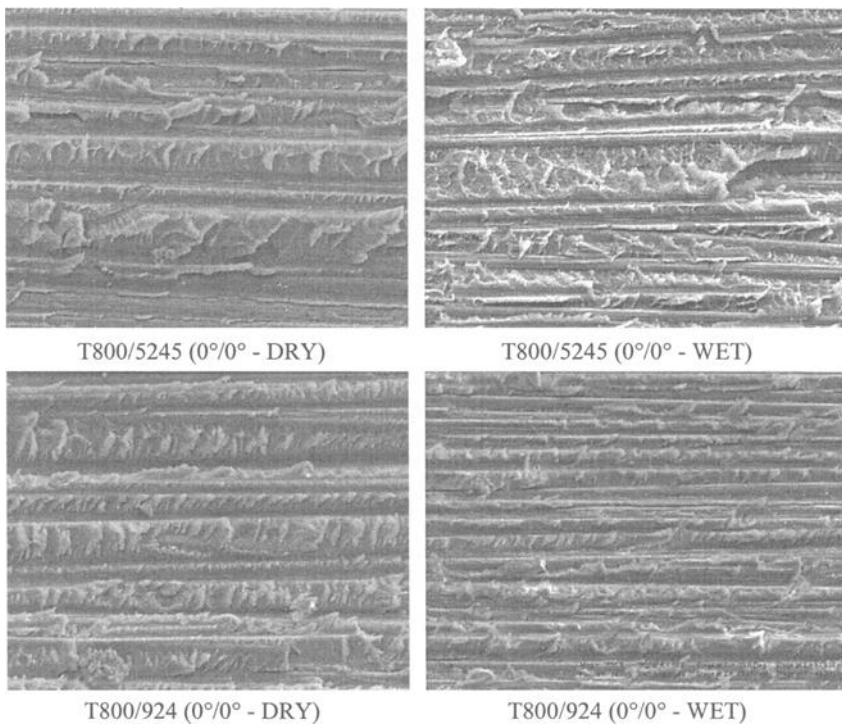


Figure 6 - Effect of moisture on fracture morphology at 50% Mode I loading (3000 \times , 30° tilt).

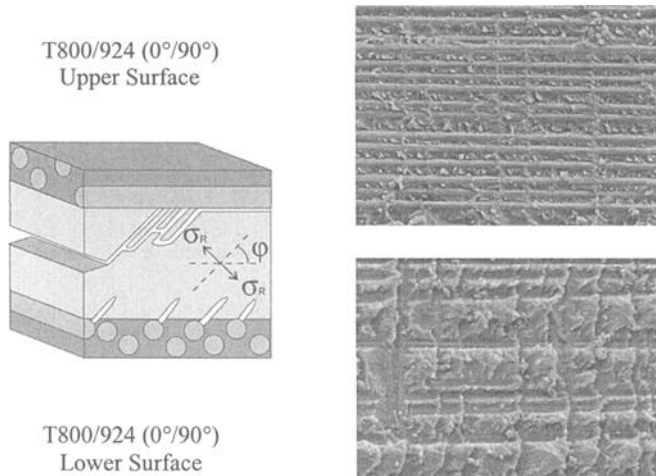


Figure 7 - Effect of ply interface on fracture morphology at 50% Mode I loading (3000 \times , 30° tilt).

The upper and lower fracture surfaces from a 0°/90° ply interface specimen tested at 50% Mode I are shown in Figure 7, with an illustration of the mechanism that led to the observed morphology [7]. As had been discussed elsewhere [7], under Mode I dominated loading the fracture surfaces were similar to those from the 0°/0° specimens (Figure 5). As the proportion of Mode II loading increased, transverse features ('ribs') perpendicular to the 0° fibres developed and became increasingly numerous. On the lower surface the impressions of the ribs developed as deep cracks, extending from the 90° fibres on the lower ply (see Figure 7). Shear cusps were more prevalent on the lower surface (matrix dominated) and, as with unidirectional materials, these become more upright and numerous as the Mode II component increased. Under Mode II dominated loading, the 0° fibres on the upper surface were quite devoid of resin, although there were some isolated islands of resin fracture. On the matching lower surface, the fracture was dominated by closely spaced shear cusps, interspersed with deep ribs, forming a grid pattern.

Discussion

In general, all the laminates studied exhibited the same trends; the toughness was a maximum under pure Mode II loading and decreased as the proportion of Mode I increased. This trend was attributed to cusp formation, as described by Hahn and Johannesson [8]. Under Mode I loading, the fracture of the matrix was by brittle cleavage and the process zone at the crack tip was relatively small. However, as the proportion of Mode II increased, the process zone grew, leading to the formation of cusps. These features became more upright, generating a larger effective area of fractured material per unit of surface area; increasing the toughness. The tilt of the shear cusps was directly related to the toughness, as discussed elsewhere [1]. Although cusp formation was the dominant energy absorbing mechanism during delamination, other mechanisms contributed to the fracture processes, leading to the observed differences in failure loci.

The toughness of unidirectional T800/5245 was dominated by a second mechanism: fibre bridging. This led to a significant increase in the toughness under Mode I dominated loading, producing the hump in the failure locus. When the hump was significant, such as at large crack lengths or when moisture was present, most of the failure criteria gave poor fits (χ^2) and predictions of G_{IC} and G_{IIC} . Criteria with four parameters (General Interaction and Power criteria) were best able to model the behaviour of T800/5245.

For unidirectional T800/924 fibre bridging was negligible and the toughness was dominated by the matrix fracture (cusp formation). Consequently the failure loci were fairly smooth in shape (no hump) and most of the criteria modelled the behaviour quite well. The General Interaction criterion was clearly the best model, giving the lowest values of χ^2 and the best predictions of G_{IC} and G_{IIC} . For T800/924 (0°/90° ply interface) rib formation contributed to the toughness, leading to the hump in the failure loci at about 50% Mode I loading. However, this hump was not as localised as that for T800/5245, so many of the failure criteria were capable of modelling the behaviour. As with previous materials, the General Interaction criterion was the best model, giving the low values of χ^2 , although the best predictions of G_{IIC} were given by the Ramkumar criterion.

There was no clear relationship between the material variables (such as crack length) and the parameters in any of the criteria. This implies that, in general, the criteria are empirical fits to the experimental data, and do not model the physical processes that occur during fracture. However, the General Interaction and Power criteria were overall the best models for the failure loci. The General Interaction criterion was physically based and quantified the interaction between the Mode I and II components, which gives confidence when using this criterion for design. The Power criterion is entirely empirical, but can model a wide range of loci. The Linear criterion, which is most commonly used by industry, was one of the poorest models, particularly for representing the shape of the failure loci.

The effect of crack length and moisture on the failure loci can be seen in Figure 1. There was a high degree of fibre bridging in T800/5245, which led to an increase in toughness with crack length and moisture. As the proportion of Mode II increased, there was a reduction in fibre bridging, reducing the effect of crack length. However, under Mode II loading, the increased degree of fibre/matrix failure when moisture was present may have reduced the toughness of T800/5245. These results indicate that the hump in the failure locus under Mode I dominated loading is due to fibre bridging. The observed increases in the degree of bridging (with crack length and moisture) correlated with an increase in the size of the hump.

For T800/924 crack length and moisture had much less effect on the toughness, which was attributed to the limited degree of fibre bridging in this material. The effect of matrix type on the failure loci is also illustrated in Figure 1. Fractography had indicated that the matrix fracture in T800/5245 were more brittle than in T800/924, although there was significantly more fibre bridging in the former. At short crack lengths, the superior resin toughness in T800/924 [9] was balanced by toughening contribution by fibre bridging in T800/5245, so the toughnesses were similar. However, at longer crack lengths, the fibre bridging mechanism dominated and T800/5245 was the tougher, particularly under Mode I dominated loading.

In T800/924, there was a significant difference in the shape of failure loci for 0°/0° and 0°/90° ply interfaces, with the latter exhibiting a shallow hump at 50% mode I loading. This effect was attributed to rib formation which only occurred at the 0°/90° ply interface. As discussed elsewhere [7], under Mode I dominated loading there were few ribs, so the toughnesses of the two ply interfaces were similar. Similarly, under Mode II dominated loading, although the ribs were numerous, the distance they extended through the resin layer between the plies (the interply zone) was relatively short, so the contribution to the toughness was small. However, under mixed-mode loading, the ribs were relatively numerous and they extended a significant distance through the interply zone; consequently the greatest difference in toughness from the unidirectional case.

Conclusions

In this paper the fracture micro-mechanisms, gleaned through fractographic analysis, were related to the delamination failure loci generated using mixed-mode bend tests (MMB). Two 0°/0° ply interface materials, at two different moisture contents, were characterised and, in one material, 0°/90° ply interface toughness was also characterised. Using this data, eleven failure criteria from the literature were

ranked according to which were most capable of modelling composite behaviour. From this study the following conclusions were drawn.

1. Generally, toughness was a minimum under pure Mode I loading and increased as the proportion of mode II increased, which was attributed to cusp formation mechanisms. However, other mechanisms contributed to the fracture processes, leading to the differences in failure loci observed between the different materials, moisture contents and ply interfaces. Most of the failure criteria bore no relationship with the fracture mechanisms but when the loci were smooth, most criteria fitted the test data quite well.
2. The toughness of T800/5245 ($0^\circ/0^\circ$ ply interface) was dominated by fibre bridging, which led to a significant increase in the toughness under Mode I dominated loading; producing a hump in the failure locus. This mechanism also led to a strong dependence of the toughness on the crack length and moisture content. The hump proved difficult for most of the failure criteria reviewed to model.
3. The toughness of T800/924 ($0^\circ/0^\circ$ ply interface) was dominated by the matrix fracture (cusp formation) and the effect of fibre bridging was negligible. The failure loci were quite smooth in shape, with no hump under Mode I dominated loading; most of the criteria modelled the behaviour quite well. In addition there was only a limited effect of crack length and moisture in this material.
4. For T800/924 there was a significant difference in the failure loci for $0^\circ/0^\circ$ and $0^\circ/90^\circ$ ply interfaces; rib formation contributed to the toughness in the latter, leading to a hump in the failure loci at about 50% Mode I.
5. Overall, the General Interaction and Power criteria were the best models for delamination. The General Interaction criterion was physically based and quantified the interaction between the Mode I and II components, which gives confidence when using for design. The Power criterion is entirely empirical, but could model a wide range of loci. The Linear criterion, which is most commonly used by industry, was one of the poorest models, particularly for representing the shape of the failure loci.

Acknowledgements

This work was in part funded by the UK MOD Corporate Research (TG04) and Applied Research (7B) Programmes and the UK DTI CARAD Programme. The authors would like to acknowledge the contributions of Matthew Hiley (QinetiQ) and Prof Frank Matthews (Imperial College).

References

- [1] Greenhalgh, E., "Characterisation of Mixed-Mode Delamination Growth in Carbon Fibre Composites," PhD Thesis, Imperial College, London, 1998.
- [2] Robinson, P. and Song, Q., "A Modified DCB Specimen For Mode I Testing Of Multidirectional Laminates," *Journal of Composite Materials*, Vol. 26, 1992, pp. 1554-1577.

- [3] Ljung, K., "Mixed Mode Bending Test Of The Interlaminar Fracture Toughness Of Carbon/Epoxy," FFA TN 1992-04, Aeronautical Research Institute of Sweden, 1992.
- [4] Juntti, M., "Theoretical And Experimental Evaluation Of The Mixed-Mode Bending Test," FFA TN 1997-28, Aeronautical Research Institute of Sweden, 1997.
- [5] Juntti, M., Asp, L. and Olsson, R., "Assessment Of Evaluation Methods For The Mixed Mode Bending Test," *Journal of Composites Technology and Research*, Vol. 21, 1999, pp. 37-48.
- [6] Purslow, D., "Matrix Fractography Of Fibre Epoxy Composites," Technical Report 86046, Royal Aerospace Establishment, UK, 1986.
- [7] Singh, S. and Greenhalgh, E., "Micromechanisms of Interlaminar Fracture in Carbon-Fibre Reinforced Plastics at Multidirectional Ply Interfaces Under Static and Cyclic Loading," *Plastics, Rubber and Composites Processing and Applications*, Vol. 27, 1998, pp. 220-226.
- [8] Hahn, H. and Johannesson, T., "A Correlation Between Fracture Energy And Fracture Morphology In Mixed Mode Fracture Of Composites," *4th International Conference on the Mechanical Behaviour of Materials*, Stockholm, 1983, pp. 431-438.
- [9] Hiley, M., "A Fractographic Study of Static and Fatigue Failures in Polymeric Composites", *Plastics, Rubber and Composites Processing and Applications*, Vol. 27, 1998.

Anders Sjögren,¹ Leif E. Asp,¹ Emile S. Greenhalgh,² and Matthew J. Hiley²

Interlaminar Crack Propagation in CFRP: Effects of Temperature and Loading Conditions on Fracture Morphology and Toughness

REFERENCE: Sjögren, A., Asp, L. E., Greenhalgh, E. S., and Hiley, M. J., "Interlaminar Crack Propagation in CFRP: Effects of Temperature and Loading Conditions on Fracture Morphology and Toughness," *Composite Materials: Testing, Design, and Acceptance Criteria, ASTM STP 1416*, A. T. Nettles and A. Zureick, Eds., American Society for Testing and Materials, West Conshohocken, PA, 2002.

ABSTRACT: This paper presents a survey of fractographic features associated with interlaminar failure of HTA/6376C carbon fiber/epoxy laminates. The interlaminar toughness and fracture morphology are investigated for effects of fatigue and static loading at elevated temperatures. In particular, Mode II loading conditions are investigated. Special emphasis is on initiation of matrix rollers and striations, two features indicative of Mode II fatigue failure. The initial mechanisms for delamination in this material under static and fatigue loading were found to be the same; the development of angled cracks ahead of the crack front, initiating from the fiber/matrix interface. Subsequent growth of the delamination was dependant on the loading conditions; under static loading shear cusps developed and coalesced whilst under cyclic loading increased plasticity led to development of matrix rollers. Fatigue striations observed in the fiber imprints were also found to initiate from the fiber/matrix interface cracks. The morphology of the striations, however, depended on the magnitude of the fatigue loading.

KEYWORDS: carbon fiber reinforced plastics, CFRP, fatigue, delamination, fractography

¹Senior scientist and associate professor, respectively, Swedish Institute of Composites (SICOMP), Box 104, SE-431 22 Mölndal, Sweden.

²Principle scientists, Structural Materials Centre, Building A7, DERA Farnborough, Hants, GU14 6TD, UK.

Introduction

Efficient design of composite structures requires a detailed understanding of both the failure behavior of the structure and the fracture behavior of the material. Therefore, in structures designed with laminated fiber-reinforced composites, a detailed understanding of the interlaminar fracture toughness of the material is important. Interlaminar fracture may arise from microcracks and cavities formed during manufacture, or from in-service damage caused, for example, by impact loading. Interlaminar cracks in composite structures are detrimental since they, firstly, are difficult to detect and, secondly, can significantly reduce both the stiffness and the strength of the material. The interlaminar toughness of laminated fiber-reinforced composites must therefore be considered in both the design and use of structures made from these materials.

Interlaminar crack propagation can take place in either Mode I (opening), Mode II (shearing), Mode III (tearing), or a combination thereof. The interlaminar fracture toughness of laminated fiber-reinforced composites is to a large extent controlled by the loading-mode, but other factors such as fiber, matrix, fiber/matrix interface, lay-up, temperature, moisture, *etc.*, are also of great importance. Detailed examination of the fracture surfaces is often helpful in understanding the mechanisms that govern the interlaminar fracture toughness of laminated fiber-reinforced composites. These types of studies have been conducted on carbon fiber-reinforced plastics (CFRP) for more than 20 years. Most of these studies have dealt with statically generated failures at room temperature, and the fractographic features characteristic of static failures under Mode I, Mode II and mixed-mode I/II loading are fairly well understood and documented [1].

In brief, the Mode I failure of unidirectional laminates is generally characterized by cohesive fracture of the matrix, fiber/matrix separation and fiber bridging [1-4]. The fracture surfaces often appear rather flat and exhibit pronounced river markings and resin microflow features. For failures between plies of different orientations, additional failure mechanisms can occur (*e.g.* ply jumping), which will significantly affect the toughness and fracture morphology [5].

Mode II and mixed-mode I/II interlaminar failures of unidirectional laminates generally take place through the formation of shear cusps (huckles) by the coalescence of microcracks, as described by Purslow [6]. The microcracks initiate and grow in the matrix in the plane subjected to maximum resolved tensile stress. If the compressive side is considered to be the upper half of the test specimen when it is flexing, the preferential direction of growth is upwards at an angle from the principal fracture plane. The microcracks grow until they reach the fibers at the upper boundary of the interply zone. The microcracks do not grow further since this would require fiber fracture or large-scale plasticity. The upper boundary therefore forms the fracture surface, which results in fibers at the upper fracture surface and fiber imprints at the lower fracture surface [7].

The difference in angle between the preferential direction of crack growth on microscopic (through the matrix) and macroscopic (along the ply boundary) levels will increase with increasing portion of Mode II. Under pure Mode II loading the orientation of the cusps is almost perpendicular to the principal fracture plane. This is due to, firstly, a large angle between the microscopic and macroscopic crack growth (approximately 45°) and, secondly, a rotation of the cusps prior to microcrack coalescence. The rotation of the cusps is interesting since this leads to a local crack tip opening (local Mode I) even for a pure Mode II loading [8,9].

Work undertaken by Singh and Greenhalgh [7] has shown that the tilt of the cusps allows the direction of the crack growth to be ascertained. If the fracture surface being examined contains mainly fibers then it corresponds to the upper surface in a mixed-mode test and the cusps then appear to tilt in the direction of crack growth. Conversely, if the fracture surface contains mainly fiber imprints it corresponds to the lower fracture surface and the cusps tilt in the direction opposite the crack growth.

In multidirectional laminates, Mode II and mixed-mode I/II interlaminar failures preferentially occur between plies of different orientation. When the shear direction is at an angle to the fibers the cusps tend to be aligned perpendicular to the shear stress, but with a clear preference to be driven along the fiber direction [10]. Furthermore, deep matrix cracks are often seen in interlaminar failures of multidirectional laminates. These cracks form a grid pattern with the fibers (fiber imprints) under Mode II and mixed-mode I/II loading [7].

The fractographic features described above are characteristic of interlaminar failures caused by static loading. The fractographic features typical of fatigue failures are less well known. However, with the advent of tougher material systems and higher design strains the fatigue properties will be of importance and the fractographic features associated with fatigue failure must be recognized and understood.

The objective of the present work was to improve the understanding regarding fracture morphology and key damage mechanisms associated with interlaminar failure of CFRP, and to identify a relationship between fracture mechanisms and toughness. In particular, fracture surfaces generated under pure Mode II loading conditions (static and cyclic loading) have been investigated. In fatigue, special interest was given to the initiation and growth of matrix rollers and striations, *i.e.*, the two fractographic features that are indicative of fatigue loading.

Experimental

Specimen Details

All specimens were manufactured from Hexcel HTA/6376C carbon fiber/epoxy prepreg and cured according to the supplier's recommendations. The quality of the laminates was assessed by ultrasonic C-scanning prior to being cut into specimens. The nominal ply thickness was 0.13 mm, and the dimensions of the specimens were: width $b=20$ mm, length $l=150$ mm, and nominal thickness $2h=3.1$ mm.

The specimen lay-up was $[0_{12}/(\pm 5/0_4)_S]$, where the sign “//” refers to the plane of the artificial delamination. This specific lay-up was chosen to allow a small off-axis interface angle, to reduce fiber bridging during interlaminar crack propagation, whilst keeping the specimen properties close to those of a unidirectional specimen. The ability of this layup to reduce fiber bridging has been shown in ref [11]. The anticlastic coupling ratio $D_{12}^2/D_{11}D_{22}$ discussed by Davidson and Schapery [12] was low in both specimen legs, 0.007 for the unidirectional leg, and 0.010 for the leg with off-axis plies. The difference in the leg's axial bending stiffness, D_{11} , was less than 1%.

The 35 mm long artificial delamination was made of 7.5 μm thick Upilex® 7.5S polyimide film from UBE. The thickness of the resin pocket in the $0^\circ/5^\circ$ interface was measured in an optical microscope and varied between 0-20 μm . No pre-cracking was conducted prior to testing.

Test Procedure

The three most commonly employed test methods for studying interlaminar toughness were used. For pure Mode I and Mode II the DCB and ENF tests were utilized, respectively, whilst for mixed mode ($G_{II}/G=0.5$) a modified version of the MMB test was employed [13]. Tests were performed in MTS servo-hydraulic test machines. Load-cell capacity was 250 N for the DCB and MMB tests and 1250 N for the ENF tests. The test specimens were connected to the test rig by self-aligning hinges with a quick-mounted coupling [14], which does not require bonding. The distance between the load point and the fulcrum, c , was determined for a mode mixity of $G_{II}/G=0.5$, by the analysis suggested by Reeder and Crews [13], to $c=41$ mm.

All fatigue tests were performed at a frequency of 5 Hz. The specimens were tested at an R-value of 0.1, at constant displacement amplitude. A minimum of seven specimens were tested for each mode condition and temperature, except for Mode I, DCB, at 100 °C for which three specimens were tested from high loads until crack arrest as outlined by Martin and Murry [15]. After the testing, two specimens from each loading condition were separated in tension and bonded to aluminum stubs, followed by gold sputter coating and examination using a scanning electron microscopy (SEM) at magnifications between x50 and x20 000.

Experimental Results

Results from static and fatigue tests at room temperature (20 °C) and elevated temperature (100 °C) are presented in Table 1. In this table, G_C refers to the critical strain energy release rate under static loading, whereas G_{th} refers to the threshold value for delamination growth under fatigue loading. The static test results have previously been published by Juntti et al. [16] and Asp [11]. The G_C reported for the MMB test is the sum of the Mode I and Mode II components. The constants C and r are fatigue life constants described in a modified Paris law as

$$\frac{da}{dN} = C(G_{max})^r. \quad (1)$$

In Eq. (1) G_{max} refers to the maximum energy release rates, G_I , G_{II} and G_I+G_{II} in the DCB, ENF and MMB tests respectively. A detailed description of the data reduction of test data is given in a previous study [17].

Table 1 -Measured static critical energy release rate, G_C , fatigue energy release rate threshold, G_{th} , and fatigue life constants; da/dN evaluated in mm/cycle.

Test method	20 °C				100 °C			
	G_C (J/m ²)	G_{th} (J/m ²)	C	r	G_C (J/m ²)	G_{th} (J/m ²)	C	r
DCB	260 (± 10)	60	$1.2 \cdot 10^{-7}$	5.5	249 (± 26)	30	$4.2 \cdot 10^{-6}$	4.2
MMB	447 (± 23)	66	$2.5 \cdot 10^{-8}$	6.3	535 (± 26)	42	$1.4 \cdot 10^{-6}$	4.6
ENF	1002 (± 63)	100	$7.5 \cdot 10^{-7}$	4.4	701 (± 84)	70	$9.1 \cdot 10^{-7}$	4.6

The DCB and MMB delamination growth was stable in the static tests, but the delamination growth in the static ENF tests was unstable. The results presented in Table

1 shows a strong effect of fatigue loading on the threshold value for delamination growth. The greatest relative reduction is found for the mixed mode case at 100 °C, for which the threshold, G_{th} , value is only 8% of the critical strain energy value, G_c . The threshold value at room temperature, as well as at 100 °C, for the ENF test is 10% of the corresponding critical strain energy release rate. It should, however, be noted that the critical strain energy release rate in the static ENF test at elevated temperature is only 70% of that at room temperature. For fatigue tests at room temperature, the effect is found to be largest under pure Mode II loading conditions in the ENF test.

Fractographic Examination

Previous studies at ambient conditions by the authors [7,17] have shown that the *initial* damage mechanisms in interlaminar failure of thermoset-matrix composites are identical under static and fatigue loading. The reason is that the thermoset matrix is, at a microscopic level, more or less homogeneous and there is no mechanism (comparable to dislocation movements in metals) by which damage can migrate and accumulate under low cyclic stresses. Fatigue failure in thermoset-matrix composites can, therefore, be considered as a series of interrupted static failures. This may not be the case for more advanced toughened matrices that can have a significant crystalline thermoplastic component.

Although the initial damage mechanisms are similar, mechanisms for damage (*i.e.* delamination) propagation may be different. In this paper, the fractographic features of specimens tested under pure Mode II loading conditions are discussed. The focus on Mode II test is motivated by the fact that no differences in fracture surfaces generated in fatigue and static tests for this material and lay-up have been observed under pure Mode I, DCB [17]. Furthermore, features observed in the ENF specimens are more pronounced than those on the surfaces of specimens tested under mixed-mode loading conditions, MMB. The results of the examination are presented and discussed below.

Effect of Fatigue (Mode II at RT)

This section describes the effects of fatigue loading on the fracture morphology of the investigated material. The results outlined within this section serve as a reference for discussions in the following sections. Figure 1 shows typical Mode II fracture surfaces generated under static and fatigue loading at room temperature (RT). The fatigue fracture surface was taken from an ENF specimen that had run 2 900 cycles at $G=0.64G_{Ic}$. The figure illustrates that the crack has grown at the upper fiber boundary under both static and fatigues loading, generating typical matrix dominated fractures on the lower fracture surfaces. The static fracture surface is covered with shear cusps, one of the most important fractographic features observed in composite materials. The fracture of the shear cusps was seen to be fairly brittle, with only a limited amount of plastic deformation. It should be noted that the cusp size is dependent on the amount of matrix between the fibers. In regions with tightly packed fibers there are many small cusps, whereas in regions with high matrix content there are larger, but less numerous, cusps. Figure 1 also shows that the cusp-like features that are generated under fatigue loading are more rounded and worn than the cusps generated under static loading. As discussed in previous work [1], these features are subtly different to the cusps generated under static loading. Also, these features seem to have been torn away from the surface

by the fretting between the upper and lower fracture surfaces. The fatigue fracture shown in (Figure 1b) is not representative of the whole fatigue fracture surface; the area presented in the figure only represents a region very close to the final crack front. Further beyond the crack front, towards the insert tip, these cusp-like features were completely torn away, giving rise to an abundance of rounded pieces of matrix material, as seen in Figure 2.

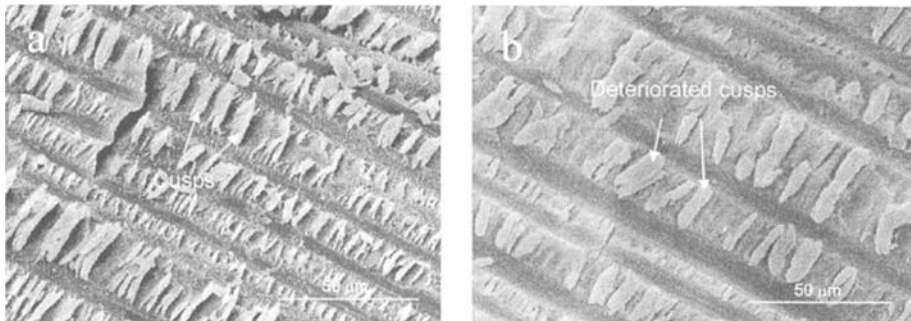


Figure 1 – Fracture surfaces generated under Mode II (a) static and (b) fatigue loading ($\times 1500$, 30° tilt).

Matrix rollers – Mode II fracture surfaces generated under fatigue are generally covered extensively with rounded pieces of matrix material, oriented more or less perpendicular to the fiber direction, see (Figure 2). These often wormlike shafts of matrix material were termed “matrix rollers” by Hiley [1], a term consistent with their appearance. The exact formation of the matrix rollers has, however, not been fully understood. The initial interpretation was, of course, that the matrix rollers form in the same manner as cusps produced during static fracture, and simply are cusps deformed as a result of the fretting action between the two surfaces. However, work undertaken by Hiley [1] revealed that statically generated cusps subjected to fretting retained much of their original shape, which suggests that the mechanism by which cusps/rollers morphology develops under fatigue loading is different to the mechanism by which cusps develop under static loading.



Figure 2 – Matrix rollers generated under Mode II fatigue loading ($\times 4550$).

An explanation for the difference between the morphology generated under static and fatigue loading, and thereby also an explanation to the formation of matrix rollers, was suggested in previous papers [1,17]. By careful examination of the crack fronts in specimens subjected to static and fatigue loading, the initial damage mechanism was found to be microcracking at the fiber/matrix interface under both loading conditions. Figure 3 shows how microcracks have initiated at the fiber/matrix interface and then grown into the matrix between the fibers. (Note the shift from Mode II fatigue to Mode I static loading, when the specimen was separated after testing, which produces a feather-like fracture extending from the multiple microcracks).

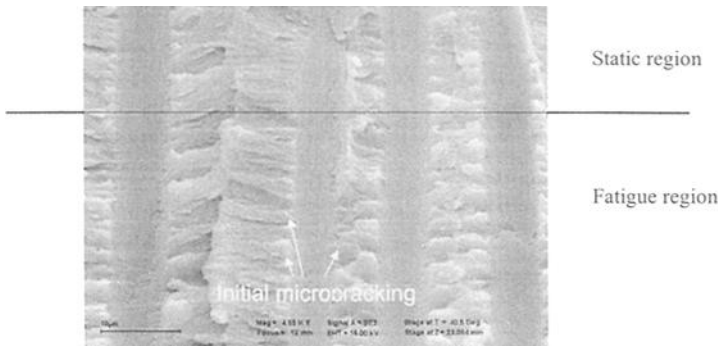


Figure 3 – Initiation and growth of microcracks at the fiber/matrix interface close to the crack front under Mode II fatigue loading ($\times 4550$).

A close-up of the crack front in Figure 3 is shown in Figure 4a. The microcracks at the fiber/matrix interface have formed on a number of planes and generated the features labeled “serrated feet” in the figure. Although the initial microcracking was similar under fatigue and static loading, a difference in the appearance of the serrated feet is observed, see Figure 4. Under static loading (Figure 4b) the multiple microcracks adjacent to the fibers (serrated feet) coalesce in the resin to form cusps. However, under fatigue loading, the plasticity in the fracture of the matrix increases, possibly due to local heating during the fatigue loading, and the cracks adjacent to the fibers (serrated feet)

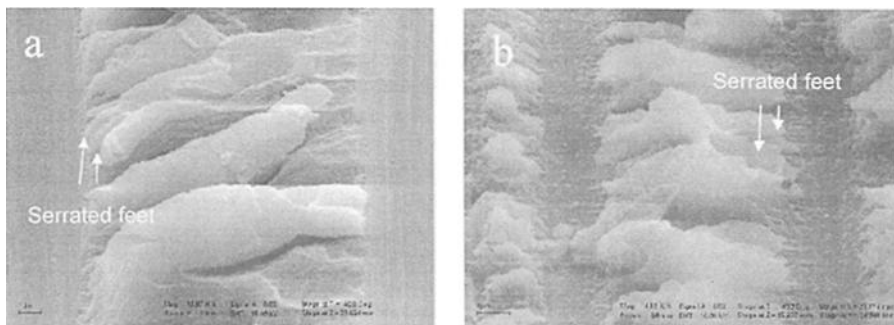


Figure 4 – Shear cusps at the crack tip generated under (a) fatigue loading ($\times 15K$), and (b) static loading ($\times 15K$).

extend into the matrix along a different path. Then, as the interlaminar crack extends along the specimen, fretting between the fracture surfaces leads to detachment of the rollers from the surface.

Striations – An important fractographic feature under Mode II fatigue loading is striations. These features appear as lines or shallow steps within the fiber imprints, or on the fibers, oriented perpendicular to the fiber orientation. In using the term striation it should be noted that this does not imply that the mechanism by which these fractographic features arise is the same as in metals, only that they are broadly similar in appearance.

The formation of striations in CFRP has been studied by Franz [4] and Hiley [1]. Based on their work, striations in CFRP consists of small steps in the matrix resin, which becomes apparent when the fracture surface is tilted more than 50° in the scanning electron microscope (SEM). Work was undertaken by Hiley to compare the interstriation spacing with the number of load cycles. However, no relationship could be established since the spacing between the striations varied considerably even within single fiber imprints.

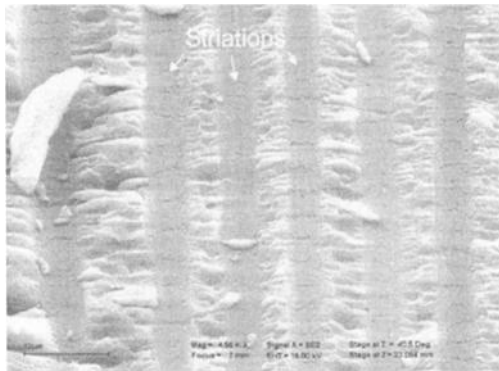


Figure 5 – *Striations in fiber imprints, generated under Mode II fatigue loading (x4550).*

Striations in HTA/6376C, the material examined in this study, are presented in Figure 5. The striations appear as distinct cracks in the fiber imprints, with a rather uniform interstriation spacing. These striations could also be seen on the fibers, as small matrix residues attached to the fibers. A close-up of the striation cracks is presented in Figure 6. From this figure the matrix fracture (textured microflow) shows that the striation cracks are extensions of the microcracks that initiate at the fiber/matrix interface. In the same way as microcracks propagate through the matrix to form shear cusps/rollers, the microcracks also propagate through the matrix around the fibers. Furthermore, by examining the crack front it was seen that the striations extend well into the Mode I static region (caused by the separation of the specimens), which suggests that the initiation and growth of striations may run ahead of the main crack front.

A detailed examination of the fiber imprints revealed smaller striations between the deep striation cracks. These smaller striations were similar in shape to the striations presented by Franz [4] and Hiley [1].

Based on the results from the fractographic study on HTA/6376C, and the information available in the literature, it is clear that the initiation and growth of striations depends on a number of factors such as fiber, matrix, fiber/matrix interface, local stress intensity, temperature, moisture, *etc* [1]. At low global load levels, *i.e.* low local stress intensities, striations probably do not form, or at least they are very difficult to detect by electron microscopy. For higher global load levels ($G=0.4G_{IIc}$) striations form as small steps within the matrix resin [1]. At very high global load levels ($G=0.64G_{IIc}$), deep striation cracks are formed within the fiber imprints. However, the interstriation spacing does not correlate with the number of load cycles either for the small striations [1] or the deep striation cracks [18].

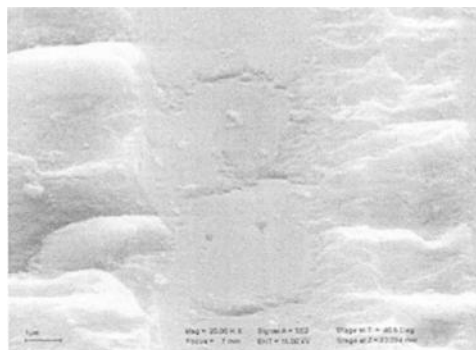


Figure 6 – Close up of striation cracks in fiber imprint (x20K).

Effect of Fatigue (Mode II at 100 °C)

The effects of fatigue at elevated temperatures are generally the same as those at room temperature. However, one significant difference between static and fatigue fracture surfaces for the pure Mode II tests at elevated temperature was the absence of exclusively matrix and fiber dominated surfaces in the former. Figure 7 shows fracture surfaces of static (Figure 7a) and fatigue (Figure 7b) specimens at elevated temperature.

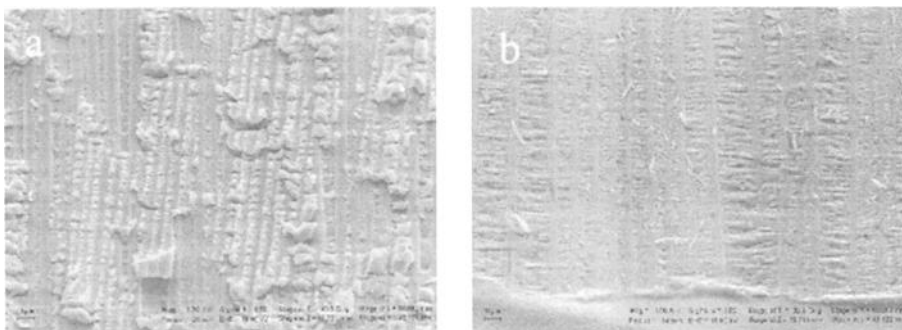


Figure 7 – Fracture surfaces generated under pure Mode II (a) static and (b) fatigue loading at 100 °C (x1000, 30° tilt).

In Figure 7a, the fracture surfaces of the static specimens exhibit a mixed appearance, where the crack has progressed alternatively at the upper and lower interfaces. Figure 7b depicts a matrix dominated fracture surface of a fatigue loaded specimen (701 000 cycles at $G_H=0.18G_{Hc}$) which was similar to those observed at room temperature (*i.e.*, exclusively fiber or matrix dominated). This morphology is discussed in more detail in the next Section.

Effect of Temperature (Mode II Static Test)

As described earlier, delamination growth in the static ENF specimen was unstable both at room temperature as well as at 100 °C. For this reason, when comparing the toughness, the particular area of interest is the crack growth initiation region, *i.e.*, at the crack tip because the remaining surface did not contribute to the toughness value. Figure 8 depicts two such growth initiation regions of ENF specimens tested at room and elevated temperature. The regions shown are the lowermost face ('matrix dominated'). The fracture surfaces present evidence that the higher temperature has reduced the fiber/matrix strength. Closer details of the fiber-dominated surfaces of the same specimens are shown in Figure 9. Clearly, the fiber/matrix bonding is poorer at the

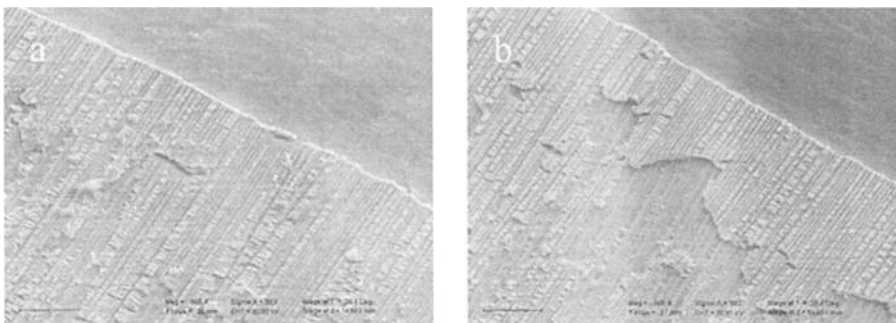


Figure 8 – *Initiation regions of ENF specimens tested at (a) room temperature and (b) 100 °C (x500).*

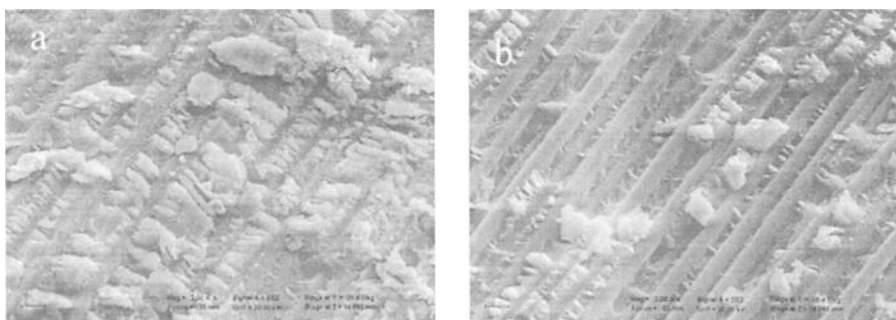


Figure 9 – *Close-ups of the initiation regions of ENF specimens tested at (a) room temperature and (b) 100 °C (x2000).*

higher temperature (Figure 9b). The shape of the shear cusps is also different; the room temperature morphology (Figure 9a) exhibits less resin plasticity but better adhesion of the resin to the fibers. This results in more serrated feet but less deformation in the cusps at room temperature. Figure 9 also suggests that the cusps of the fracture surface generated at 100 °C were thicker than those generated at room temperature.

As already mentioned, the delamination jumped between the upper and lower interply boundaries during growth in the static ENF test at elevated temperature. This jumping was not observed in the ENF specimens tested at room temperature. Detailed inspection of the morphology in these regions (Figure 10) indicates that deep cracks in the resin developed ahead of the crack front. Then, from the interpretation of the detailed morphology (textured microflow), it was determined from riverlines and textured microflow that delamination had grown from these deep cracks backward *towards* the main crack front. This is akin to the mechanisms that occur during fiber bridging in composites under Mode I dominated loading [1]. The delamination growth *towards* the main crack growth was occasional, but was significantly common at elevated temperature. This reversal mechanism may blunt the process zone during crack propagation and may therefore act as a toughening mechanism. However, it should be remembered that the reduced fiber/matrix strength would contribute to a lower toughness.

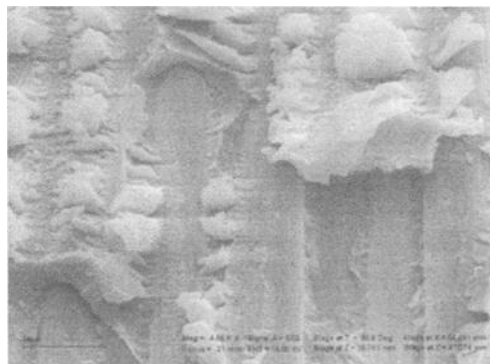


Figure 10 – *Detail of a region in which the delamination plane has jumped from fiber to matrix dominated planes in an ENF specimen tested at 100 °C (x4550).*

Effect of Temperature (Mode II Fatigue Test)

The effect of temperature on the fracture morphology of ENF specimens loaded in fatigue is demonstrated by comparing two specimens. The first specimen was loaded at $G_{II}=0.64G_{IIc}$ for 2 900 cycles at room temperature and the second was loaded at $G_{II}=0.18G_{IIc}$ for 701 000 cycles at 100 °C. However, this difference in fatigue cycles and magnitude of loading must be considered in the analysis as it may influence the fracture morphology.

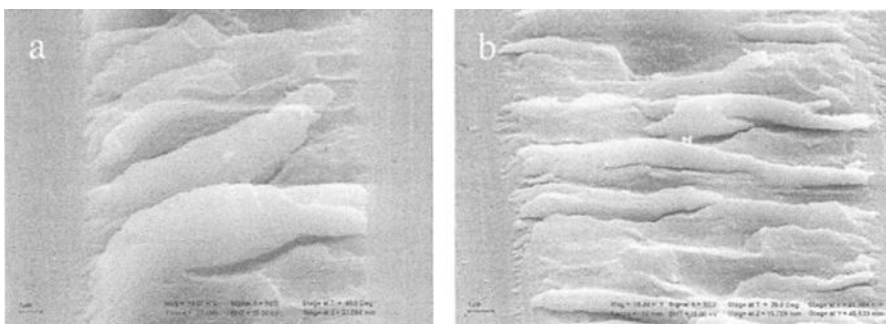


Figure 11 – Fracture surfaces generated under fatigue at (a) room temperature and (b) 100 °C (x15K).

Both specimens generally exhibited exclusively fiber or matrix dominated surfaces. However, close to the insert, the appearance of the surfaces was very different. The RT specimen exhibited a lot of abrasion and very few rollers were visible. The initiation region of the specimen loaded at 100 °C, however, had a flatter surface and a massive number of loose rollers. The more prevalent and looser matrix rollers in the 100 °C specimen compared to the RT specimen could be attributed to the poor fiber/matrix adhesion at the elevated temperature. However, an alternative explanation, that crack growth in the RT specimen was too rapid for rollers to form and detach completely, should be considered. Figure 11 presents shear cusps formed during crack propagation in these two specimens. The features found on the RT specimen surface are more like static shear cusps in appearance, with less flattening and clearly defined surface features. The 100 °C rollers are smoother and have more linear cracks visible and there is more plastic deformation rather than matrix cleavage.

No distinct difference between striations formed at room temperature and at elevated temperature was established. However, the global load level for striation formation was affected by the temperature, and most likely moisture content, of the material [1]. Increasing the temperature is found to soften the matrix material and to reduce the global load necessary to form striations. As an example, for pure Mode II fatigue loading, striations were found in specimens loaded at $G_H=0.64G_{Hc}$ (RT) and specimens loaded at $G_H=0.22G_{Hc}$ (100 °C), but not specimens loaded at $G_H=0.24G_{Hc}$ (RT).

Although in general the surfaces of the specimens loaded in fatigue were exclusively fiber or matrix dominated, at some isolated locations, sites of jumping were observed, see Figure 12. This image is from a specimen tested in fatigue at room temperature and shows a central region in which the failure is locally matrix dominated, surrounded by a fiber-dominated surface. The global crack growth direction is up the image. Striations were seen on the surface of the matrix dominated region, but the orientation of these striations indicated growth down the image, *i.e.* opposite of the global crack growth direction. The interpretation of this morphology is that a local delamination has initiated from the deep resin crack (angled towards the top of the image) and grown backwards, towards the main crack front. This morphology supports the finding discussed earlier in the paper and suggests a very unusual damage growth mechanism.

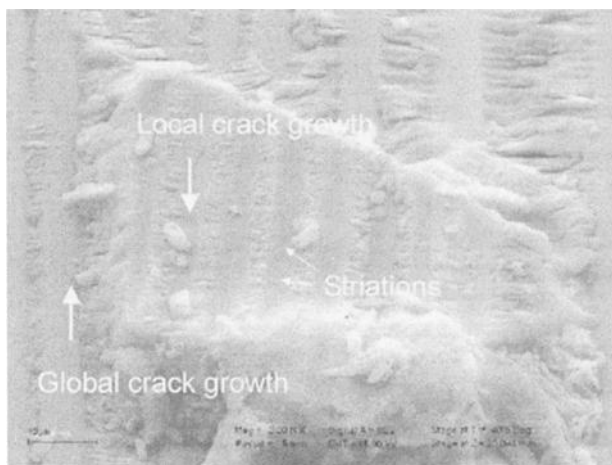


Figure 12 – Example of a region in which the fracture has initiated ahead of the main crack front and grown backwards towards the main crack front ($\times 3000$, 40° tilt).

Mixed-Mode (50% Mode II)

The fracture surfaces for 50% Mode II static and fatigue loading is presented in Figure 13. The fatigue fracture surface was taken from a MMB specimen that had undergone 1 450 000 cycles at $G=0.25G_c$. As for pure Mode II loading the crack growth has taken place along the upper fiber boundary, leaving matrix-dominated fractures at the lower fracture surfaces. The fracture surface generated under 50% Mode II static loading is covered with shear cusps, similar to the ones seen under pure Mode II static loading. The cusps are thinner than for pure Mode II and have a smaller tilt angle. Under fatigue loading the cusp/roller morphology has been completely crushed by the fretting action of the upper and lower surfaces, see Figure 13b. Closer examination of the morphology revealed similar shape and tilt of the features under static and fatigue loading, and the failure mechanisms were therefore deduced to be identical to those under Mode II loading.

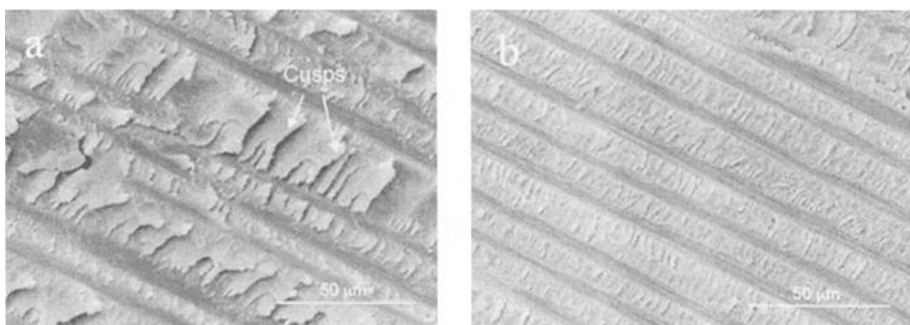


Figure 13 – Fracture surfaces generated under 50% Mode II (a) static and (b) fatigue loading ($\times 1500$, 30° tilt).

Matrix rollers are generally characteristic for Mode II dominated loading [1], but were also observed for 50% Mode II fatigue loading. The size of the rollers was, however, substantially smaller and the number of rollers much fewer. Striations were also observed under 50% Mode II fatigue loading, but their occurrence was rather sparse.

Mode I (opening)

Under pure Mode I loading the crack growth was primarily in the interply matrix region between the 0°/5° layers for both static and fatigue loading, see Figure 14. Examination of the entire upper and lower fracture surfaces revealed areas where the crack had grown in the fiber/matrix interface, but the main crack growth was in the matrix (cohesive fracture). The fatigue fracture surface was taken from a DCB specimen that had undergone 9 mm growth during 700 000 cycles at $G_f=0.62G_{lc}$.

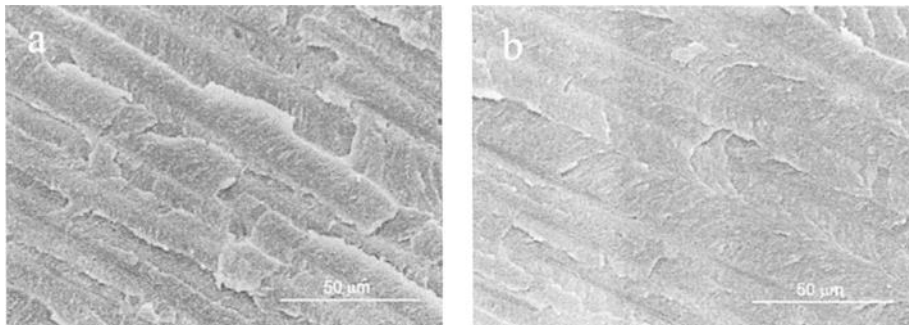


Figure 14 – Fracture surfaces generated under Mode I (a) static and (b) fatigue loading ($\times 1500$, 30° tilt).

No fractographic features characteristic of fatigue, such as matrix rollers or striations, was observed on the Mode I fracture surfaces. The very subtle difference in fracture morphology between static and fatigue failures under Mode I loading will result in considerable difficulties in distinguishing the difference between in-service static and fatigue failures. However, help can sometimes be gained by optical examination of the fracture surfaces; fatigue failures are generally somewhat macroscopically smoother than the static failures, which results in an enhanced reflectivity that can be noticed under careful optical examination.

Relationship between Toughness and Fracture Morphology for Mode II Tests

The understanding of the detailed fracture mechanisms developed from the fractography can be used to interpret the toughness and possibly the r -parameter in Eq. (1). This gives an indication of the important energy absorbing mechanisms during fracture in these materials. However, for Mode II specimens it is difficult to compare the performance under static and fatigue loading because, under the former, the fracture is unstable whilst, under the latter, it is stable. Therefore, the effect of temperature is only discussed in relation to the toughness results, *i.e.* critical and threshold values of the energy release rate G .

Static Loading

Under static loading, the main mechanisms for energy absorption during crack growth are formation of the microcracks ahead of the crack tip and development of these features into shear cusps. At room temperature, the fracture of the shear cusps is brittle and the fiber/matrix strength relatively high. The fracture surfaces present evidence that at higher temperature the fiber/matrix strength is reduced, which would tend to reduce the toughness of the material. The reduced fiber/matrix strength would also contribute to the formation of deep resin cracks and local reversals in the growth direction (jumping of the surface from matrix to fiber dominated, *etc.*). It is suspected that these mechanisms would tend to increase toughness of the material by complicating the crack path.

The shape of the shear cusps indicated that the resin exhibits increased plasticity at higher temperatures. However, under elevated temperatures the cusps are thicker and more block-like, resulting in a lower total fractured area generated per unit area of delamination. The observed reduction in toughness with elevated temperatures indicates that the fiber/matrix strength reduction is probably the dominant factor in controlling the toughness.

It has been argued by a number of authors [19,20] that G_{IIc} is not a material property but can be derived from the Mode I toughness (G_{Ic}). The fractographic evidence presented here indicates that this is not the case. Energy absorbing mechanisms, such as fiber/matrix debonding, roller formation and shear cusp deformation and coalescence were observed under Mode II loading, which cannot be inferred from the Mode I toughness or fracture morphology. The fractographic evidence shows that Mode I and Mode II toughnesses are a combination of energy absorbing mechanisms and that both Mode I (DCB) and Mode II (ENF) tests are required to characterize these material properties.

Fatigue Loading

Under fatigue loading the energy absorbing mechanisms are slightly different from those under static loading. The initiation mechanism, the formation of the microcracks ahead of the crack tip is the same (fracture initiation from the fiber/matrix boundaries). However, development of these features into rollers rather than shear cusps means the energy absorption is slightly different. Also, the formation (depth and spacing) of the striations changes with magnitude of the fatigue load, suggesting a different degree of energy absorption.

The reduced threshold (G_{th}) value at elevated temperature may be related to the reduced static toughness (G_c). This leads to the conclusion that the threshold value of the toughness for fatigue growth is related to the fiber/matrix strength. Fractographic evidence supports this. At room temperature, the morphology of the matrix rollers is brittle and the fiber/matrix strength relatively high. At elevated temperature, however, the rollers are more plastically deformed, but the fracture surfaces present evidence that at higher temperature the fiber/matrix strength is reduced.

The r -values from the Mode II fatigue tests at room temperature and 100 °C are almost the same (5% difference). Physically, the r -value, as presented in Eq. (1), relates to the rate at which the crack grows (da/dN) as a function of the amplitude of applied load expressed in energy release rate, G . Thus, the unaffected r -value of the Mode II

tests suggest that, although the static toughness is affected by temperature, the rate at which a crack grows in fatigue is not. Consequently, one would not expect to find differences in mechanisms controlling the fatigue growth at different temperatures. This implies that the observed reduction in fiber/matrix strength is less of a factor in fatigue rate than it is at initiation of static failure.

Conclusions

Mode I, Mode II and mixed mode tests were conducted under static and cyclic loading on Hexcel HTA/6376C laminates to characterize the toughness of the 0°/5° interface at room and elevated temperatures (100 °C). The results of the tests are described elsewhere [17,18] but this paper describes the findings of the fractographic analysis of these specimens and uses these to interpret the test results. From the findings of this work the following conclusions were drawn;

1. The initial mechanisms for Mode II delamination in this material under static and fatigue loading were the same; the development of angled cracks ahead of the crack front, initiating from the fiber/matrix interface.
2. The subsequent growth of the delamination was dependant on the loading conditions; under static loading shear cusps developed and coalesced whilst under cyclic loading increased plasticity led to development and detachment of rollers from the surface.
3. Fatigue striations also initiated from the fiber/matrix interface cracks; the morphology of these features was dependent on the magnitude of the fatigue loading. Striations do not appear to correlate to the loading history of the laminate.
4. For static failures under elevated temperatures, the fiber/matrix strength significantly reduces, leading to local diversion of the crack path and detachment of the fracture morphology from the surface. Despite the increase in matrix plasticity, the fiber/matrix strength reduction dominates, leading to a reduction in toughness.
5. At elevated temperatures, the reduction in fiber/matrix strength led to crack initiation ahead of the main crack front and local growth in the opposite direction to the main front.
6. For fatigue failures at elevated temperatures, there was again evidence that the fiber/matrix strength was reduced, although not to the same extent as was observed under static loading. However, it was difficult to isolate the effect of temperature from the effects of the different loading conditions under fatigue.
7. The reduced fatigue threshold value, G_{th} , at elevated temperature was found to relate to the impaired fiber/matrix strength. The impaired fiber/matrix interface had, however, no effect on the fatigue growth rate.
8. Features observed on mixed mode loading, MMB, specimens were similar to, but much less pronounced than, those on the surfaces of specimens tested under pure Mode II loading conditions.
9. Under pure Mode I, DCB, no differences in fracture surfaces generated in fatigue and static tests for this material and lay-up were observed.
10. The fractographic evidence presented in this paper demonstrates that a number of failure mechanisms contribute to the Mode II toughness (G_{IIc}) and these mechanisms are unique to Mode II; they cannot be derived from Mode I test results.

The results of this study have improved the understanding of fatigue mechanisms in composite laminates at room and elevated temperatures. It is particularly important to relate the observed fracture mechanisms to the mechanical behavior; both under static and cyclic loading. Such knowledge can be used to identify the critical loading conditions for current designs and the development of tougher, more durable materials for future aircraft structures.

Acknowledgements

This work was performed at the Aeronautical Research Institute of Sweden, FFA, under a grant from the Swedish Defense Material Administration (FMV).

References

- [1] Hiley, M. J., "Fractographic Study of Static and Fatigue Failures in Polymer Composites," *Plastics, Rubber and Composites*, Vol. 28, No. 5, 1999, pp. 210-227.
- [2] Bascom, W. D., Boll, D. J., Hunston, D. L., Fuller, B., and Phillips, P. J., "Fractographic Analysis of Interlaminar Fracture," *Toughened Composites, ASTM STP 937*, N. J. Johnston, Ed., American Society for Testing and Materials, Philadelphia, 1987, pp. 131-149.
- [3] Lee, S., Gaudert, C., Dainty, R. C., and Scot, R. F., "Characterization of the Fracture Toughness Property (G_{Ic}) of Composite Laminates Using the Double Cantilever Beam Specimen," *Polymer Composites*, Vol. 10, No. 5, 1989, pp. 305-312.
- [4] Franz, H. E., "Microfractography of Fiber Reinforced Composite Materials," *Practical Metallurgy*, Vol. 28, 1991, pp. 404-419.
- [5] Robinson, P., and Song, D. Q., "A Modified DCB Specimen for Mode I Testing of Multidirectional Laminates," *Journal of Composites Materials*, Vol. 26, No. 11, 1992, pp. 1554-1577.
- [6] Purslow, D., "Matrix Fractography of Fiber-Reinforced Epoxy Composites," *Composites*, Vol. 17, No. 4, 1986, pp. 289-303.
- [7] Singh, S., and Greenhalgh, E., "Micromechanisms of Interlaminar Fracture in Carbon Fiber Reinforced Plastics at Multidirectional Ply Interfaces under Static and Cyclic Loading," *Plastics, Rubber and Composites Processing and Applications*, Vol. 27, No. 5, 1998, pp. 220-226.
- [8] Hibbs, M. F., and Bradley, W. L., "Correlations Between Micromechanical Failure Processes and the Delamination Toughness of Graphite/Epoxy Systems," *Fractography of Modern Engineering Materials: Composites and Metals, ASTM STP 948*, J. E. Masters and J. J. Au, Eds., American Society for Testing and Materials, Philadelphia, 1987, pp. 68-97.
- [9] Paris, I., "In-Situ Measurements of Delamination Crack Tip Behavior in Composite Laminates Inside a Scanning Electron Microscope," PhD-thesis, The University of British Columbia, Canada, 1998.
- [10] Purslow, D., "Some Fundamental Aspects of Composites Fractography," RAE Technical Report 81127, Farnborough, UK, 1981.

- [11] Asp, L. E., "The Effects of Moisture and Temperature on the Interlaminar Delamination Toughness of a Carbon/Epoxy Composite," *Composites Science and Technology*, Vol. 58, No. 6, 1998, pp. 967-977.
- [12] Davidson, B. D., and Schapery, R. A., "Effect of Finite Width on Deflection and Energy Release Rate of an Orthotropic Double Cantilever Specimen," *Journal of Composite Materials*, Vol. 22, No. 7, 1988, pp. 640-656.
- [13] Reeder, J. R., and Crews, Jr., J. H., "Mixed-mode Bending Method for Delamination Testing," *AIAA Journal*, Vol. 28, No. 7, 1990, pp. 1270-1276.
- [14] Brandt, F., "A new load introduction concept for improved and simplified delamination beam testing," *Experimental Techniques*, Vol. 2, No. 1, 1998, pp.17-20.
- [15] Martin, R. H., and Murry, G. B., "Characterization of Mode I and Mode II delamination growth and thresholds in graphite/PEEK composites," TM 100577, NASA, 1988.
- [16] Juntti, M., Asp, L. E., and Olsson, R., "Assessment of Evaluation Methods for the Mixed-Mode Bending Test," *Journal of Composites Technology and Research*, Vol. 21, No. 1, 1999, pp. 37-48.
- [17] Asp, L. E., Sjögren, A., and Greenhalgh, E. S., "Delamination Growth and Thresholds in a Carbon/Epoxy Composite under Fatigue Loading," *Journal of Composite Technology and Research*, Vol. 23, No. 2, 2001, pp. 55-68.
- [18] Sjögren, A., and Asp, L. E., "Effects of Temperature on Delamination Growth in a Carbon/Epoxy Composite under Fatigue Loading," accepted for publication in *International Journal of Fatigue*.
- [19] O'Brien, T., "Composite Interlaminar Shear Fracture Toughness G_{IIc} ; Shear Measurement Or Sheer Myth?," NASA TM 110280, (1997).
- [20] Piggot, M., Liu, K. and Wang, J., "New Experiments Suggest that all Shear and Some Tensile Failure Processes are Inappropriate Subjects for ASTM Standards," In *Composite Structures; Theory and Practice*, ASTM STP 1383, P Grant & C Rousseau Eds, ASTM, West Conshohocken, Philadelphia, 2000, pp. 324-333.

Basant K. Parida,¹ K. Vijayaraju,² and P. D. Mangalgiri²

Buckling and Fracture Behavior of Tapered Composite Panels Containing Ply Drops

Reference: Parida, B.K., Vijayaraju, K., and Mangalgiri, P.D., "Buckling and Fracture Behavior of Tapered Composite Panels Containing Ply Drops," *Composite Materials: Testing, Design, and Acceptance Criteria, ASTM STP 1416*, A. Zureick and A.T. Nettles, Eds., American Society for Testing and Materials International, West Conshohocken, PA, 2002.

Abstract: In typical applications like in the top skin of the wing or in control surfaces of an airframe, laminated composites are often found to be buckling-critical. Under excessive compression loading composite panels may undergo buckling and failure mechanisms would generally involve delamination or fiber breakage. Tapered composite panels with ply drops, when employed in wing skin, are expected to be more prone to the above mode of failure. This is one important area of concern to the designers of composite structures and both analysis and experimental verification of the buckling behavior is recommended as a part of design validation effort. However, data from such analysis are scarce in open literature. In this paper, results of a study on buckling and fracture behavior of laminated Carbon Fiber Composite (CFC) panels containing ply drops are presented. CFC panels of varying thickness with normal and inclined ply drop were tested under compression loading until buckling and ultimate failure. Nearly simply supported boundary conditions at the ends and along the edges were simulated with the help of specially designed test fixtures. Tests were conducted both under room temperature and hot-wet ($100^{\circ}\text{C} \pm 3^{\circ}\text{C}$ and $\geq 85\%$ RH) environmental conditions. Back-to-back strain gage output and out-of-plane deformation data were recorded and analyzed to determine the critical buckling loads and corresponding mode shapes. Finite element analysis using MSC NASTRAN was also made in order to predict critical buckling loads and corresponding mode shapes. These results were compared with those obtained from experiments and the agreement was found to be good in most cases. It was also found that under hot-wet conditions, both critical buckling loads and failure loads were lower compared to the room temperature values.

Keywords: carbon fiber composite panels, tapered, ply drop, buckling load, finite element analysis, room temperature test, hot/wet environment, fracture behavior

The last few decades of the twentieth century had witnessed a kind of material revolution in engineering with the coining of terms like engineered materials and advanced composite materials. These new materials were developed specifically to assist the designers of engineering structures with the ability to improve specific performance and durability of the new structures. Among the varieties of advanced composite materials developed and employed in real-life structures, polymeric composites, more specifically carbon fiber reinforced composites, have been very extensively employed in aerospace structures, because

¹Scientist, Structural Integrity Division, National Aerospace Laboratories, Bangalore 560 017, India.

²Scientists, Aeronautical Development Agency, Vimanapura Post, Bangalore 560 017, India.

of their high specific strength and good resistance to failure under fatigue loading. With extensive use of carbon fiber composites (CFC) in both civilian and military airframes, presently the composites account for almost 40-50% of the structural weight fraction of the airframe, in some instances, which has met the prediction made by Sanger et al. [1] over a decade ago. However, in view of the lack of an extensive data base and very limited service usage experience with composites as compared with metallic materials, it is always advisable and is also a common practice to follow the “building block approach” for validating the soundness of any new composite design [2]. The advantages of using composites in airframe structures are that, unlike in metals, they have inherent resistance to fatigue crack initiation and propagation at stress raisers when subjected to cyclic or fatigue loading. However, composites are likely to lose their specific strength advantage because of loss of strength with impact damage and environmental degradation [3-4]. In hybrid structures or in stiffened structures like in aircraft wings, layered composite laminates/panels connected through fastener joints may exhibit variations in buckling strength and mode of failure, depending on the boundary conditions, lamina configuration and environmental conditions. The combined effects of humidity and elevated temperature on the buckling strength of composite plates have been studied by Flaggs et al. [5] and Collings et al. [6], who have shown that hygrothermal conditions have a tendency to decrease the buckling strength of CFC laminates.

In recent times, laminated composite materials have found extensive use in the construction of aircraft structural components. Aircraft wing skins are supported by spar-rib substructure and the skins are designed to carry in-plane loads. Skins are generally designed as buckling-critical parts. In most practical structural applications, the laminated composite panels are likely to have a combination of 0° , 90° , and $\pm 45^\circ$ ply angles. In such instances, some form of coupling responses, like the stretching-bending, stretching-twisting, shearing-twisting, bending-twisting, etc. may be present. An analytical closed form solution in such cases is virtually impossible. In the past, Chamis [7] and Ashton [8] have used approximate methods using the energy approach to determine critical buckling loads.

The elastic buckling problem of flat laminated composite panels has been investigated by Vinson et al. [9], Chamis [10] and Whitney et al. [11]. The post-buckling behavior of flat laminated composite plates has been studied by Chia et al. [12] and Chia [13]. Leissa [14] has provided a good overview of a large number of papers available in open literature on this topic and has pointed out the need to generate more experimental data. Chai [15] has presented a buckling analysis of generally laminated composite plates with simple supported boundary condition. He has used a total potential energy approach together with Rayleigh-Ritz method [16] to study analytically the stability behavior of laminated composite plates with different edge-support conditions. In a recent study, Parida et al. [17] have investigated the compression buckling behavior of uniform thickness CFC panels under simply supported and clamped boundary conditions, both experimentally and through finite element analysis. They have also evaluated the effect of hot/wet environmental conditions on the compression buckling behavior of CFC panels.

However, it may be noted that while employing the laminated composite materials in the construction of aircraft wing skin-like structures, thickness and lay-up of each zone is required to be optimised, and hence this would be different in various zones. These thickness changes are achieved by internal ply drops at the time of fabrication. Hence, the buckling behavior of thickness tapered composite panels, (i.e., laminates containing ply drops) is of relevance and concern to the design of skin-like structural elements in aerospace industry. Unfortunately, reference of such work in open literature is scarce. In order to understand the structural stability behavior of thickness tapered panels, an attempt has been made in this paper to analyze compression buckling of tapered panels using a general-purpose FEM

package, namely NASTRAN. Present work attempts to study the effects of different ply-drop configurations and hot/wet environment on the buckling behavior of CFC panels. Critical buckling loads and buckling mode shapes for different panel configurations have been determined, both from FEM analysis and from experimental investigation, under room temperature and hot/wet environmental conditions.

Numerical Analysis

Method and Modeling

Details of the CFC laminates taken up for this study are presented in Table 1. Geometry and details are shown schematically in Figure 1. Thickness change and angle of orientation of the tapering zone to the loading axis along with the lay-up sequence are given in Table 1. Plies, which are underlined in the lay-up sequence, are dropped to effect the thickness change. The order of ply drop in five steps, numbered 1 to 5, for both the laminate configurations have been shown below the identified (to be dropped) ply angles in Table 1.

Table 1 - *Details of the analysed tapered panels.*

Panel ID	Orientation of ply drop zone to loading direction	Nominal Thickness in mm		Lay-up sequence
		Thick zone	Thin zone	
STE-24 Order of Ply drop	70°	6.6	5.1	$\{(\pm 45)_4/45/90_2/0/\underline{\pm 45}/45/0_2/90/\underline{90}/0/90/0\}_s$ <u>5</u> <u>1, 4</u> <u>2</u> <u>3</u>
STE-26 Order of Ply drop	90°	7.2	5.7	$\{(\pm 45)_2/90_4/0/\underline{\pm 45}/45/90/\pm 45/\underline{90}_2/\pm 45$ <u>1</u> <u>3, 2</u> $/45/90/45/0/90\}_s$ <u>4</u> <u>5</u>

The test area of the panels that was used in this investigation was 450 mm X 225 mm, which results in a/b ratio of 2. In view of the difficulties in realising the ideal simply supported conditions particularly on loading ends, the following scheme was devised to get as nearly simply supported conditions as possible. Additional area was provided in the test panels at both the ends for tab bonding and on the sides to place the knife-edges. This resulted in an increase of the panel size to 540 mm X 241 mm. The tab-bonded area on one end of the panel was held in a snug-fit condition inside the grooves of two split clamping end-plates. Tab-bonded area on the opposite end of the panel was also similarly held between a pair of split type clamping end-plates that were connected to the cross-head of the testing machine through a load-cell. Nearly simply supported boundary condition was realised over the panel area of interest, using two sets of back-to-back knife-edges on all the edges and ends. These boundary conditions are referred to as "pseudo simply supported" conditions in this paper. In order to simulate realistically the loading and boundary conditions applied during the test, complete area of the laminates including regions under tabs and those surrounded by the knife-edges was modeled in the FEM analysis.

FEM Modeling

All the models for this numerical (FEM) study were created using MSC PATRAN Version 8.5, and the buckling analysis was carried out using MSC NASTRAN Version 70.5.0. For the buckling analysis, the solution method of SOL105 has been used. Four-noded quadrilateral composite shell elements (CQUAD4/PCOMP) have been used to model the laminate geometry. It has been attempted to maintain the aspect ratio of the element to be around $1 \sim 1.5$. This had resulted in approximately 2000-2300 elements and 2300-2600 nodes. The tapered region of the laminate has been modeled as a stepped geometry. At each ply-drop station, two plies were dropped and a distance of 6 mm (STE-24) and 3 mm (STE-26) staggered the ply drop stations.

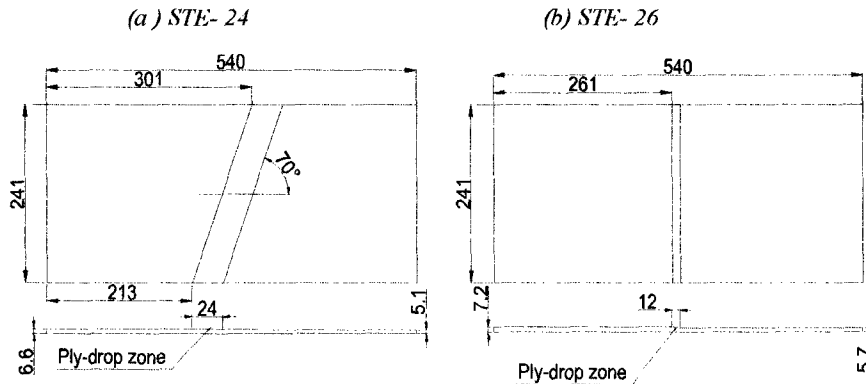


Figure 1 - Schematic diagrams of tapered panels with different ply drop configurations:
(a) STE-24 and (b) STE-26.

Modeling of the tapered zone is explained below. For example, consider the tapered laminate (STE-26) with a thickness of 7.2 mm reducing to 5.7 mm along the longitudinal direction of laminate. Initial thickness of 7.2 mm made up by 48 plies was dropped at five stations to arrive at a thickness of 5.7 mm, which was made up by 38 plies. Tapered region of the laminate has been modeled as a stepped region with the corresponding thickness and number of plies, shown in parentheses. This is schematically shown in Figure 2.

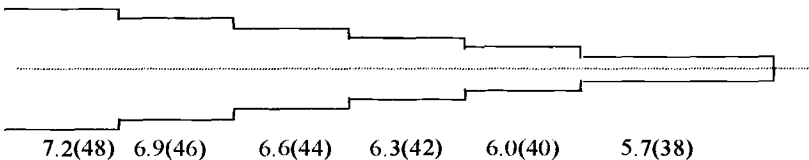


Figure 2 - Schematic diagram of the dropping of plies in the tapered region of STE-26.

Material Properties

The values of elastic constants for a unidirectional laminate under the room temperature condition used for the computation of buckling loads are presented in Table 2. In-plane material data, namely, E_1 , E_2 , G_{12} and ν_{12} have been taken from the in-house test data. The shear modulus G_{13} is assumed to be same as G_{12} , which appears to be reasonable since the unidirectional laminate can be considered transversely isotropic. The shear modulus G_{23} would normally be less than G_{12} and more dominated by the resin property. Hence, the shear

modulus value of G_{23} was assumed to be close to the resin shear modulus of 3.2 GPa. A sensitivity analysis made with variations of these moduli values (G_{13} and G_{23}) did not show any significant change in the eigenvalues.

Degraded unidirectional laminate properties were employed to investigate the environmental effect (under the H/W condition) on the compression buckling of these panels. Degraded U.D. laminate properties, obtained from earlier in-house hot/wet tests, were taken for modulus values along directions 1 and 2 and the shear modulus in Planes 1-2 and 1-3, ($E_1 = 127$ GPa, $E_2 = 5$ GPa, $G_{12} = G_{13} = 3.6$ GPa), while other properties were maintained as those used for room temperature conditions [17].

Table 2 – CFC material properties employed in the analysis.

Property	Symbol	RT/AR values	H/W values
Longitudinal Young's Modulus, GPa	E_1	130.0	127.0
Transverse Young's Modulus, GPa	E_2	10.0	5.0
In-plane Poisson's Ratio	ν_{12}		0.35
In-plane Shear Modulus, GPa	G_{12}	5.0	3.6
Shear modulus, GPa	G_{23}		3.2
Shear Modulus, GPa	G_{13}	5.0	3.6
Nominal ply thickness, mm			0.15

In the analysis, actual lay-up sequence was effected by adopting the composite laminate option in MSC-PATRAN and by giving the sequence for the total laminate. Reference 0° for the lay-up was oriented along the longitudinal dimension of the laminate, which was also the loading direction. As mentioned earlier, analyses were carried out with pseudo simply supported boundary conditions. The 540 mm X 241 mm panel was adopted for modelling this configuration. While modelling, it was ensured that the nodes were located at points on the panel where the boundary conditions were to be applied. For pseudo simply supported conditions, nodes falling on the lines of knife-edge placement on the panels were constrained for out-of plane deflection, and rotations were constrained about the x-axis or the y-axis appropriately. At one end of the laminate, only in-plane deflection along the loading direction was permitted and the rest of deflections and the rotations were suppressed. On this end, the load was applied uniformly. At the other end of the panel, all the deflections and rotations were suppressed. Applied boundary conditions and loads are shown schematically in Figure 3.

Results of FEM Analysis

From the FEM analysis, mode shapes and corresponding buckling loads were obtained for at least first five modes from the eigenvectors and the corresponding eigenvalues. The load corresponding to the lowest eigenvalue and therefore the lowest buckling load was taken as the critical buckling load for the panel and the corresponding mode shape was considered as the first buckling mode shape.

The predicted lowest buckling loads, based on nominal ply thickness, have been shown in Table 3 and predicted mode shapes for the two ply-drop panel configurations are presented in Figure 4. . The deformed contour of panel with 70° ply drop zone orientation, varied along the ply drop zone.

The second half-sine-wave began along the ply drop zone. Mode shapes observed for the lowest buckling load in all the panels were found to be similar. Mode shape, corresponding

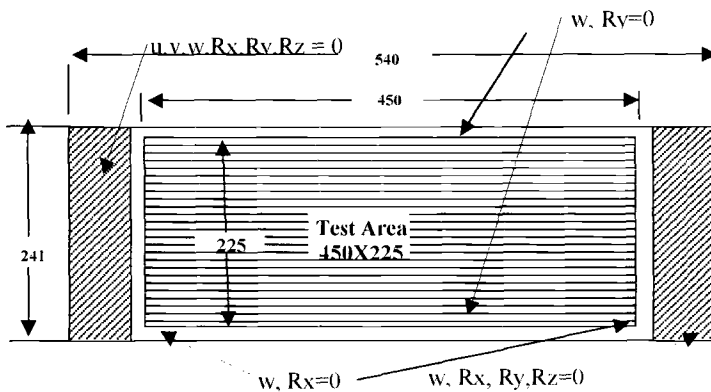


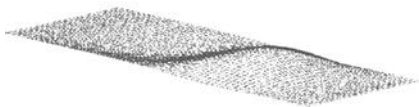
Figure 3 - Schematic drawing describing the boundary conditions applied in the FEM Analysis.

to the lowest buckling load or the first flexural mode, consisted of two half-sine waves, as expected for a panel of a/b ratio = 2. The half-sine wave corresponding to the thicker zone of the CFC panel exhibited lesser out-of-plane deflection, also as expected. A larger deflection was observed for the region corresponding to the thinner portions of the panels. Mode shape did not vary for the analysis carried out with degraded material properties, simulating the hot/wet environmental conditions. Critical buckling loads obtained from the analysis carried out with original room temperature properties and degraded hot/wet properties have been compared with the experimentally obtained buckling loads under Room Temperature As Received (RT/AR) and Hot/Wet (H/W) environmental conditions.

Table 3 – FEM predicted buckling loads and mode shapes.

Specimen ID	FEM RT/AR (kN)	FEM Hot/Wet (kN)	Laminate ply drop configuration & Mode Shape
STE-24	176.05	162.62	
STE-26	206.00	186.68	

STE - 24



STE - 26

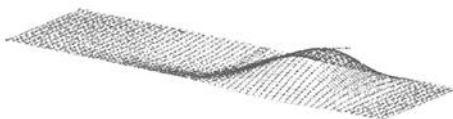


Figure 4 - Buckling mode shapes predicted from FEM analysis.

Experimental Analysis

Materials and Test Panels

In this study, buckling tests on composite panels containing ply drops have been carried out as part of the structural integrity test program to substantiate the soundness of design for buckling-critical CFC skin-like structures and prediction capability of FEM analysis. CFC panels have been fabricated from unidirectional prepreg tapes of T300/914C with a nominal ply thickness of 0.15 mm. Panels tested had two different ply-drop configurations as described earlier under FEM analysis. The panel dimensions were 540 mm X 241 mm and a pseudo simply supported boundary condition was provided on the boundary of 450 mm X 225 mm area of the CFC panels as explained earlier, thus providing an aspect ratio of 2 for compression loading along the longitudinal axis. The lay-up and stacking sequence of the panels tested have been shown earlier in Table-1. Glass fiber reinforced plastic (GFRP) tabs were provided at the loaded ends to provide proper support and to prevent end-brooming under compressive loading.

Specimen Preparation for Room Temperature and Hot/Wet Test

CFC panels made of two different ply drop configurations were fabricated and delivered for testing after ascertaining through Ultrasonic C-Scan testing that none of them had any manufacturing defects. All the panels were suitably strain gaged, with back-to-back strain gages at around one-quarter and three-quarter distances along the unsupported length dimension of the panels. However, in the thicker portion of the test panels, the back-to-back gages were fixed close to the ply drop region. The strain gages on the test panels that were identified to be tested under hot/wet conditions, were very carefully moisture-proofed with a four-layered technique to protect the foil gage grids against corrosion during the long exposure to hot and humid environment. The selected specimens were placed in an environmental conditioning chamber that was maintained at a temperature of $70^{\circ}\text{C} \pm 2^{\circ}\text{C}$ and $85\% \pm 5\%$ relative humidity. Since the panels could not be taken to sensitive electronic weighing balance, smaller coupons representative of the higher thickness portion of the specimens, called the traveler coupons, were also placed inside the environmental chamber. The percentage weight gains of the traveler coupons were monitored at frequent intervals. Based on the past experience with moisture conditioning of uniform thickness CFC panels [17], it was necessary to moisture-condition them up to 1% moisture gain by weight over a period of almost six months after which these panels were taken out for testing under hot/wet environmental condition at $100^{\circ}\text{C} \pm 3^{\circ}\text{C}$ and $\geq 85\%$ Relative Humidity.

Design and Development of Test Fixtures

The two different ply drop configurations selected for testing under this program necessitated design and development of three different sets of knife edges. With a view to accomodate all the different configurations of panels within the same main test fixtures, two similar front and back support plates were employed with a provision to fix variable depth knife edges of detachable type to their inner faces. Since the base plate remained the same, only the knife edges(of different depths) were changed for different ply drop configurations. The fixture details of a sample configuration is shown in Figure 5. During the assembly of test fixtures and trial loading, it was observed that with rotation freely allowed at the knife edge supports, upon loading, the ends of the panel moved sidewise(out of plane). This created a problem in maintaining perfect load-line alignment, which could be effectively monitored from the comparison of the output of the back-to-back strain gages at any location on the CFC panel. In order to over come this difficulty, the ends were located inside grooves in the pair of end plates, thereby partially preventing the free lateral movement of the loading ends. The simply support condition (of position-fixed and direction-free) at the loading ends was therefore simulated only at the knife-edges attached to the front and back support plates, but the GFRP-tabbed-ends were not freely allowed to rotate about the knife-edges. The boundary conditions achieved is therefore called as "pseudo simply support" condition. However, this has been accounted for in the FEM analysis carried out by using MSC PATRAN / NASTRAN Packages.

For conducting the test under a hot/wet environment, the above test fixtures were required to be enclosed within a split type environmental test chamber made of aluminum sheets. The sheets were suitably shaped to enable in-situ mounting around the test specimen during the test. The environmental test chamber had the openings for inlet of steam, insertion of stems of LVDTs or dial gages, thermocouples and outlets for the lead wires of all strain gages. These openings were properly sealed with adhesive tape to minimize the steam leakage during the test.

Test Procedure

All the tests were carried out on a servo hydraulic test system of adequate capacity (500 kN). For room temperature test, the CFC laminate was fixed to the two sets of end-clamping plates with grooves. The front and back support plates with appropriate knife-edges were carefully mounted on the plate at the desired position, and these were then clamped together. Then this plate assembly was mounted on to the test machine and attached to the top and bottom clevices. All the transducers, including strain gages, LVDTs / dial gages, load and stroke channel outputs were connected to the data acquisition system. Initially, an attempt was made to provide some clearance between the tabbed ends of the panels and the inner-edges of the clamping plates at each end, so that the panel ends could rotate about the knife-edges at the onset of out-of-plane deformation of the panels or at buckling. Unfortunately, that created a major problem in the proper alignment of the mid-thickness plane of the panels with the compression loading axis of the test machine load frame and even under small compression loads in the order of 20 kN to 30 kN, the out-of-plane deformations and inequality of back-to-back strain gage output were observed to be primarily due to bending as a consequence of the eccentricity of loading caused by the lateral shifting of the panel-ends inside the grooves

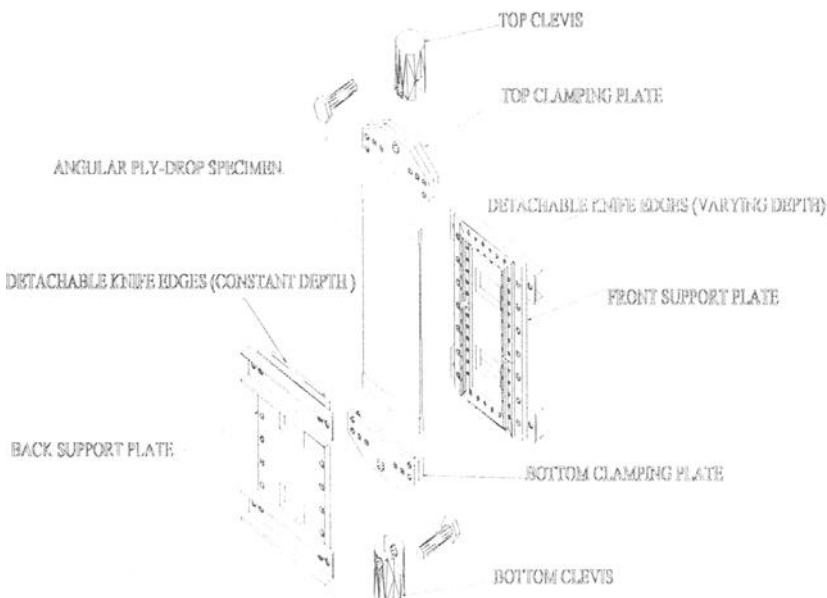


Figure 5 - Schematic diagram of test fixtures employed for compression buckling of CFC panels containing ply drops.

of the clamping plates. In view of this, the snug-fit condition between the panel-ends and the grooves of the split-type clamping plates was necessary to proceed with the test. After ensuring proper load line alignment, a small load was applied in a few steps and the outputs of back-to-back strain gages and out-of-plane displacement readings were critically examined. In the event of large differences in the above readings, the test panel alignment with loading axis was considered to be improper and the test fixtures were dismantled and reassembled again with thin aluminum shims inserted in the grooves of the bottom/top clamping plates to ensure proper in-plane compression loading without bending of the CFC panel. The tests were carried out under stroke control and generally at a rate of 0.009 mm/sec up to buckling and beyond up to ultimate failure. The transducer output data were recorded in the data acquisition system. In a few cases where the out-of-plane displacements were measured with dial gages, the load application was carried out in small steps. While close to the buckling load, the out-of-plane deformed shape of the thinner and thicker portions of the CFC laminate could be seen through the top and bottom cut-outs on the front and back support plates. The loading was continued in the post-buckling regime until the final failure of the CFC panel. The output of all the back-to-back strain gages and out-of-plane displacement transducers were observed in real time on the monitor of the data acquisition system during the test.

In a hot/wet test, the CFC panel had to be removed from the environmental chamber after proper moisture conditioning and then positioned between the top and bottom clevices in the

test system as in the case of room temperature testing. After ascertaining proper alignment of the CFC panel with the loading axis as before, the two halves of the split type environmental test chamber were assembled enclosing the front and back support plates. Then the two pairs of steel channels at top and bottom were assembled and clamped to provide lateral support to the test chamber. Next, all the transducers were placed in position and connected to the data acquisition system and the steam inlet was connected to a steam supply line. Two button-head type thermocouples were fixed to the CFC skin at the front and back of the panel for monitoring the temperature in real time during the hot/wet test. Figure 6 shows typical test setup for CFC panel buckling test in a 500 kN servo-hydraulic test machine. Figure 6(a) shows a room temperature test setup and Figure 6(b) shows a typical test setup used for panel buckling test under hot/wet environmental condition. At the commencement of the hot/wet test, steam was let in until the temperature on both faces of the CFC panel reached the desired value of $100^{\circ}\text{C} \pm 3^{\circ}\text{C}$ with a soaking time of about 5 minutes. Next, all strain channels were re-zeroed and recalibrated before application of load. Subsequently, the test was conducted as before (as for the room temperature test) while monitoring all the transducer output on the monitor screen in real time. All the recorded data were later reduced to appropriate format and analyzed for proper determination of the critical buckling load of the CFC panels.

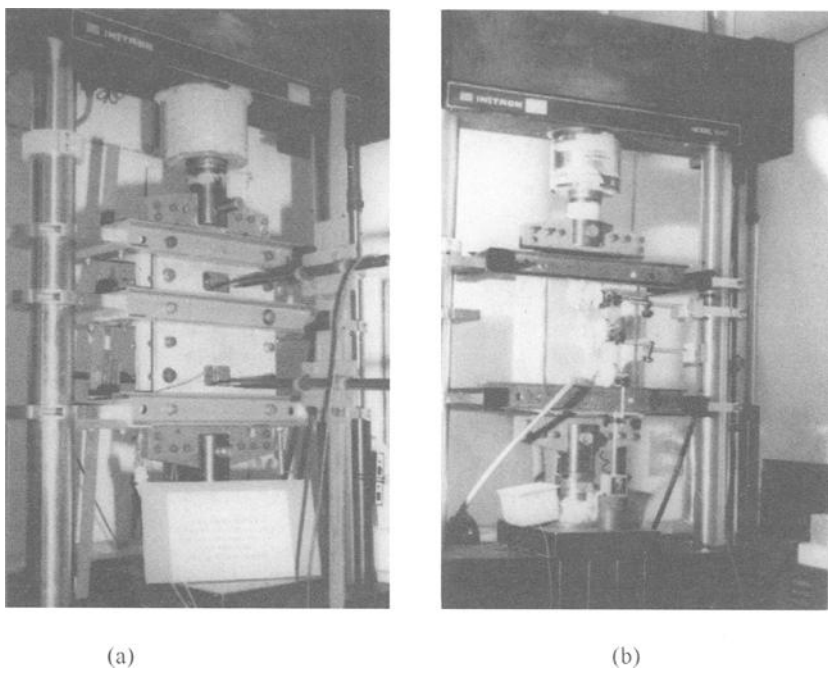


Figure 6 – Typical test setup for CFC panel buckling test in a 500 kN servo-hydraulic test machine: (a) under room temperature, (b) under hot/wet environmental conditions.

Analysis of Test Results

The test data in the form of output of load cell, strain gage, LVDT/dial gage, thermocouple, etc. were acquired/recorder during the CFC panel buckling tests. These data were subsequently analysed with a view to determine the critical buckling load for each panel tested under compressive loading. Keeping in view the likely scatter in the evaluation of buckling loads of the CFC panels with different ply drop configurations, at least two panels were tested for each ply drop configuration under both room temperature and hot/wet environmental conditions.

Figure 7 shows some typical strain and out-of-plane deformation data plotted against applied compressive load. Figure 7(a) shows the variation of out-of-plane deformations under room temperature testing at four LVDT locations, roughly corresponding to the one-quarter points, along the length of the panel, between the top and bottom knife-edge support positions. It may be noted that all the panels tested were mounted at the test fixture in such a way that the thicker portion of the panel was always held in the bottom clevis and the thinner portion of the panel was held in the top clevis. From the magnitudes of the out of plane deformations in Figure 7(a), it can be seen that all the LVDTs had virtually no deflection up to about 150 kN of load and that the back-to-back LVDTs connected to the bottom (thicker portion) of the plate had almost half the deflection of that of the two LVDTs mounted at the top of the panel close to ultimate failure. It may also be noted from the nature of these deflections that the buckled shape of the CFC panel had concavity (caved in) in the top portion and it had convexity (bulged out) in the bottom portion of the panel, as viewed from the front of the panel. The magnitude of bulging in the bottom was much less compared to the caving in at the top of the panel. This was also confirmed by visual inspection through the top and bottom cut-outs in the front and back support plates.

Figure 7(b) shows typical microstrain output versus load response of two pairs of strain gages mounted back to back close to the top and bottom one-quarter points (as described above). It is observed that the strain magnitudes of the top (thinner) portion of the CFC panel are much higher than that of the gages mounted to the bottom (thicker portion) of the panel. Also, from the nature (tensile/compressive) of the strains, it is easy to deduce that, viewed from the front of the panel, the top portion had caved in and the bottom portion had bulged out due to buckling. Similarly, two typical out of plane displacement and strain response plots using data from hot/wet test have been shown in Figure 7(c) and Figure 8(a). Here too, the conclusion on higher deformation of the thinner portion of the ply drop panel can be ascertained and the buckling mode shape can be deduced from the nature of deformation and strain data acquired from the hot/wet test.

It may be noted that determining the critical buckling load of a panel from the out-of-plane deformation plots or strain response plots directly is rather difficult and may have subjective error. In order to objectively derive the same, the use of the Southwell method [17, 18] has been found to be pragmatic in the past. This method, which was originally developed to determine critical Euler buckling load for an axially loaded strut, pre-supposes that for an out-of-plane deformation, v , under given axial load, P , the Euler buckling load, P_E satisfies with sufficient accuracy a relation of the form, $P_E \cdot v/P - v = \text{constant}$. Hence, by plotting v against v/P one obtains a straight line, the slope of which gives the critical buckling load, P_E . This very useful and simple method for the interpretation of buckling test results was originated by R. V. Southwell in 1932 [18]. It has often been used also in the case of other buckling and structural instability experiments. Figure 8(b) and Figure 8(c) show two sample Southwell plots drawn respectively for hot/wet and room temperature tests, based on the strain output data acquired. In the present analysis, considering the average value of the buckling loads, determined from several strain/displacement channel data in each panel,

the critical buckling loads have been obtained which have been listed in Table 4 along with the ultimate failure loads. Figure 9 shows a schematic of a sample buckled mode shape deduced from the transducer output data during the test. This was necessary, especially in hot/wet tests, as the front and back support plate cut-outs were inaccessible during such a test. It has been ascertained that the first mode of buckling for a panel of aspect ratio 2.0 as predicted by FEM (Figure 4) was realized in all the specimens tested.

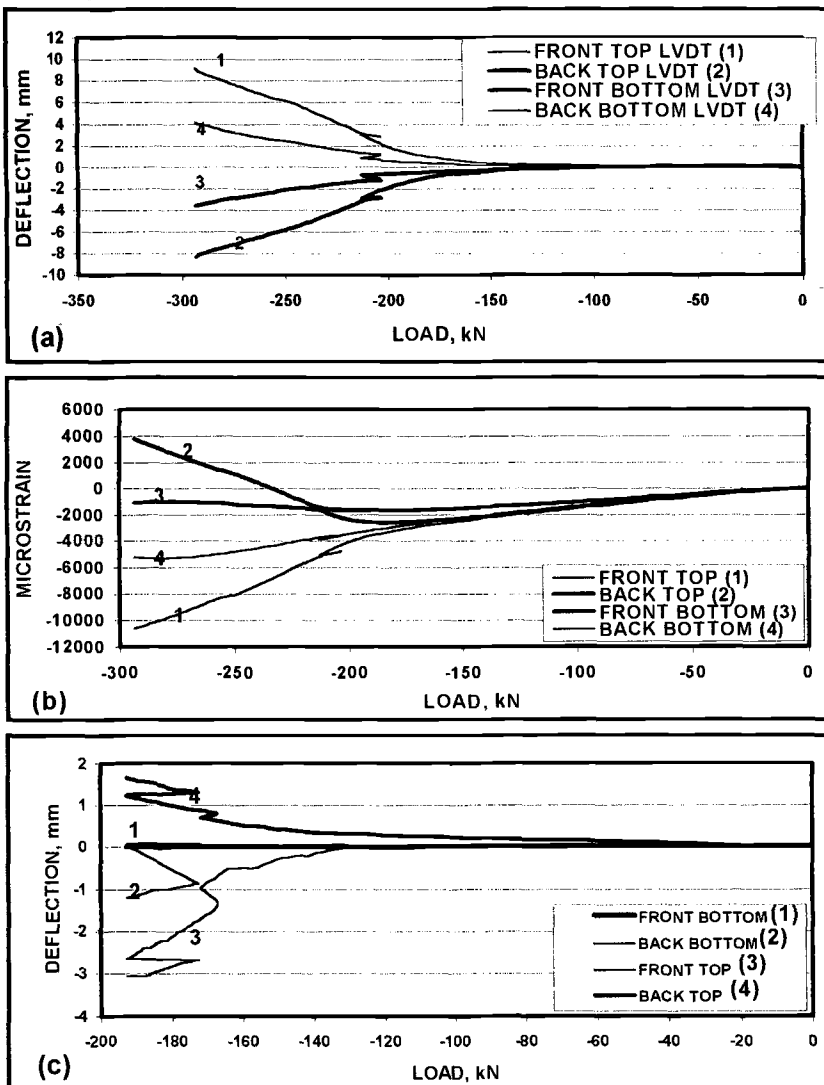


Figure 7 – Sample plots showing variation of transducer output with compression load from test: (a) typical out-of-plane deformation Vs. load (RT/AR). (b) typical strain response plot (RT/AR). (c) typical out-of-plane deformation plot under hot/wet conditions.

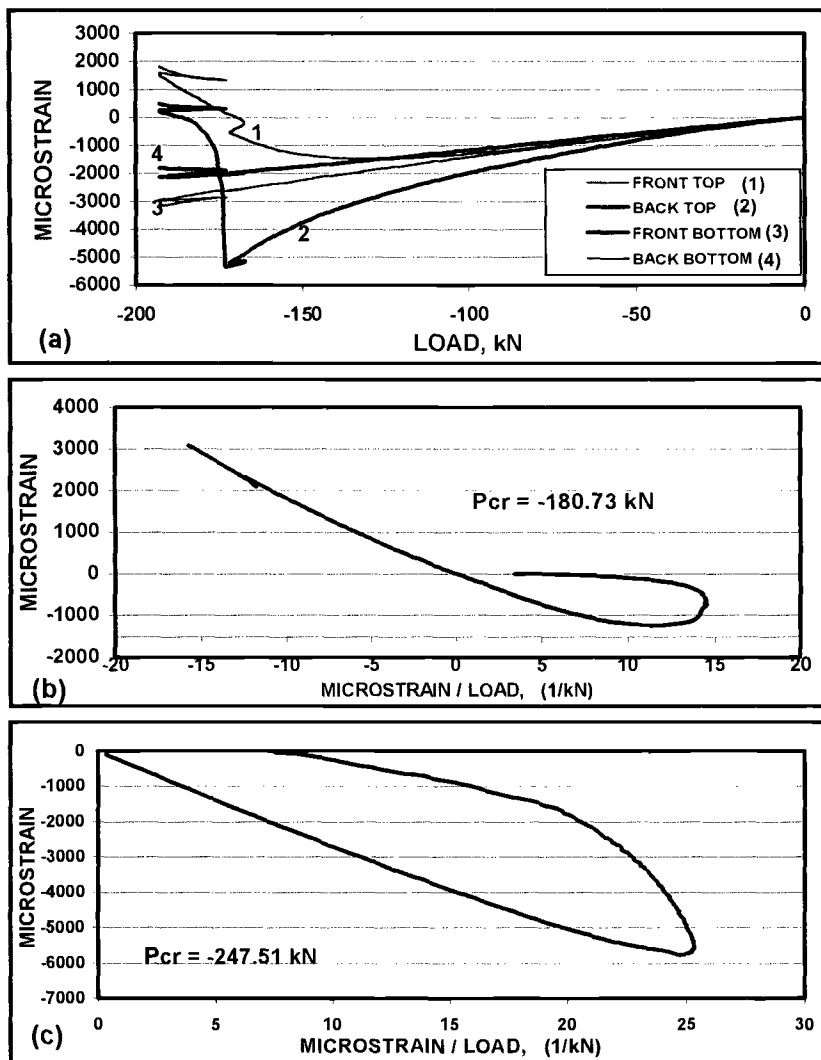


Figure 8 – Sample transducer output from test and determination of critical buckling loads: (a) typical strain response plot under hot/wet condition, (b) typical Southwell plot based on strain response (hot/wet), (c) typical Southwell plot based on strain response (RT/AR).

During the test, almost all the CFC panels exhibited considerable post-buckling strength prior to ultimate failure. The ultimate fracture modes of the CFC panels with two different ply-drop configurations have been found to be different from the test. The panels with

normal ply drop (ply drop zone normal to the loading axis) invariably failed by delamination near the thinner or the thicker tabbed-ends. But, the panels containing inclined ply drops

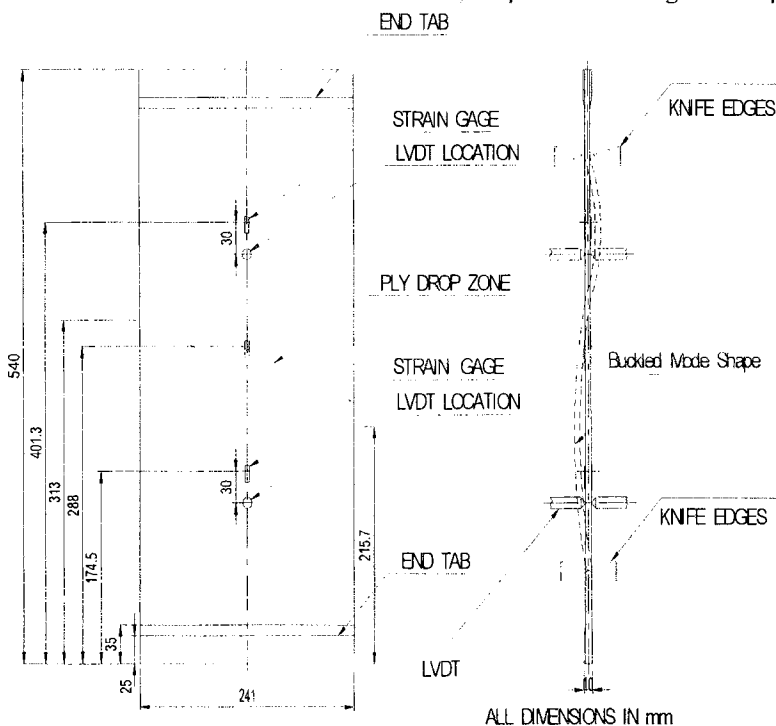


Figure 9 – A sample schematic sketch showing transducer locations in CFC panel buckling test and visualization of buckling mode shape from transducers output.

exhibited large out-of-plane deformations of the thinner portion of the panel and at least two panels failed in the mid-section of thinner portion of the panel. It was observed that none of the panels failed close to the ply drop region despite the large out of plane deformation suffered by the thinner section of the panel. It is conceivable that had the end-tabbing been made proper to withstand higher compressive loads (above almost 300 kN), possibly the fracture would have initiated in the ply drop region.

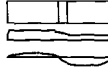
In Table 5 average buckling loads and buckling mode shapes, obtained from the test, have been compared with those predicted from FEM analyses that were based on both nominal ply thickness, $t = 0.150$ mm and average ply thickness of $t = 0.155$ mm, deduced from actually measured test laminate thickness. It may be noted that while using the actual ply thickness, the modulus values (notably E_1) need also to be corrected to reflect change in volume fraction ($E \cdot t = \text{constant}$). Following common practice, the values of E_1 , both under RT/AR and H/W conditions, have been revised, while assuming other elastic constants (mainly resin dominated properties) to remain unchanged. With these corrections, the FEM loads have been computed and presented in column 4. Column 3 of this table shows the modulus values of E_1 used in FEM analyses corresponding to different ply thickness. In the 5th column the critical buckling loads obtained from two panels for each ply drop configuration under room

temperature test condition and for actual ply thickness of $t = 0.155$ mm have been shown. It may be observed that while the mode shapes of buckling were identical both from analysis

Table 4 – Summary of test results from CFC panel buckling test under RT/AR and Hot/Wet conditions.

SL. NO	SPECIMEN ID and Mode of Fracture	PLY DROP TYPE	TEST CONDITION	FAILURE LOAD (kN)	BUCKLING LOAD, P_{cr} (kN)
1	NT-FFC-STE-026(1) Tabbed end delamination	NORMAL PLY DROP	RT	280.00	247.51
2	NT-FFC-STE-026(2) Tabbed end delamination	NORMAL PLY DROP	RT	250.00	227.46
3	NT-FFC-STE-026(3) Tabbed end delamination	NORMAL PLY DROP	H/W	224.37	187.82
4	NT-FFC-STE-026(4) Tabbed end delamination	NORMAL PLY DROP	H/W	184.67	158.15
5	NT-FFC-STE-024(1) Failed at thin section	INCLINED PLY DROP	RT	281.50	231.21
6	NT-FFC-STE-024(2) Tabbed end delamination	INCLINED PLY DROP	RT	263.27	204.48
7	NT-FFC-STE-024(3) Failed at thin section	INCLINED PLY DROP	H/W	197.88	180.63
8	NT-FFC-STE-024(4) Tabbed end delamination	INCLINED PLY DROP	H/W	192.85	177.61

Table 5 – Comparison of buckling loads from test and FEM analysis.

Panel ID	Critical buckling loads, P_{cr} (kN)								Ply drop configuration and mode shape FEM/Test	
	RT/AR				Hot/Wet					
	FEM		Test [†]		FEM		Test [†]			
	t (mm)	E_1 (GPa)	P_{cr} (kN)		t (mm)	E_1 (GPa)	P_{cr} (kN)			
	0.150 0.155	130.0 125.8	176.05 187.59	- 231.2 204.5	0.150 0.155	127.0 122.9	162.62 173.81	- 180.6 177.6		
STE24										
STE26	0.150 0.155	130.0 125.8	206.00 220.82	- 247.5 227.5	0.150 0.155	127.0 122.9	186.68 199.70	- 187.8 158.1		

[†] Two specimens were tested under each ply drop configuration and environmental condition.

and test, the magnitudes of critical buckling loads, obtained from tests, were somewhat higher than those computed by FEM with nominal ply thickness of 0.150 mm. The revised FEM values computed considering actual ply thickness of 0.155 mm and corresponding modulus value of E_1 , were somewhat higher and therefore closer to the buckling loads, obtained from test. Similarly, under hot/wet environmental conditions, the computed buckling load values have been shown in column 8 and the test values have been shown in column 9. It is seen that with the corrected ply thickness and modulus values, the predicted buckling loads are slightly lower but close to the test values, except in the case of hot/wet

buckling test result for one panel of STE-26, which for some reason exhibited relatively lower test value. This could have been due to slight initial load line misalignment of panel, STE-026(4) during the hot/wet test, which had resulted in a rather low critical buckling load of 158.15 kN. It may also be noted from Table 4 that this panel had failed due to tabbed end delamination at an ultimate load of 184.67 kN, the lowest in this series of test.

Concluding Remarks

In this investigation, the effect of thickness tapering through ply drops in composite laminates was studied using FEM analysis and actual testing with simulation of nearly simply supported boundary conditions. The influence of hot/wet environmental conditioning on the critical buckling load and ultimate failure of CFC panels with two different ply drop configurations has also been studied. For FEM analysis, an MSC NASTRAN software package has been used. Critical buckling loads and mode shapes obtained for all the cases have been presented and compared with the experimental values. It is seen that thickening of a portion of the laminates and use of different ply-drop configurations had resulted in variation of flexural rigidity and hence in buckling behavior.

The comparison between the FEM and actual test results with regard to critical buckling loads and mode shapes indicate that the mode shape corresponding to the lowest buckling load was identical between the analysis and test. However, the magnitudes of critical buckling loads were invariably under-predicted by the FEM analysis as compared to the experimentally obtained values. This has been ascribed to the slightly higher thickness of the CFC panels actually measured at the time of test. A revised FEM analysis carried out, considering the increased ply thickness of the panels and corresponding correction to the modulus, E_1 , has yielded revised critical buckling loads that are closer to the test values. It has been observed that all the CFC panels tested had exhibited reasonably good post-buckling strength before failure. On examination of the modes of failure, it is seen that in most cases the failure of the panels was due to the tabbed end delamination despite locating the tabbed ends of the panels inside the grooves of end-clamping plates. Indeed, the panels could have shown much higher post-buckling strength and could have reached still higher ultimate failure loads had the panel-ends been prevented from premature delamination failure at the time of testing.

Acknowledgments

The authors would like to thank the National Team CFC Wing for undertaking this investigation. They are grateful to Dr. K.N. Raju for his encouraging support and to the authorities of HAL, Bangalore, for fabrication of the specimens. They would like to thank Sri M.V. Mukund for the design support on the test fixtures, Sri A.S. Babu for strain gaging and all the MEL-staff of SID for conducting the test.

References

- [1] Sanger, K. B., Dill, H. D., and Kautz, E. F., "Certification of Testing Methodology for Fighter Hybrid Structure," *Composite Materials: Testing and Design (Ninth Volume)*, ASTM STP 1059, S. P. Garbo, Ed., American Society for Testing and Materials, West Conshohocken, PA, 1990, pp. 34-37.
- [2] "Polymer Matrix Composites – Guidelines," MIL-HDBK-17-1C, Vol. I, Department of Defense, Washington DC, 1988.

- [3] Berg, M., Gerharz, J. J., and Gokgol, O., "Consideration of Environmental Condition for the Fatigue Evaluation of Composite Airframe Structures," *Composite Materials: Fatigue and Fracture, ASTM STP 1012*, P.A. Lagace, Ed., American Society for Testing and Materials, West Conshohocken, PA, 1989, pp. 29-44.
- [4] Verette, R. M. and Labon, J. D., "Structural Criteria for Advanced Composites," AFFDL-TR-76-142, Air Force Flight Dynamics Laboratory, Dayton, OH, 1976.
- [5] Flaggs, D. L. and Vinson, J. R., "Hygrothermal Effects on the Buckling of Laminated Composite Plates," *Fibre Science and Technology*, Vol. 11, 1978, pp. 353-356.
- [6] Collings, T. A. and Stone, D. E. W., "Hygrothermal Effects in CFRP Laminates: Strains Induced by Temperature and Moisture," *Composites*, Vol. 16, No. 4, 1985, pp. 307-316.
- [7] Chamis, C.C., "Buckling of Anisotropic Composite Plates," *Journal of the Structural Division (ASCE)*, Vol. 95, 1969, pp. 2119-2139.
- [8] Ashton, J. E., "Approximate Solutions for Unsymmetrically Laminated Plates," *Journal of Composite Materials*, Vol. 3, 1969, pp. 189-191.
- [9] Vinson, J. R. and Chou, T. W., *Composite Materials and Their Use in Structures*, Applied Science Publishers Ltd., London, 1976.
- [10] Chamis, C. C., "Theoretical Buckling Loads of Boron/Aluminium and Graphite/Resin Fibre Composite Anisotropic Plates" NASA TN D-6572, December 1971.
- [11] Whitney, J. M. and Leissa, A. W., "Analysis of Simply Supported Laminated Anisotropic Rectangular Plate," *AIAA Journal*, Vol. 8, 1970, pp. 28-33.
- [12] Chia, C. Y. and Prabhakara, M. K., "Postbuckling Behaviour of Unsymmetrically Layered Anisotropic Rectangular Plates," *Transactions of ASME, Journal of Applied Mechanics*, Vol. 4, 1974, pp. 155-162.
- [13] Chia, C. Y., *Nonlinear Analysis of Plates*, McGraw Hill Inc., New York, 1980.
- [14] Leissa, A. W., "Buckling of Laminated Composite Plates," *Composite Structures*, Vol. 1, 1983, pp. 51-66.
- [15] Chai, G.B., "Buckling of Generally Laminated Composite Plates," *Composite Science and Technology*, Vol. 45, 1992, pp. 125-133.
- [16] Chai, G. B., "Buckling of Laminated Composite Plates with Edge Supports," *Composite Structures*, Vol. 29, 1994, pp. 299-310.
- [17] Parida B K., Prakash R V, Ghosal A K, Mangalgiri P D, and Vijayaraju K, "Compression Buckling Behavior of Laminated Composite Panels", *Composite Materials : Testing and Design, Thirteenth Vol., ASTM STP 1242*, S J Hooper, Ed.. American Society for Testing and Materials, 1997, pp. 131-150.
- [18] Southwell, R. V., "On the analysis of experimental observations in problems of elastic stability," *Proceedings of Royal Society (London), Series A, Vol. CXXXV*, 1932, p. 601

Author Index**A**

Adams, D. F., 3
 Asp, L. E., 235

M

Mangalgiri, P. D., 253
 Moon, T. J., 30

C

Case, S. W., 173
 Chelladurai, K., 69
 Cohen, D., 17

N

Neft, J. F., 156
 Nettles, A. T., 116, 139

D

Dash, P. K., 69
 Douglas, M. J., 116, 139

P

Pagano, N. J., 200
 Parida, B. K., 69, 253
 Phelon, P., 212
 Prabhakaran, R., 139

G

Greenhalgh, E. S., 221, 235

R**H**

Hakeem, S. A., 69
 Hiley, M. J., 235

Reifsnider, K. L., 173
 Ruffner, D., 85
 Russell, S. S., 131

J

Jouin, P., 85
 Joyce, P. J., 30

S**K**

Krishnaswami, P., 188

Saha, M., 139
 Schulte, K., 156
 Schwarzer, P., 156
 Shyprykevich, P., 99
 Singh, S., 221
 Sjögren, A., 235
 Sun, C., 200
 Sun, X., 200

L

Lansing, M. D., 131
 Lesko, J. J., 173
 Li, W.-Y., 212

T

Terpant, G., 188
 Tomblin, J. S., 99
 Tseng, A. A., 212

INDEX 271

V

Vangel, M. G., 99
Vijayaraju, K., 253
Violette, M. G., 30

W

Walker, J. L., 131
Wang, Y., 188, 200

Z

Zhu, H., 212

Subject Index

A

Acceptance criteria, 99

B

Batch variability, 85
 Bending tests, 156
 Braid sequence, 188
 Buckling load, 253
 Buckling strength, 69

C

Carbon/epoxy material, 99, 235
 Carbon fiber, 17, 69
 composite panels, 253
 laminates, 235
 reinforced plastics, 235
 Coefficient of thermal expansion, 212
 Combined loading compression test fixture, 30
 Composite pressure test boxes, 69
 Composite tube test method, 17
 Compression, 139
 loading, 253
 strength, 85
 testing, 3, 30, 156
 Compressive strength, 3, 30
 Contact stresses, 116
 Coupon test, 85
 Crack front, 221
 Crack, interlaminar, 235
 Crack length, back surface, 116

D

Damage mechanisms, 173, 221
 Damage modes, 116
 Damage resistance, 139
 Damage tolerance, 139
 Database, common, for composite materials, 99
 Debonding, 30

Deformation, out-of-plane, 253
 Delamination, 116, 131, 221, 235
 Dent depth, 116
 Design limit load, 69
 Design ultimate load, 69
 Displacement, 200
 Durability assessment, 173

E

ELFINI, 69
 Epoxy resin, 17
 Equivalency tests, 99
 Equivalent hole diameter, 139
 Experimental design, 85

F

Failure criteria, 17, 221
 Failure, interlaminar, 235
 Failure mechanisms, 156
 Failure mode, 173
 Fatigue loading, 235
 Fiber/matrix interface cracks, 235
 Fiber wound composite tubes, 173
 Filament wound, 17
 Finite element analysis, 3, 30, 188, 253
 ELFINI, 69
 MSC NASTRAN, 253
 Fractography, 221, 235
 Fracture behavior, 253
 Fracture toughness, 221
 Fuel feedline characterization, 131
 Fuel tank characterization, 131

G

Glass/polypropylene, 156
 Glass transition temperature, 85

H

Homogenization, 200

H
Hot-wet environment, 69, 253
Hot-wet tension strength, 85
Hydroburst testing, 131

I

Impact testing, 116
Indentation
 testing, quasi-static, 116
 transverse, 139
Interlaminar crack, 235
Isostatic polypropylene, 156

L

Laminate, 99, 116, 156
 carbon fiber composite
 panels, 253
 carbon fiber/epoxy, 235
 fabrication, 85
Life prediction, 173
Load-central displacement, 139
Load-deflection behavior, 116
Loading, 3, 173
 combined, 30
 cyclic, 156
 fatigue, 235
 hydroproof, 131
 static, 156
 transverse, 116
Local domain test, 200

M

Material allowables, 99
Matrix effects, 221
Mechanical degradation, 156
Micro-mechanical test, 212
Micro-mechanics, 200
Microstructure, 131, 156
Mixed-mode bend, 221
Moisture, 221
MSC NASTRAN, 253
Multi-axial composite tube test
 method, 17
Multi-level analysis, 200

N

Nested experimental design, 85

O

Optimization approach, 188

P

Ply drop, 253
Ply interface, 221
Pooling, 99
Porosity, 131
Pressure test box, 69
Pressure vessels, 17
 imperfections, 131
Pultruded composites, 139
 shapes, 173

R

Regression, 85
Reliability, 173
Residual strength, 173
Room temperature test, 253

S

Specimen configurations, 3
Specimen optimization, 30
Static indentation, 116
Statistical methods, 99
Stiffness, 173
Strain, 212
Strain distributions, 139
Strain gages, 69, 212, 253
Stress analysis, 30, 200
Stressed specimens, 212
Structural integrity test, 69

T

Tabs, specimen, 3, 30
Technical textile, 156
Temperature, reduced, 212
Tensile tests, 156
Tension/compression, 17, 85
Thermal mechanical analyzer,
 212
Thermography, 131
Thermoplastics, 156
Three-dimensional braided
 composites, 188
Torsion, 17

274 COMPOSITE MATERIALS

Toughness, fracture, 235	X
Transverse indentation, 139	
Transverse loading rate, 116	
Tube test method, 17	X-radiography, 139
W	
Weibull distribution statistics, 99	
Y	
	Yarn structure, 188